Adaptive Ultrasound Neuroimaging

Waasdorp, R.

DOI
10.4233/uuid:606050e5-c38b-47b2-ba6b-c403c1245535

Publication date
2025

Document Version
Final published version

Citation (APA)
Waasdorp, R. (2025). *Adaptive Ultrasound Neuroimaging*. [Dissertation (TU Delft), Delft University of Technology]. https://doi.org/10.4233/uuid:606050e5-c38b-47b2-ba6b-c403c1245535

Important note
To cite this publication, please use the final published version (if applicable).
Please check the document version above.

Adaptive Ultrasound Neuroimaging

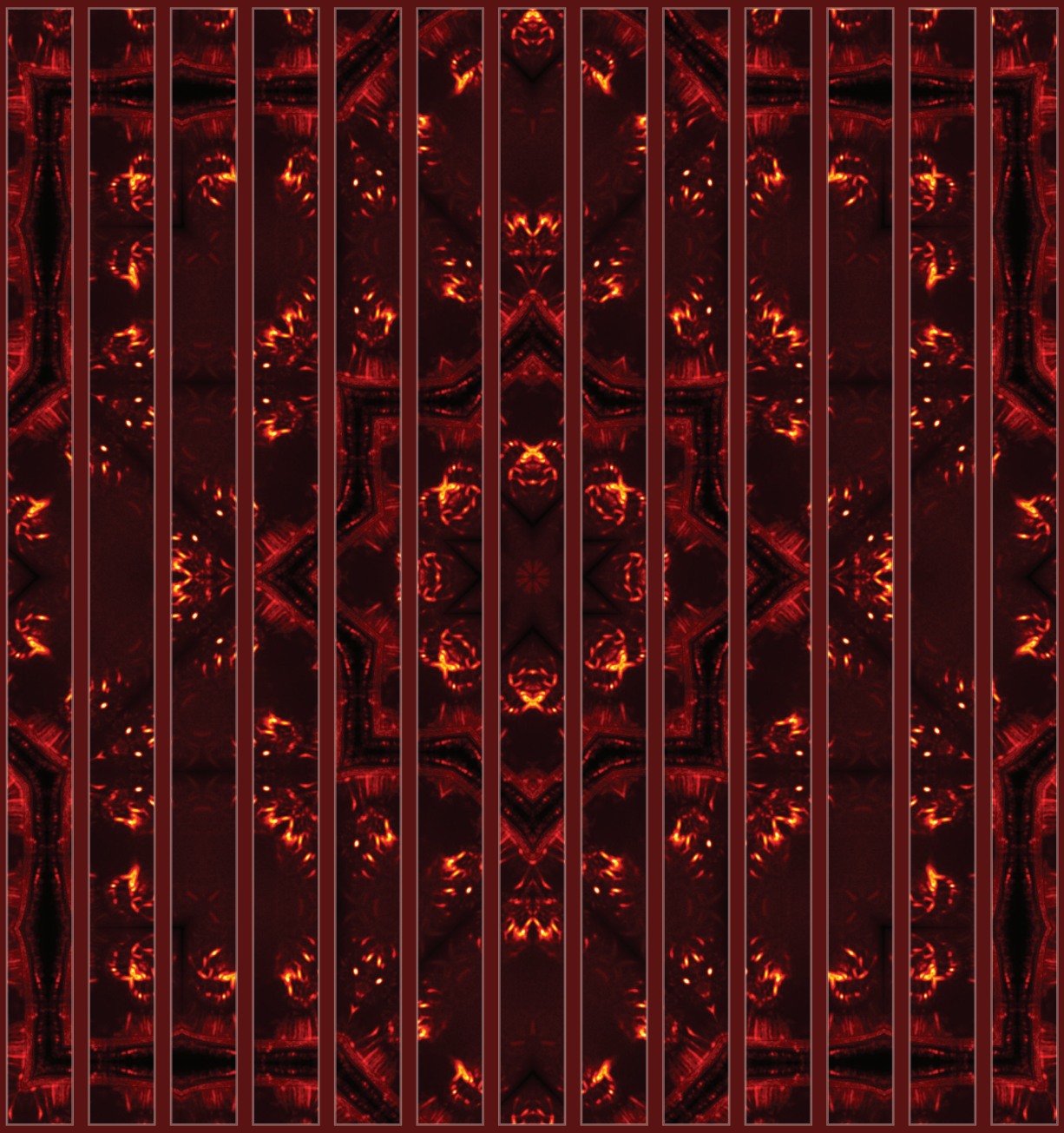

Rick Waasdorp

Adaptive Ultrasound Neuroimaging

Adaptive Ultrasound Neuroimaging

Proefschrift

ter verkrijging van de graad van doctor
aan de Technische Universiteit Delft,
op gezag van de Rector Magnificus prof. dr. ir. T.H.J.J. van der Hagen,
voorzitter van het College voor Promoties,
in het openbaar te verdedigen
op vrijdag 14 november 2025 om 12.30 uur

door

Rick Waasdorp

Master of Science in Mechanical Engineering,
Technische Universiteit Delft, Delft,
geboren te Heemstede, Nederland.

Dit proefschrift is goedgekeurd door de

Promotor: Prof. dr. N. de Jong
Copromotoren: Dr. D. Maresca, Dr. Dipl.-Ing. G.G.J. Renaud

Samenstelling promotiecommissie:

Rector Magnificus,	voorzitter
Prof. dr. N. de Jong,	Technische Universiteit Delft
Dr. D. Maresca,	Technische Universiteit Delft
Dr. Dipl.-Ing. G.G.J. Renaud,	Technische Universiteit Delft
Onafhankelijke leden:	
Prof. dr. ir. A.C. Schouten	Technische Universiteit Delft
Dr. T. Deffieux	Institute Physics for Medicine Paris
Dr. V. Giagka	Technische Universiteit Delft
Dr. D.H.M. Meijer	Technische Universiteit Delft
Prof. dr. S.M. Witte	Technische Universiteit Delft, reservelid

The work in this dissertation was conducted at the Laboratory of Medical Imaging, Department of Imaging Physics, faculty of Applied Sciences, Delft University of Technology. The work has been partially funded through the Medical Delta Ultra HB program.

Keywords:	medical ultrasound, aberration correction, transcranial imaging, functional ultrasound, speed of sound estimation, ray tracing, row column addressed arrays, biomolecular ultrasound
Printed by:	Gildeprint
Cover:	Designed by Rick Waasdorp. The cover shows two kaleidoscopic transformations of an aberration corrected transcranial Doppler image of the rat brain.

ISBN 978-94-6518-183-7

An electronic version of this dissertation is available at
http://repository.tudelft.nl/.

Contents

Summary

Ultrasound imaging is a widespread clinical tool, known best for prenatal examinations of developing human embryos. Recently, a technological breakthrough has revolutionized the field of ultrasound imaging by enabling imaging at thousands of frames per second. This increase in temporal resolution has opened the door to many new applications, such as monitoring the subtle motion of heart walls, measuring electromechanical waves in muscles and detecting the stiffness of organs. Furthermore, the fast frame rates have significantly improved ultrasound sensitivity to small vessels and enables monitoring of local changes in blood flow. This has let to the development of functional ultrasound imaging (fUS) in 2011.

Functional ultrasound is a new neuroimaging modality that allows imaging of brain function at high spatial and temporal resolution. fUS measures variations in cerebral blood flow that occur in response to neuronal activation, a phenomenon known as neurovascular coupling, and therefore provides an indirect measure of brain activity. The underlying principle is similar as what is measured in functional magnetic resonance imaging (fMRI), the current clinical standard for brain imaging. Compared to fMRI, fUS offers several advantages, it is portable, cost-effective, higher temporal resolution, and higher sensitivity to cerebral blood flow. This makes it a promising tool for both preclinical neuroscience, and clinical application. However, there remain significant challenges to overcome before fUS can be widely adopted in clinical settings.

First, the brain is protected by the skull, which poses a barrier for ultrasound waves. The skull bone distorts and attenuates ultrasound signals, leading to decreased transcranial image quality. Therefore, most studies to date are restricted to animal models, where the skull can be surgically removed or thinned. In humans, fUS has been applied during intraoperative procedures, where the skull is removed, and the brain is exposed. Second, fUS generates enormous amounts of data, which complicates its use in real-time applications.

This thesis addresses both challenges. It focuses on enhancing transcranial image quality, bringing us closer to fully noninvasive, high resolution brain imaging. In addition, it introduces methods for reconfigurable functional imaging, aimed at reducing data rates to enable real time decoding of brain activity into actionable outputs. Together, these advances increase the translational potential of fUS and lower the barrier for clinical and neuroscience adoption.

The field of aberration correction consist in improving image quality by compensating for distortions caused by the medium through which the ultrasound waves travel. In this thesis, we apply aberration correction to restore transcranial image quality. Aberration correction starts with knowing the exact properties of the ultrasound probe. Chapter 2

introduces a simple method to estimate the speed and thickness of the silicone lens on 1D transducers. This calibration is essential to accurately estimate the speed of sound in a medium, independent of imaging depth and transmission parameters. Using optimal lens parameters, and the estimated sound speed, we demonstrated an improvement in image resolution and contrast.

In chapter 3, attention shifts to the challenge of restoring transcranial image quality. An adaptive aberration correction approach is presented, using ray tracing through four tissue layers: transducer lens, skin, skull, and brain. This model estimates wave speeds in each layer, then reconstructs images based on the actual (refracted) wave paths. Applied to Doppler imaging in rats, the method improves both resolution and sensitivity, especially in cortical areas where skull induced aberrations are strongest.

Chapter 4 takes on the problem of high data rates in 3D imaging. Since functional activation in the brain is typically sparse, volumetric imaging often captures unnecessary data. Here, a new technique called selective-plane fUS is introduced. It combines focused wave transmission with a Row-Column Addressed (RCA) transducer to target only the brain regions of interest. This significantly reduces the computational and data transfer load and potentially paves the way for lightweight, portable brain-machine interfaces based on fUS.

In chapter 5, the thesis explores imaging of cellular activity and capillary flow using ultrasound contrast agents. We introduce a technique called Nonlinear Sound-sheet Microscopy (NSSM), that enables high resolution imaging of contrast agents within thin planes. This approach captures both vascular and gene expression data in living tissue and extends ultrasound imaging toward cellular resolution in opaque organs.

Together, these chapters lay the technical foundation for next-generation functional and biomolecular ultrasound: systems that are more accurate, less invasive, and better suited for high resolution brain imaging in real time. By addressing both the physical challenges of wave distortion and the computational load of volumetric data, this thesis brings fUS a step closer to clinical and translational neuroscience applications.

Samenvatting

Echografie is een alom beschikbaar klinisch hulpmiddel, wat vooral bekend is van prenatale onderzoeken van ontwikkelende embryo's. Recentelijk heeft een technologische doorbraak het vakgebied van echografie ingrijpend veranderd door beeldvorming met duizenden beelden per seconde mogelijk te maken. Deze toename in temporele resolutie heeft de deur geopend naar veel nieuwe toepassingen, zoals het monitoren van subtiele bewegingen van hartwanden, het meten van elektromechanische golven in spieren, en het detecteren van de stijfheid van weefsel. Bovendien hebben de hoge framerates de gevoeligheid voor kleine bloedvaten aanzienlijk verbeterd en maken ze het mogelijk om lokale veranderingen in bloedstroom in kaart te brengen. Dit leidde in 2011 tot de ontwikkeling van functionele echografie (fUS).

Functionele echografie is een nieuwe neuroimagingmethode waarmee hersenfuncties met een hoge ruimtelijke en temporele resolutie in beeld kunnen worden gebracht. fUS meet variaties in de cerebrale bloedstroom die optreden als reactie op neuronale activatie, een fenomeen dat bekend staat als de neurovasculaire koppeling. fUS biedt daarom een indirecte meting van hersenactiviteit. Het onderliggende principe is vergelijkbaar met wat wordt gemeten bij functionele *magnetic resonance imaging* (fMRI), de huidige klinische standaard voor hersenbeeldvorming. Vergeleken met fMRI biedt fUS verschillende voordelen: het is mobiel, kosteneffectief, heeft een hogere temporele resolutie en een hogere gevoeligheid voor de cerebrale bloedstroom. Dit maakt het een veelbelovend instrument voor zowel preklinische neurowetenschappen als klinische toepassingen. Er zijn echter nog aanzienlijke uitdagingen die moeten worden overwonnen voordat fUS breed kan worden toegepast in klinische setting.

Ten eerste, de hersenen worden beschermd door de schedel, en die vormt een barrière vormt voor ultrageluidsgolven. Het schedelbot vervormt en verzwakt ultrageluidssignalen, wat leidt tot een verminderde transcraniële beeldkwaliteit. Daarom beperken de meeste onderzoeken zich tot nu toe tot diermodellen, waarbij de schedel chirurgisch kan worden verwijderd of verdund. Bij mensen is fUS alleen nog toegepast in onderzoek, en gelimiteerd tot intraoperatieve ingrepen, waarbij de schedel deels wordt verwijderd en de hersenen worden blootgelegd. Ten tweede genereert fUS enorme hoeveelheden data, wat het gebruik ervan in real-time toepassingen bemoeilijkt.

Dit proefschrift behandelt beide uitdagingen. Het richt zich op het verbeteren van de transcraniële beeldkwaliteit, waardoor we dichter bij volledig niet-invasieve, hogeresolutie hersenbeeldvorming komen. Daarnaast introduceert de thesis een methode voor herconfigureerbare functionele beeldvorming, met als doel het verlagen van benodigde datasnelheden, om zo uiteindelijk hersenactiviteit in real-time te kunnen decoderen naar bruikbare signalen. Samen verhogen deze ontwikkelingen het translationele potentieel van fUS en verlagen ze de drempel voor klinische en neurowetenschappelijke toepassing.

Aberratiecorrectie bestaat uit het verbeteren van de beeldkwaliteit door te compenseren voor vervormingen die worden veroorzaakt door het medium waardoor de ultrageluidsgolven zich voortplanten. In dit proefschrift passen we aberratiecorrectie toe om de transcraniële beeldkwaliteit te herstellen. Aberratiecorrectie begint met het identificeren van de exacte eigenschappen van de ultrageluidstransducer. Hoofdstuk 2 introduceert een eenvoudige methode om de snelheid en dikte van de siliconenlens op 1D-ultrageluidstransducer te bepalen. Deze kalibratie bleek essentieel om de geluidssnelheid in een medium nauwkeurig te kunnen bapen, onafhankelijk van de beelddiepte en ultrageluid transmissieparameters. Met behulp van de gevonden optimale lensparameters en medium geluidssnelheid hebben we een verbetering in beeldresolutie en contrast aangetoond.

In hoofdstuk 3 verschuift de aandacht naar de uitdaging van het herstellen van de transcraniële beeldkwaliteit. Er wordt een adaptieve aberratiecorrectiemethode gepresenteerd, die gebruikmaakt van raytracing door vier weefsellagen: de lens van de transducer, de huid, de schedel en de hersenen. Dit model schat de golfsnelheden in elke laag en reconstrueert vervolgens beelden op basis van de werkelijke (gebroken) golfpaden. Toegepast op Doppler-beeldvorming bij ratten verbetert de methode zowel de resolutie als de gevoeligheid, met name in corticale gebieden waar door de schedel veroorzaakte aberraties het sterkst zijn.

Hoofdstuk 4 behandelt het probleem van hoge datasnelheden in 3D-beeldvorming. Omdat functionele taak gerelateerde activatie in de hersenen doorgaans gelokaliseerd is, legt volumetrische beeldvorming vaak onnodige data vast. We introduceren een nieuwe techniek geïntroduceerd, genaamd *selective-plane* fUS. Deze combineert gefocusseerde golftransmissie met een Row-Column Addressed (RCA) transducer om alleen de relevante hersengebieden te targeten. Dit vermindert de reken- en dataoverdrachtsbelasting aanzienlijk en maakt mogelijk de weg vrij voor lichtgewicht, draagbare hersen-machine-interfaces op basis van fUS.

In hoofdstuk 5 onderzoeken we de beeldvorming van cellulaire activiteit en capillaire stroming met behulp van ultrageluidscontrastmiddelen. We introduceren een techniek genaamd *Nonlinear Sound-sheet Microscopy* (NSSM), die hoge-resolutiebeeldvorming van contrastmiddelen in dunne vlakken mogelijk maakt. Deze aanpak legt zowel vasculaire als genexpressiegegevens vast in levend weefsel en breidt ultrageluidsbeeldvorming uit naar cellulaire resolutie in ondoorzichtige organen.

Samen leggen deze hoofdstukken de technische basis voor de volgende generatie functionele en biomoleculaire echografie: systemen die nauwkeuriger, minder invasief en beter geschikt zijn voor real-time beeldvorming van de hersenen met hoge resolutie. Door zowel de fysieke uitdagingen van golfvervorming als de rekenkracht van volumetrische data te adresseren, brengt dit proefschrift fUS een stap dichter bij klinische en translationele neurowetenschappelijke toepassingen.

1

Introduction

1.1 Functional Neuroimaging

When an ice skater waits at the starting line, the brain prepares to react to the start shot with extreme speed and coordination. The process begins when the starting gun fires and the sound is captured by the ears. Within the ear, mechanical vibrations are converted into neural impulses by sensory hair cells, and these impulses are then transmitted via the auditory nerve to the primary auditory cortex in the temporal lobe, where the sound is registered and identified. This process happens within the first 10 to 30 milliseconds after the sound is heard.

Once the start signal is recognized, activity quickly shifts to brain areas involved in planning and initiating movement. Even before the movement starts, the premotor cortex and supplementary motor area begin preparing the body for action based on previous training and the urgent need to explode off the line [1]. Interestingly, this preparation doesn't start from zero, since many neurons in the motor cortex already show anticipatory activity before any cue appears. Some of these neurons ramp up their firing rate in anticipation, while others decrease their activity, likely to keep the system balanced and prevent making a false start.

Once the motor system receives the go-ahead, these planning areas activate the primary motor cortex, which transforms the prepared plan into precise motor commands. These commands travel down the brain stem and spinal cord, and reach the motor neurons, that finally trigger muscle contractions throughout the body. This entire sensory-to-motor sequence, from detecting the sound to initiating movement, typically happens within 100 to 150 milliseconds. While the skater's muscles contract and push off the starting line, the body simultaneously sends feedback signals about muscle force, length and velocity measured with the sensors in the muscles (such as muscle spindles and Golgi tendon organs [2, 3]) to the spinal cord. Here the signals are feed into reflex loops that enable rapid motor corrections. Shortly after, the feedback also reaches the cerebellum and somatosensory cortex, where it contributes to more refined control. This sensorimotor feedback loop continues throughout the movement, allowing quick adjustments that keep the skater

stable and composed, as they launch into the race with precision and flair.

Of course, the smooth execution of a race start on ice skates isn't always guaranteed, even for elite athletes. Physical and mental factors can disrupt the sensory-motor flow that makes explosive motion possible. Stress, for example, can interfere with focus and decision-making, altering how the brain processes the start signal or prepares the movement. Fatigue from a long season may dull neural responsiveness or slow the fine-tuned muscle control needed for balance and power. Emotional states like anxiety or over excitement can throw off timing or lead to rushed, poorly coordinated starts. Even when the athlete has trained the motion countless times, these internal states can subtly impair performance. In the high-stakes environment of competition, where milliseconds matter, the ability to regulate these influences becomes just as crucial as strength or technique, and show that starting a race is truly a whole-brain event. In daily life, the complexity only increases as we interact with family, friends, colleagues, different environments, and continuously make decisions in a wide range of contexts and internal states.

While stress and fatigue can disrupt motor control in otherwise healthy individuals, for many, the challenges go far deeper. A wide range of neurological conditions can severely impair the brain's ability to process sensory input, plan actions, or control movement. For instance, people with hearing impairments may not register a start signal at all, making it challenging to synchronize actions with external cues. Others may suffer from motor cortex damage due to stroke, trauma, or degenerative diseases, which can impair the brain's ability to plan and execute voluntary movement. Even if the legs are physically capable, the coordination required to initiate and control motion may be lost.

To understand how the brain works, and what goes wrong when it doesn't, we need tools that can capture brain activity when it happens. The field of neuroengineering is dedicated to develop technologies that can record, analyze, and interpret brain signals. Achieving this understanding requires technologies capable of capturing brain activity across different spatial and temporal scales, from the firing of individual neurons to the dynamics of large-scale brain networks. Cellular-resolution techniques, like single-cell electrophysiology or two-photon imaging, are typically performed in animal models and reveal the rapid, precise dynamics of individual neurons. At the other end of the spectrum, imaging methods such as functional magnetic resonance imaging (fMRI) allows measurement of large-scale activity patterns across the human brain. But between these extremes lies a critical translational gap, since it is hard to link the cellular findings in animals to the whole brain measurements in humans [4, 5].

In the following section, I will describe electrophysiology to measure single-cell activity, fMRI to measure whole-brain activity, and finally functional ultrasound (fUS) imaging, which is a new technique that can bridge the gap between these two scales.

1.1.1 Single cell activity: electrophysiology

The most direct way to detect brain activity is through electrophysiology. When a neuron fires, it generates an action potential, a short electrical pulse. A single spike may not carry much information on its own, but together, the timing and frequency of many action potentials form patterns that encode how the brain processes and transmits information.

Electrophysiology measures these firing patterns directly, and therefore provides a direct readout of the bioelectrical messages that are passed between neurons.

Electrophysiology is used across various organs to monitor electrical activity. For example, electrocardiography (ECG) captures heart signals, electromyography (EMG) detects muscle activity, and electroencephalography (EEG) measures brain activity. These methods rely on electrodes placed on the skin or scalp and thus capture the summed activity of many cells firing at once. In the case of EEG, signals must pass through the skull, which is a poor conductor of electricity. This causes substantial attenuation and distortion, limiting both the spatial resolution and the ability to detect deep brain activity. As a result, EEG is unable to isolate the activity of small neural populations or neurons located in subcortical regions.

To measure the electrical activity of individual or small groups of neurons, you need to bring electrodes directly into contact with the brain [6]. Implanting electrodes is highly invasive, requiring surgery that carries risks such as infection, inflammation, or hemorrhage, and is therefore limited to animal studies or patient populations.

Despite its invasiveness, implanted electrophysiology offers several key advantages. It provides millisecond-level temporal resolution and high spatial precision, allowing researchers to isolate signals from single neurons. The recording hardware is relatively compact, making the technique well-suited for chronic or mobile setups. However, over time, the immune system can form scar tissue around the electrodes, degrading signal quality [7]. Additionally, electrodes only record from the regions they physically contact, requiring deep implantation to reach subcortical areas [8]. The spatial coverage is also limited, making it difficult to capture large-scale interactions between distant brain regions.

Clinically, electrophysiology it is used to monitor neural activity during surgeries such as tumor resections [9], and forms the foundation of brain-machine interface technologies that allow paralyzed individuals to control robotic limbs or computer cursors with their brain activity [10, 11]. Summarizing, electrophysiology provides incredibly detailed information at the single neuron level, it is characterized by a limited brain coverage and cannot look at the large scale interactions between brain regions.

1.1.2 Whole brain recording: fMRI

One of the most widely used techniques to detect whole brain activity is functional magnetic resonance imaging (fMRI). Unlike electrophysiology, fMRI does not measure neuronal activity directly through electrical signals, but instead, it detects changes in blood flow and oxygenation, known as the blood-oxygen-level dependent (BOLD) signal [12]. When a brain region becomes active, it demands more oxygen, triggering a localized increase in blood flow, known as the neurovascular coupling (see detailed description in section 1.2.2). fMRI captures these changes using strong magnetic fields, which interact with the hydrogen atoms in water molecules throughout the body. Since these fields pass harmlessly through soft tissue and the skull bone, there is no need for surgery or implanted devices. Importantly, fMRI also avoids the use of ionizing radiation, unlike imaging techniques such as CT or PET scans, which expose the body to X-rays or radioactive tracers. This allows

researchers and clinicians to image the human brain in a completely non-invasive way, even in deep regions that are inaccessible to surface electrodes.

fMRI offers a millimeter spatial resolution, and covers the entire brain, and can measure large-scale network dynamics across cortical and subcortical regions. However, its temporal resolution is relatively low, in the range of seconds, since it measures hemodynamic responses rather than direct neural firing. There exists a trade-off between spatial and temporal resolution. Higher spatial resolution can be achieved, but often at the cost of slower temporal sampling. This balance can be tuned depending on the application, whether the goal is to image the whole brain or focus on specific localized regions. Furthermore, fMRI is not portable, requires large and expensive equipment, and typically confines participants to a lying position inside a scanner, where they must keep their head as still as possible to avoid motion artifacts that can degrade the quality of the data.

Despite these limitations, fMRI has been a key imaging technique in modern neuroscience. It has helped map functional brain networks, and has deepened our understanding of cognitive control, language, memory, emotion, and consciousness [13]. It is used clinically to map functional brain regions and guide surgical planning for tumor resection, helping to minimize the risk of impairing critical functions such as movement, language, or sensation [14].

1.1.3 Bridging the translation gap: fUS?

A critical problem in translational neuroscience, is how to link the cellular findings in animals to the whole brain measurements in humans. Since fMRI and electrophysiology are fundamentally different techniques, and measure different signals, it is difficult to directly compare the results and translate findings [4, 5]. This is where fUS is emerging as a powerful modality in preclinical neuroimaging [15].

Like fMRI, fUS leverages neurovascular coupling, using changes in cerebral blood volume (CBV) as an indirect measure of neural activity. However, thanks to recent advances in ultrafast ultrasound imaging, fUS achieves much higher sensitivity to slow blood flow, enabling it to detect fine-grained hemodynamic changes in tiny vessels at frame rates of thousands of images per second. Therefore, fUS measured CBV increases are in the order of 20%, whereas fMRI measured BOLD fluctuations are in the order of a couple percents [16].

fUS offers a unique combination of high spatial resolution (down to 100-300 μm) and temporal resolution in the 100 ms range, which is significantly faster than fMRI while still covering relatively large areas. The required equipment is compact and portable, allowing integration in a wide range of experimental setups, including awake, behaving animals or even freely moving animals when an ultrasound probe is mounted to the head. fUS is compatible with many cellular resolution techniques, such as calcium imaging, optogenetics, and electrophysiology, allowing simultaneous readout of cellular activity and hemodynamics in animal models [5]. fUS has shown many promising results in preclinical research, but there are still several challenges that need to be addressed before it can be widely adopted in neuroscience research and clinical practice.

One major hurdle is formed by the skull. Although the skull does a fantastic job of

protecting the brain, it is a nuisance for ultrasound imaging. The skull bone is a dense structure, that has a high speed of sound and density compared to soft tissues. This causes distortion of the ultrasound signal (further detailed in section 1.3.1), and makes it challenging to image through the skull. Therefore, most preclinical studies rely on surgical removal of a part of the skull to create an acoustic window. This hampers the clinical translation of fUS to humans, and currently restricts human fUS to guide tumor resection surgeries [17, 18], through the fontanel in newborns [19, 20], or in patients with a hemicraniectomy (chronic partial skull removal) [21].

A challenge in volumetric fUS imaging is caused by the large amounts of data it generates, which makes real-time processing difficult. Recently, fUS has attracted growing interest from the brain-machine interface (BMI) community, after demonstration that 2D fUS can decode movement intentions from neural activity in non-human primates [22, 23]. While 2D imaging can successfully capture activity from neural populations within a single imaging plane, it inherently misses activations occurring outside that plane. Capturing these additional signals can lead to improved decoder accuracy, and can increase the set of possible actions of the BMI. To access these additional signals, you can apply volumetric fUS, however, the jump to 3D comes with a substantial increase in data throughput. This significantly complicates real-time processing and poses a major hurdle for implementing closed-loop fUS based BMI systems.

1.2 Ultrasound Functional Neuroimaging

Functional ultrasound imaging is relatively new, with its first introduction by Macé *et al.* in 2011 [24]. It relies on ultrafast ultrasound, a high frame rate ultrasound technique, that is fundamentally different from conventional clinical ultrasound imaging. Before we dive into the specifics of functional ultrasound imaging, it is worth taking a moment to understand how ultrafast imaging works, and describe how it differs from the conventional clinical approach.

1.2.1 Clinical vs Ultrafast Ultrasound

Ultrasound is one of the most widely used imaging techniques in clinical medicine. Most people know it from the familiar black-and-white images seen in hospitals in typical use cases like detecting muscle and tendon injuries, assessing cardiac function, evaluating abdominal organs, and to monitor the development of a fetus during pregnancy. These applications rely on ultrasound's ability to generate anatomical images of soft tissues in real time, making it an invaluable tool across many clinical disciplines. Interestingly, ultrasound exams do require significant expertise and are therefore carried out by dedicated ultrasonographers, rather than general radiologists. The operator must skillfully position the probe and mentally interpret anatomical structures in three dimensions from an imaging plane, which makes technique highly operator dependent.

In most clinical ultrasound applications, images are being formed by sending focused ultrasound waves into the body. These waves are reflected back by tissue interfaces, such as the boundary between skin and muscles, or between blood and heart muscle, referred to as backscatter or echoes. In addition, backscatter also comes from small-scale inhomogeneities

within organs, such as collagen fibers or other cellular structures that contribute to the overall ultrasound signal. By measuring the time it takes for these echoes to return to the probe, and delaying the received echoes by this time, an image line can be reconstructed. Although one line can be informative, it is not a full image, and therefore a next focused wave is transmitted at a slightly shifted position to form the next line. This process is repeated until an entire plane is imaged, and can be continuously repeated to allow real time imaging at typically 30-100 frames per second. Since the image formation depends on the travel time of the sound waves through the medium, there exists a trade-off between frame rate and imaging depth, with lower frame rates for deeper imaging. The propagation speed depends on the speed of sound in the medium, which is typically 1540 m/s in soft tissue. Focused wave imaging yields high-resolution and contrast anatomical images, that are invaluable for clinical diagnosis. However, due to the low frame rates, applications were mostly restricted to imaging relatively slow or static physiological processes, such as organ anatomy, or fetal development, until recently...

Over the past two decades, ultrasound imaging has taken a radically different direction. Instead of sending narrow, focused beams one line at a time, researchers began transmitting unfocused, angled plane waves [25]. A plane wave is a broad wave front that insonifies the entire field of view in a single shot, and subsequently, echoes from the entire field of view are recorded. Echoes from multiple angled plane waves are combined to form an image by synthetically focusing, using a technique called delay-and-sum beamforming [26]. This change in approach marks a fundamental shift in how images are formed: the focus that was handled acoustically by transmitting focused waves is now handled computationally by synthetic focussing. Because of this, standard clinical scanners cannot run ultrafast modes, as they lack the necessary computational power and memory bandwidth.

In comparison, plane wave imaging can reduce the number of transmits by at least a factor 10 without significant loss of image quality [25]. Since images can be formed by significantly fewer transmissions, frame rates in the kilohertz range are now possible. This dramatic increase in temporal resolution compared to conventional methods is what earned it the name ultrafast ultrasound imaging. Although the higher frame rates lead to significantly increased data rates, advances in computational power, especially with the advent of graphics processing units (GPUs) [27], now make it possible to process this data in real time.

The benefits of ultrafast imaging are profound. The ability to image tissue dynamics at high frame rates has opened the door to a range of new applications that were previously out of reach [28]:

- **Shear wave elastography**: Ultrafast imaging enables the generation and tracking of shear waves propagating through tissue, allowing clinicians to measure tissue stiffness non-invasively. This technique has been applied in breast cancer diagnosis by identifying stiff lesions [29], assessing cardiac stiffness to evaluate diastolic function and myocardial remodeling [30], and staging liver fibrosis, where increased stiffness indicates progression of chronic liver disease [31].
- **Tendon and muscle motion tracking**: By capturing the fine-scale dynamics of tissue motion, ultrafast ultrasound allows researchers to measure how muscles

contract and tendons elongate in real time. This has provided new insights into joint mechanics, injury mechanisms, and musculoskeletal coordination during natural movements [32–34].

- **Electromechanical wave imaging**: Ultrafast imaging enables the tracking of electromechanical waves, the mechanical response of tissues following electrical activation. In the heart, this allows visualization of the propagation of electrical impulses through the myocardium, offering a new window into arrhythmias and conduction abnormalities [35]. In skeletal muscle, it can reveal how neural activation leads to contraction patterns. This holds promise in assessing muscle contraction efficiency, monitor the progression of neuromuscular diseases, and determine the efficacy of new treatment options. [36, 37].
- **High-sensitivity blood flow imaging**: Ultrafast Doppler techniques significantly improve sensitivity to slow and small-vessel blood flow. This enables visualization of microvascular networks, tumor perfusion, and measuring brain activity [24, 38].

These advances in ultrafast ultrasound imaging laid the technical foundation for a new class of applications, including functional ultrasound neuroimaging, which leverages ultrafast Doppler to measure cerebral blood flow as a proxy for neural activity [24, 39]. In the following sections, I introduce the physiological and physical principles behind fUS, its implementation, and how it is transforming our ability to image brain function at the mesoscopic scale.

1.2.2 The relation between blood flow and brain activity

When neurons become active, they quickly demand more oxygen and energy to support their function. The brain does not have a place to store energy, so to meet demand, the brain responds by increasing blood supply to the region where activity occurs. This is known as the neurovascular coupling, and involves the dilation of nearby blood vessels, leading to a localized rise in both blood flow [40]. It is the fundamental mechanism that links brain activity to blood flow and forms the physiological mechanism underlying many functional imaging techniques.

The exchange of energy between the brain and the blood takes place in the capillary bed, while arterioles control the energy supply by regulating local blood flow. Together they form the smallest vessels in the body, with diameters ranging from 5 to 100 micrometers and flow speeds between 0.1 and 10 mm/s in rodents [41]. The arterioles are the first vessels to dilate after neuronal activation, and after a delay of a few hundred milliseconds, the blood flow starts to increase, peaking a few second after activation [42] (see Fig. 1.1).

To detect this response, imaging systems need to track subtle changes in blood flow over time. Because the flow changes occur in such small vessels, with relatively low velocities, this requires a modality with both high sensitivity and spatial resolution. If these conditions are met, blood flow in the capillary bed can serve as a reliable, although indirect measure of neural activity, turning blood flow imaging into functional imaging.

1

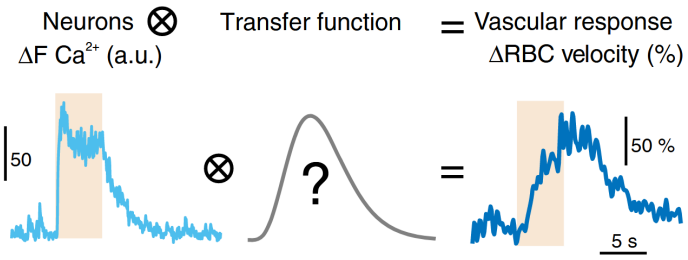

Figure 1.1 – The neurovascular coupling. When a neuron fires, it generates an electrical signal called an action potential. This electrical activity can be measured using electrophysiology, where electrodes detect the voltage changes of neurons. After this, neurons release signaling molecules that boost local blood flow, ensuring a fresh supply of oxygen and glucose to restore energy levels. This vascular response peaks with a delay of a few seconds relative to the initial neural activity. This means that that imaging blood flow can be used as an indirect measure of neural activity, and is the physiological phenomenon that underlies functional ultrasound. Figure adapted from [43].

1.2.3 Imaging blood flow

fUS leverages high frame rate plane wave ultrasound to achieve high sensitivity to blood flow. The core principle behind imaging blood flow is the Doppler effect, the observed change in frequency of a wave when there is relative motion between the wave source and observer. In simpler terms, fUS relies on the same effect that makes the pitch of a passing ambulance siren appear to change.

If we transmit a single plane wave in a simple medium, with one vessel and a moving red blood cell, we see that we receive a single echo from the blood cell, arriving at a time that depends on the distance between the transducer and the blood cell, and the sound speed in the brain (Fig 1.2a). When we send another pulse the echo arrives at a slightly different time due the movement of the red blood cell. We repeat this process, of sending and receiving ultrasound pulses at a known frame rate, and can see how the blood cell moves over time (Fig 1.2b). If we look at the signal at a fixed depth, we see a time-varying signal, which is called the Doppler signal (Fig 1.2c). The frequency of this signal is proportional to the velocity given by the Doppler frequency shift,

$$f_D = 2v_z \cos(\theta)\frac{f_{US}}{c}, \tag{1.1}$$

with v_z the velocity of the blood cell, θ the angle between the blood cell and the ultrasound beam, f_{US} the ultrasound frequency, and c the speed of sound in the brain. If the particle is moving towards the transducer, the frequency shift is positive, and if it is moving away, the frequency shift is negative. These Doppler frequencies are collected in a Doppler spectrum (Fig 1.2d).

In the brain, we do not have a single vessel with one blood cell, but a complex network of vessels with many blood cells moving in different directions, at different speeds. Therefore, our Doppler spectrum is a linear combination of the Doppler frequencies corresponding to each red blood cell (Fig 1.2e,f). From this we can take the summation of the intensity at

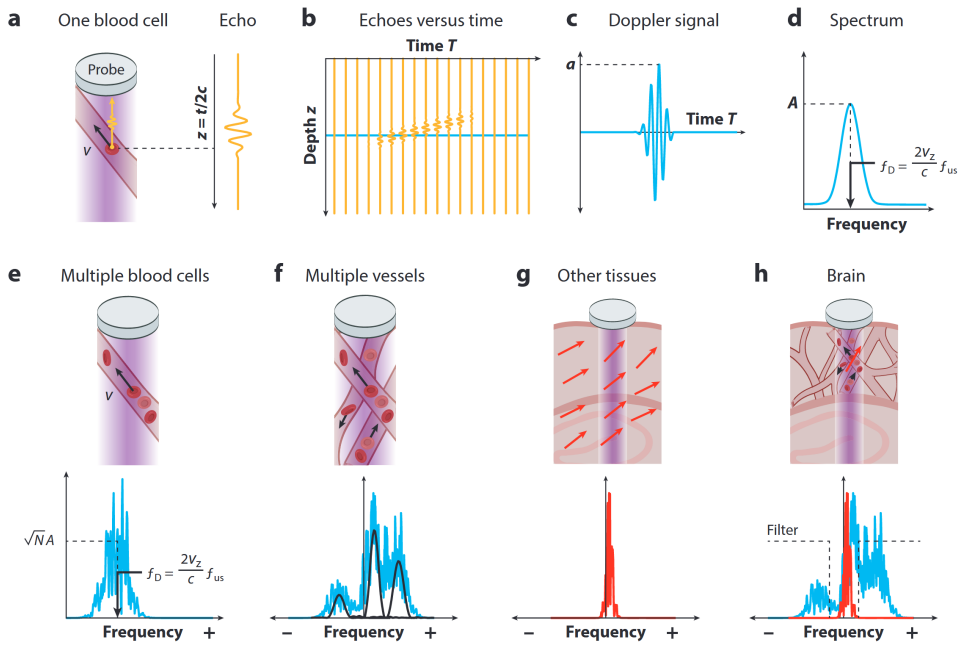

Figure 1.2 – Imaging blood flow with ultrasound using the Doppler effect. (a) A single red blood cell moves through a vessel, and is hit by an ultrasound pulse. Its echo is received by a single transducer element. **(b)** As the blood cell moves through the vessel, and we keep sending and receiving ultrasound pulses, we see that the depth of the echo changes, where depth corresponds to the arrival time of the echo. **(c)** If we look at the echo signals at a fixed depth, we see a time-varying signal, which is called the Doppler signal. The frequency of this signal is proportional to the velocity of the blood cell. **(d)** By computing the frequency spectrum of the Doppler signal, we can estimate the Doppler frequency of the red blood cell, and determine its velocity. A positive frequency indicates that the cell is moving toward the transducer, while a negative frequency means it is moving away. **(e)** When there are multiple blood cells at different velocities, the Doppler spectrum is a linear combination of all the individual Doppler spectra. **(f)** Same when there are multiple vessels. **(g)** Other tissue surrounding the blood cells also reflect ultrasound waves, and contribute to the Doppler spectrum. These tissues are moving at a much slower speed, but are not entirely static, due to natural vibrations in the body caused by the heartbeat, breathing, and movement. The velocities are lower than the blood flow velocities, and are captured in the Doppler spectrum as clutter around the 0 Hz frequency. **(h)** To visualize blood flow, we can filter out the clutter signal, and isolate the Doppler signal of the blood cells. Figure adapted from [44].

each frequency, which gives of the power Doppler signal and is proportional to the number of red blood cells at our fixed depth. Therefore, the power Doppler signal measures the cerebral blood volume (CBV).

There are other tissues, like gray matter, white matter, and vessel walls, that reflect ultrasound waves, and contribute to Doppler spectrum. If these tissues were static, they would end up around the 0 Hz frequency in the Doppler spectrum. However, in real life

measurements, everything is moving due to vibrations in the body caused by the heartbeat, breathing, and movement (Fig 1.2h). We are typically not interested in these vibrations, but they are captured in the Doppler spectrum and are called clutter. To remove clutter, we can apply frequency filtering on an individual voxel basis, to isolate the Doppler signal of moving blood cells. However, there exists an overlap between the blood spectrum of slow flow and the spectrum of clutter, which makes it challenging to separate them by frequency filtering. The blood flow most closely linked to brain activity occurs in the capillaries, where velocities are relatively slow, typically between 0.1 and 10 mm/s [41]. Luckily there exist a different kind of filter that helps us in keeping as much of the slow blood flow as possible, while removing the clutter.

To better isolate blood signals from clutter, we can apply a filter that leverages spatio-temporal coherence [45]. Clutter signals tend to be highly coherent across neighboring voxels, while blood signals are less coherent. By applying singular value decomposition (SVD), we can separate these components: the coherent clutter ends up in the lower-rank singular values, while the less coherent blood flow appears in the higher-rank components. Filtering out the lower ranks effectively suppresses clutter and enhances sensitivity to slow flow. This method has become the gold standard in functional ultrasound imaging.

To generate vascular brain, or angiograms, images, a sequence of angled plane waves is transmitted into the brain. Each wave is reconstructed into a low-resolution image, and by combining multiple angles, a single high-resolution image is formed. The image acquisition is repeated at high frame rates around 1 kHz, to form a Doppler ensemble. Typically, the length of this ensemble is chosen to capture a full cardiac cycle, to average out the pulsatile blood flow. The ensemble of frames is then filtered using the spatio-temporal SVD method, and we end up with a vascular map, or angiogram, in which each pixel intensity is proportional to the cerebral blood volume (Fig 1.3).

1.2.4 Revealing brain activity

While a single angiogram provides a high-resolution map of the brain's vasculature, it does not by itself reveal neural activity. Ultrasound imaging can become a neuroimaging tool when we go beyond static blood volume maps and start tracking dynamic changes in cerebral blood volume (CBV) over time. To capture this, fUS imaging is performed continuously over a period of time, for example during a behavioral task or while presenting a specific stimulus. The result is a time series of angiograms, in which each pixel reflects not just the baseline blood volume, but how the CBV changes throughout the experiment. By analyzing these CBV fluctuations, we can reveal which regions of the brain were active over time.

To turn the variations in CBV over time into activity maps, the CBV time course in each pixel is compared to timing of a stimulus or task, using correlation-based analysis or linear regression. Regions where CBV strongly correlates with the stimulus are assumed to be involved in processing it. Because fUS has both high spatial resolution and sub-second temporal resolution, it allows us to localize brain activity at the mesoscopic scale, capturing fine-grained patterns that would be missed by slower or lower-resolution techniques.

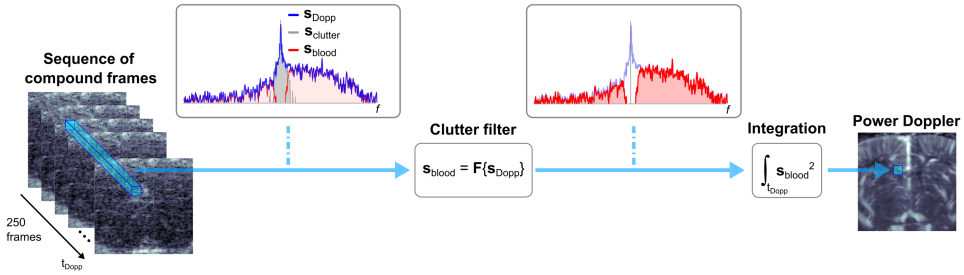

Figure 1.3 – Visualizing blood flow in a Doppler ensemble. [46]

fUS has been used in a variety of neuroscience applications, spanning from small animal studies to human brain imaging. In rodents, it enables high-resolution imaging of whole-brain activity while the animals are awake and head-fixed, for example during visuomotor tasks where specific brain regions can be tracked in 3D as they activate in response to visual stimuli and motor actions (Fig. 1.4a). fUS has also been adapted for freely moving animals, allowing researchers to correlate brain activity with natural behaviors like running, using correlation maps that highlight activation of neural circuits across different brain planes (Fig. 1.4b). In non-human primates, fUS can target deep cortical structures during cognitive tasks, for instance, decoding neural activity in macaques performing a reaching task, allowing to predict movement intentions (Fig. 1.4c). In humans, fUS has shown promise in neonatal care by imaging brain activity at the bedside through the fontanelle, providing noninvasive 3D maps of vascular structure and functional connectivity in newborns (Fig. 1.4d).

Summarizing, functional ultrasound transforms detailed vascular imaging into a dynamic map of brain function, providing a powerful tool for studying how neural activity unfolds across space and time.

1.2.5 Volumetric functional imaging

Until now, we discussed 2D ultrasound, that relies on 1D arrays with elements along a single line. To create 2D images with a 1D array, we use time as second dimension, that can be converted into space via the speed of sound in tissue. To create a 3D image with a 1D array, you could do a motorized sweep of the probe [47, 48]. Although this solution has its merits, it is not able to sample the whole brain at once and makes ultrasound less portable.

Recent developments in transducer technology have made it possible to extend functional ultrasound imaging into three dimensions, enabling the visualization of brain activity across the entire volume of the rodent brain in real time [49–51]. This is achieved using 2D matrix transducers, which allows transmission and reception of ultrasound waves in 3D field of view. As a result, activity from the whole rodent brain can be measured simultaneously, with the perspective of revealing how their interactions give rise to behavior.

Matrix arrays open many new possibilities for neuroscientific experiments, but come with significant hardware challenges. First, fabrication of matrix arrays is currently chal-

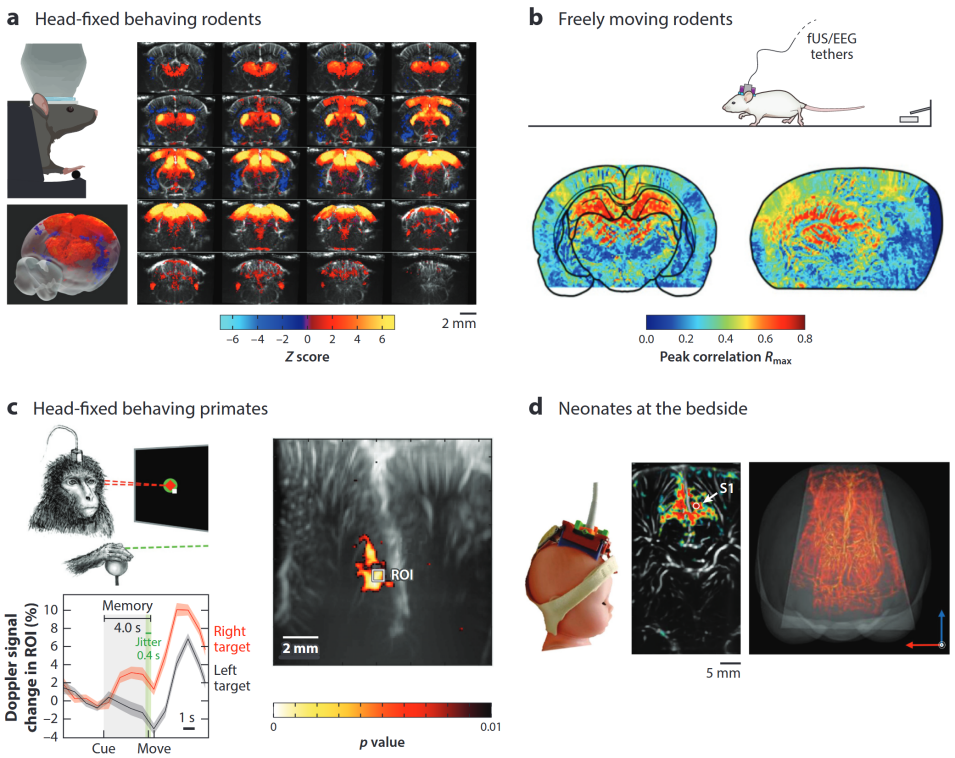

Figure 1.4 – Applications of fUS in preclinical and clinical studies. (a) 3D brain activation in awake, head-fixed rodents during visuomotor tasks. **(b)** Functional maps in freely moving animals during natural behaviors. **(c)** Deep cortical imaging in non-human primates during cognitive tasks. **(d)** Bedside imaging in human neonates revealing vascular structure and functional connectivity. Figure adapted from [44].

lenging, and their sensitivity is lower than 1D arrays, which have been under development for much longer. Furthermore, a matrix requires N^2 independent channels to fully address the aperture, which quickly becomes complex to manage in terms channel availability, memory, data bandwidth, and processing speed. To work around this, current systems rely on multiplexing strategies, sequentially activating parts of the array [49], resulting in lower frame rates. Alternatively, multiple ultrasound scanners can be linked to increase the number of channels [52], which compromises the portable and cost-effective properties of ultrasound imaging.

To overcome the limitations induced by the high channel count, researchers have developed an alternative: Row-Column Addressed (RCA) arrays [53, 54]. Instead of using a full matrix of elements, RCA transducers consist of two orthogonal 1D arrays with long, thin elements that span the full aperture in one direction. This design drastically reduces the number of required channels from N^2 to $2N$, enabling large field-of-view volumetric imaging with a single ultrasound scanner.

RCA-based systems have already shown promising results in 3D anatomical imaging [55] and whole-brain fUS in rats [51]. However, achieving high sensitivity and resolution for fUS still requires numerous plane wave transmissions [51], which means that data load and computational demand remain critical bottlenecks.

1.3 Transcranial functional imaging

The skull bone distorts and attenuates ultrasound waves, which degrades image quality when trying to visualize the anatomy or blood flow inside the brain. To overcome this, most preclinical studies in rodents or other animals rely on craniotomies, a surgical procedure in which part of the skull is removed to create an acoustic window (see Fig. 1.5) [56]. The skull section is often replaced by an acoustically transparent plastic material, to protect the brain. Although craniotomies are effective for improving signal quality, this approach is highly invasive, and raises serious ethical concerns regarding animal welfare. Even though craniotomies are performed by trained personnel and under anesthesia and analgesia, the procedure still exposes animals to pain, stress, and discomfort.

If the ethical concerns were not enough, there are also scientific drawbacks. Once the skull is removed, the brain is exposed to inflammation, infection, and chronic tissue changes, which limits the feasibility of longitudinal studies. That's unfortunate, because repeated imaging of the same animal over time is essential for studying processes like learning, recovery, and disease progression, insights that are lost if imaging can only happen over a limited time.

Finally, the need for skull removal is a major barrier in bringing fUS to the clinic. In adult humans, the only viable acoustic skull window is the temporal bone, which is thinner than the rest of the skull but still presents a significant challenge. As a result, current human fUS applications are largely restricted to intraoperative imaging during brain surgery [17, 18], to patients with chronically implanted cranial windows [21], or to newborns, who naturally have an acoustic window through the fontanel [19, 20].

Developing effective transcranial fUS methods is key to expanding its use in both animal research and clinical neuroimaging. In the following sections, we will discuss the physics that underlie the problem in transcranial imaging, and see how different methods can tackle part, but not the full problem.

1.3.1 The skull problem: aberrations

The skull bone presents a major obstacle for ultrasound imaging due to its physical properties. Compared to soft tissue, bone is much denser and has a significantly higher speed of sound. Soft tissue like brain and skin typically has a speed of sound of 1540 m/s and density of 1000 kg/m^3. In contrast, the speed of sound in bone is around 3000 m/s, and the density is around 2000 kg/m^3. The large differences in both density and speed of sound produce a strong acoustic impedance mismatch at the interface between soft tissue and skull. This acoustic impedance mismatch causes several distortions, being multiple reflections, attenuation and refraction, together called aberrations. These aberrations degrade image quality and reduce the sensitivity of ultrasound imaging through the skull.

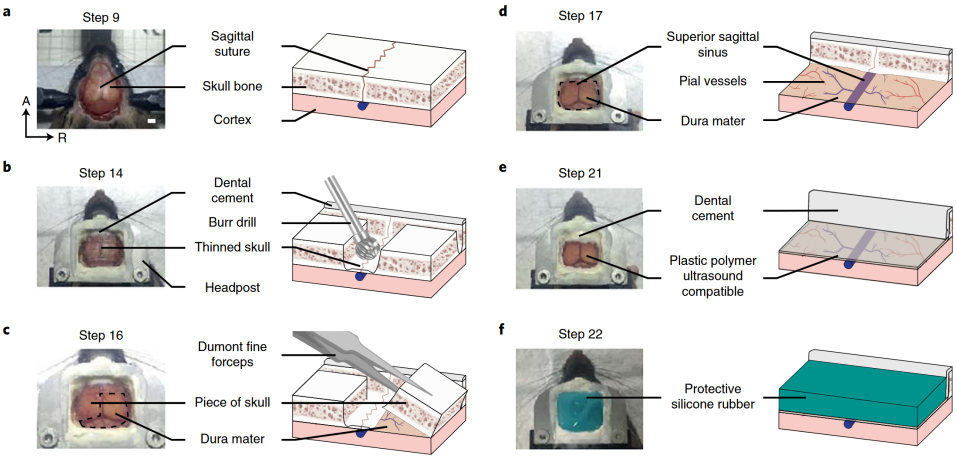

Figure 1.5 – Surgical procedure to create an acoustic window to the rodent brain for functional ultrasound imaging. Adapted from [56].

Multiple Reflections

When the transmitted wave reaches the outer skull surface, a significant portion reflects immediately back to the transducer. These reflections become trapped between the skull and the transducer, and start bouncing back and forth multiple times. Each time the trapped reflections hit the transducer, they will be recorded as an echo. This leads to the appearance of reverberation artifacts, often seen as stripe-like patterns in the image (see Fig. 1.6), that overshadow the underlying brain structures and reduce image quality.

Attenuation

The portion of the wave that does enter the skull is subject to strong attenuation [58, 59]. One component of attenuation is absorption, the conversion of ultrasound energy into heat. Absorption is frequency dependent, with higher frequencies being absorbed more strongly than lower frequencies. Heat conversion only accounts for a fraction of the attenuation, the majority is caused by (multiple) scattering and mode conversion.

The skull bone is not a uniform layer but rather a sandwich structure consisting of an outer and inner cortical layer with diploë in between (see Fig. 1.7). The diploë is a spongy trabecular bone layer and typically constitutes about one-fifth of the total skull thickness [60, 61]. Due to the heterogeneous microstructure of the trabecular bone, ultrasound waves scatter in many directions, reducing the strength of the signal that reaches the brain, and causing a loss in focus of the wave. Additionally, when ultrasound enters the bone, part of the longitudinal wave energy is converted into shear waves, which are more strongly attenuated and do not efficiently transmit through fluid interfaces.

These effects cause substantial energy loss and distortion of the wavefront, leading to weaker and less focused signals beyond the skull. Taken together, scattering, reflection, and mode conversion dominate the attenuation profile, especially at ultrasound frequencies used in functional imaging.

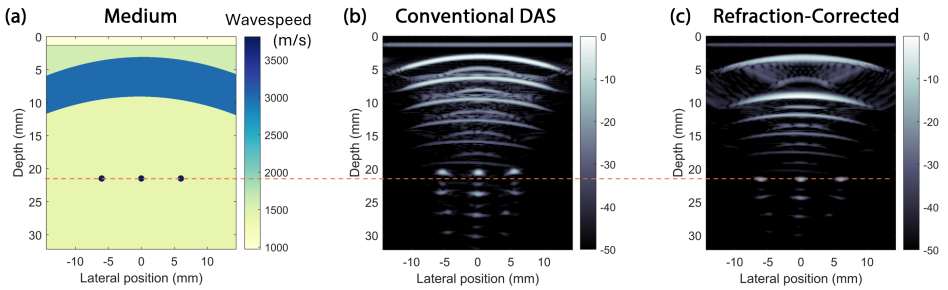

Figure 1.6 – Simplified simulation of ultrasound imaging through the skull. (a) The simulated medium, with an artificial skull bone with high speed of sound surrounded by soft tissue. Below the skull are three point scatters to illustrate the effect of skull aberrations. **(b)** If we do a conventional delay-and-sum (DAS) image reconstruction, the propagation velocity through the skull is underestimated, and the skull bone shows up too thin. In addition, the point scatters are out of focus, and show up at the wrong location. **(c)** If we apply a refraction correction to account for the higher speed of sound in the skull, the skull bone shows up with the correct thickness and the scatters are in focus and at their intended location. **(b,c)** In both conventional reconstruction and refraction correction, we see multiple reflections due to the skull bone.

Refraction

In addition to multiple scattering and attenuation, ultrasound waves also undergo refraction as they enter and exit the skull. Refraction occurs because of the difference in the speed of sound between soft tissue and bone. Since the wavelength of sound depends on the speed of sound in the medium, the wavefront must bend to remain continuous across the interface. This bending of the wave is described by Snell's Law:

$$\frac{\sin(\theta_1)}{c_1} = \frac{\sin(\theta_2)}{c_2}, \tag{1.2}$$

where θ_1 and θ_2 are the angles of incidence and refraction, and c_1 and c_2 are the speeds of sound in the two media. In the context of transcranial imaging, this means that as the wave enters the skull, it bends due to the higher sound speed of bone. When it reaches the inner skull surface, it is refracted again, bending in the opposite direction as it exits into the brain.

This two-step refraction alters the wave's path compared to what is assumed in homogeneous media. The true path of the ultrasound beam deviates from the straight-line assumption typically used in image reconstruction. Moreover, because the time of flight depends on the speed of sound in each tissue layer, ignoring the higher wave speed in bone leads to underestimation of the actual travel time. The result is an image that is out of focus and suffers from a distorted aspect ratio.

In refraction, an important parameter is the critical angle, which is the angle of incidence at which the refracted wave travels along the interface. When the angle of incidence exceeds this value, total internal reflection can occur, preventing any transmission of the wave into the next medium. This effectively limits the range of angles that can be used for imaging,

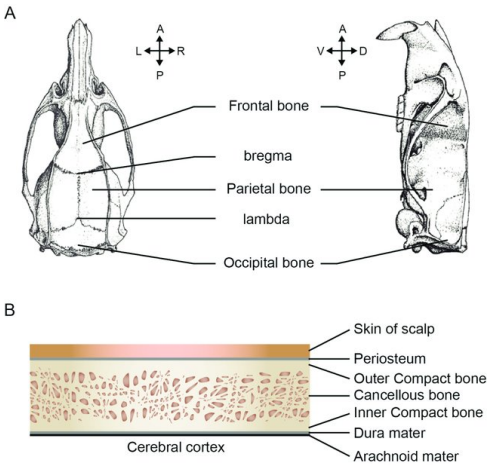

Figure 1.7 – The structure of the rat skull bone. The skull bone consists of three layers: the outer and inner cortical layers, and the diploë in between. Adapted from [57].

particularly in systems relying on plane wave compounding.

1.3.2 Overcoming skull induced aberrations

Several strategies have been developed to address skull-induced aberrations, but no single solution currently resolves all challenges across different imaging contexts.

Overcoming attenuation

As an alternative to surgical removal of the whole skull, skull thinning can be applied to reduce the effect of aberrations [62]. Alternatively, you can raise the echo signal that comes from the blood by using ultrasound contrast agents (UCA) [63]. Microbubbles are the most common UCA, and are small gas-filled bubbles that are injected into the bloodstream. When hit by an ultrasound wave, the bubbles oscillate and reflect sound strongly, due to the high acoustic impedance mismatch between blood and the gas. This enhances the visualization of blood flow and vascular structures.

A downside is that the echo enhancement is short-lived, due to gradual elimination of the contrast agent. Therefore, you would require a continuous administration for sustained enhancement in the context of functional imaging. Additionally, microbubbles introduce random fluctuation in the functional signal, making it harder to pinpoint whether a change in the signal is due to neural activity or the acoustic response of the contrast agent [64].

Aberration correction methods

Instead of directly tackling the problem of ultrasound wave attenuation, another approach is to improve the focus of the wave using aberration correction techniques [65]. In other words, even if part of the wave energy is lost, we can still sharpen the image by correcting for how the wavefront has been distorted during its journey.

Most classical methods to correct this distortion treat the problem as if all the error happens at a single "virtual" layer, right where the transducer sends out the wave. This is known as the near-field phase screen model [66]. In this model, we imagine there's a thin, invisible barrier at the transducer surface that distorts the ultrasound wavefront before it even enters the body. If we can figure out how this distortion happened, we can undo it by shifting the timing (delays) for each individual transducer element.

These delays are typically estimated using strategies such as: Maximizing correlation between neighboring elements [67], maximizing spatial coherence [66], or maximizing speckle brightness [68]. One major benefit of this method is its versatility, it works with both bright, isolated reflectors (like injected microbubbles) [69–71] and with diffuse scatterers [72, 73]. However, while these methods can improve image clarity, they typically don't correct for positional errors (where the structure appears in the wrong location), depth compression (where distances appear squashed), or distorted aspect ratios (where objects appear stretched). Especially in the precense of strong aberrations caused by the skull, the near-field phase screen model is limited in its ability to accurately correct for these effects [74].

To go beyond these limitations, some researchers have turned to modeling the actual path the ultrasound wave takes as refracts through the layers of tissue and bone. This is a more physics-based approach, and while it's more complex, it allows correction of large phase aberrations.

To make this work, you need two things: Accurate model of the wave speeds of different tissue types, and an accurate delineation of tissue boundaries. This model can be obtained in a few different ways. One option is to use ultrasound imaging itself, and use autofocusing to test different wave speeds per layer, and maximize the focus in the image [75–77]. Alternatively, you can combine ultrasound with CT imaging, which gives high-resolution structural information and allows you to extract the skull geometry and sound speed profile [78–80]. The downside of using CT is that it introduces extra cost and potential co-registration errors when combining data from ultrasound and CT.

Once you have the full sound speed map, you can determine how an ultrasound wave would travel through the tissue using the Eikonal equation, which describes how waves bend and slow down through a medium with varying speed of sound. Another option is two-point ray tracing [81], which finds the fastest refracted path between each transmitter, receiver and image point. This technique has been successfully applied in simulations, phantom studies, and even in *ex vivo* skull specimens [75, 82–84]. Once the actual travel times (called aberrated delays) are calculated for each transducer pair, these can be plugged directly into traditional beamforming algorithms like delay-and-sum (DAS) to reconstruct sharp, geometrically accurate ultrasound images [26].

1

1.4 Thesis outline

The chapters follow a progression from fundamental ultrasound system calibration, through improved brain image quality through the skull in preclinical models, to reconfigurable ultrasound for functional and cellular imaging. Each chapter contributes to the broader goal of making ultrasound a more accurate, versatile, and scalable tool for imaging dynamic biological processes.

Chapter 2: Estimation Transducer Parameters
A prerequisite for transcranial aberration correction is a well-calibrated transducer. 1D transducers often have a silicone rubber lens with a lower sound speed than soft tissue, causing wave refraction that's typically ignored in image reconstruction. In this chapter, we introduce a simple method to characterize lens speed and thickness, and show how accurate lens parameters are essential for recovering the correct wave speed in the medium and maximizing spatial resolution and contrast.

Chapter 3: Transcranial Doppler imaging of the brain
In chapter 3, we use refraction correction to improve transcranial Doppler imaging of the rat brain. We present an adaptive aberration correction method based on ray-tracing through four tissue layers: transducer lens, gel and skin, skull, and brain. The method estimates wave speeds in each layer and corrects phase aberrations using a ray-tracing beamformer that accounts for refraction. It consistently outperforms conventional delay-and-sum Doppler imaging in both resolution and sensitivity.

Chapter 4: Selective-plane fUS
In chapter 4, we shift focus from transcranial imaging to addressing data bottlenecks in volumetric functional ultrasound. Since functional activations in the brain are sparse, transmitting plane waves across the whole volume results in a lot of redundant information. Instead, we combine the RCA architecture with focused wave transmission to target selective planes at high frame rates. This approach reduces computational load, enhances sensitivity, and opens the door to multi-region fUS based brain-machine interfaces.

Chapter 5: Sound Sheet microscopy
In chapter 5, we continue the philosophy of adapting the transmit beam to the imaging task, now for nonlinear contrast-enhanced imaging. We introduce nonlinear sound-sheet microscopy (NSSM), which enables fast, volumetric imaging of molecular and vascular targets using tailored ultrasound beams and amplitude modulation. NSSM reveals tumor gene expression and resolves capillary-scale blood flow, pushing ultrasound toward cellular imaging in opaque tissues.

2

Assessing Transducer Parameters for Accurate Medium Sound Speed Estimation and Image Reconstruction

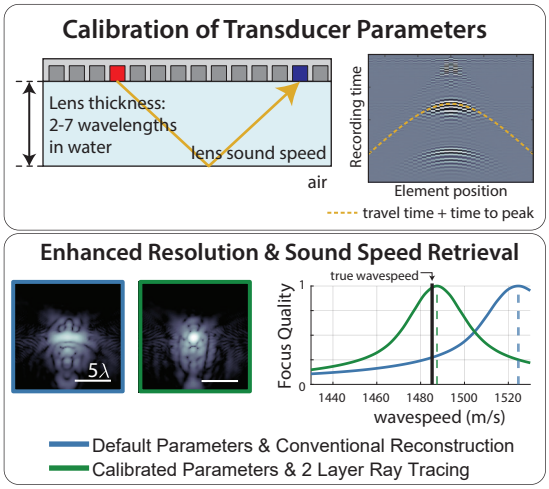

This chapter is based on: *Waasdorp, Rick, David Maresca, and Guillaume Renaud. "Assessing Transducer Parameters for Accurate Medium Sound Speed Estimation and Image Reconstruction." IEEE Transactions on Ultrasonics, Ferroelectrics, and Frequency Control (2024). CC BY 4.0* [85].

The influence of the transducer lens on image reconstruction is often overlooked. Lenses usually exhibit a lower sound speed than soft biological tissues. In academic research, the exact lens sound speed and thickness are typically unknown. Here we present a simple and nondestructive method to characterize the lens sound speed and thickness as well as the time to peak of the round-trip ultrasound waveform, another key parameter for optimal image reconstruction. We applied our method to three transducers with center frequencies of 2.5, 7.5 and 15 MHz. We estimated the three parameters with an element-by-element transmission sequence that records internal reflections within the lens. We validated the retrieved parameters using an autofocusing approach that estimates sound speed in water. We show that the combination of our parameters estimation method with two-layer ray tracing outperforms standard image reconstruction. For all transducers, we successfully improved the accuracy of medium sound speed estimation, spatial resolution and contrast. The proposed method is simple and robust and provides an accurate estimation of the transducer lens parameters and of the time to peak of the ultrasound waveform which leads to improved ultrasound image quality.

2.1 Introduction

Delay-and-sum (DAS) is the most common technique for medical ultrasound image reconstruction [26]. In DAS, the recorded echo signals are summed along the estimated round-trip travel times from the transmit sub-aperture to the image pixel and back to the receive sub-aperture. The pulse-echo travel time can be divided in three components: the travel time in the transducer lens, the travel time in the scanned medium, and the time to peak of the round-trip ultrasound waveform. Because these three components are rarely accurately known, DAS is often applied using approximated travel times which leads to suboptimal image resolution and contrast.

The travel time through the transducer lens depends on the geometry and acoustic properties of the lens, i.e. the sound speed and thickness of the lens. However, transducer manufacturers rarely report accurate values for the lens sound speed and thickness. Instead, a lens travel time correction $t_{\text{lens cor}}$ is often reported to account for the difference in sound speed in the lens and the scanned medium [26]. A transducer lens is usually made of silicone rubber and its sound speed is lower than that of soft tissue ($c_{\text{lens}} \approx 1000\,\text{m/s}$ [86] versus $c_{\text{soft tissue}} \approx 1540\,\text{m/s}$). The lens thickness typically measures 2 to 7 ultrasound wavelengths (λ) in water. Lenses are typically used to focus the ultrasound beam in the elevation direction for 1D arrays. Recent advances in acoustic lenses for 2D arrays show that 2D arrays where each element has its own diverging lens leads to increased sensitivity and focusing capabilities [87]. Due to the different sound speed in the lens and in the scanned medium, an ultrasound ray between a transducer element and a point in the scanned medium is refracted (Fig. 2.2c). Modeling the travel time through the lens as a time offset neglects the dependence of the traveling distance in the lens on the ultrasound ray angle and ignores wave refraction at the interface between the lens and the scanned medium.

Ultrasound scanners typically transmit short sine-bursts with few cycles of vibration at the center frequency of the ultrasound probe. For accurate image reconstruction, it is important to account for a delay equal to the time to peak (t_{ttp}) of the received imaging waveform envelope (Fig. 2.1a). The time to peak is usually estimated based on a simulated

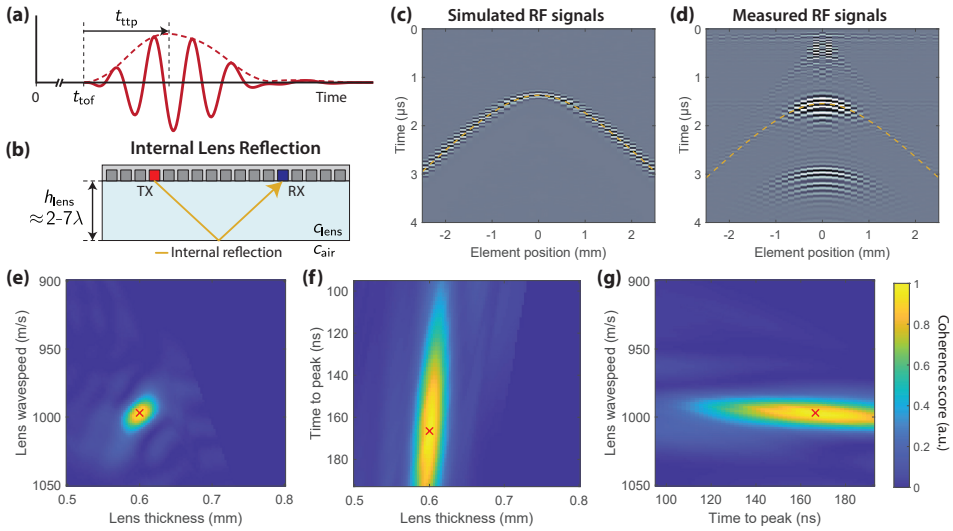

Figure 2.1 – **(a)** At time $t = 0$ the transducer emits a short ultrasound pulse, and the scanner starts to record echo signals. In the recorded echo signals (red solid line), the time to peak corresponds to the max in the envelope of the echo signals (red dashed line). **(b)** Schematic representation of the internal lens reflection when firing the transducer in air. The lens thickness typically corresponds to 2-7 ultrasound wavelengths (λ) in water. **(c)** Simulated internal lens reflection echo signals using a modelled L6-24D transducer. Dashed line indicates the calculated arrival time of the envelope peak, calculated using the estimated transducer parameters. **(d)** Measured echo signals from internal lens reflection with a L6-24D transducer firing in air. Dashed line indicates the calculated arrival time of the envelope peak, calculated using the estimated transducer parameters. The signal recorded after 3 μs is a secondary reflection. **(e-g)** The normalized coherence of the numerically generated echo signals (panel c) along the arrival time hyperbolas for different tested values for lens thickness, lens sound speed and time to peak. The estimated transducer parameters are indicated by the red cross.

waveform using the convolution of the two-way impulse response of a transducer and the driving electrical signal. But such simulated backscattered waveforms do not always exactly resemble the experimentally received pulse due to inaccurate knowledge of the transmit and receive impulse responses and the driving electrical signal. An inaccurate time to peak leads to an additional source of error for the delays used in DAS.

To the best of our knowledge, no nondestructive method to estimate the transducer parameters has been reported. Gray & Coussios [88] proposed a method to characterize the lens parameters by partially cutting away the silicone rubber lens, and interrogating the imaging transducer with a focused transducer in a calibration setup. By comparing the arrival times of the focused transmit for the cutaway section and the intact section, they could assess the lens thickness and sound speed. However, the time to peak could not be assessed using this method.

Here we present a simple nondestructive method that enables accurate estimation of the lens thickness, the lens sound speed and the time to peak of the backscattered imaging

Table 2.1 – Overview of transducers properties of used transducers.

	P4-1	L12-3v	L6-24D
Array Type	Phased	Linear	Linear
Pitch (mm)	0.295	0.200	0.135
Center frequency (MHz)	2.5	7.5	15
Number of elements	96	192	192
Elevation focus depth (mm)	80	20	12
Transmit Frequency (MHz)	2.5	8.93	15.625
Default Parameters			
Time to peak $t_{\text{ttp,m}}$ (µs)	0.83	0.22	-
Lens correction $t_{\text{lens cor,m}}$ (µs)	3.33	1.60	-

waveform. The method leverages internal lens reflections recorded using a synthetic aperture imaging sequence with single-element transmissions [89], and does not require any calibration setup. We validated our method with numerically generated echo signals and experimentally by estimating the sound speed in water with a known speed of sound, using an autofocusing method [76, 77, 90–93]. Finally, we demonstrate that the accurate estimation of transducer parameters leads to improved ultrasound imaging resolution and contrast, using thin wires immersed in water.

The MATLAB (The MathWorks Inc., Natick, MA) code to estimate transducer parameters and example data for two transducers is available on Github: https://github.com/MarescaRenaudLabs/ProbeParameterEstimation.

2.2 Methods

2.2.1 Calibrating transducer parameters

Experimental data acquisition

We characterized the lens properties of three ultrasound transducers with different frequencies and pitch, including a 2.5 MHz phased array transducer (P4-1 ATL/Philips, Bothell, WA, USA), a 7.5 MHz linear array transducer (L12-3v, Verasonics Inc., Kirkland, WA, USA) and a 15 MHz linear array transducer (L6-24D, GE Healthcare, Frankfurt, Germany). An overview of transducer specifications is provided in table 2.1. All experimental data acquisition was performed with a programmable ultrasound imaging system (Vantage, Verasonics Inc., Kirkland, WA).

To calibrate the acoustic and geometric lens properties and the time to peak of the ultrasound waveform, we record the internal lens reflections, while the probe is coupled with air. We used a synthetic aperture imaging sequence [89] with single-element transmissions and recorded with all elements (Fig. 2.1b). Each single element is electrically excited with a one-cycle signal at the center frequency. The sampling frequency of the recorded echo signals was equal to 4 times the ultrasound center frequency. To avoid overheating the transducer arrays, acquisitions in air were done at a low pulse repetition frequency of 100

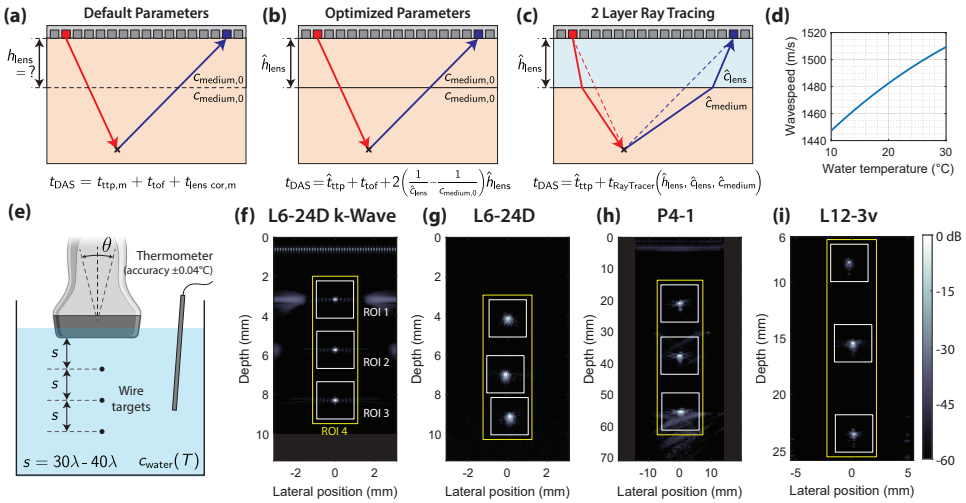

Figure 2.2 – Validation of the calibrated transducer parameters. **(a)** Conventional DAS image reconstruction using uncalibrated transducer parameters, called "Default parameters" in this work. **(b)** The "Default Parameters" reconstruction approach using calibrated transducer parameters. **(c)** The "two layer ray tracing" reconstruction approach using calibrated transducer parameters. **(d)** The temperature of the water was converted to the ground truth sound speed of the water by using a calibration curve as published in [94]. **(e)** The validation setup consisting of three thin wires at a vertical distance of 30-40λ submerged in water. The transducer position was slightly changed between each of the 10 acquisition repeats. The temperature of the water was measured using a high-accuracy thermometer. **(f-i)** B-Mode images reconstructed using the two layer ray tracing approach and the calibrated transducer parameters. In the images 4 regions of interest (ROIs) are defined, three around the individual wires, and a fourth larger ROI that contained all the wires.

Hz. Received data was averaged 200 times to improve the signal-to-noise ratio of internal lens reflections.

Next, we combined multiple single-element transmits into one averaged dataset. We selected sub-apertures of an odd number of elements N_b. For a transducer with N_e elements, we define $N_e - N_b + 1$ symmetric sub-apertures that could be averaged. The resulting averaged echo signals are shown in Fig. 2.1d. In the present study, we used N_b between 41 and 51 for all transducers.

Estimation of transducer parameters

We estimated the lens sound speed $\hat{c}_{\text{lens}}$, lens thickness $\hat{h}_{\text{lens}}$ and time to peak $\hat{t}_{\text{ttp}}$ of the transducer with a grid search approach by computing the arrival times for the first internal reflection and maximizing the coherence of the echo signals across receive channels. When the correct lens sound speed c_{lens}, lens thickness h_{lens} and waveform time to peak t_{ttp} are used the calculated arrival time hyperbolas of the internal reflection will match the peak envelope of the measured echoes, and lead to maximum coherence.

We define the analytic echo signal for receiving element i as s_i obtained by Hilbert

transform of the averaged echo data. The round-trip travel time $\tau_{\mathrm{rt},i}$ for the primary reflection in the lens is given by,

$$\tau_{\mathrm{rt}}(\Delta x_i) = \frac{2}{c_{\mathrm{lens}}} \sqrt{\left(\frac{\Delta x_i}{2}\right)^2 + {h_{\mathrm{lens}}}^2}, \tag{2.1}$$

with $\Delta x_i = x_{\mathrm{tx},i} - x_{\mathrm{rx},i}$ the lateral distance between the transmitting and receiving element. Then, the arrival time hyperbola τ_i is obtained by adding the time to peak t_{ttp} to the round-trip travel time τ_{rt} ($\tau_i = t_{\mathrm{ttp}} + \tau_{\mathrm{rt}}$). Then, we compute the coherence weighted by the signal power C_w as,

$$C_w = \left| \sum_{i=1}^{N_b} \frac{s_i(\tau_i)}{|s_i(\tau_i)|} \right|^2 \sum_{i=1}^{N_b} |s_i(\tau_i)|^2 . \tag{2.2}$$

During the grid search, we compute the coherence C_w for all tested values for lens sound speed c_{lens}, lens thickness h_{lens}, and the time to peak t_{ttp}. The lens sound speed was varied from 900 to 1100 m/s, considering the wave speed of silicone rubber is around 1000 m/s [86]. The lens thickness was varied from 2 to 7 ultrasound wavelengths (in water), and the time to peak was varied from $\frac{N_c}{f_c} - \frac{1}{f_c}$ to $\frac{N_c}{f_c} + \frac{4}{f_c}$, with f_c the transducer center frequency and N_c the number of cycles in transmit.

Numerical simulation of internal transducer lens reflections

To validate the method to calibrate transducer parameters, we simulated a L6-24D transducer with the numerical wave solver k-Wave [95] which consists of 128 elements with a pitch of 0.135 mm. The lens was modeled as a 0.6 mm thick layer of silicone rubber with a sound speed of 1000 m/s and a density of 1000 kg/m^3 [86]. Below the lens, a layer of air mimicking material was modeled with a sound speed of 341 m/s and a density of 600 kg/m^3. Note that the density was chosen higher than the actual density of air (1.2 kg/m^3) to avoid numerical instabilities in the simulation.

For numerical stability and to minimize numerical dispersion, we used a small grid step ($\Delta x = 1.18\,\mu$m) that corresponds to 80 grid points per wavelength in water and a Courant-Friedrichs-Lewy condition of 0.3. The thickness of the perfectly matched layer (PML) was set to 4 wavelengths in water. The element in the center of the array transmitted a 4 cycle pulse centered at 15 MHz with a Hanning envelope. The numerically-generated echo signals were decimated to 4 samples per period (same sampling rate as the experimental data). The simulated echo signals are shown in Fig. 2.1c.

2.2.2 Validation of the estimated transducer parameters

To validate the calibrated transducer parameters we performed a sound speed estimation of water with known sound speed using an autofocusing approach [76, 92].

Image Reconstruction Approaches

Throughout the paper, three image reconstruction approaches are compared. All reconstruction approaches rely on Delay-and-Sum (DAS) beamforming [26], however, the approaches differ in the calculation of the round-trip travel times t_{DAS}. In the following, the subscript $_{,\mathrm{m}}$ denotes a manufacturer reported variable, the subscript $_{,0}$ denotes a literature value, and the circumflex $\hat{}$ denotes a variable calibrated with the proposed method.

Image reconstruction with default parameters This approach is most prevalent and is schematically represented in Fig. 2.2a. The travel time for DAS is given by,

$$t_{\text{DAS}} = t_{\text{tof}} + t_{\text{ttp,m}} + t_{\text{lens cor,m}}. \tag{2.3}$$

The first term, t_{tof} is the round-trip travel time in the medium as if the lens did not exist. The round-trip travel time depends on the transmitter position, the receiver position, the coordinates of the image pixel and the sound speed in the medium $c_{\text{medium,0}}$. This approach assumes a straight ultrasound ray between an array element and an image pixel. In this approach, typical literature medium sound speed will be used, e.g. 1480 m/s for water [96, 97].

The value for the time to peak $t_{\text{ttp,m}}$ will be taken as the estimated value provided by the scanner manufacturer. The lens correction term $t_{\text{lens cor,m}}$ is also taken from the manufacturer and corrects for the fact that the ultrasound wave travels through a lens layer with lower speed of sound than the medium. Therefore, $t_{\text{lens cor,m}}$ does not represent the round trip travel time through the lens, but rather the difference caused by underestimation of the round trip travel time.

Image reconstruction with optimized parameters In this approach (Fig. 2.2b), the travel time for DAS is given by,

$$t_{\text{DAS}} = t_{\text{tof}} + \hat{t}_{\text{ttp}} + \hat{t}_{\text{lens cor}}, \tag{2.4}$$

with $\hat{t}_{\text{ttp}}$ the calibrated value for time to peak of the waveform. The calibrated round trip lens correction term $\hat{t}_{\text{lens cor}}$ is defined by,

$$\hat{t}_{\text{lens cor}} = 2\left(\frac{1}{\hat{c}_{\text{lens}}} - \frac{1}{c_{\text{medium,0}}}\right)\hat{h}_{\text{lens}}. \tag{2.5}$$

Where $\hat{c}_{\text{lens}}$ is the calibrated lens sound speed, $c_{\text{medium,0}}$ is a literature value for the medium sound speed, and $\hat{h}_{\text{lens}}$ is the calibrated lens thickness. Like with the Default Parameters approach, this second approach assumes a straight ultrasound ray between an array element and an image pixel, and t_{tof} denotes the round trip time of flight as if the lens did not exist.

Image reconstruction with two-layer ray tracing In this approach, two layer ray tracing is used to account for the phase aberration caused by the transducer lens (Fig. 2.2c). By using ray tracing, Snell's law of refraction is imposed on the lens-medium interface to find the refracted wave path. The first layer has a thickness $\hat{h}_{\text{lens}}$ and speed of sound $\hat{c}_{\text{lens}}$, and the second layer has a sound speed $\hat{c}_{\text{medium}}$. To find the refracted wave path, we perform two point ray tracing using Fermat's principle [81]. The travel time is computed for every transducer element and image point pairs, and used as an input for the delay-and-sum reconstruction algorithm. The travel time for DAS is given by,

$$t_{\text{DAS}} = \hat{t}_{\text{ttp}} + t_{\text{RayTracer}}\left(\hat{h}_{\text{lens}}, \hat{c}_{\text{lens}}, \hat{c}_{\text{medium}}\right), \tag{2.6}$$

with $\hat{t}_{\text{ttp}}$ the calibrated value for time to peak of the waveform, $\hat{c}_{\text{lens}}$ the calibrated lens sound speed, $\hat{c}_{\text{medium}}$ the calibrated medium sound speed as found by autofocusing (see 2.2.2). The round trip travel time computed by the ray tracer $t_{\text{RayTracer}}$ inherently includes the travel time through the lens and in the scanned medium. The ray tracing algorithm is described in detail in [76].

Experimental setup and data acquisition

A tank with an acoustic absorbing layer at the bottom was filled with pure water (milli-Q). In this tank we submerged a phantom with 3 vertically positioned wires, spaced with an inter-wire vertical distance of 30-40λ (see Fig. 2.2e). The wire phantom for the P4-1 had 50 µm diameter copper wires, for the L12-3v and the L6-24D nylon wires with a diameter of 10 µm were used. Next, the probe was positioned above the wires at a distance of 30-40λ, and the wires were imaged using a synthetic aperture sequence with single-element transmissions. The acquisition was repeated 10 times, and in each trial the angle of the probe in the imaging plane was slightly varied.

At the start and end of the imaging session, the temperature of the water was measured with a high accuracy thermometer (PT100 thermocouple, accuracy $\pm 0.04\,^{\circ}\text{C}$, Greisinger electronics, Germany). To obtain the ground truth sound speed of the water, the temperature was converted to sound speed using a calibration curve (Fig. 2.2d) [94].

Estimation of the sound speed of the medium using autofocus

The sound speed of water was estimated using autofocusing [76, 92]. To start, an initial reconstruction using the two layer ray tracing approach with an initial estimate of the sound speed $c_{\text{medium},0}$ =1480 m/s was done. In the images, the locations of the three wires were detected using peak finding, and around the center of each wire, a $20 \times 20\lambda$ region of interest (ROI) was defined (see Fig. 2.2f-i). A fourth ROI that contained all wires was defined.

Autofocusing was done per ROI and for each acquisition repeat. The sound speed was estimated by reconstructing a ROI with a range of speed of sound values, and computing a focus quality metric for each tested value. During image reconstruction for autofocusing purposes, it is important to use the largest aperture possible. As focus metric, a combination of the image intensity and two metrics of image sharpness was used as validated before in [76, 92]. The intensity of the ROI image was calculated as the sum of the squared amplitude of the image envelope. The sharpness was assessed with two metrics, the Brenner gradient and the normalized variance [92]. Each focus metric was individually normalized by dividing by the maximum value, and the three normalized focus metrics were summed with equal weights to compute focus quality. The estimated water sound speed $\hat{c}_{\text{medium}}$ is the value that maximizes focus quality.

Impact of transducer lens correction on image quality

To assess the impact of the lens on B-mode imaging, we compared images of the wire targets using the three reconstruction approaches. Images were reconstructed with F-number 2.0. We assessed the axial and lateral resolutions using the full width at half maximum (FWHM) of the point spread function (PSF). We assessed contrast of the PSFs using the cystic resolution [98]. The cystic resolution is used to quantify the capacity for detecting

Table 2.2 – Estimated transducer parameters using the proposed method.

		L6-24D k-Wave	L6-24D	P4-1	L12-3v
$\hat{c}_{\text{lens}}$	(m/s)	997.0	1015.2	924.7	1009.6
$\hat{h}_{\text{lens}}$	(mm)	0.600	0.615	1.236	0.663
$\hat{t}_{\text{ttp}}$	(ns)	166.5	331.8	742.9	486.9
$\hat{t}_{\text{lens cor}}$	(μs)	0.39	0.38	1.00	0.42

an anechoic cyst within a uniformly scattering medium. It is defined as the ratio of energy outside a circular region centered around the PSF with radius r, normalized by the total energy of the PSF,

$$C(r) = 10 \log \sqrt{\frac{E_{\text{out}}(r)}{E_{\text{total}}}}. \tag{2.7}$$

To obtain a single metric from the $C(r)$-curve, you can find the relative intensity for a particular cyst size or determine the size needed to reach a specific relative energy. In this study, contrast is assessed using a fixed radius of 2.5 ultrasound wavelengths [99].

Simulation of the effect of lens correction as a function of depth

To assess the impact of accurate transducer lens parameters on sound speed retrieval and image quality, we simulated the acquisition of echo signals backscattered by three small targets with the L6-24D transducer using the numerical wave solver k-Wave [95]. The simulation parameters are described in section 2.2.1. Below the lens layer, we defined a layer of water with a sound speed of 1480 m/s and a density of 1000 kg/m^3. We modelled three wire targets with a diameter 10 times smaller than the wavelength submerged in water at three depths corresponding to 40, 80 and 120 ultrasound wavelengths. We simulated an element-by-element transmission scheme for synthetic aperture imaging. The echo signals were decimated to obtain a sampling frequency of $4f_{\text{tx}}$ (like the experimental data), where f_{tx} is the ultrasound transmit frequency.

The Optimized Parameters and Two Layer Ray Tracing approaches were used to estimate the sound speed in the simulated water layer. The sound speed was estimated using the autofocusing approach described in section 2.2.2. The calibrated sound speed was compared to the ground truth sound speed of water. Next, we reconstructed B-mode images and assessed the image quality in terms of resolution and contrast, described in detail in section 2.2.2.

2.3 Results

2.3.1 Calibration of transducer parameters

Simulation results

We used the k-Wave simulation of the internal lens reflections (Fig. 2.1c) to validate our proposed method. In simulation, no multiple reflections are visible in the echo signals since we modeled a semi infinite medium. The coherence score for the tested values of lens

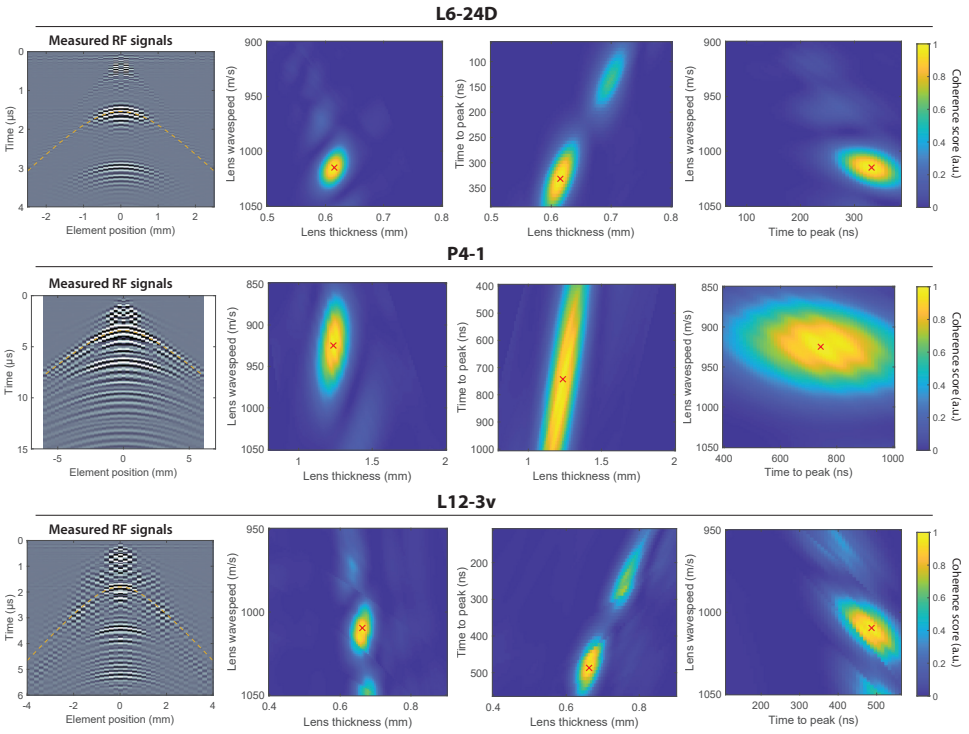

Figure 2.3 – The normalized coherence of the RF along the travel time hyperbolas for different tested values for lens thickness, lens sound speed and time to peak in the grid search. The estimated transducer parameters are indicated by the red cross.

thickness, lens sound speed and time to peak in the grid search is shown in Fig. 2.1e,f,g. The estimated transducer parameters are shown in table 2.2. The error for the retrieved parameters was 3.03 m/s for the lens sound speed, below 0.1 µm for the lens thickness and 0.71 ns for the time to peak.

Experimental results

We calibrated the three transducer parameters using the proposed method. The echo signals and the results of the parameter optimization for all three transducers is shown in Fig. 2.3. The estimated transducer parameters can be found in table 2.2.

2.3.2 Validation of estimated transducer parameters with autofocusing in water

We validated transducer lens parameters estimated in simulation and experimentally by performing autofocusing with the two-layer ray tracing reconstruction approach in a water medium with a known speed of sound.

Table 2.3 – Mean (standard deviation) error in estimated water sound speed (m/s), found by autofocusing using the three different reconstruction approaches. Negative numbers indicate underestimation. We compare the error for the different regions of interest (ROI) defined in Fig.2.2

		Speed of sound error (m/s)		
		Default Parameters	Optimized Parameters	2 Layer Ray Tracing
L6-24D k-Wave	ROI 1		-46.7	0.5
	ROI 2		-25.5	0.2
	ROI 3		-17.2	0.3
	ROI 4		-44.5	0.5
L6-24D	ROI 1		-37.4 (5.2)	2.4 (1.4)
	ROI 2		-20.9 (2.4)	0.9 (0.2)
	ROI 3		-16.1 (1.4)	0.7 (0.3)
	ROI 4		-33.7 (5.5)	2.3 (1.3)
P4-1	ROI 1	41.9 (1.7)	-16.8 (0.9)	-1.3 (1.1)
	ROI 2	18.8 (0.6)	-14.5 (0.8)	-6.5 (0.6)
	ROI 3	6.5 (3.0)	-15.3 (2.9)	-10.3 (2.8)
	ROI 4	41.7 (1.6)	-17.1 (1.6)	-1.4 (1.2)
L12-3v	ROI 1	42.8 (1.9)	17.2 (0.4)	3.5 (0.8)
	ROI 2	22.8 (0.7)	10.6 (0.3)	1.0 (0.4)
	ROI 3	15.9 (0.3)	6.8 (0.3)	0.8 (0.3)
	ROI 4	23.8 (0.9)	11.1 (0.4)	1.4 (0.6)

Simulation

In simulation, the ground truth water sound speed was 1480 m/s. The results for autofocusing with the Optimized Parameters reconstruction and the two layer ray tracing reconstruction are shown in Fig. 2.4a. An error of up to 45 m/s is obtained with the Optimized Parameters reconstruction, while the two layer ray tracing reconstruction provides a error smaller than 0.5 m/s (Table 2.3).

Experimental

Experimentally, we measured the temperature of the water with a high precision thermometer. For experiments with the P4-1, we measured a temperature of 20.88 °C, for the L12-3v we measured 20.91 °C and for the L6-24D we measured 21.71 °C. The measured temperatures corresponded to a ground truth sound speed in water of 1485.14 m/s for the P4-1, 1485.23 m/s for the L12-3v and 1487.61 m/s for the L6-24D.

Because lens properties for the L6-24D are not provided by the manufacturer, we only compared image reconstruction with optimized parameters to image reconstruction with two-layer ray tracing.

Fig. 2.4 shows the result for autofocusing with the three approaches per ROI. For ROI

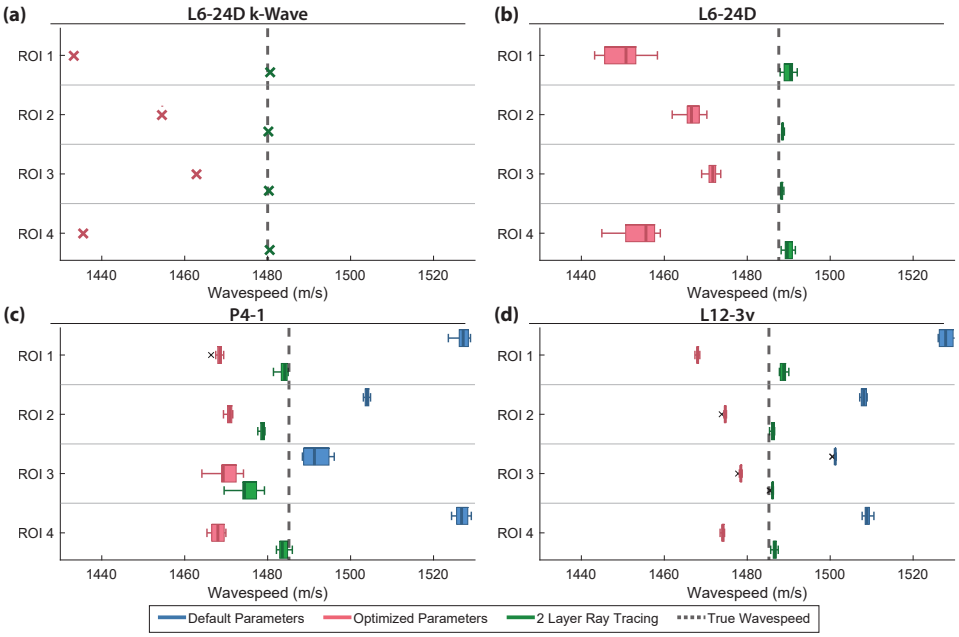

Figure 2.4 – Result of autofocusing to find the sound speed of water for the 4 different ROIs. We compare the result of autofocusing for the three reconstruction approaches. For the physical transducers, the boxplots indicate the statistics over the 10 acquisition repeats. For the simulated transducer no statistics are available. Gray dashed line indicates the ground truth water sound speed as obtained by temperature measurement. **(a)** Results of autofocusing for the simulated L6-24D transducer. **(b)** Results of autofocusing for the L6-24D, **(c)** for the P4-1 and **(d)** the L12-3v.

1, it is clear that for all transducers, the two-layer ray tracing reconstruction provides estimates that are closer to the ground truth sound speed. Table 2.3 shows the error in sound speed for all transducers and the three reconstruction approaches. The optimized parameters reconstruction underestimates the water sound speed for every ROI. For the P4-1 and L12-3v, the default parameters reconstruction overestimates the water sound speed for every ROI. The most accurate sound speed estimation is obtained with the two layer ray tracing reconstruction, and the corresponding small error (< 10m/s) is nearly independent of depth. In contrast, the error in estimated sound speed increases as depth decreases (up to 41 m/s error) for the default parameters and optimized parameters reconstruction approaches.

2.3.3 Accurate estimation of transducer parameters improves image quality

After optimizing the transducer parameters, and retrieval of the water sound speed with autofocus, we characterized the resolution and contrast for the wire PSFs. In the default parameters and optimized parameters reconstruction approaches, we reconstructed the images of the wire with a literature value for the sound speed of water at 20 degrees Celsius,

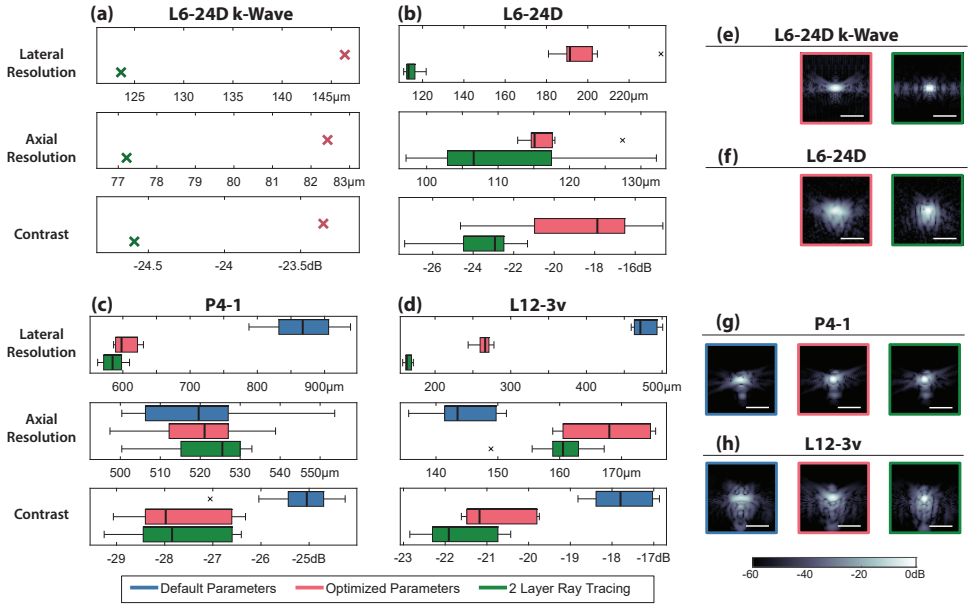

Figure 2.5 – **(a-d)** Results of PSF characterization for each transducer. All shown results are for the wire in ROI 1 (see Fig. 2.2f-i). We compared the image quality of the three reconstruction approaches. Lateral and axial resolution was determined using the full width half max (FWHM). Contrast was determined using the cystic resolution [98]. **(e-h)** Zoom of the PSF of the wire in ROI 1. The PSF is shown for the three approaches, the PSF surrounded by the blue rectangle is obtained by reconstruction with the default parameters, the PSF in the red rectangle is obtained using the optimized parameters, and the PSF in the green rectangle is obtained by two layer ray tracing. Scale bars denote 5 wavelengths.

i.e. $c_{\text{water},0} = 1480\text{m/s}$. For the two layer ray tracing reconstruction, we used the result of autofocusing for ROI 4.

Figure 2.5 depicts the largest improvement in lateral resolution (up to a two-fold improvement) and contrast (up to 4dB improvement) observed in ROI 1, *i.e.* with the wire that is the closest to the transducer (depth = 30-40 ultrasound wavelengths). The detailed characterization of the resolution and contrast for all wires is shown in table 2.4. Table 2.4 shows that the improvement in resolution and contrast is depth dependent, the improvement is the largest for the shallow targets. As expected, mild variations in axial resolution were measured (Figure 2.5 and Table 2.4) since axial resolution is essentially determined by the temporal duration of the ultrasound pulse.

Table 2.4 – Detailed results of PSF characterization for all three wires. Results are shown as mean (standard deviation).

		Lateral resolution (µm)			Axial resolution (µm)			Contrast (dB)		
		Default	Optimized	2L Ray	Default	Optimized	2L Ray	Default	Optimized	2L Ray
L6-24D k-Wave	ROI 1		146.4	123.6		82.4	77.2		-23.3	-24.6
	ROI 2		149.2	114.2		83.4	74.8		-29.0	-31.0
	ROI 3		136.0	107.1		81.5	78.2		-31.3	-33.9
L6-24D	ROI 1		198.2 (17.9)	114.6 (3.7)		117.0 (4.9)	111.1 (11.8)		-18.8 (3.4)	-23.6 (2.0)
	ROI 2		148.1 (9.5)	114.1 (4.0)		117.0 (14.3)	116.9 (16.5)		-24.2 (1.6)	-26.2 (1.7)
	ROI 3		137.0 (6.3)	123.1 (2.9)		123.7 (12.4)	131.8 (19.8)		-24.1 (2.0)	-25.1 (1.9)
P4-1	ROI 1	867.5 (51.1)	604.9 (16.6)	585.9 (16.5)	520.8 (16.0)	520.5 (12.4)	522.0 (10.4)	-25.2 (0.8)	-27.7 (1.0)	-27.7 (1.0)
	ROI 2	872.5 (23.6)	867.8 (7.2)	863.6 (9.7)	520.2 (10.3)	510.7 (12.8)	511.3 (11.4)	-22.8 (0.9)	-23.9 (0.8)	-23.8 (0.9)
	ROI 3	1087.5 (25.9)	1092.5 (35.8)	1090.1 (38.6)	524.1 (8.8)	522.3 (11.6)	524.6 (12.1)	-21.1 (0.6)	-21.3 (0.6)	-21.3 (0.6)
L12-3v	ROI 1	477.7 (16.7)	263.3 (11.4)	164.4 (4.8)	144.4 (5.4)	167.5 (6.4)	160.1 (5.1)	-17.8 (0.7)	-20.9 (0.8)	-21.8 (0.8)
	ROI 2	356.3 (18.2)	221.3 (5.8)	189.0 (2.8)	149.0 (1.9)	155.5 (1.3)	160.2 (3.3)	-24.6 (0.7)	-27.2 (0.7)	-27.9 (0.4)
	ROI 3	281.3 (20.3)	229.2 (7.3)	220.6 (7.0)	151.6 (10.4)	153.5 (11.1)	155.8 (11.0)	-21.4 (2.1)	-23.4 (2.4)	-23.8 (2.4)

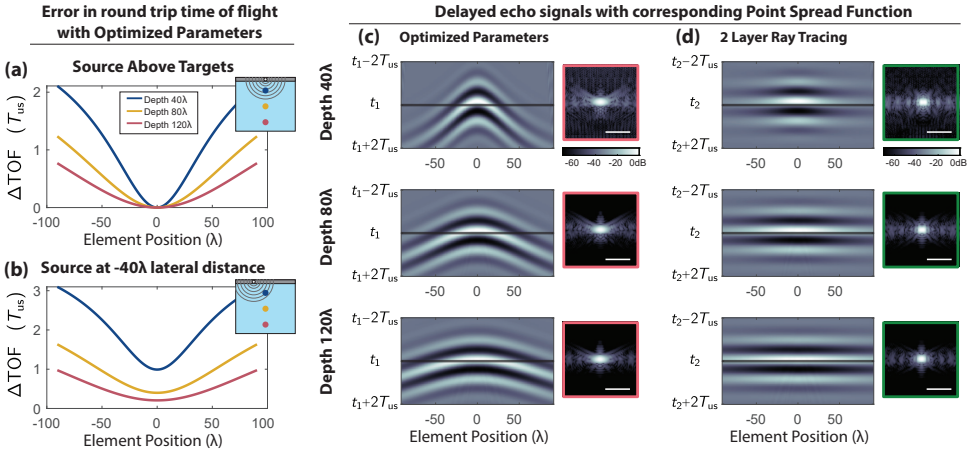

Figure 2.6 – Investigating the impact of lens correction on the estimated round trip time of flight (TOF) with the k-Wave simulation of the L6-24 transducer. Difference in the estimated round trip time of flight (ΔTOF) between the Optimized Parameters and the 2 Layer Ray Tracing reconstruction approaches if **(a)** the source is located directly above the targets, and if **(b)** the source is located at -40λ lateral distance from the targets. ΔTOF is presented in units of the ultrasound wave period $T_{\text{us}} = 1/f_{\text{tx}}$. The TOF computed using 2 Layer Ray Tracing can be considered the ground truth. **(c)** The TOF is computed using the Optimized Parameters for the three wire targets, given by the hyperbola t_1. When delaying the echo signals using TOF hyperbola t_1, it becomes clear that the TOF is underestimated for all wire targets, since the echo signals do not line up with t_1. Signals are displayed in a temporal window of $t_1 \pm 2T_{\text{us}}$. The corresponding PSF for each imaging depth is shown right of the echo signals. Scale bar corresponds to 5 wavelengths in water. **(d)** When the TOF is computed using 2 Layer Ray Tracing, resulting in hyperbola t_2, the delayed echo signals line up perfectly with t_2 for all wire targets.

2.4 Discussion

2.4.1 Importance of the lens thickness

The smallest improvement in image quality was achieved with the P4-1 and the largest improvement with the L6-24D. This is due to the difference in relative lens thickness (in terms of ultrasound wavelengths). The lens thickness was found to be close to 2 wavelengths for the P4-1, 4.5 wavelengths for the L12-3v and 6.5 wavelengths for the L6-24D. The thicker the lens (in wavelengths), the stronger the effect of the lens. Therefore transducers with thick lenses will benefit the most from the two-layer ray tracing reconstruction.

The default parameters reconstruction overestimated sound speed in water. This is because the estimated lens correction provided by the scanner manufacturer was largely overestimating the lens thickness (Tables 2.1 and 2.2). During autofocusing, the overestimation of the travel time in the lens causes an overestimation of the sound speed in water.

2.4.2 Shape of the lens and effective lens thickness

Silicone rubber lenses most often have either a weakly (cardiac phased-array transducers like the P4-1) or a more pronounced convex shape (linear array transducers like the L6-24D and L12-3v) to produce elevational focusing. If the lens would be flat, our approach estimates the true lens thickness. If the lens has curvature, our approach estimates an effective lens thickness. The validation using autofocusing in water demonstrates that for a wide range of lens curvatures, the lens is well approximated by a flat lens with an effective thickness.

2.4.3 Advantages of air-coupled acquisition for the estimation of transducer parameters

Using air as a coupling medium to record internal reflections in the lens has multiple advantages. Thanks to the high acoustic impedance contrast, the echo signals reflected at the interface between the silicone rubber of the lens and air have sufficient amplitude. Using a liquid like water is not advantageous, because there would exist a critical angle $\theta_c = \arcsin(c_{\text{lens}}/c_{\text{water}}) = 42.5$ degrees. Part of the wavefront emitted by a single transducer element would experience supercritical reflection at the interface between the lens and the fluid. As a consequence a phase shift would occur in part of the reflected wavefront. This phase shift would bias the coherence metric. In addition, a measurement in air is simpler and quicker than a measurement in a liquid.

Although designed for scattering from a medium containing small heterogeneities, methods proposed for sound speed estimation in the scanned medium [100–102] could be potentially adapted to the estimation of the sound speed in the lens of the transducer and applied to an air-coupled data acquisition. However, these methods would not provide an accurate estimate of the lens thickness and do not estimate the time-to-peak of the ultrasound waveform.

2.4.4 Different components in the estimated time to peak

The time to peak parameters estimated with the proposed method contains actually three components: (i) the actual time to peak of the backscattered ultrasound pulse, (ii) the two-way travel time in the matching layers (a diced matching layer only causes a delay), and (iii) any time lag caused by the scanner during transmit and receive. It is worth mentioning that the true time to peak of the backscattered ultrasound pulse is determined by the electric excitation waveform. Therefore, it is advised to perform the proposed calibration of the transducer parameters every time the electric excitation waveform is modified.

2.4.5 Challenges in estimation of transducer parameters

When the internal specular reflection in the lens is clearly recorded, the estimation of transducer parameters is straightforward, like for the simulated and experimentally acquired L6-24D data (Fig. 2.1). Transducers with less advanced design and poorer manufacturing quality may produce internal reflection signals of poor quality, because guided waves inside the different layers in the transducer may generate signals with an amplitude similar to that of the internal specular reflection in the lens. Fig. 2.3 shows that the L12-3v and the P4-1 transducers produce internal reflection signals that are more challenging to exploit for

estimating the transducer parameters. When the signal quality is insufficient, it is possible to extend the method by using both the primary and secondary (two round-trips in the lens) reflections. To construct the arrival time hyperbola of the secondary reflection, the round-trip travel time through the lens is determined using,

$$\tau_{\text{rt-2}}(x_{\text{tx}}, x_{\text{rx}}) = \frac{4}{c_{\text{lens}}} \sqrt{\left(\frac{x_{\text{tx}} - x_{\text{rx}}}{4}\right)^2 + {h_{\text{lens}}}^2}, \tag{2.8}$$

with x_{tx} the lateral coordinate of the transmitting element and x_{rx} the lateral coordinate of the receiving element. Finally, the time of flight hyperbola can be constructed by adding the time to peak to $\tau_{\text{rt-2}}$ and a correction term for the round-trip propagation time through the matching layers t_{ml}. An ultrasound transducer possesses often two matching layers. The thickness of a matching layer is one quarter wavelength, therefore the round-trip travel time through the matching layers is $t_{\text{ml}} = \frac{1}{f_c}$, with f_c the center ultrasound frequency of the transducer frequency bandwidth (calculation at normal incidence, a valid assumption if the matching layers are diced).

2.4.6 Depth dependence of sound speed estimation

The estimated sound speed in water was nearly independent of the target depth with the two-layer ray tracing reconstruction approach (Fig. 2.4), unlike with the other two reconstruction methods. This is due to the fact that for shallow targets, the ultrasound ray angle (defined from the normal at the transducer surface) in the lens are larger, thus ignoring wave refraction causes a significant error in the travel times. The same depth dependence is visible in the image quality improvements (Table 2.4). The biggest improvement for image resolution and contrast was made for the superficial targets (depth $30 - 40\lambda$). For deeper targets, the image quality remains the same.

To explain the depth dependence, we took a closer look at the k-Wave simulation. We consider the time of flight obtained with two layer ray tracing the true time of flight, as it accounts for the speed of sound difference between the lens and water and accounts for refraction. Comparing the time of flight of the optimized parameters and two layer ray tracing, we see that there is a substantial difference between the two (Fig. 2.6a,b). When the source is located directly above the wire targets, the difference between the two methods is 0 for every depth for the transducer element above the targets, since the path through the lens is straight and no refraction occurs. For the neighboring elements, the path is refracted, and the error in round trip time of flight increases rapidly with increasing lateral distance. For the deeper targets, the error in round trip time of flight is smaller, since the ray angles become smaller. When a source is located at a lateral distance of the target, the optimized parameter reconstruction underestimated the time of flights for all elements.

The underestimation of the round trip time of flight is very apparent when overlaying the hyperbolas of the two methods on the echo signals. Or alternatively, when the echo signals are delayed by the time of flights, as depicted in Fig. 2.6c and d. The underestimation of the time of flight explains why the speed of sound estimation with autofocusing consistently underestimated the true water sound speed. By using a lower speed of sound in water, the time of flight is increased, and the echo signals line up better with the arrival time hyperbola. When using the correct transducer parameters in conjunction with two

layer ray tracing, the echo signals line up perfectly with the hyperbola regardless of target depth (Fig. 2.6d).

2.4.7 Considerations when using sound speed as a biomarker

The field of sound speed imaging aims to use sound speed as a potential biomarker to discriminate healthy versus diseased tissue [103]. For instance, the difference in sound speed between healthy liver tissue and tissue with advanced steatosis is close to 100 m/s or less [104]. It is even more difficult to discriminate between different stages of steatosis, since the difference in sound speed is in the order of tens of meters per second [105].

Our results indicate that both reconstruction algorithm and transducer parameters have a large influence on the retrieved medium sound speed. Although the ground truth sound speed for all experiments was very close, around 1486 ± 2 m/s, we retrieved speed of sound values ranging from $1450 - 1525$ m/s (Fig. 2.4). This indicates that results from various studies with different scanners, transducers and sound speed retrieval methodologies are difficult to compare, and highlights the need for technical standardization in order to use sound speed as a reliable biomarker [106].

2.5 Conclusion

We described a simple, nondestructive method to estimate the transducer lens thickness, the transducer lens sound speed and the time to peak of the backscattered ultrasound pulse. We demonstrated that the combination of calibrated transducer parameters with a two-layer ray tracing reconstruction approach enables accurate sound speed estimation, and improves ultrasound image resolution and contrast up to a depth of 100 wavelengths, across the medical ultrasound frequency range.

Acknowledgment

The work was supported in part by funding from the Medical Delta Ultrafast Heart and Brain Program. The authors would also like to thank Henry den Bok for his support in making wire phantoms and Nico de Jong for the valuable discussions.

3

Adaptive Transcranial Doppler imaging of the adult rat brain

The development of fully noninvasive, transcranial functional ultrasound (fUS) would increase the translatability and clinical potential of this neuroimaging modality. Unfortunately, transcranial fUS is hindered by skull-induced aberrations which degrade power Doppler image quality and lower sensitivity. As a result, a majority of fUS imaging studies rely on craniotomies or acoustically transparent cranial windows. To advance fUS technology further, we present an adaptive aberration correction method based on ray-tracing through 4 tissue layers (transducer lens, gel & skin, bone and brain tissue). Our method segments these layers, and estimates ultrasound wave speeds in each layer iteratively. Once a velocity model of the imaging plane of interest is retrieved, ultrafast power Doppler imaging of the brain is performed using a ray-tracing beamformer that accounts for wave refraction. We tested our method in three adult rats, and estimated wave speeds for the skin/gel layer (1628 ± 7 m/s*), skull bone (*3247 ± 110 m/s*), and brain tissue (*1526 ± 55 m/s*). After aberration correction, we measured an average adult rat skull thickness of* 395 ± 41 µm *in agreement with anatomical records. The largest improvements in Doppler imaging quality were observed in cortical brain layers adjacent to the skull, specifically lateral spatial resolution was improved by 32%. Our method consistently outperformed Doppler imaging based on traditional delay-and-sum (DAS) beamforming, which assumes a uniform sound speed.*

3.1 Introduction

Functional ultrasound (fUS) has emerged as a valuable imaging modality for detecting cerebral blood volume correlated associated with neural activity [24, 107]. fUS stands out for its portability, sensitivity, and spatio-temporal resolution compared to functional magnetic resonance imaging [15]. Clinically, fUS has been used at bedside to monitor neonate health [19] and intraoperatively in adults during tumor resection surgeries [17, 18, 108]. fUS allows analysis of cerebral hemodynamic signals on a signal trial basis, making transient neural activity detectable [109]. These capabilities led to decoding of movement intentions in nonhuman primates, which represented a fundamental step towards the

development of ultrasound brain-computer interfaces [22]. In spite of these advances, the skull remains a highly attenuating and aberrating barrier for ultrasound waves that prevents the development of fully non-invasive fUS and wider adoption of this technology.

The skull bone has a high density and speed of sound (typically 3000 m/s) compared to soft tissues (skin 1600 m/s, brain 1570 m/s) [110]. As a result, transcranial ultrasound images are degraded by several physical effects including multiple scattering, refraction [111], mode conversion [112] and absorption [58]. This currently restricts the use of fUS in adult humans to intraoperative procedures [17] or chronically implanted acoustic transparent windows [21]. Transcranial fUS is feasible in mice and young rats due to the relatively thin skull [113, 114], but as animals age and the skull develops [115], other solutions are needed. To overcome skull aberration, most studies resort to surgery, such as craniotomies [24] or skull-thinning to allow chronic imaging [116]. As an alternative to surgical procedures to the skull, the echogenicity of vascular signals can be enhanced using contrast agents [63, 64]. However, the effect is transient due to gradual elimination of the agent, requiring continuous administration for sustained enhancement. Moreover, use of contrast agents remains minimally invasive and only addresses ultrasound signal attenuation.

Alternative to addressing the attenuation problem, the loss of focus can be restored by aberration correction techniques [65]. Most techniques rely on near field phase-screen modeling [66], where the aberrating layer is modeled as a thin phase screen located at the transducer surface. The phase aberration is corrected by finding the delays to apply to each transducer element, typically by maximizing the correlation between elements [67], maximizing spatial coherence [66], or maximizing speckle brightness [68]. This method can be used in the presence of either bright reflectors such as microbubbles [69–71] or diffuse scatterers [72]. Another class of aberration correction methods use ultrasound matrix imaging [117], which has been applied to transcranial ULM [118]. Finally, deep learning-based aberration correction [119, 120] has been developed but requires either contrast agents or has only been tested in weak aberrating conditions. However, all forementioned methods are limited in their ability to restore positional errors and the aspect ratio of the image.

Another group of methods uses a layered tissue velocity model to compute the refracted wave path and correct for phase aberration. This requires wave speeds for every tissue layer and an accurate delineation. The skull shape and wave speed can be obtained by ultrasound imaging [75–77], or by using other imaging modalities such as computed tomography (CT) [78–80]. However, relying on other imaging modalities has the drawback of potentially introducing co-registration errors and the need for additional costly imaging systems. Once a complete sound speed map is obtained, the propagation of a wavefront through the medium can be computed using the Eikonal equation, and the aberration corrected time of flights are obtained. The Eikonal equation can be solved using the fast marching method [121]. This has been used in simulation, phantoms [80, 82, 83], and *ex vivo* human skull [75, 84]. Alternatively, the refracted wave path can be found using two point ray-tracing [81], allowing imaging of the bone cortex [76, 77], and *ex vivo* human skull imaging [84]. The aberrated delays can be computed for every source-receiver pair, and finally be used in delay-and-sum (DAS) beamforming [26].

Here we present an adaptive transcranial ultrasound imaging method to estimate the rat skull geometry and wave speed, and corrects for wave refraction in transmission and reception using ray tracing. Compared to previously published methods, we do not require a priori information on the wave speeds or geometry of the different tissue layers, and use only ultrasound to identify aberrations induced by each layer on a per-subject basis. To evaluate the performance of this approach, we performed transcranial Doppler imaging in adult rat brains with and without aberration correction.

3.2 Methods

3.2.1 Animal procedures

Three adult male Sprague Dawley rats were imaged in this study (6-8 weeks old; 260-360 grams; Janvier Labs, France). Animals were socially housed in groups of 2-3 in a 12h reversed light-dark cycle and had ad libitum access to food and water. All experiments were approved under CCD license number AVD8010020209725 and by the animal welfare body at the Netherlands Institute for Neuroscience under Study Dossier number NIN21.36.02.

Prior to imaging, the rats were anesthetized using 5% isoflurane in an induction chamber and then transferred to an inhalation mask with 3% isoflurane for depilating over the head. Next, the rats were placed on a heating pad set to 37 °C, and head-fixed in a stereotactic frame attached to an inhalation mask, delivering 1.5% isoflurane to maintain anesthesia. Centrifuged ultrasound gel (Ultrasonic 100, Parker Laboratories, Orange, NJ, USA) was applied to couple the scalp to the probe.

3.2.2 Ultrasound acquisitions

Ultrasound acquisitions were performed with a L6-24-D transducer (192 elements; 135 µm pitch; GE HealthCare, Chicago, IL, USA) connected to a programmable ultrasound scanner (Vantage 256 High frequency configuration, Verasonics, Kirkland, WA, USA).

Our aberration correction method requires an accurate segmentation of the skull bone. To this end, we implemented a high resolution skull segmentation sequence that relies on synthetic aperture imaging with element-wise transmissions [89]. To obtain the best axial resolution we transmitted short single-cycle sine-bursts centered at 13.9 MHz.

After bone image acquisition, we switched to plane wave imaging to acquire Ultrafast Power Doppler images. We transmitted 3 cycles sine-bursts centered at 13.9 MHz and 26 plane waves ranging from -5 to 5°, resulting in 700 Hz frame rate after coherent compounding [25]. We set the duration of frame ensembles to 250 ms to capture a full cardiac cycle of the rat in each Doppler image.

To correct for refraction effects in the skull bone, the inner and outer skull interfaces must be clearly resolved in the B-mode. This requires to position the probe to obtain specular echoes from both skull interfaces (see Fig. 3.2). We used live B-mode imaging to find maximal specular reflections from outer and inner skull interfaces. The probe was positioned 2 mm above the skull surface. Next, we acquired an ultrafast power Doppler image in the same plane using the plane wave sequence described previously.

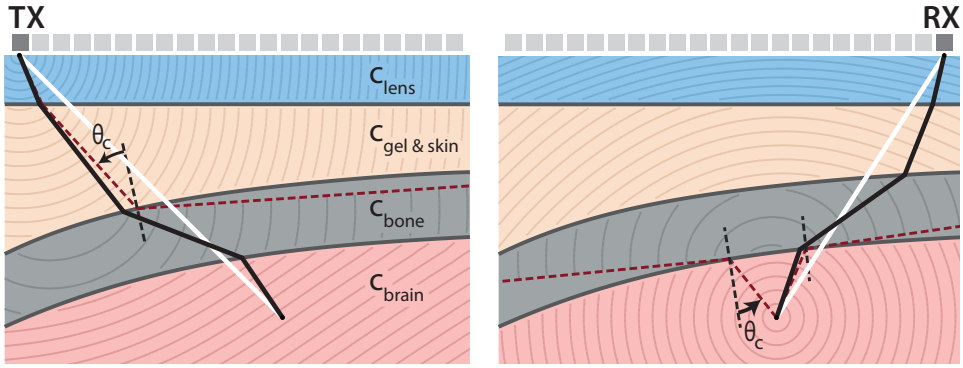

Figure 3.1 – Wave refraction during transcranial ultrasound imaging. (a) Wave propagation in transmission and **(b)** reception, through 4 layers with distinct sound speeds: the transducer lens, acoustic coupling gel and skin tissue, the skull bone, and finally brain tissue. White lines show the wave path in conventional image reconstruction assuming homogeneous wave speed. Black lines show the refracted path through the medium, fulfilling Snell's law. Iso-phase lines (wave front) in each layer are spaced at one wavelength λ in water. The dark red dashed lines indicate the paths subject to total internal reflection due to the critical angle θ_c.

We used a real-time DAS (delay-and-sum) beamformer implemented in CUDA on a GPU (GeForce RTX 3090, NVIDIA, USA) for live display. After beamforming, power Doppler images were formed by separating blood signals from tissue signals using a singular value decomposition (SVD) spatio-temporal clutter filter [45]. Since motion is minimal in experiments conducted under anesthesia, we used a fixed threshold and removed the first 20% of singular vectors (35 out of 175 frames). RF data from both skull segmentation and brain angiography sequences were saved and processed offline.

3.2.3 Delay-and-Sum Beamforming

The gold standard for ultrasound image reconstruction is DAS beamforming. For each pixel point, the time of flight of the ultrasound wave is calculated for each combination of transmitting and receiving elements. In conventional DAS, the medium is assumed to have a homogeneous sound speed c_0 of 1540 m/s and straight paths are assumed between the source, pixel point and receiver (Fig. 3.1a,b). The image magnitude $s(\vec{x}_p)$ at pixel point $\vec{x}_p$ is given by,

$$s(\vec{x}_p) = \sum_{i=1}^{M} \sum_{j=1}^{N} \mathrm{RF}(t = \tau, i, j)\, w(\vec{x}_p, j), \tag{3.1}$$

with M the number of transmissions, N the number of receiving elements, RF the recorded data, τ denotes the delay for pixel $\vec{x}_p$, transmission i and receiving element j, and $w(\vec{x}_p, j)$ a weighting to account for element directivity [122]. Ultrasound scanners usually emit short bursts of sine waves, consisting of a few periods of oscillation at the probe's central frequency. To ensure accurate image reconstruction, it is critical to delay the ultrasound signals to the crest of the envelope of the received waves, i.e. the time to peak t_{ttp} of the envelope of the received waveform [85]. Finally, transducers have a lens to focus the

ultrasound beam in the elevation plane. Lenses typically have a lower sound speed than soft tissue, and the difference in sound speed has to be accounted for. An estimation for the time to peak and the lens correction term is often given by transducer manufacturers.

To evaluate the aberration correction approach, we reconstructed reference images using the conventional DAS beamforming method with a homogeneous sound speed of 1540 m/s, manufacturer reported values for time to peak and lens correction, and a standard binary element weighting using F number 2 [26].

3.2.4 Aberration Correction Method

In transcranial imaging, the homogeneous wave speed assumption fails. The skull bone has a significantly higher wave speed than the soft tissues and therefore time of flights are underestimated using conventional DAS and wave refraction is not accounted for (Fig. 3.1a,b). To obtain accurate time of flights, we used an adaptive aberration correction method that estimates the wave speed in four tissue layers and corrects the time of flight by retrieving the refracted wave path through ray tracing.

The method is divided in three reconstruction steps. In the first step, we use a 2-layer model to correct lens refraction, which allows to accurately estimate the wave speed in the gel/skin layer by autofocusing [85], and segmentation of the outer skull surface. In the second step we use a 3-layer model to estimate the wave speed of the skull bone and segment the inner skull surface. During the final step, we use a 4-layer model to estimate the wave speed in the brain tissue and perform the final aberration correction. A graphical overview of the method is shown in Fig. 3.2.

Transducer parameters: acoustic lens and time-to-peak

A prerequisite to all aberration corrections reported in the rest of the manuscript is to characterize the lens and waveform parameters of the transducer. We transmitted a 1-cycle imaging pulse in air in a synthetic aperture sequence, and received the internal lens reflections. Then we found the time to peak, lens thickness and lens wave speed by maximizing the coherence of the internal lens reflections as described in [85]. We found a lens wave speed of 1009.6 m/s, a lens thickness of 518.5 μm, and a time to peak of 0.335 μs for the single cycle waveform and 0.467 μs for the three cycle waveform.

4-Layer Velocity Model

Ultrasound transducers have a silicone rubber lens to focus the ultrasound beam in the elevation direction. The first layer models the transducer lens. Lenses have a wave speed of ≈ 1000 m/s [86] and a thickness of 2-7 ultrasound wavelengths in water. The lens wave speed and thickness are rarely reported by transducer manufacturers, and were therefore estimated using our earlier reported calibration method that capitalizes on internal lens reflections [85].

The second layer models both the acoustic coupling gel and skin tissue. The heterogeneity within this layer is assumed to be small, since ultrasound gel used for coupling is matched with skin tissue in terms of acoustic impedance. Skin wave speed is reported to be $1600-1620$ m/s, slightly higher than soft tissue [110, 123].

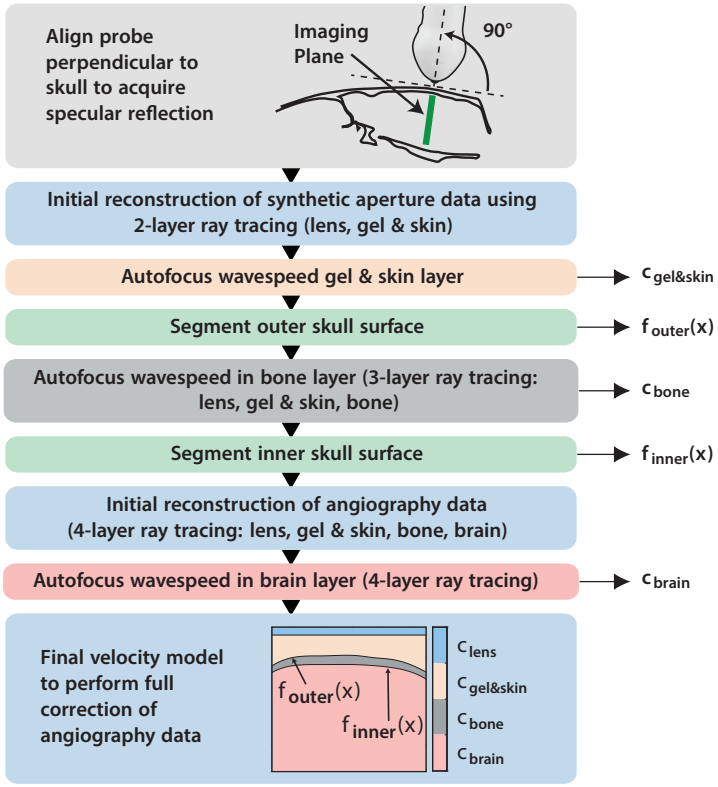

Figure 3.2 – Graphical overview of the adaptive aberration correction method.

The third layer in our model represents the skull bone, characterized by its high density and a reported wave speed ranging from 2400 to 3500 m/s [124–126]. The thickness and curvature of the skull vary considerably, with the supraoccipital bone at the back measuring between 0.6 and 1.2 mm, and the parietal bone in the middle ranging from 0.2 to 0.6 mm, mainly depending on body mass [127]. Rat skulls consist of plates that grow together and are connected by sutures. The speed of sound in the skull increases with age due to changes in mineral content of the cortical bone. The sutures consist of collagen-rich connective tissues with sound speeds closer to soft tissue. The skull bone is not a uniform layer but rather a sandwich structure consisting of an outer and inner cortical layer with diploë in between. The diploë is a spongy trabecular bone layer and typically constitutes about one-fifth of the total skull thickness [60, 61]. Given that the diploë layer is too thin to resolve using ultrasound imaging and accounts for a small thickness fraction, we simplify the skull as a single homogeneous layer in our ray-tracing model. The varying curvature and thickness is modeled by segmenting the outer and inner surfaces using piece wise cubic splines.

The final layer models the brain tissue. There is no literature reported value for the wave speed in rat brain tissue at high frequency. In fresh *ex vivo* canine brain samples, the

wave speed was reported to be between $1563-1570$m/s [128, 129], measured at 37 °C at 5 MHz, slightly higher than the averaged soft tissue value of 1540 m/s.

Adaptive Ray Tracing

To find the aberrated round trip time of flight, we use a ray tracing method adapted from Renaud *et al.* [76] that finds the refracted wave path in the 4-layer model. The estimated time of flight is used in conventional DAS beamforming to reconstruct the corrected image [26].

The refracted path is found by two-point ray tracing, a technique that is commonly used in seismic imaging [81]. In this technique, Snell's law of refraction is imposed on all but the last interface. The aberrated wave path is found by minimizing the time of flight between a source and pixel point, or receiver and pixel point, following Fermat's principle. Specifically, for each source and pixel combination, we test different emerging ray angles form the source, traverse the layers by computing the refracted ray at each interface intersection, except for the last. The last interface intersection point is connected to the end point, to compute a time of flight for the tested angle. Finally, we find the path fulfilling Snell's law by minimizing the time of flight using Brent's algorithm [130]. This process is repeated for all combinations of sources and pixel points and receivers and pixel points.

The algorithm gives access to the reception angle for each source-pixel-receiver combination, which is used to account for element directivity in the beamforming process [122]. The algorithm is implemented in C++ and parallelized using OpenMP.

Intersection of rays with interfaces

During the minimization, the speed of sound map is traversed by rays with different angles. This requires finding the intersection points of a ray with the lens and skull surfaces. The intersection point on the lens surface follows from the tested ray angle and the lens thickness. The intersection point of the refracted ray with the outer skull surface is found by a line-spline intersection algorithm.

To find the intersection point of the ray and the piece wise cubic spline, we need to find in which subdomain the intersection point lies. This is done by testing the ray against all spline segments with potential intersections.

For a ray described by $z = px + q$, and a cubic spline section $z = ax^3 + bx^2 + cx + d$, we find their intersection point by computing the roots of the equation,

$$ax^3 + bx^2 + (c-p)x + (d-q) = 0. \tag{3.2}$$

This cubic is reduced to a depressed cubic equation of the form,

$$t^3 + pt + q = 0. \tag{3.3}$$

Finally, we apply Cardano's formula to find only the real roots [131]. We obtain 1 root if the discriminant is positive and 3 otherwise. Next we need to test if the found roots are in the domain of the current spline segment. The root is discarded if it is not in the domain, otherwise, we find the intersection point by evaluating the line equation at the root. If no

valid real roots are found for a spline segment, the next segment is tested. If no valid roots are found for any segment, the ray does not intersect the spline.

Wave speed Estimation

We find the wave speed in each layer by autofocusing, in which we reconstruct a region of interest (ROI) of the aberrated image with different wave speeds, until we maximized the image sharpness. Image sharpness is defined by the Brenner gradient,

$$F_{\text{Brenner}} = \sum_{x,y} \left(I_{x+2,y} - I_{x,y}\right)^2 + (I_{x,y+2} - I_{x,y})^2, \tag{3.4}$$

where $I_{x,y}$ is the image intensity at location (x, y) [92].

The wave speed in the gel/skin layer is found by using the 2-layer model on the synthetic aperture data from the skull-segmentation sequence. After an initial reconstruction at 1600 m/s we define a region of interest (ROI) around the skull bone (Fig 3.3b) and autofocus. The wave speed that maximizes sharpness is selected as the wave speed of the gel/skin layer.

Secondly, the wave speed in the skull bone is found using the 3-layer model. We define a ROI around the bone (Fig 3.3d) and maximize the sharpness of the inner skull surface. To avoid influence of the outer bone surface during maximization of the sharpness, a mask that mutes the outer bone surface is applied. After obtaining the wave speed of the skull bone, we can reconstruct a high resolution B-mode of the total skull, and segment the inner skull surface.

To segment the skull, we use Dijkstra's algorithm to find the lateral path through the image that has maximizes brightness. This path is smoothed with a 3 sample moving average filter. Then, a piece wise cubic spline is fitted to the path. To have a precise segmentation, the image is reconstructed with an isotropic pixel size of $\frac{\lambda}{4}$.

To estimate the final missing velocity in the 4-layer model, we use the data from the brain angiography sequence. We reconstruct the brain using the 4-layer model and an initial wave speed of 1540 m/s, and form the Power Doppler image. In this image we define a ROI around the brain vasculature (Fig. 3.3g), and autofocus the ROI to maximize the sharpness of the Power Doppler images. We use the Power Doppler image to autofocus since the synthetic aperture image has too low SNR. Instead, we could have used the B-mode of the brain angiography sequence, but the presence of multiple reflections of the skull biases the autofocusing. Finally, we use the fully characterized 4-layer model to reconstruct the full aberration corrected brain angiographic image.

During the autofocusing process for brain tissue, the vascular content within the region of interest (ROI) changes depending on the tested wave speeds, which biases the focus quality metric. To mitigate this effect, the bounding box of the ROI was shifted by

$$\Delta z = (z_{\text{ROI,center}} - z_{\text{skull}}) \frac{c_{\text{test}} - c_{\text{center}}}{c_{\text{center}}}, \tag{3.5}$$

with $z_{\text{ROI,center}}$ the depth of the center of the ROI for autofocusing, z_{skull} the depth of the inner skull surface at the center of the image, c_{test} the wave speed tested, and c_{center} the mean value of the tested wave speeds.

Phantom validation
To validate our adaptive aberration correction technique, we estimated the wave speed of three distinct layers in a phantom setup. We submerged a wire phantom with 3 nylon wires with a diameter of 10 µm in a tank with degassed water. We positioned a 300 ± 10 µm PVC aberrating layer above the wires (measured with caliper; Mitutoyo, Kawasaki, Japan). The phantom was imaged using the skull segmentation and brain Doppler sequences. Before and after imaging, the water temperature was measured using a high accuracy thermometer with an accuracy of 0.04 °C (PT100 thermocouple, Greisinger electronics, Germany).

After imaging, we first we autofocused the layer of water between transducer and PVC using the 2-layer model, then used the 3 layer model to find the wave speed in the PVC, and finally used the 4-layer model on the plane wave data to estimate the wave speed in the water around the wires. The temperature of the water was converted to the ground truth sound speed of the water using a calibration curve [94]. When the ultrasound estimated thickness of the PVC layer and the wave speed of the water in the third layer match the ground truth, our method is validated.

3.2.5 Evaluation of image quality improvement
We use three reconstruction approaches to compare image quality. The reference image has no correction (NC) and relies on conventional DAS. We compare the reference images to a lens corrected image (LC) using the 2-layer model, and a full correction (FC) with the 4-layer model.

To evaluate the resolution improvement and the ability to resolve more vessels, we analyze the Doppler intensity profile along a line through the cortex. Since vessels rarely exhibit a prominence of at least 6 dB relative to adjacent local minima, the conventional full width at half maximum (FWHM) metric is not reliably applicable. Instead, we identify vessels with a minimum peak prominence of 2 dB, and compute their width at the -2 dB level.

To assess whether the improvement of our aberration correction technique varies over imaging depth, we compute the mean value and sharpness of the power Doppler image in three ROIs: cortex, midbrain and deep (Fig. 3.7a). We then determine the improvement with respect to the reference image, by computing the ratio for both the magnitude and sharpness of the power Doppler image, of LC and FC over NC. Since in the three reconstruction approaches the skull depth and apparent thickness is different, the ROIs are offset by the difference in apparent skull depth with respect to NC.

To further understand the effect of our aberration correction, we determined the phase aberration law for the different points in the image (see crosses in Fig. 3.7a). The aberration law was found by taking the difference between the return time of flight from the conventional DAS approach and the full correction.

Since the skull is reconstructed with a too low wave speed in the NC and LC images, the bone appears too thin. In addition, the bone layer acts as a diverging lens. When using our 4-layer model to correct for the aberrations, this leads to a lateral and axial shift of the brain vasculature in the FC image.

To quantify the thickness of the bone layer, we measured the distance between the outer and inner skull segmentations. We determined the minimum distance of the outer skull segmentation to the inner skull segmentation for every pixel to obtain the skull thickness as a function of lateral position. Finally, we compute the mean skull thickness per subject.

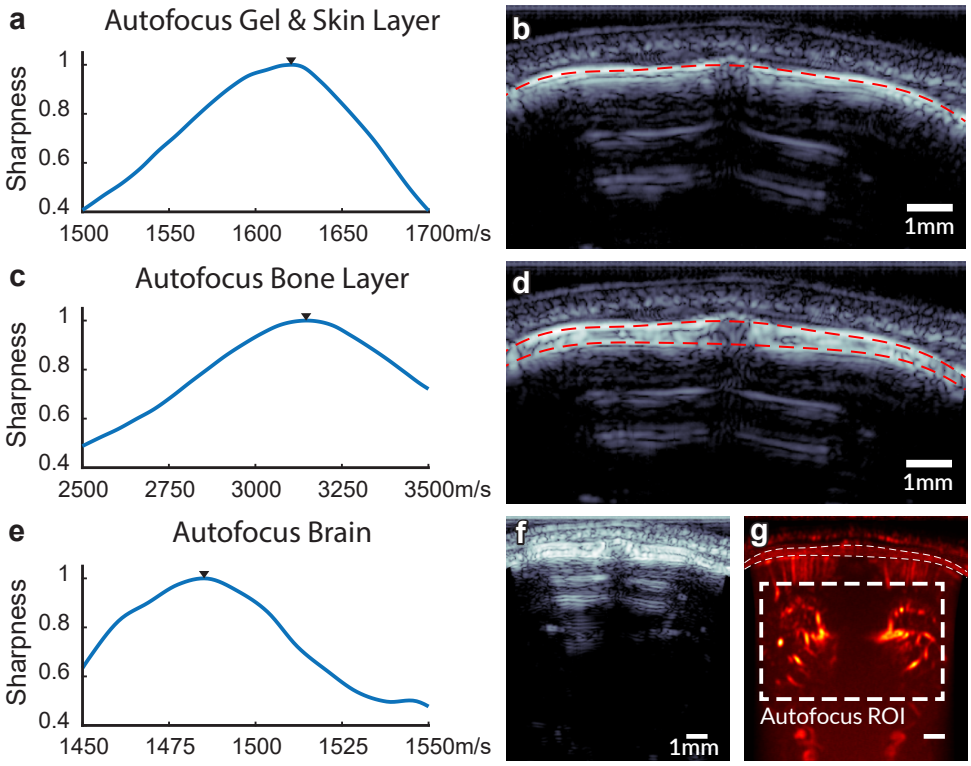

Figure 3.3 – Wave speed estimation. (a) Result of autofocusing the gel and skin layer using the synthetic aperture data. The image is reconstructed using the 2-layer model. **(b)** The synthetic aperture image reconstructed with the estimated wave speed of the gel/skin layer. In this image, the outer skull surface is segmented using Dijkstra's algorithm (red dashed line). **(c)** Result of autofocusing the skull bone layer using the synthetic aperture data and the 3-layer model. **(d)** The synthetic aperture image reconstructed with the estimated wave speeds. The inner skull surface is segmented, indicated by the lower red dashed line. **(e)** Finally, the brain angiography data is used with the 4-layer model to autofocus the wave speed in the brain tissue. **(f)** Aberration corrected plane wave B-mode. **(g)** Power Doppler data to estimate the brain wave speed.

3.3 Results

3.3.1 Phantom validation

To validate our adaptive aberration correction method, a phantom experiment was conducted using a layered setup consisting of water, a PVC film, and wire targets submerged in water (Fig. 3.4). The water temperature was measured to be 22.80 °C, corresponding to a wave speed of 1491 m/s [94]. The results of autofocusing for each layer are shown in Fig. 3.4. The synthetic aperture imaging sequence was used to estimate wave speeds in the first water and PVC layers, resulting in 1499 m/s and 2244 m/s respectively. The segmentation of the PVC film revealed a thickness of 290 µm. Finally, autofocusing of the wire targets in the water layer below the PVC film yielded a wave speed of 1491 m/s for both synthetic aperture and plane wave imaging methods. The full aberration corrected phantom synthetic aperture image is shown in Fig. 3.4b, and the plane wave image in Fig. 3.4c. These findings validate our method's ability to accurately estimate wave speeds and segment layer boundaries of a thin aberrating layer, under controlled experimental conditions.

3.3.2 Wave speed estimation

Fig. 3.3 shows the autofocusing curves and step by step B-mode images of the rat skull. Fig. 3.3a shows the image sharpness for the tested wave speeds in the gel/skin layer, where we found a mean wave speed of 1628 ± 7 m/s for all rats. Fig. 3.3b shows the lens corrected synthetic aperture image of the rat skin and skull with the outer skull surface segmentation. In this image, the bone is reconstructed with a too low wave speed, and shows up with an underestimated thickness. Fig. 3.3c shows the bone autofocusing curve, resulting in a mean wave speed of 3247 ± 110m/s for all rats. Fig. 3.3d shows the full aberration corrected synthetic aperture image of the rat skull, where the inner skull surface is segmented. Compared to the lens corrected image, the bone is now reconstructed with the correct wave speed and shows up with the correct thickness. The average thickness for all rats was 395 ± 41 µm. Fig. 3.3e shows the autofocusing result for the brain, where we found a mean wave speed of 1526 ± 55m/s for all rats. Finally, Fig. 3.3f,g shows the full aberration corrected plane wave B-mode of the rat skull and power Doppler of the brain vasculature. Due to the presence of multiple reflections in the B-mode, we used the shown autofocusing ROI in the Power Doppler to retrieve the brain wave speed. The results of the wave speed estimation and segmentation for each rat are shown in Table 3.1.

3.3.3 Improvement of image quality

Fig. 3.5 shows the Doppler images of the three rats, for no correction (NC), lens correction (LC) and full correction (FC). Vessels appear sharper and with higher intensity in FC compared to LC and NC, and blurry vessels are resolved after correction. In the FC images, there are dark areas on the sides of the images, which originate from the limited lateral extend of the segmentation.

Fig. 3.6 shows a quantitative analysis of the resolution improvement in the cortex due to aberration correction. Fig. 3.6d shows that the full correction allows to individually resolve more vessels in the cortex, compared to no correction and lens correction. This finding was consistent for all three rats. In addition to resolving more vessels, Fig. 3.6e

Table 3.1 – Age, weight, the results of autofocusing for all layers, and the average segmented skull thickness for each rat.

Rat	Age (days)	Weight (g)	Wave speed (m/s) Skin/Gel	Bone	Brain	Thickness skull (μm)
1	47	260 gr	1626	3310	1590	361
2	47	288 gr	1622	3120	1486	385
3	54	368 gr	1636	3309	1503	441

shows that vessel width (FWHM) decreases in LC and FC, indicating an improvement in lateral resolution. For rat 1 the median vessel width was 239.7 μm for NC, 213.2 μm for LC and 155.7 μm for FC. For rat 2 the median vessel width was 217.5 μm for NC, 224.0 μm for LC and 162.6 μm for FC. For rat 3 the median vessel width was 256.5 μm for NC, 208.7 μm for LC and 149.7 μm for FC. On average, the improvement in vessel width was 9% for LC and 32% for FC.

Fig. 3.7 shows the improvement of the aberration correction method as a function of imaging depth. Fig. 3.7b shows the aberration law for three different depths in the image, corresponding to the cortex, midbrain and deep brain and both brain hemispheres. It becomes clear that the aberration is the strongest for the ROI closest to the aberrating layer, and decreases with imaging depth. The maximum time difference of the aberration law is ≈1.15 μs, which corresponds to approximately 16 ultrasound periods at 13.9 MHz. Fig. 3.7c,d show the relative improvement in magnitude and sharpness of the power Doppler image for the three ROIs at different depths. The relative magnitude improvement for LC was 1.3 in the cortex, 1.5 in the midbrain and 1.4 in the deep brain. For FC the relative magnitude improvement was 2.1 in the cortex, 1.8 in the midbrain and 1.6 in the deep brain. The relative sharpness improvement for LC was 3.9 in the cortex, 8.2 in the midbrain and 4.5 in the deep brain. For FC the relative sharpness improvement was 31.8 in the cortex, 19.8 in the midbrain and 8.4 in the deep brain. The improvement in magnitude and sharpness of the FC power Doppler image is highest for the cortex, and decreases with imaging depth. The improvement in FC is higher than in LC for all ROIs and depths.

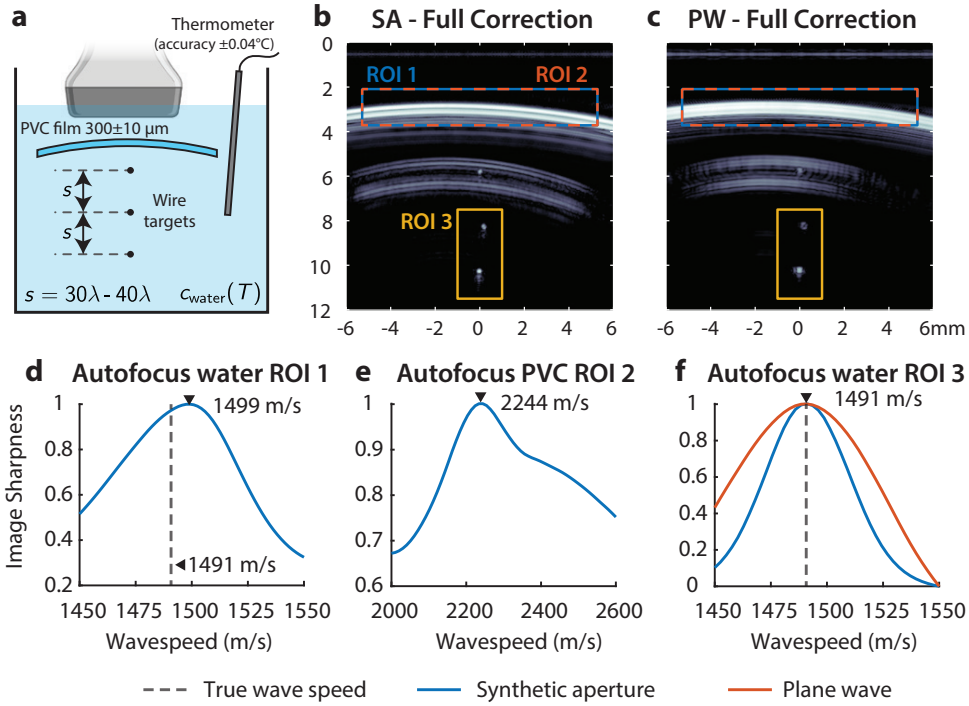

Figure 3.4 – **(a)** Phantom validation setup. **(b)** The aberration-corrected synthetic aperture. **(c)** Aberration-corrected plane wave image of the plastic film and wires. **(d)** Autofocusing of the first water layer in ROI 1, using the synthetic aperture data. **(e)** Autofocusing of the PVC layer in ROI 2, using the synthetic aperture data. **(f)** Autofocusing of the last water layer in ROI 1, using both the synthetic aperture (blue line) and plane wave (orange line) data.

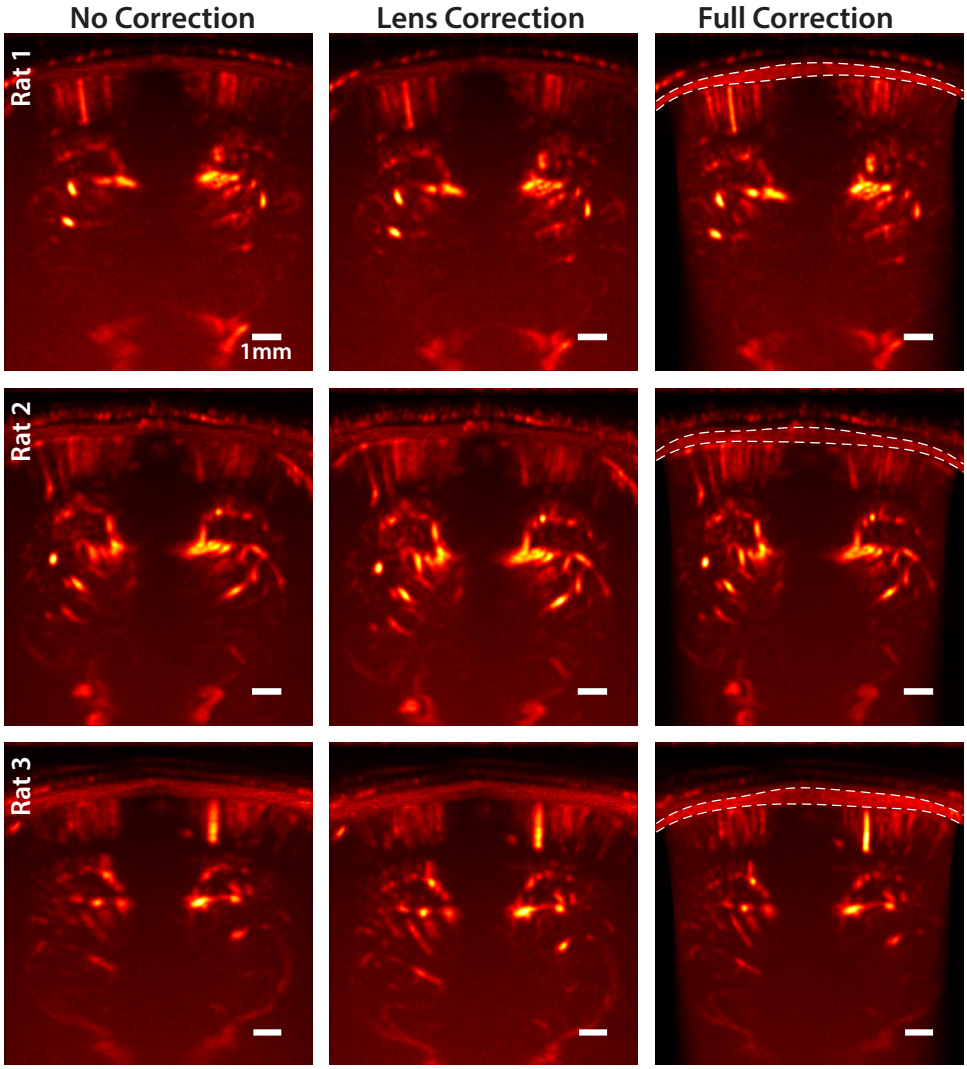

Figure 3.5 – Power Doppler ultrasound images of three living rat brains. First column the uncorrected image using conventional DAS. The second column shows the lens aberration corrected image using the 2-layer model. The third column shows the fully corrected image using the 4-layer model. The last column shows an overlay of the uncorrected image (NC in green) and the fully corrected (FC in magenta) image. All scale bars denote 1 mm.

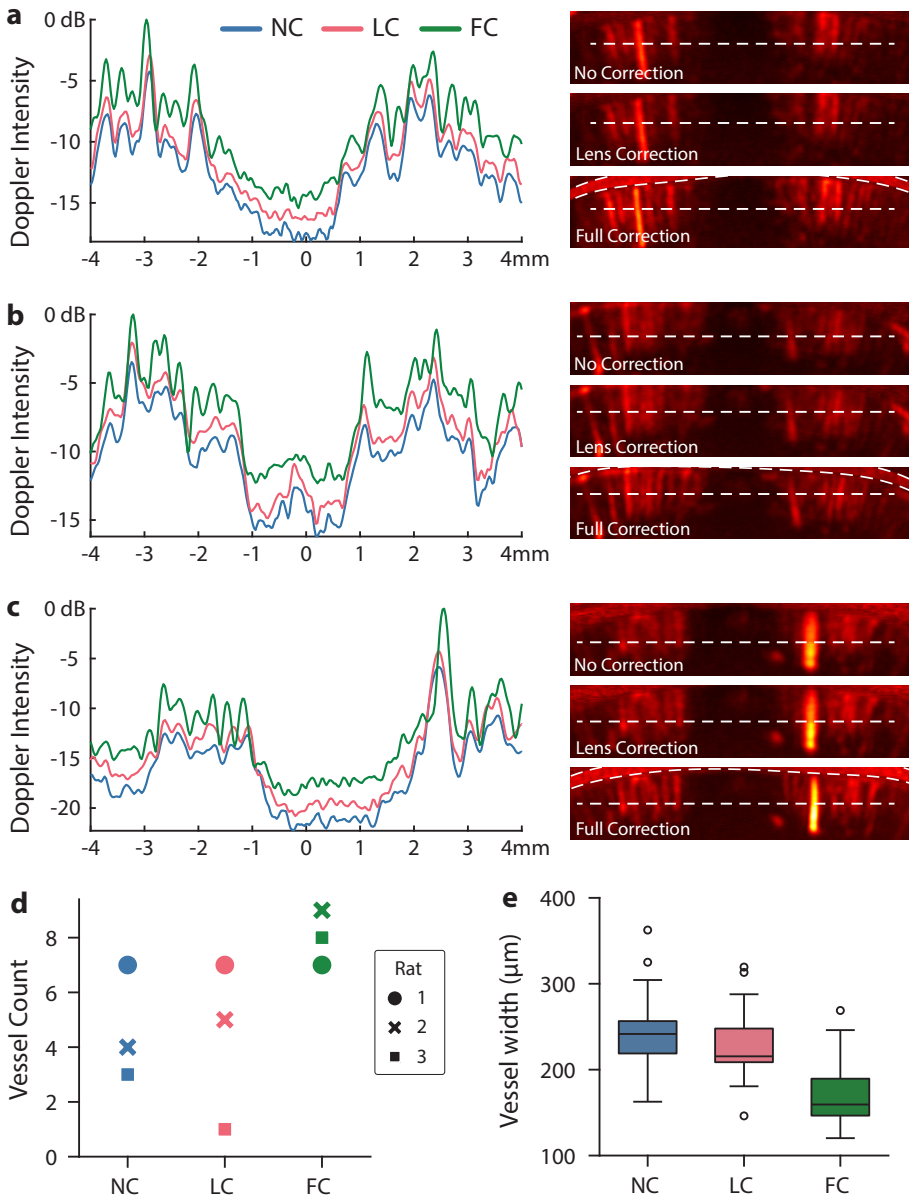

Figure 3.6 – Power Doppler profiles through the cortex, of rat 1 **(a)**, rat 2 **(b)** and rat 3 **(c)**. Colors indicate the different reconstruction approaches, with in blue No Correction (NC), in red Lens Correction (LC) and in green Full Correction (FC). The profile corresponds to the white dashed line overlaid on the cortex zooms on right of the profiles. Panel **(d)** shows a vessel count for the three reconstruction approaches. The vessel count is obtained by identifying peaks in the Doppler intensity profile with a minimum prominence of 2 dB relative to adjacent local minima. **(e)** Shows the vessel width, defined as the width at the -2 dB level for peaks found in the power Doppler image. The box plots show the combined statistics of the three rats.

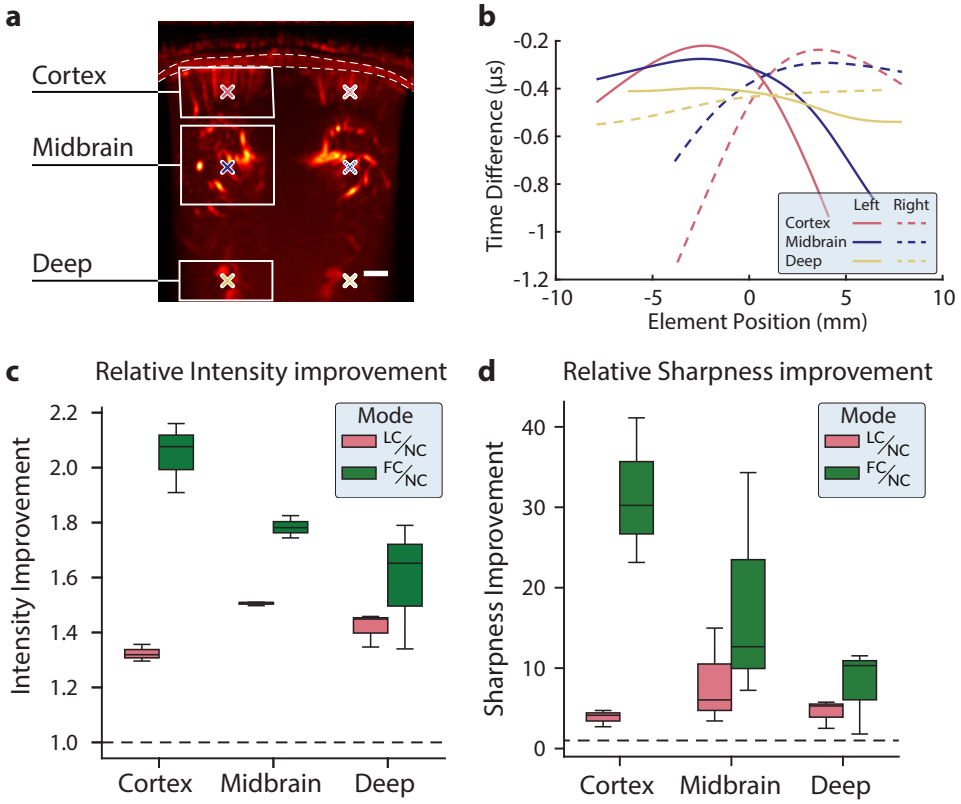

Figure 3.7 – Aberration correction performance across depth. (a) Three regions of interest (ROIs) at different depths in the image, corresponding to the cortex, the midbrain and deep. The scale bar denotes 1 mm. **(b)** Aberration law for three different depth (colors correspond to the markers colors in **(a)**). Solid lines denote the left hemisphere and the dashed lines the right hemisphere. The aberration law is found by the different in return time of flight between the No Correction and Full Correction travel time lookup tables. **(c)** Relative improvement in magnitude of the Lens Correction (LC) and Full Correction (FC) power Doppler images, with respect to No Correction (NC) for the three ROIs at different depth. The black dashed line at 1.0 indicates no improvement. **(d)** Relative improvement in the Doppler sharpness for three ROIs at different depth of Lens Correction (LC) and Full Correction (FC) with respect to No Correction (NC).

3.4 Discussion

3.4.1 Estimation of tissue wave speed and skull thickness

In this study, we report an adaptive 4-layer ray-tracing method approach to correct skull aberrations in transcranial ultrasound imaging of the adult rat brain. We first validated on a phantom experiment with an aberrating layer having known thickness and a known wave speed in water. The wave speed in water was estimated with an accuracy equal or better than 0.56%. The wave speed found for the PVC layer is in line with the reported values in the literature, and the estimated thickness retrieved by segmenting the PVC layer in the B-mode is within the error margin of the caliper measurement.

The wave speed in the gel/skin layer and in the bone layer estimated in vivo was in agreement with the literature. The variability in wave speed may originate from subject variability in age, diet, or experimental conditions such as the probe-skull angle and the fact that the inner and outer skull surface may not be perfectly parallel, reducing specular reflection. The skull thickness retrieved from the aberration corrected synthetic aperture images matched well with earlier reports on body mass and skull thickness in rats [127]. For the brain, the estimated wave speeds showed larger standard deviation, but were still in line with expected values from the literature.

3.4.2 Depth-dependence of aberration and its correction

Evaluating the impact of aberration correction as function of imaging depth, showed that the correction performed best in the cortex, as evidenced by magnitude profiles of the power Doppler image through the cortex (Fig. 3.6), along with the magnitude and sharpness ratios of the power Doppler images (Fig. 3.7c,d). For all imaging depths, both the fully corrected (FC) and lens corrected (LC) methods outperformed the non-corrected (NC) approach. As imaging depth increased, the performance of FC became closer to that of LC. This trend can be explained by the nature of aberrations, which are the strongest near the aberrating layer where the incident angles are steepest. This observation aligns with the aberration law shown in Fig. 3.7, which demonstrates that as depth increases, the aberration law flattens. The flattening explains why the performance difference between LC and FC diminishes with depth. Closer to the aberrating layer, the aberration law also reveals that it is not possible during ray-tracing to find a path to all receiving elements (indicated by pink lines in Fig. 3.7). This is caused by steep incident angles at the bone interface, which lead to critical reflection, as shown in Fig. 3.1b. For deeper regions, the incident angles at the bone interface decrease, and the ray-tracer successfully can find a path for all receiving elements.

3.4.3 Challenges in skull segmentation and alignment between transducer and skull

The main challenge of the aberration correction method introduced in this manuscript lies in skull segmentation. For young animals with very thin skulls, the axial resolution of the imaging system can become insufficient and prevent the accurate delineation the outer and inner skull interfaces. For example, our validation experiment demonstrated that a 300 µm aberrating layer could be resolved using a 1-cycle imaging pulse at 15 MHz, but the 3-cycle long plane wave Doppler sequence had an insufficient resolution to detect outer and inner

interfaces of the PVC layer. This highlights the need for a high resolution sequence for skull segmentation. In the current implementation, the axial resolution of our imaging system allows imaging of rats weighing 200 g or more approximately [127].

The accuracy of the skull segmentation also depends on obtaining clear specular reflections from both the outer and inner surfaces of the bone. The outer specular reflection could be reliably obtained during the in vivo data acquisition by verifying with live imaging. However, achieving a clear specular reflection from the inner surface proved challenging due to the absence of an aberration-corrected preview. Obtaining a specular reflection from the inner skull surface is even more challenging when the skull surfaces in the imaging plane are not parallel.

Implementing the method in 3D using a 2D matrix array would offer significant advantages. In 3D imaging, the requirement for precise probe positioning to acquire specular reflections is virtually eliminated. Furthermore, 3D imaging allows imaging of the brain below non-parallel skull surfaces.

3.4.4 Implications for transcranial functional imaging

The advancements presented in this study have significant implications for 2D fUS. A remaining challenge in 2D transcranial fUS is navigating to brain regions of interest. The requirement of positioning the probe perpendicular to the skull, often results in a power Doppler image of the brain that differs significantly from the standard brain atlas.

One key advantage of our method is the ability to retrieve the wave speed model once and apply it across any other acquisition sequence. After initialization, functional recordings can be aberration corrected at no additional computational cost, provided that the transducer stays in place.

Our method improves the reconstruction accuracy to show brain regions at the correct anatomical locations and with the correct shape, thus facilitating accurate comparisons with anatomical and functional data from other imaging modalities. Furthermore, enhanced spatial resolution in cortical regions substantially improves the spatial specificity of the fUS signal, improving the usability of transcranial fUS in functional connectomics [132].

Our improved resolution in the cortex would make fUS more sensitive to weak and or transient neural activity. For instance, to create accurate somatotopic mappings during whisker stimulation experiments. The barrelfield is located in the primary somatosensory cortex, and contains distinct neuronal clusters, known as barrels, which correspond one-to-one with the whiskers on the rat's face. With inter-barrel distances of approximately 50 – 100 µm, our enhanced resolution would allow the detection of single-whisker activations [133]. Similarly, our method can achieve higher resolution retinotopic mappings of the visual system [134] and tonotopic mappings of the auditory system [135].

To fully unlock the potential of noninvasive fUS and overcome the current limitations of this study, future efforts will focus on extending our aberration correction method to 3D imaging. This advancement would enable 4D transcranial imaging, offering comprehensive spatio-temporal resolution and further advancing the utility of fUS in functional brain research.

3.5 Conclusion

We developed an adaptive aberration correction method using 4-layer ray-tracing that can improve image quality and signal spatial specificity in transcranial ultrasound Doppler imaging of the adult rat brain. The method adapts to each subject and each brain section being imaged without requiring prior information from additional imaging modalities like a CT or MRI scan. The method consistently outperformed conventional delay-and-sum image reconstruction, and holds promise for functional imaging applications that require high spatial sensitivity.

3.6 Acknowledgment

We thank Ruud van Tol (NIN, KNAW) for designing the ultrasound probe holder, Henry den Bok (ImPhys, TU Delft) for fabricating wire phantoms, Ronald Ligteringen (ImPhys, TU Delft) for facilitating access to computational resources, and Gert Jan de Fluiter (NIN, KNAW) for his assistance with animal care.

4

Multi-Slice Functional Ultrasound Neuroimaging

Functional ultrasound (fUS) has emerged as a sensitive neuroimaging modality that relies on high frame rate ultrasound imaging of the brain hemodynamics to infer neural activity. Recent advances have shown that fUS is a viable technology for brain- machine interfaces (BMIs) in both non-human primates and humans. To date, BMI studies based on 2D fUS lock in on a single brain section which hampers decoding of widespread neuronal activity. 3D fUS can potentially address this limitation but presents significant challenges in terms of data bandwidth, computational demands, and higher temperature increases due to the requirement of a higher number of transmitted waves. However, we do not need to capture the entire field of view to decode brain activity, only specific neurons respond to specific stimuli. We introduce selective- plane fUS, an approach that takes advantage of the large field of view of row-column addressed (RCA) transducer arrays to monitor neural activity in one or multiple brain regions without moving the probe. Since the selection of the planes is done electronically, it can operate with a higher spatio-temporal resolution and a reduced data and pulse repetition rate compared to 3D fUS while maintaining high sensitivity to neurovascular changes. Our imaging pipeline consists in the acquisition of a 3D functional activation map to guide plane selection, followed by high frame rate focused wave (FW) imaging in selected coronal or sagittal brain sections. Selective-plane fUS exhibits lower signal variability than 3D fUS and robust detection of visually evoked activity in the rodent brain. By targeting functional regions of interest without recording the entire fields of view, selective-plane fUS reduces computational overhead by one order of magnitude, unlocks continuous 1000 Hz recording at the functional pixel level and decreases functional signal variability by a factor 5. We envision that this method will allow tailored continuous functional imaging of widespread neuronal activity in the human brain in a BMI context.

4.1 Introduction

fUS imaging has emerged as a valuable tool for detecting neural activity in preclinical and clinical research [24, 136]. Thanks to the high scalability of ultrasound, fUS has

been applied to various neural systems across a wide range of species, including rodents [49, 134, 137, 138], pigeons [139], ferrets [135], non-human primates [109, 140] and humans [17, 19, 21]. Recently, fUS has garnered significant interest from the field of Brain Machine Interfaces (BMIs). BMIs enable direct communication between the brain and external devices, allowing users to control computers or prosthetics [10]. By decoding the brain functions, neural implants can offer solutions for people with reduced mobility [141] or speech disabilities [142]. Critical requirements for BMIs are portability and real-time imaging to allow closed-loop control, which is essential for accurate translation of the user's neural signals to intended actions [143, 144]. fUS is a good candidate for BMI due to its attractive spatio-temporal resolution (100µm and 100ms at 15 MHz), high sensitivity to slow blood flow (> 2mm/s) [145], portability, and large field of view depth-resolved imaging capabilities [44].

The first demonstration of fUS for BMI showed that it was capable of predicting movement intentions of non-human primates on a single-trial basis [22]. This work relied on offline analysis of prerecorded data. Subsequent work made advances by improving the decoding ability from 2 to 8 movement directions, and allowing online, closed-loop control [23]. These first implementations of fUS-BMIs were constrained to a single imaging plane, and therefore miss potentially informative functional signals out of the selected plane. They also suffer from motion of the brain during long acquisitions which means the informative functional signal could go out of the plane of imaging. To further advance fUS-BMI performance, there is growing interest in applying volumetric fUS to capture activations in a larger field of view, with the perspective of improved decoder accuracy and extension of possible actions.

Rabut *et al.* [50] and Brunner *et al.* [49] pioneered whole brain volumetric fUS using a fully populated 2D matrix array with 1024 elements. In current implementations, imaging with the full aperture requires multiplexed acquisitions [49], thereby reducing the frame rate, or connecting multiple scanners [52], decreasing portability. Moreover, due to fabrication constraints, 2D matrix imaging remains limited to a relatively small field of view with piezoelectric elements several times the wavelength, decreasing imaging quality. Addressing the full aperture also requires many channels, leading to high memory and processing bandwidth demands, incompatible with BMIs requirements. To address these limitations in the context of fUS imaging, Row Column Addressed (RCA) arrays have been proposed as a promising alternative [53, 54].

RCA transducers consist of two stacked 1D arrays with long thin line transducer elements that extend the whole aperture. The two 1D arrays (rows and columns) are oriented orthogonally to each other (Fig. 4.1a), allowing cylindrical focusing in transmit with one array, and cylindrical receive focusing with the other.

Compared to a fully populated 2D matrix array, the channel count is significantly reduced from N^2 to $2N$, eliminating the need for multiplexing and lowering memory bandwidth requirements. The RCA architecture allows production of larger aperture arrays with a lower channel count, thereby significantly increasing the field of view. RCAs have successfully demonstrated whole brain 4D fUS in rats [51], 3D anatomical imaging [55] and 3D imaging of cellular function [145]. However, due to their inherent degraded reception

focusing in one direction, RCA sequences to date require many transmits to reach sufficient resolution and sensitivity, decreasing frame rate and increasing the transmitted power in tissue which should be limited to guarantee safety. Although both 2D matrix and RCA arrays have significantly advanced volumetric fUS imaging, the current implementations still require substantial memory and computational bandwidth. This poses a challenge in achieving low-latency, real-time 4D fUS imaging, and hinders the application of volumetric imaging in BMIs.

There is a need for data-efficient methods to image functional brain regions with high spatio-temporal resolution while retaining an adaptive field of view. In this study we address this need, by leveraging the RCA architecture to transmit focused waves and selectively insonify functional areas of interest at high frame rates. Our working hypothesis is that task- or stimulation-related brain activity is spatially sparse. Our approach enables sampling of the brain with highly reduced memory bandwidth requirements, and simultaneously covers coronal and sagittal planes, without the need of moving the transducer. Furthermore, the plane selection is electronically reconfigurable, allowing for a flexible and adaptive wide field of view in real-time, an interesting capability in the context of permanently implanted prosthetics.

4.2 Methods

4.2.1 Simulation of Selective-plane fUS Imaging

To estimate the resolution of OPW and focused wave (FW) imaging using a row-column addressed (RCA) array, we first simulated a single point scatterer in Field II [146]. We modelled an RCA of 80 elements per array, 0.11 mm pitch, a center frequency of 15 MHz and 80% frequency bandwidth. We defined the medium with a speed of sound of 1540 m/s, and simulated a single point scatter at a depth of 5 mm centered below the array.

OPW Sequence

32 plane waves with angles ranging from $\pm 15.5^{\circ}$ are transmitted with the columns and then received with the rows (Fig. 4.1a). Using a conventional delay-and-sum beamforming algorithm, we obtain a volume presenting an elongated point spread function (PSF) in the direction of the receiving elements. For the second set of transmits, the role of the rows and columns are reversed. The beamformed data of these two orthogonal transmit sets is then summed to obtain the final volume (Fig. 4.1a). The resulting PSF presents a reflectional symmetry along the direction of the two orthogonal arrays leading to degraded resolution compared to fully addressed arrays. To suppress grating lobes and achieve sufficient sensitivity for functional imaging, numerous transmissions per volume are required. Finally, we determined the axial, lateral and elevation resolution in the C-scan and B-mode through the PSF using the full width at half maximum (FWHM). Furthermore, we squared the PSFs to find the power Doppler resolution [134].

FW Sequence

A focused wave was transmitted with the rows. The resulting waves propagate and focus in an elliptic cylinder (Fig. 4.1c,e), from which the echoes are received by the columns. The cylinder location can be adapted by changing the active aperture on the RCA. The

image from the insonified volume is reconstructed by conventional 2D delay-and-sum beamforming. To investigate the resolution in elevation, we have transmitted several focused waves in the elevation direction.

We varied the transmit f-number and aperture size to investigate the trade-off between field of view, resolution and slice thickness. For all simulations the focus depth was set to the point target depth (5 mm). For a focal depth d and transmit f-number f, the aperture size is given by $A = {}^{d}/_{f}$. The transmit-delays for a slice positioned at x_s are given by,

$$\tau_{\mathrm{TX}} = \frac{1}{c_0}\sqrt{(x_e - x_s)^2 + \left(z_e - d_f\right)^2}, \tag{4.1}$$

with c_0 the speed of sound, x_e the x-coordinate of the elements, and z_e the z-coordinate of the elements.

We transmitted n focused waves with the columns to scan the entire medium with increments of $p = 0.11$mm of the focal point lateral position, with n,

$$n = \left\lfloor \left(N_e p - \frac{d}{f} \right) / p \right\rfloor, \tag{4.2}$$

with N_e the number of elements and pitch p. The reconstructed images were concatenated, and used to determine the elevation resolution and contrast of the point target (Fig. 4.1d).

Finally, we determined the axial, lateral and elevation resolution in the B-mode using the full width at half maximum (FWHM). Furthermore, we squared the PSFs to find the power Doppler resolution [134].

4.2.2 Animal Procedures

All animal experiments were approved under CCD license number AVD8010020209725 at the Koninklijke Nederlandse Akademie van Wetenschappen with Study Dossier number 213601. Adult male Sprague Dawley rats weighting 470-490 g were used in this study. Animals were group housed, and kept in reversed day-night cycle with food and water available ad libitum.

Surgery Procedure

The animal was anesthetized in a prefilled induction chamber with 5% isoflurane. After induction, the animal was transferred to a nose cone to maintain anesthesia, and placed on a heating pad of 37 °C. Anesthesia was maintained with 1-2% isoflurane, and pain was managed with carprofen (5 mg/kg) and butorphanol (2 mg/kg) with subcutaneous delivery. Dexamethasone (2.5 mg/kg)was delivered subcutaneously to prevent intracranianal edema. Eye ointment (Duratears ®) was applied to prevent ocular drying, and protective eye caps were placed over the eyes. The animal was head fixed in a stereotactic frame and its scalp was shaved and depilated. The skin was cleaned, and a sagittal incision was made to reveal the skull after local anesthesia with Lidocaine. A 14x14 mm craniotomy was performed to reveal the brain, and saline was delivered subcutaneously to prevent dehydration. After the surgery, the animal was transferred to the imaging setup. The anesthesia was switched

from isoflurane to medetomidine, initiated with a bolus of 0.5 mg/kg. After 3 mintutes, we switched to continuous infusion of 0.01 mg/(kg h) delivered subcutaneously throughout the imaging session. Acoustic coupling gel was placed on the surgical window, and the RCA was positioned 2 mm above the brain. The RCA was centered above the brain using live volumetric Doppler imaging.

Visual Stimulation

To elicit brain activity, we presented visual stimuli on a 22-inch screen placed 20 cm in front of the animal (Fig. 4.2a). Animals were habituated to the dark prior to and in between functional recordings. Visual stimulation patterns were implemented in PsychoPy [147]. We used drifting gratings (black and white) with a spatial frequency of 30°, moving at 50 °/s. The propagation direction was switched randomly every 2 seconds to multiples of 45°. The stimuli were presented for 15 seconds, followed by 30 seconds of rest. This cycle was repeated 4 times after an initial 45 seconds baseline. During rest and baseline, the screen color was gray. The total duration of one functional recording was 3m45s.

Eye Patch Experiment

To assess the stability of the functional signal under conditions of diminished neural activity,we performed an eye patch experiment. By occluding one eye with an eye patch, the activations in the contralateral hemisphere are expected to be significantly reduced, providing a controlled condition to determine the robustness of the signal.

Before conducting the eye patch experiment, we recorded 3D functional activity without eye occlusion. Based on the activity map, we selected the coronal plane for which the peak correlation was the highest, and used this plane for a selective plane functional recording. Next, we occluded the right eye, and repeated the 3D and selective plane experiments. There was a 5min rest between successive functional recordings, to avoid habituation to the visual stimuli.

4.2.3 Selective-plane Functional Imaging

Pressure waves were transmitted with an 80+80 element RCA (center frequency 15 MHz, pitch 110 µm; Verasonics, Kirkland, WA, USA) connected to a Vantage 256 channel research scanner (Verasonics, Kirkland, WA, USA). For both OPW and focused wave imaging, the imaging waveform was 2 cycles at a transmit frequency of 13.9 MHz.

3D Functional Imaging

We implemented the OPW sequence by transmitting 32 angled transmissions per array ranging from ±15.5° with an angular pitch of 1°. After angular and orthogonal compounding, the effective volume rate was 400 Hz. We acquired Doppler ensembles of 500 ms (200 frames per ensemble), followed by a 500 ms pause, resulting in a power Doppler volume rate of 1 Hz. During acquisition, RF data was saved to disk and reconstructed in parallel in a separate thread. 3D GPU accelerated delay-and-sum beamforming was implemented in CUDA and executed on a GPU (GeForce RTX 3090, NVIDIA, USA). The resulting IQ volumes $s_{\mathrm{OPW}}(x, y, z, t)$ had an isotropic pixel size of 110 µm^3, and were saved to disk for subsequent functional data processing.

We perform 3D orthogonal plane wave fUS analysis of the Power Doppler signals to create a 3D activation map [51]. We elicit functional activations by presenting visual stimulation on a screen, and record the brain response with the OPW sequence. After typical spatio-temporal filtering and functional correlation (see section 4.2.4), we generate a 3D map of the brain activations. This map is used to select the slices for the selective-plane sequence.

Selective-plane Sequence

After acquiring the 3D activation map, we perform selective-plane functional imaging by transmitting focused waves. The focus depth was tuned to the depth of the functional activations obtained with the 3D sequence. This was around 5 mm for the superior colliculus (SC). After simulations in Field II, we used a transmission f-number of 3, resulting in an aperture of 1.65 mm and a field of view of 7.2x8.8x10 mm^3. We found this to be a good trade-off between elevational resolution and field of view. We used a fixed frame rate of 1000 Hz per selected plane, and ran the sequence continuously for the total duration of the functional recording. Notably, the frame rate could be increased up to the pulse repetition frequency of OPW imaging, allowing a maximum of 25.6 kHz for a single plane. Continuous recording allows overlapping of Doppler ensembles, thereby increasing the power Doppler frame rate [109]. For clutter filtering, we used the same Doppler ensemble length of 500 ms as in OPW imaging, and an ensemble overlap of 400 ms, resulting in an effective power Doppler frame rate of 10 Hz.

To record visually evoked activations, we ran two subsequent recordings of the selective-plane sequence (Fig. 4.3a). First, we scanned the brain coronally, by selecting three planes spaced at 440 µm (4 pitch) to cover the SC, guided by the 3D activation map. Next, we recorded two sagittal planes through the left and right hemisphere, positioned at the centers of the left and right SC. The plane spacing was 2.42 mm (22 pitch).

Due to the fact the FW imaging requires only one transmit per region, we could run it continuously, and at higher frame rates than OPW. This significantly reduces the data collection rate, and pulse repetition frequency, as shown in Fig. 4.2 and table 4.3.

4.2.4 Functional Data Processing

3D Activation Map Generation

After beamforming the OPW data to image volumes, blood signal was separated from static tissue using a 3D singular value decomposition (SVD) clutter filter [45]. We used a fixed threshold to remove the first 50 singular vectors, since there was no motion and a minimal variation of heart rate in the anesthetized experiments. We spatially smoothed the power Doppler volumes using a 3D Gaussian kernel with $\sigma = 100$ µm. Next, we temporally detrended the power Doppler signal for each pixel using a cubic polynomial [114]. We determined the relative cerebral blood volume (ΔCBV) by dividing the detrended signal by the fitted trend.

The 3D functional activation map was obtained by computing the Pearson's correlation coefficient $r(x, y, z)$ between the normalized temporal ΔCBV signal $s_D(t_i)$ and the

normalized stimulus signal $a(t_i)$ using,

$$r(x,y,z) = \frac{\sum_i (s_D(t_i) - \bar{s}_D)(a(t_i) - \bar{a})}{\sqrt{\sum_i (s_D(t_i) - \bar{s}_D)^2}\sqrt{\sum_i (a(t_i) - \bar{a})^2}}, \tag{4.3}$$

with $\bar{s_D}$ and $\bar{a}$ the temporal means [138]. To account for the activation delay due to the neurovascular coupling, we lagged the stimulation signal by increments of one sample within a ±2s window, and computed the peak Pearson's correlation for each lag. We finally used the correlation map of the lag that showed the maximum correlation score.

To superimpose the 3D activation map on the power Doppler volumes, we kept only voxels where the correlation score was $r > z_{\text{score}}\sigma$, with σ is the spatial standard deviation of $r(x,y,z)$ in a superficial noise box [64, 109]. We used a $z_{\text{score}} = 3$ to find the correlation threshold r_{OPW}.

The functional processing pipeline is shown in Fig. 4.2b, and a representative 3D activation map is shown in Fig. 4.2c.

We used the registration software developed by Brunner *et al.* [56] to manually register the volumetric OPW angiogram to the Waxholm Space atlas of the Sprague Dawley rat brain [148, 149]. 3D renders were made in Blender (Blender Foundation, Amsterdam, the Netherlands) using the Scan Data Visualizer template by Cartesian Caramel [150].

Selective-plane Functional Maps

After beamforming the selective-plane images, we performed SVD clutter filtering on each individual 2D plane. We used a fixed threshold of rejecting the first 100 singular vectors. Since frames were acquired continuously, we could compute power Doppler images using overlapping ensembles, resulting in an effective power Doppler frame rate of 10 Hz. We temporally smoothed the power Doppler signal using a 1 s moving average filter. Next, we spatially smoothed each plane with a 2D Gaussian kernel of $\sigma = 100$ µm, detrended using a cubic polynomial, and determined the ΔCBV by dividing the detrended signal by the fitted trend.

Finally, we computed the 2D activation maps using the Pearson's correlation. To account for the activation delay due to the neurovascular coupling, we lagged the stimulation signal by increments of one sample withing a ±2s window, and computed the peak Pearson's correlation for each lag. We finally used the correlation map of the lag that showed the maximum correlation score. Next, we registered the selected planes using the affine transform obtained in the registration of the OPW vascular map. We used the same approach as in OPW imaging to find the correlation threshold r_{FW} to superimpose the activation maps on the atlas or power Doppler images. The complete functional processing pipeline is shown in Fig. 4.2b. Once the 3D activation map was obtained, we switched to our selective-plane functional sequence. Fig. 4.2d shows the top view of the 3D activation map, with two representative coronal and sagittal focused wave planes. The activity map is overlaid on the FW power Doppler for pixels above the correlation threshold.

OPW and FW comparison

To compare the functional activation maps generated by both imaging modalities, we computed the maximum intensity projection of the 3D vascular and correlation map over

an elevation range of 330 µm, or 3 pitch. This range corresponded to the FW power Doppler elevation resolution found in simulation (Fig. 4.1f).

To compare the CBV response of OPW and FW, we converted the OPW Doppler volumes to a set of selected planes, corresponding to the FW plane locations. For a FW plane position, we selected the corresponding OPW plane, and took the maximum intensity projection of the power Doppler maps over an elevation width of 330 µm.

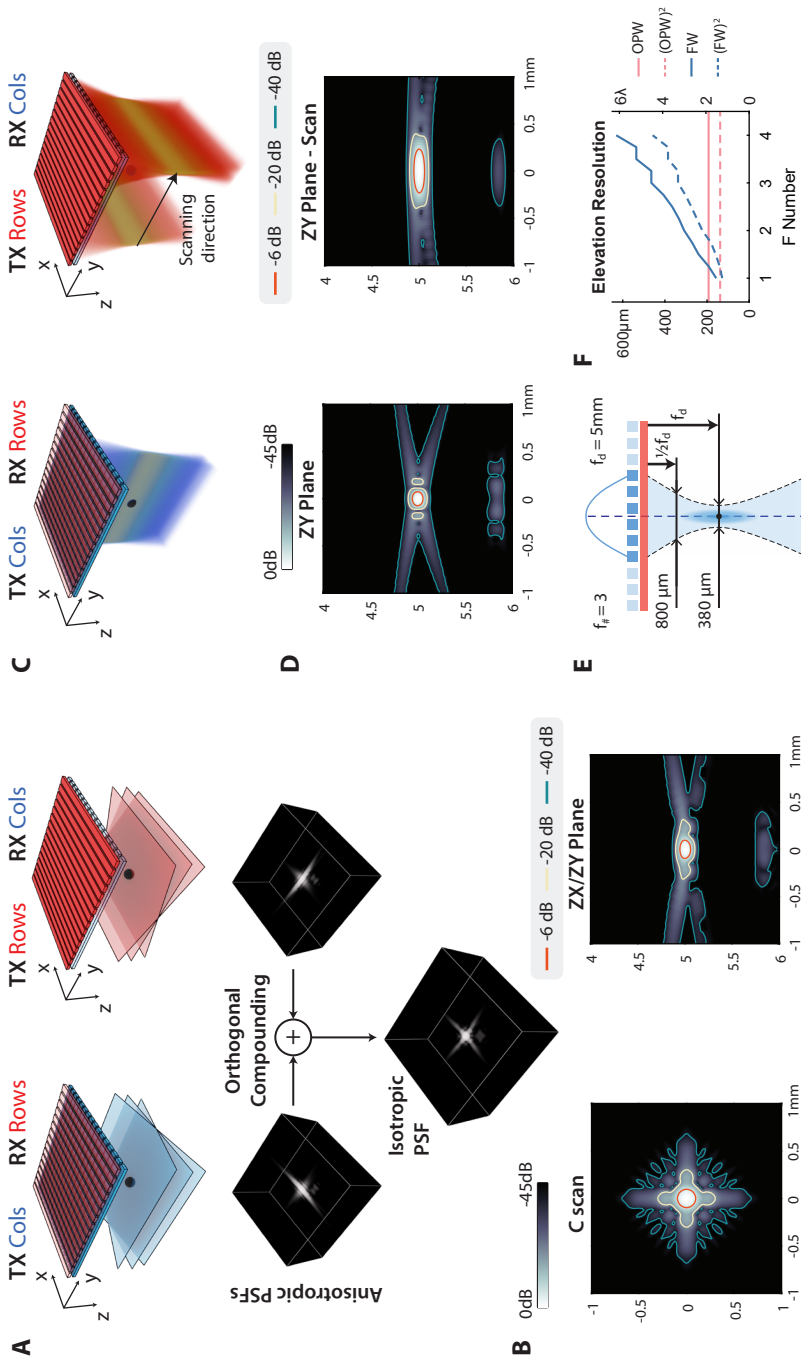

Figure 4.1 – Transmission schemes for Orthogonal Plane Wave (OPW) and Focused Wave (FW) imaging simulated in Field-II. – Caption continuous on the next page.

Figure 4.1 – (continued) **(A)** OPW imaging of a point target with a row-column addressed (RCA) array. The sequence first transmits angled plane waves using the columns and receives with the rows (CR), after which the rows transmit and the columns receive (RC). Next, the RC and CR volumes are formed using 3D delay-and-sum beamforming and angular compounding. The RC and CR volumes have an anisotropic point spread function (PSF), and are orthogonally compounded to retrieve the final reflectional symmetric image of the medium. The shown volumetric PSFs follow from a Field-II simulation of a single point target at 5 mm depth, centered below the array. **(B)** The C-scan is shown on the left, and the B-scan is shown on the right. Due to the reflectional symmetry, the ZX and ZY planes are identical. **(C)** FW imaging of a point target with a row-column addressed (RCA) array. Transmitting a focused wave with the columns insonifies the medium with an elliptic cylinder, allowing to form a 2D image in the ZY plane. **(D)** By changing the roles of the arrays, the elliptic cylinder can insonify the orthogonal ZX plane. The position of the focus can be changed, by changing the active aperture. We simulated a plane-by-plane scan by moving the active aperture with increments of one element, which was used to form a volumetric image of the point target. The center plane of this volume was used to determine the elevation resolution. **(E)** The beam width at focus depth $f_d = 5$mm and $\frac{1}{2} f_d$ is shown bottom, for transmit $f_\# = 3$. **(F)** The elevation resolution for different simulated transmit f-numbers ($f_\#$) for B-mode (solid lines) and the square of the B-mode (dashed lines) to find the power Doppler resolution. In **(B, D)**, the orange, yellow and blue lines indicate the -6, -20 and -40dB isolines, respectively.

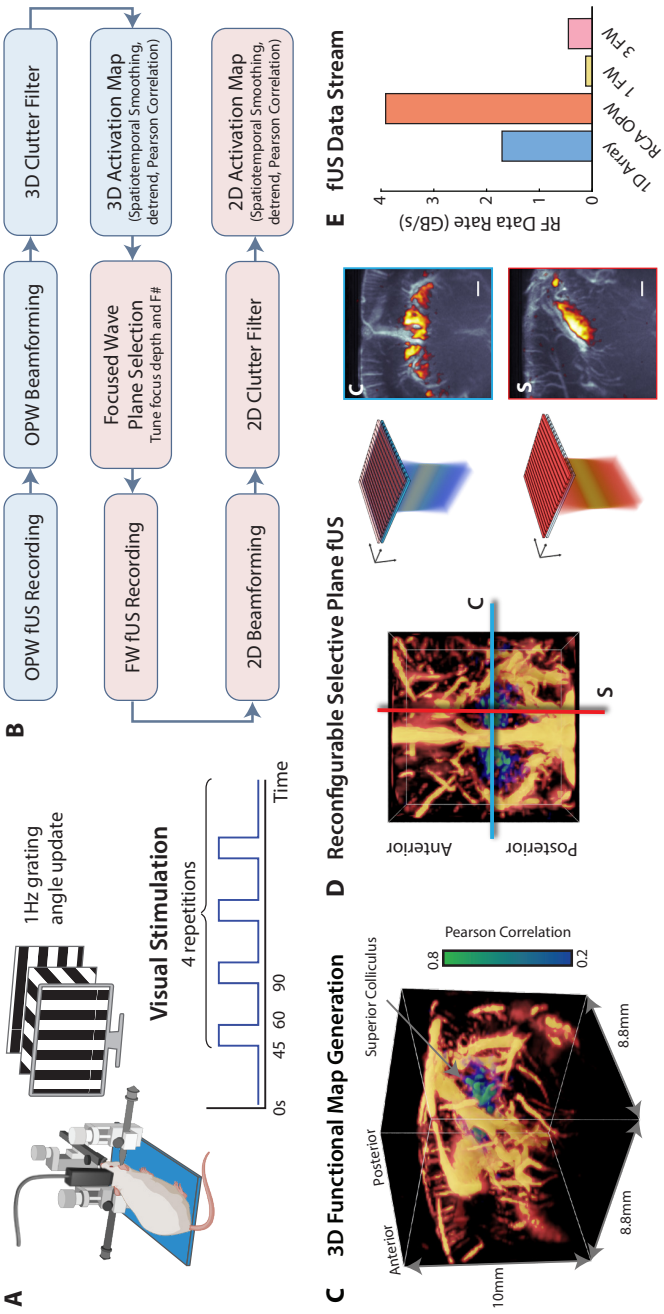

Figure 4.2 – Functional selective plane imaging pipeline. – Caption continuous on the next page.

Figure 4.2 – (continued) **(A)** Functional imaging setup with visual stimulation. The craniotomized rat is head fixed in a stereotactic frame, and placed on a heat pad. The row-column addressed (RCA) array is positioned above the center of the craniotomy. During functional recordings, grating bars are shown on a PC screen in front of the animal. The Functional recording consists of an initial 45s baseline recording, followed by 4 repeats of 15s stimulation, and 30s of rest. The total recording duration is 225s. During stimulation, the grating bars on screen change orientation every 1s. **(B)** Functional data processing pipeline. **(C)** Generated 3D functional map, showing Pearson correlation overlayed on a 3D Power Doppler render. The activated region was the superior colliculus (SC). The 15MHz RCA allows to image a volume of 10x8.8x8.8 mm^3. **(D)** Reconfigurable plane selection for the focused wave multi-plane sequence. After acquiring the 3D activation map, coronal and sagittal planes that section the activated regions can be chosen, and imaged at high frame rate. On the right example coronal and sagittal activation maps overlaid on the focused wave power Doppler are shown. **(E)** Comparison of RF data transfer rate required for 1D array imaging, RCA OPW imaging, and 1 and 3 selective planes FW imaging. Sequence parameters used to determine the data rates are listed in table 4.3.

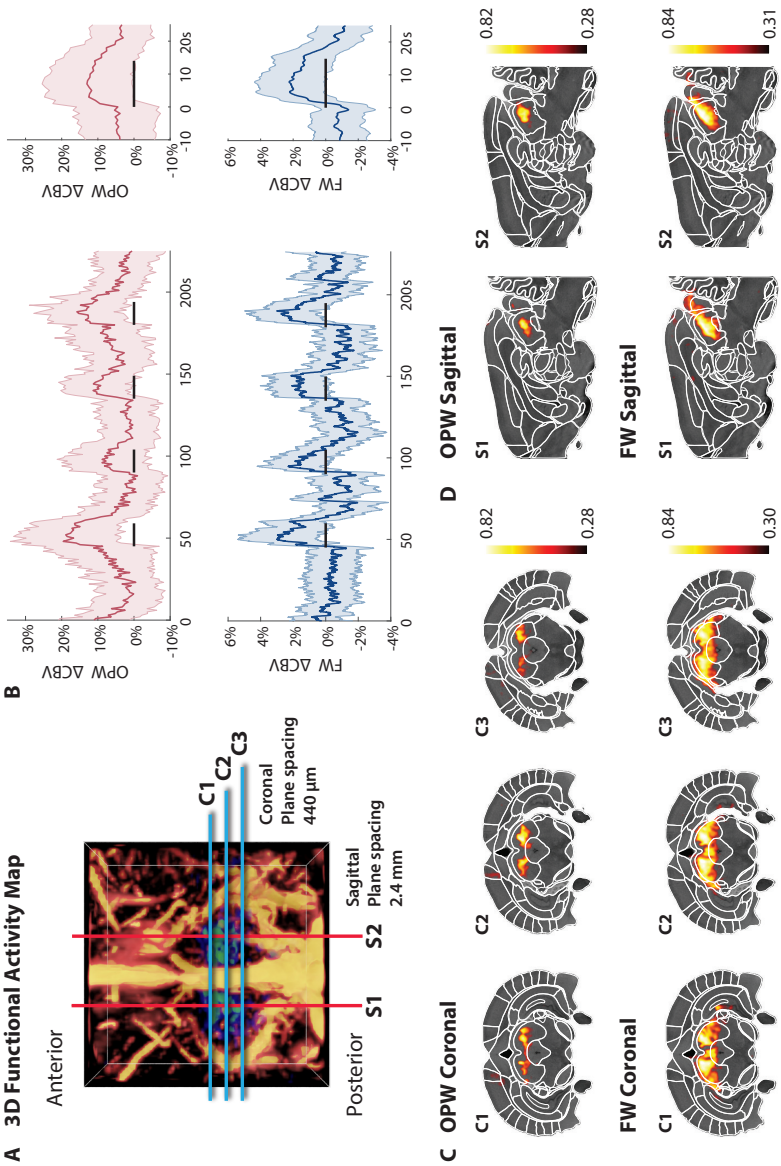

Figure 4.3 – Selective-plane functional ultrasound imaging of the superior colliculus. (A) Orthogonal Plane Wave (OPW) generated 3D activation map, showing the selected planes for coronal and sagittal focused wave imaging (FW). **(B)** The relative increase in cerebral blood volume (CBV) during visual stimulation for OPW and FW, for significantly activated voxels. On the right, the average response for the 4 stimulation repeats is shown. **(C, D)** Neural activation overlaid on the Waxholm Space Sprague Dawley rat atlas, for OPW (top) and FW (bottom) coronal and sagittal planes. Note that the coronal and sagittal scans were acquired sequentially. FW imaging consistently reveals a larger activated brain area than OPW, and for both modalities the activation is well confined within the bounds of the Superior Colliculus. Color bars indicate the correlation threshold to the peak correlation for each recording.

4.3 Results

4.3.1 Simulation OPW and FW

We compared the PSFs of OPW and FW obtained with simulation in Fig. 4.1. For the OPW B-mode, we found a lateral and elevation resolution of 193 µm (1.7λ), and an axial resolution of 114 µm (1.0λ). To estimate the power Doppler resolution, we squared the PSFs, and found a lateral resolution of 137 µm (1.2λ) and an axial resolution of 81 µm (0.7λ).

For focused wave imaging, we tested different transmit f-numbers. The B-mode axial and lateral resolution were scarcely affected by the transmit f-number, and were 113.0 ± 0.2 µm (1.0λ) and 148.0 ± 0.3 µm (1.3λ) respectively. In the squared PSFs the axial and lateral resolution were 80.0 ± 0.2 µm (0.7λ) and 106.0 ± 0.2 µm (1.0λ), respectively. The elevation resolution varied with the transmit f-number, as shown in Fig. 4.1f. The aperture size is defined by the choice of transmit f-number and focus depth, with an aperture of 5.2 mm for $f_\# = 1$ and 1.2 mm for $f_\# = 4$. Given the limited available aperture of the transducer, imaging with $f_\# = 1$ restricts the possible field of view to a 3.6x8.8x10 mm^3 volume. To retain a wide field of view, we opted for a middle ground in elevation resolution and aperture size. For $f_\# = 3$, the aperture size is 1.65 mm, allowing scanning of a 7.2x8.8x10 mm^3 volume, with a power Doppler elevation resolution of 303 µm at focus. Therefore, $f_\# = 3$ was chosen for all focused wave functional recordings.

4.3.2 3D Functional Imaging

To guide the plane selection in our selective-plane imaging, we first acquired a 3D activation map. Fig. 4.2c shows the activation map superimposed on the power Doppler resulting from visual stimulation. After defining a noise box, we determined the significant correlation threshold for OPW of $r_{\mathrm{OPW}} = 0.281$. The shown volumetric correlation map only shows voxels that are above the correlation threshold. The peak correlation score was 0.817. The shape and location of the activated area corresponds well with the Superior Colliculus, as reported earlier by [137].

Fig. 4.3a shows the selected slices for the coronal and sagittal selective-plane recordings. For the coronal planes, we determined the maximum intensity projection of the OPW Doppler planes over 330 µm corresponding to the simulated FW elevation resolution, and spatially averaged the CBV response over all significantly activated voxels (see Fig. 4.3b). From this it becomes clear that the OPW CBV increased by $6.5 \pm 11.9\%$ during stimulation.

4.3.3 Selective-plane Functional Imaging

After obtaining the 3D activity map, we switched to selective-plane focused wave imaging. Fig. 4.3a shows the selected slices for the coronal and sagittal recordings. We spatially averaged the CBV response over all significantly activated voxels in the coronal planes (see Fig. 4.3b), and determined the average CBV increase across stimulation trials. The FW CBV increased by $2.3 \pm 2.1\%$ during stimulation.

Fig. 4.3c presents a comparison between the OPW and FW activation maps of the selected planes after registration with the Waxholm Space atlas. It becomes clear that for OPW, the activated area is confined within the borders of the SC, in both coronal and

Table 4.1 – Average per hemisphere CBV increase during stimulation with respect to a 10-second window before stimulation, in functional recordings with and without eye patch. Values report mean ± standard deviation.

Mode	Vision impairment	CBV increase Left (%)	CBV increase Right (%)
OPW	None	28.1 ± 16.1	18.1 ± 11.7
OPW	Left	10.5 ± 11.1	14.9 ± 12.8
FW	None	11.3 ± 4.6	10.0 ± 4.3
FW	Left	3.2 ± 2.0	5.8 ± 3.1

sagittal recordings. In FW, the activated area is larger than OPW, but is still confined within the borders of the SC. The correlation threshold for OPW and FW was similar, at 0.281 and 0.296 respectively. The peak correlation was 0.817 for OPW and 0.841 for FW, indicating a small increase in FW.

4.3.4 Diminished neural activity fUS stability

To compare the performance of OPW and FW under diminished neural activity, we performed an eye patch experiment. Fig. 4.4a,d shows the top and 3D view of the OPW activation with and without eye patch. Without eye patch, both hemispheres show activation, with similar peak correlation (difference < 0.05) in both hemispheres for both OPW and FW (see table 4.2). With the right eye patched, the left hemisphere shows lower activation, with a 0.24 decrease in correlation for OPW, and a decrease of 0.14 for FW.

Fig. 4.4b,e show the maximum intensity projected OPW correlation map over 330 µm superimposed on the OPW vascular map. The location of peak correlation corresponded well between the OPW and FW recordings without eye patch. In the eye patch experiments, the peak correlation location varied more, as can be seen by the crosses in Fig. 4.4e,f.

To determine the stability of the CBV signal in OPW and FW, we took the CBV time trace of the peak activated voxel in the left and right hemisphere, and averaged the CBV signal across stimulation repetitions. The single voxel based CBV traces shown in Fig. 4.4c,f showcase the 10-fold higher temporal sampling in FW than OPW. In the FW recording with eye patch, the diminished response in the left hemisphere is much more visible in the FW single voxel traces.

Table 4.1 presents a quantification of the average CBV increase during stimulation with respect to a 10-second window before stimulation. For both OPW and FW, the CBV response decreases in both hemispheres when one eye is patched. Furthermore, the CBV signals in the left hemisphere show lower variability, reduced from 11.1% in OPW to 2.0% in FW.

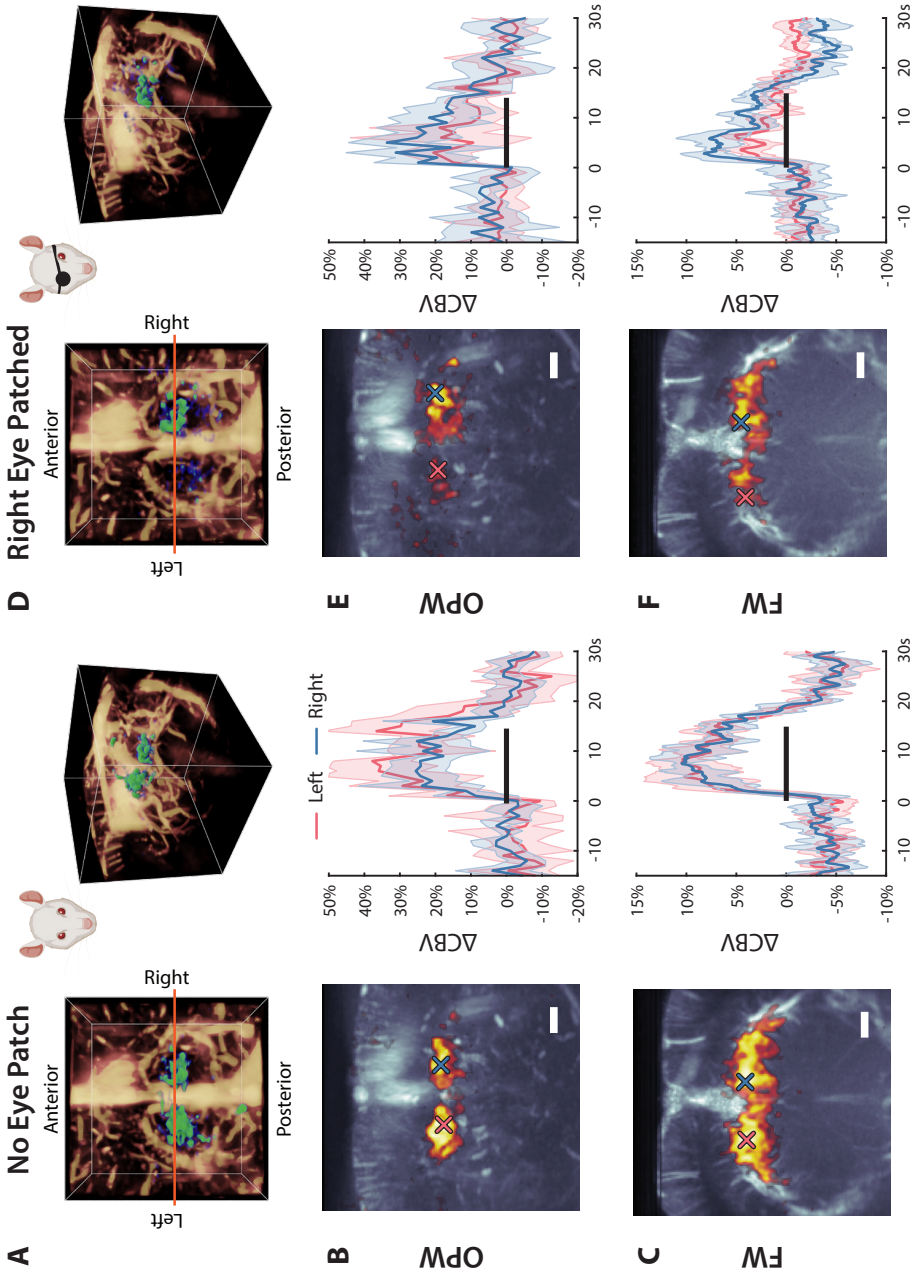

Figure 4.4 – Functional ultrasound imaging of the superior colliculus with eye patch. Caption continuous on the next page.

Figure 4.4 – (continued) **(A, B, C)** No eye patch. **(A)** the 3D activation map shows bilateral activation of the superior colliculus. The orange line overlaid on the top view shows the location of the focused wave imaging plane. **(B)** The OPW Pearson correlation is superimposed on the OPW power Doppler map. The blue and red crosses denote the location with maximum correlation in the left and right hemisphere, respectively. The relative cerebral blood volume (CBV) traces on the right show the hemodynamic response for the left and right hemisphere, corresponding to the pixel indicated by the crosses. **(C)** shows the activation map and relative CBV change for focused wave imaging. Both OPW and FW show a similar response in the left and right hemisphere. Although the CBV change for FW is lower than OPW, FW shows lower signal variability. **(D, E, F)** Experiment with right eye patched. Consequently, the left hemisphere shows a diminished response, resulting in lower correlation scores and lower relative CBV changes. This finding is consistent for OPW **(E)** and FW imaging **(F)**. The single pixel CBV traces for FW show lower variability in the left hemisphere compared to OPW.

4.4 Discussion

4.4.1 Summary Key Findings

fUS has emerged as a transformative neuroimaging modality, unlocking new possibilities for both fundamental neuroscience research and a variety of (pre)clinical applications. However, current implementations of 4D fUS demand high memory throughput and computational bandwidth, presenting a key bottleneck for achieving low-latency, real-time 4D fUS imaging, crucial for clinical application such as BMIs. While future advances in computing hardware will alleviate these limitations, we present an intermediate solution that allows efficient sampling of selective-planes in the brain, relying on the hypothesis that task- or stimulation-related brain activity is spatially sparse. We realized this selective-plane imaging by transmitting focused waves with the RCA.

By transmitting a focused wave with either the rows or columns, we insonify selected brain regions with an elliptic cylinder, from which the backscatter pressure waves are received with the orthogonal array. Utilizing this partial transmit focus, followed by 2D delay-and-sum beamforming to focus in reception, we demonstrate that you only require a single transmit per plane, in contrast to the 64 transmits needed per volume in orthogonal plane wave (OPW) imaging. This reduces the RF data bandwidth by a factor 26, from 3.9 GB/s in OPW imaging to 0.15 GB/s per FW plane. Furthermore, reconstructing FW planes is computationally more efficient, as it is a single 2D beamforming procedure, opposed to the two stage orthogonal beamforming done in OPW. Conventional focused wave imaging on 1D arrays is slow due to the line by line scanning, and is not suitable for functional imaging. The RCA architecture allows focused imaging at high frame rates by turning this into plane-by-plane scanning. The choice of planes to sample was guided by registration of a 3D activation map. For this, we used functional OPW [51]. After recording this 3D activation map once, the map can be reused to guide the choice of selective-planes and select optimal transmit parameters. Future experiments could instead register the power Doppler of the whole brain with an atlas to guide the selection of planes and transmit parameters.

In our simulations, we found that the FW elevation resolution is highly dependent on

Table 4.2 – Average and peak Pearson correlation scores per hemisphere in functional OPW and FW recordings with and without eye patch. L: left, R: right, (R-L): the difference between the right and left hemisphere for mean or peak correlation.

Mode	Vision impairment	Mean L	Mean R	Δ Mean (R-L)	Peak L	Peak R	Δ Peak (R-L)
OPW	None	0.41	0.32	-0.09	0.79	0.75	-0.04
OPW	Left	0.29	0.34	0.05	0.46	0.70	0.24
FW	None	0.46	0.53	0.07	0.82	0.81	-0.01
FW	Left	0.37	0.44	0.06	0.61	0.75	0.14

Table 4.3 – Comparison of PRF and RF data rate for various imaging modes during continuous recording, assuming 200% bandwidth sampling and 10 mm deep imaging.

Array	Imaging mode mode	TX per frame	Frame rate (Hz)	PRF (Hz)	Data rate (GB/s)	Ref
1D array	PW	7	1000	7000	1.7	[64]
RCA	OPW	64	400	25600	3.9	Current Study
RCA	1 FW	1	1000	1000	0.15	Current Study
RCA	3 FW	3	1000	3000	0.46	Current Study

the transmit f-number, and was 303 µm at focus for power Doppler imaging with $f_{\#} = 3$. As expected, the power Doppler elevation resolution for OPW is higher than FW, and as a result, FW integrates the vascular signal over a larger slice width. Although FW elevation resolution was higher than the OPW elevation resolution, it is comparable to the elevation resolution of a 1D array. Using a 15 MHz 1D array, Macé *et al.* [134] found a power Doppler elevation resolution of 303 µm when scanning a 20 µm wire submerged in a water tank (see supplementary figure S2 of [134]). However, in focused wave imaging with the RCA, it is important to note that the elevation resolution degrades rapidly when imaging away from the focus depth due to the absence of a focusing lens.

It is difficult to pinpoint why the OPW and FW show different activation maps and different increases in CBV during activation, as multiple implementation differences are at play. One reason is that in clutter filtering, the SVD for OPW works on a 3D volume, which results in a better separation of static tissue and blood flow compared to its 2D SVD counterpart in FW imaging, which potentially results in higher CBV changes for OPW. In FW imaging, the lower CBV changes could be explained by the reduced number of transmits per power Doppler frame, which was 500 for FW, and 12800 for OPW. The lower variability of the FW CBV signal likely is caused by the continuous sampling of the FW sequence, allowing overlap of Doppler ensembles and an increased power Doppler frame rate. To match the power Doppler rate of OPW imaging, we applied a temporal moving average filter with a 1-second window, which may contribute to the reduced CBV variability. Depending on the application, the FW frame rate and degree of temporal smoothing can be tuned to detect propagating brain activations, as demonstrated by [109].

When comparing the activation maps of OPW to FW, we see that FW reveals a larger activated area,likely due to the increased slice thickness resulting from the elevation resolution. The increase in relative CBV during stimulation was lower in FW than OPW.

Although this could indicate a decreased sensitivity, the lower signal variability on individual voxel basis and comparable peak correlation scores show that FW imaging has sufficient sensitivity to detect functional activations. These results are promising for application of focused wave imaging in a fUS-BMI, where low signal variability is key to facilitate decoding of brain activity on a single trial basis.

4.4.2 Comparison to Existing Methods

Alternative approaches to improve brain coverage include the recently developed 1D multi-array that enables simultaneously sampling of 4 planes at a fixed distance of 2.1 mm [114], or optimized motorized sweeping to enable 3D fUS with a 1D array [47, 48]. While these approaches leverage the superior image quality of a 1D array, the requirement of a motorized linear stage makes these solutions impractical for a portable BMI or for human fUS as a whole. Furthermore, they do not allow simultaneous high frame rate readout across the brain.

OPW presents an effective middle ground, allowing large field of view brain imaging at reduced channel count compared to fully populated 2D arrays. With its volumetric capabilities, it eliminates the need for motorized scanning. However, the computational requirements are high due to the large number of transmits required to achieve sufficient Doppler dynamic range [51]. The large number of transmits limits achievable volume rates and leads to a very high pulse repetition frequency (see table 4.3), which in turn raises concerns about element overheating. In our implementation, we should have changed the angular step to 0.5 deg as recommended by Sauvage *et al.* for a more effective suppression of grating lobes [51]. This makes it currently challenging to run continuous, high frame rate functional OPW recordings.

Our selective-plane imaging approach, allows to sample coronal and sagittal planes in the same functional recording, although in this study these recordings were performed subsequently. This is a benefit of using the RCA, and not possible with a traditional 1D array. Finally, aligning a 1D transducer with the correct plane covering brain regions of interest is challenging in the sagittal direction, due to the absence of distinct, symmetrical, anatomical landmarks. Here, registration of the 3D angiogram of activation map solves this issue, and allows accurate brain region alignment in both the sagittal and coronal planes.

4.4.3 Implications and Potential Applications

Our approach of selective-plane imaging is fully adaptive, and offers several potentials for fUS-BMI. Current fUS-BMI implementations rely on 2D imaging, thereby covering a limited region of the brain. Therefore, 2D imaging is unable to capture task related activations occurring outside the plane. As a result, there is growing interest in leveraging volumetric fUS to expand brain coverage, with the potential of enhanced decoder accuracy and broaden the range of possible outputs of a BMI. Current 4D fUS implementations using either fully populated 2D matrix arrays or row column addressed (RCA) arrays generate large datasets, imposing substantial demands on memory and computational bandwidth. This makes it challenging to apply volumetric imaging to a real time closed loop BMI.

Currently, fUS-BMI positions a 1D array in predefined slots in a 3D printed holder. Initially aligning these slots with the correct plane can be cumbersome, and over time, these predefined slots can misalign with the plane of interest, leading to decreased decoder performance [151]. Our approach enables periodic registration of a 3D angiogram or functional map and correction via electronic aperture reconfiguration to maintain proper alignment, thereby reducing the need for precise transducer positioning. In the context of implanted BMIs, the ability to electronically steer the imaging plane offers a tremendous advantage.

BMI research has demonstrated that movement-related spatial representations are typically distributed across different brain regions [23]. Therefore, simultaneously recording from multiple regions, at reduced memory and computational overhead compared to volumetric imaging, provides a significant advantage.

Although fUS-BMI research has indicated that decoding accuracy decreases with lower spatial resolution, our focused wave imaging approach allows imaging with the same spatial resolution as used by Norman *et al.* [22]. Non-human primates BMI research has shown that the most informative voxels are spread across a 5 mm depth range in the cortex [23]. Due to the poor elevation resolution away from focus, multiple focus depths are needed to ensure sufficient elevation resolution across depth, increasing the PRF and data rate. To mitigate increased memory and computational bandwidth requirements, the sequence can be further optimized to selectively receive only RF data around a small depth window, tuned per focus depth transmit. This highlights the adaptability of the method.

This study, together with the recently introduced nonlinear sound sheet microscopy [145], synthetic aperture imaging [152], and advances in orthogonal plane wave imaging [51, 153], demonstrate the versatility of the row column addressed transducer architecture in various applications. Together with sound-sheet microscopy, our work signals a shift in strategy: from brute-force volumetric plane wave insonification to efficient, application specific acoustic beams.

4.5 Conclusion

This study introduces selective-plane fUS, a reconfigurable ultrasound neuroimaging method. By efficiently sampling targeted brain sections, our approach significantly reduces data bandwidth and computational demands while maintaining a spatial resolution comparable to 2D fUS. Using selective-plane fUS, we successfully revealed activations in the superior colliculus in response to visual stimulation, observed similar peak correlation to 3D fUS, and measured a reduced functional signal variability. Together, our findings makes real-time, multi-region decoding of the brain possible, thereby addressing a pressing need for compact and human implantable fUS-BMI paradigms.

4.6 Acknowledgements

This project was partially funded through grants from the Medical Delta Ultra HB program (RW), the Chan Zuckerberg Initiative (Dynamic RFA number 2023-321233, EMI), the 4TU Precision Medicine Program (DM) and the European Union (Marie-Sklodowska Curie

Fellowship MIC-101032769, BH).

The authors thank Ronald Ligteringen for ensuring access to computational resources, Gert Jan de Fluiter for his assistance with the anesthesia setup, and all animal caretakers at the Netherlands Institute for Neuroscience. Finally, a special thanks to Cartesian Caramel for providing the Blender scan visualizer template.

5

Nonlinear sound-sheet microscopy: imaging opaque organs at the capillary and cellular scale

Light-sheet fluorescence microscopy has revolutionized biology by visualizing dynamic cellular processes in three dimensions. However, light scattering in thick tissue and photobleaching of fluorescent reporters limit this method to studying thin or translucent specimens. Here we applied non-diffractive ultrasonic beams in conjunction with a cross-amplitude modulation sequence and nonlinear acoustic reporters to enable fast and volumetric imaging of targeted biological functions. We reported volumetric imaging of tumor gene expression at the cm3 scale using genetically encoded gas vesicles, and localization microscopy of cerebral capillary networks using intravascular microbubble contrast agents. Nonlinear sound-sheet microscopy provides a ~64x acceleration in imaging speed, ~35x increase in imaged volume, and ~4x increase in classical imaging resolution compared to the state-of-the-art in biomolecular ultrasound.

5.1 Introduction

The most informative method for observing dynamic cellular processes in vivo in 3D uses light sheet microscopy that leverages genetically encoded fluorescent reporters [154]. Successive advances in light sheet microscopy now enable fast, large-volume, and high-resolution imaging of fluorescently labelled cells in transparent or cleared organisms [155, 156]. These capabilities have had a tremendous impact for example in developmental

This chapter is based on: *Baptiste Heiles, Flora Nelissen, Rick Waasdorp, Dion Terwiel, Byung Min Park, Eleonora Munoz Ibarra, Agisilaos Matalliotakis, Tarannum Ara, Pierina Barturen-Larrea, Mengtong Duan, Mikhail G. Shapiro, Valeria Gazzola, and David Maresca "Nonlinear sound-sheet microscopy: imaging opaque organs at the capillary and cellular scale." Science 388, no. 6742 (2025): eads1325. CC BY 4.0* [145].

biology by enabling long-term imaging of embryogenesis [157–160].

A next frontier would be to achieve non-toxic deep tissue imaging with cellular precision in living opaque organisms. Unfortunately, limitations inherent to optical microscopy (penetration depth < 1 mm and phototoxicity) [161, 162] prevent large scale imaging in opaque tissue. In addition, fast light sheet imaging [155] does not yet reach 1 mm^3/s volume rates in living tissue [163], which makes dynamic imaging at the mesoscale [**?**] technically challenging.

The introduction of biogenic gas vesicles (GVs) [164] as the "green fluorescent protein for ultrasound" provides an alternative to light for large-scale cellular imaging. The fortuitous physics of ultrasound enables centimeters-deep scanning of mammalian tissue, while genetically encoded GVs can interface ultrasound waves with cellular function [165, 166]. To unlock the potential of GV-based acoustic reporter genes (ARGs) [167, 168] and biosensors [169], there is a need for ultrasound imaging methods with high information content, resolution, coverage, and translatability. Recently, 4D functional ultrasound neuroimaging [49, 50] and 3D ultrasound localization microscopy [170] have positioned ultrasound as a tool for basic biology research. However, it remains difficult to visualize cellular function in three dimensions or to detect capillary networks.

Here we introduce nonlinear sound-sheet microscopy (NSSM), a method to image targeted biological functions across cm^3 of opaque living tissue. NSSM relies on a large field-of-view, high-frequency row-column addressed transducer array (RCA) [53, 55, 171] and the transmission of non-diffracting ultrasound beams to detect cells labelled with GVs [172] or vessels labelled with microbubbles (MBs) [173]. NSSM expands the field of view of biomolecular ultrasound at 15 MHz [172, 174–176] from ~3.5 x 64 x 100 λ^3 to 80x80x100 λ^3 (where λ denotes the ultrasound wavelength), the upper bound 2D imaging speed from 400 Hz to 25.6 kHz, and spatial resolution from 1x1x3.5 λ^3 to 1x1x0.6 λ^3. We demonstrate the versatility of NSSM by performing volumetric imaging of gene expression in a cancer model, and nonlinear acoustic sectioning of the living cerebral vasculature down to the capillary scale. Throughout the study, NSSM is compared to linear imaging as reference.

5.1.1 Concept

In the NSSM paradigm, a sub-aperture of RCA-transducer elements N_{ap} (Fig. 5.1A) is used to transmit cross-propagating ultrasound plane waves, or X-waves, from two adjacent half-apertures at α and $-\alpha$ angles (Fig. 5.1B). This spatially structured ultrasound transmission gives rise to a non-diffractive acoustic pressure field in the XZ plane [177] exhibiting a double acoustic pressure along the main-lobe of the beam, and a plane wave acoustic pressure field in the YZ plane [178] (Fig. 5.1C). Acoustic pressure is further modulated along the main lobe of the non-diffractive beam using a cross amplitude modulation (xAM) pulse sequence [172] (Fig. 5.1D), which confines nonlinear scattering to a thin sound sheet with a constant beam width regardless of depth (Fig. 5.1E). The sound sheet beam extends up to the cross-propagation depth $z_{cp} = N_{ap}/2cot(\alpha)$ which is typically of the order of 100λ. 2D images are reconstructed from backscattered ultrasound echoes received on elements of the orthogonal RCA array (Fig. 5.1B) using a delay-and-sum beamforming algorithm (see Materials and Methods). The point spread functions (PSF) of

resonant MBs are reported (Fig. 5.1F) for linear imaging or SSM (i.e. transmission TX1 only) and NSSM (i.e. transmissions TX1-TX2-TX3). We chose MBs as nonlinear point targets in simulation rather than GVs because equations governing their vibration in an ultrasound field are known. XZ-plane SSM and NSSM images showed similar PSFs because both imaging modes operate at the same frequency (Fig. 5.1G). To scan a volume, sound-sheet transmissions are swept electronically along the two arrays of the RCA-transducer using a sliding aperture of elements (Fig. 5.1H). A $\frac{\lambda}{2}$ micro-scanning precision is achieved by interleaving transmissions with and without a silent element at the center of the sub-aperture (Fig. 5.1H), because the pitch p or inter-element spacing of the RCA is approximately equal to λ. 3D PSFs are reported in Fig. 5.1I. Nonlinear imaging reduced the 3D PSF secondary lobes levels by 12.8dB ± 4.4dB thanks to the confinement of nonlinear MB scattering to the sound sheet plane. In terms of resolution, NSSM delivered an average 3D point spread function of 1λx0.6λx0.6λ compared to 1λx0.9λx0.9λ for SSM (Fig. 5.1J). Additional data supporting Fig. 5.1 are provided in the Materials and Methods section and in Fig. S1.

5.2 Results

5.2.1 Volumetric NSSM of gene expression at the cubic centimeter scale

Nonlinear ultrasound imaging is key to detect GVs in a tissue context with high specificity [172]. To test the ability of NSSM to visualize gene expression in 3D, we first imaged GVs adapted as nonlinear bacterial ARGs [167, 176] (Fig. 5.2). We purified Anabaena flos aquae GVs and embedded them in acoustically transparent phantoms at concentrations ranging from optical densities (OD) at 500 nm of 0.5 to 2, thereby mimicking increasing expression levels in cells [167] (Fig. 5.2A). The phantom was scanned with an orthogonal NSSM sequence using a 55 µm scanning step. SSM detected GV wells at all concentrations (Fig. 5.2B) and normalized contrast-to-noise ratios (CNR) scaled by steps of 6.9 dB on average from -20.8 dB for OD 0.5 to 0 dB for OD 2. NSSM detected GV wells at all concentrations (Fig. 5.2C) and exhibited a larger, 33 dB dynamic range between the GV well at OD 0.5 and the GV well at OD 2. We observed a lower increase in CNR from OD1.5 to OD2 possibly owing to pressure-dependent ultrasound attenuation in a medium containing buckling GVs [179]. Additional results for linearly and non-linearly scattering purified Anabaena flos aquae GVs are reported in Fig. S2. A representative dataset can be found online [**?**].

Next, we tested the ability of NSSM to visualize bacterial ARG expression, which is of particular interest for the field of engineered bacterial biosensors [180] and therapeutics [175, 176]. Two different strains of E. coli were used, a control strain and a strain transfected with plasmid pBAD-bARGSer [176] leading to intracellular production of Serratia GVs, which constitutively produce nonlinear scattering (Fig. 5.2D). Both strains of bacteria were embedded in agar phantoms and imaged with NSSM (Fig. 5.2E). Imaging volumes of 8.8 x 8.8 x 10 mm^3 were reconstructed from 108 sound sheets scanning positions of the RCA-transducer (Fig. 5.2G). As expected, the control strain did not show any nonlinear contrast, whereas bacteria expressing Serratia GVs were detected both in 2D and in 3D (Fig. 5.2E-G). NSSM detected nonlinear bacterial ARGs with a CNR of 27 dB.

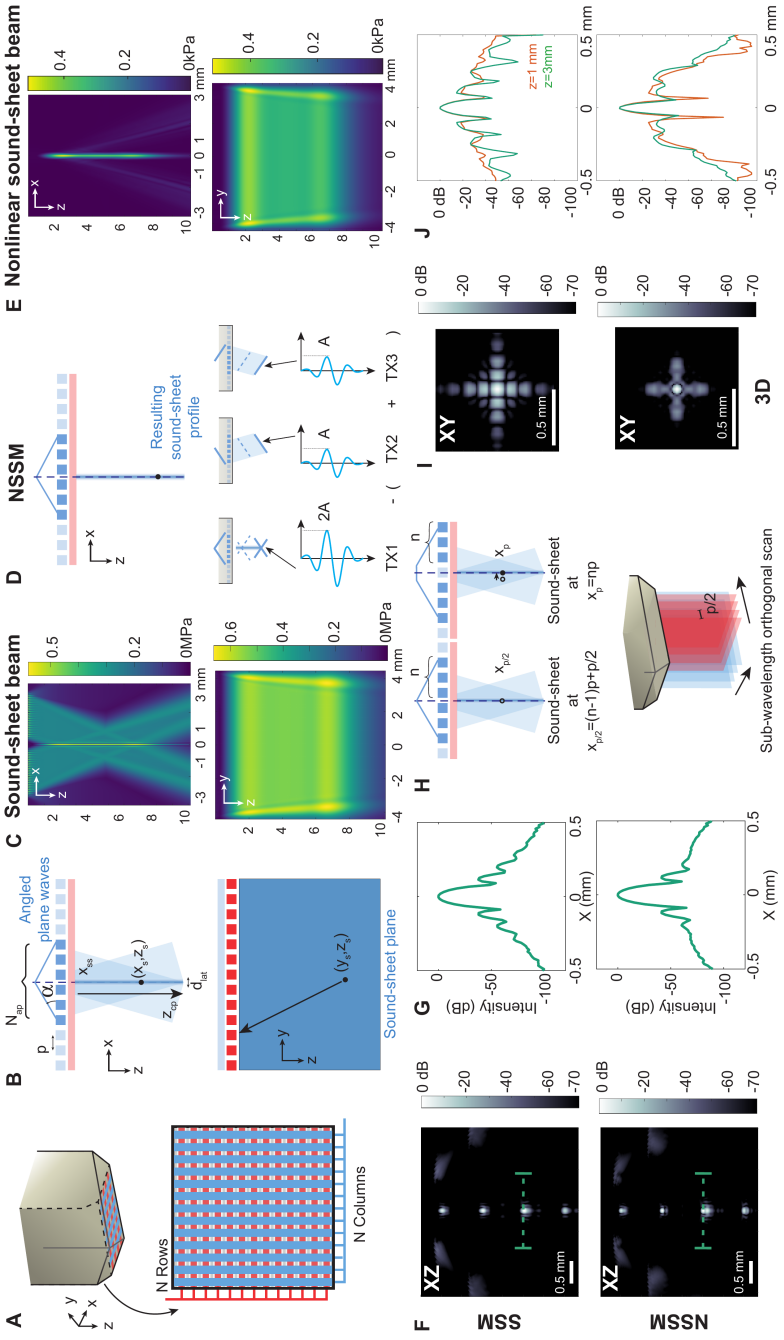

Figure 5.1 – Concept of nonlinear sound-sheet microscopy (NSSM) – Caption continues on the next page.

Figure 5.1 – (continued) **(A)** RCA design featuring long and thin transducer elements arranged as rows (red) and columns (blue). **(B)** Top, X-wave transmission with a sub-aperture of column elements. Bottom, reception of backscattered echoes with row elements. **(C)** Simulated X-wave acoustic pressure fields in the XZ and YZ direction. **(D)** Top, spatial confinement nonlinear ultrasound intensity along the main lobe of the X-wave beam using a xAM pulse sequence. Bottom, 3 pulses of the xAM sequence that modulate acoustic pressure A along the main lobe of the X-wave beam. **(E)** Simulated residual acoustic pressure field resulting from the xAM sequence in a homogeneous nonlinear water medium. **(F)** Simulated images of four resonant MBs in a water medium. Top, SSM image obtained from transmit event TX1. Bottom, NSSM image obtained from all transmissions of the xAM sequence. **(G)** Top, SSM and bottom, NSSM intensity profiles through a resonant MB. **(H)** Top, electronic sound-sheet micro-scanning along one array of the RCA. Bottom, orthogonal sound-sheet micro-scanning process. **(I)** Top, SSM and bottom, NSSM orthogonally-scanned PSFs of a resonant MB in the XY plane. **(J)** Top, SSM and bottom, NSSM intensity profiles through the center of the 1st and 3rd MB in the X direction.

5.2.2 Longitudinal NSSM of genetically labelled tumor cells

To go further, we investigated the ability of NSSM to image mammalian ARGs (mARGs) in a mouse model of cancer. Orthotopic tumors were induced bilaterally in the mammary fat pads of female immuno-compromised mice by injecting cancer cells engineered to produce nonlinearly scattering GVs [176] (Fig. 5.3A). In vivo mARG expression was induced via doxycycline injections every day until day 4 or day 8. Tumors were imaged at day 4 after induction in 3 mice and at day 8 after induction in 2 mice. A representative dataset can be found online [**?**].

While SSM images revealed anatomical structures, including tumor masses, NSSM successfully revealed spatial patterns of mARG-expression within these tumor masses (Results of Fig. 5.3B are also provided in Fig. S3 with an equal dynamic range and identical colormap). At day 8 after induction, NSSM revealed the necrotic core of breast tumors via the absence of gene expression. The high specificity of NSSM [172], which is robust to nonlinear wave propagation artifacts, was key for this experimental observation. Volumetric imaging enabled us to display cross sectional views of mARG expression in the XY plane, referred to as a C-scan (Fig. 5.3B, right column). Tumors were clearly detected at both stages, but necrotic cores were only visible at day 8 after induction.

Volumetric NSSM fused with anatomical SSM imaging is reported in Fig. 5.3C. The total volume scanned extends across 8.8x8.8x9 mm^3 and was acquired with a with scanning step of 55 µm along each array of the RCA-transducer. Fig. 5.3C displays cross sectional views of gene expression in XZ, YZ and XY planes, illustrating 3D navigation capabilities of NSSM. We quantified tumor and necrotic core volumes using a custom automatic segmentation pipeline (Fig. 5.3D). At day 4 after induction, volumes measured with and without necrotic cores were similar, whereas at day 8 after induction, volumes measured with and without necrotic cores showed a statistically significant difference. A representative automatic segmentation of tumor gene expression contours is provided in Fig. 5.3D. In these deep tissue imaging experiments, in vivo patterns of gene expression remained quasi-static because the breathing rate of anesthetized mice was ~60 breaths/min. We chose to operate orthogonally scanned volumetric NSSM at 4 volumes/s, which was enough to prevent

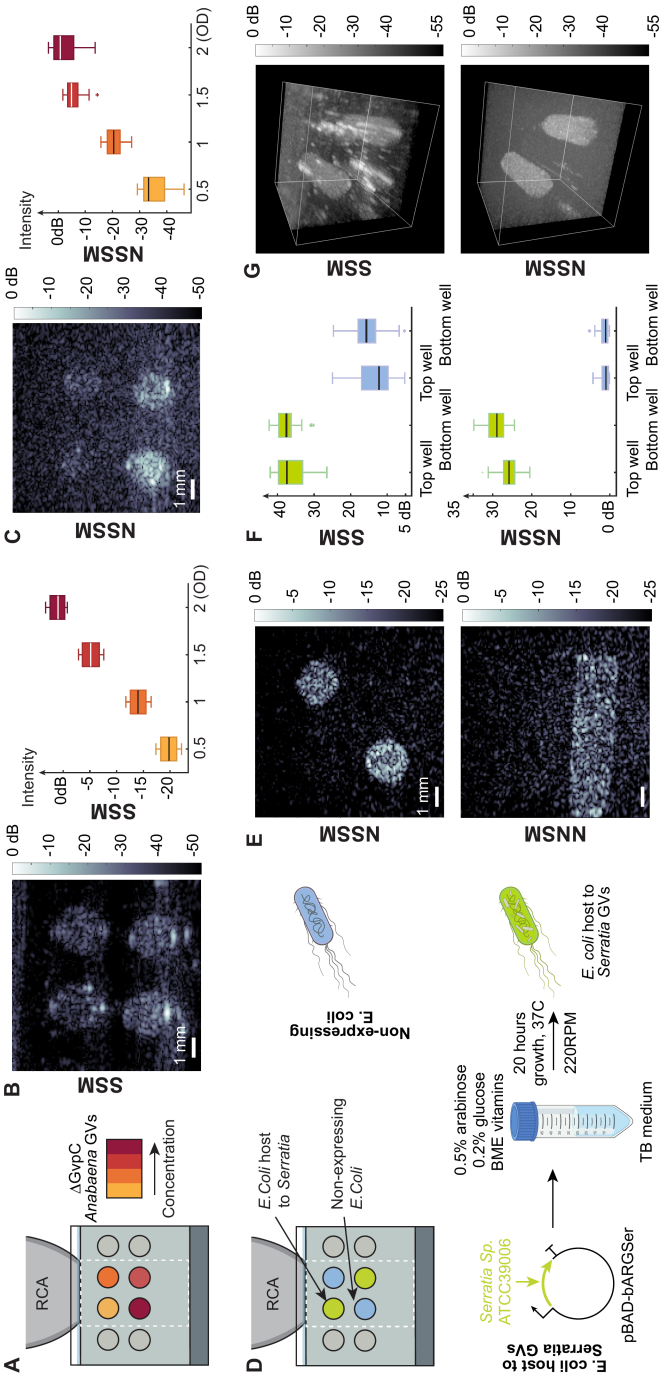

Figure 5.2 – Large volume NSSM of bacterial ARGs – Caption continues on the next page.

Figure 5.2 – (continued) **(A)** Experimental setup showing the RCA-transducer in contact with an agar phantom (gray) containing wells filled with increasing concentrations *Anabaena flos aquae* GVs stripped of the shell-stiffening protein GvpC to exhibit nonlinear ultrasound scattering. The RCA field of view is indicated in dashed white lines. **(B)** Left, SSM image for an angle α = 19 degrees. Right, contrast-to-noise ratio of each well as a function of the GV optical density. **(C)** Left, corresponding NSSM image. Right, nonlinear contrast-to-noise ratio of each well as a function of the GV optical density. **(D)** Experimental setup with wells containing two strains of *Escherichia coli* bacteria, wild type *E. coli* (blue) and GV-expressing *E. coli*. (green). See protocol (*28*) for bacterial ARG expression. **(E)** Short axis and long axis NSSM images obtained with rows and columns of the RCA respectively. **(F)** SSM and NSSM contrast-to-noise ratios measured out of 108 sound sheet positions across the GV wells. The blue and green boxes correspond to CNR measured for respectively non-expressing E. coli bacteria and E. coli expressing *Serratia* GVs. **(G)** 8.8x8.8x10 mm^3volumetric SSM and NSSM images of the phantom.

breathing motion artifacts. Note that in imaging scenarios that would require higher volume rates such as imaging of calcium signaling, 3D NSSM could reach 200 volumes/s (see table S1). The quantification of in vivo tumor volumes would have been impossible based on anatomical ultrasound imaging alone, which highlights the potential of this imaging method.

5.2.3 Ultrasound sectioning of the brain vasculature with Doppler NSSM

Alongside genetically encoded GVs, synthetic lipid-shelled MBs are another class of ultrasound contrast agents used as vascular reporters. MBs exhibit amplitude-dependent ultrasound scattering [181], which makes them detectable with amplitude modulation pulse sequences as well [173, 182]. To test the capacity of NSSM to visualize MBs circulating in blood vessels, we performed high-speed nonlinear Doppler imaging of the rat brain vasculature (Fig. 5.4).

MBs tuned for high-frequency ultrasound were administered via tail vein injections in anesthetized head-fixed rats (Fig. 5.4A). As reference, linear Doppler SSM images were acquired at a 4.4 kHz framerate (Fig. 5.4B) and generated results similar to ultrafast Doppler images of the rat brain [39]. Doppler NSSM images (Fig. 5.4C) were obtained using amplitude modulated data and a high-pass filter to remove residual static echoes (see Materials and Methods). Note that nonlinear Doppler results did not rely on any singular value decomposition (SVD) filter [45]. Because nonlinear Doppler processing spatially confines image data to a 100 µm x 9.6 mm x 8.8 mm thin sound sheet plane, we detected fewer vessels in Fig. 5.4C than in Fig. 5.4B, which projects in one image echoes arising from the oblique paths of each plane waves (see Fig 1C). As a result, the cortical surface was clearly delineated in Doppler NSSM (Fig. 5.4C) whereas vascular signals projected from the oblique paths of each plane waves were visible above the cortex in Fig. 5.4B. Supplementary Fig. S4 shows that Doppler NSSM is more sensitive to slow blood flows than Doppler SSM based on SVD filtering, in line with previous observations [183].

Next, we performed ultrasound sectioning the rat brain vasculature with sub-wavelength

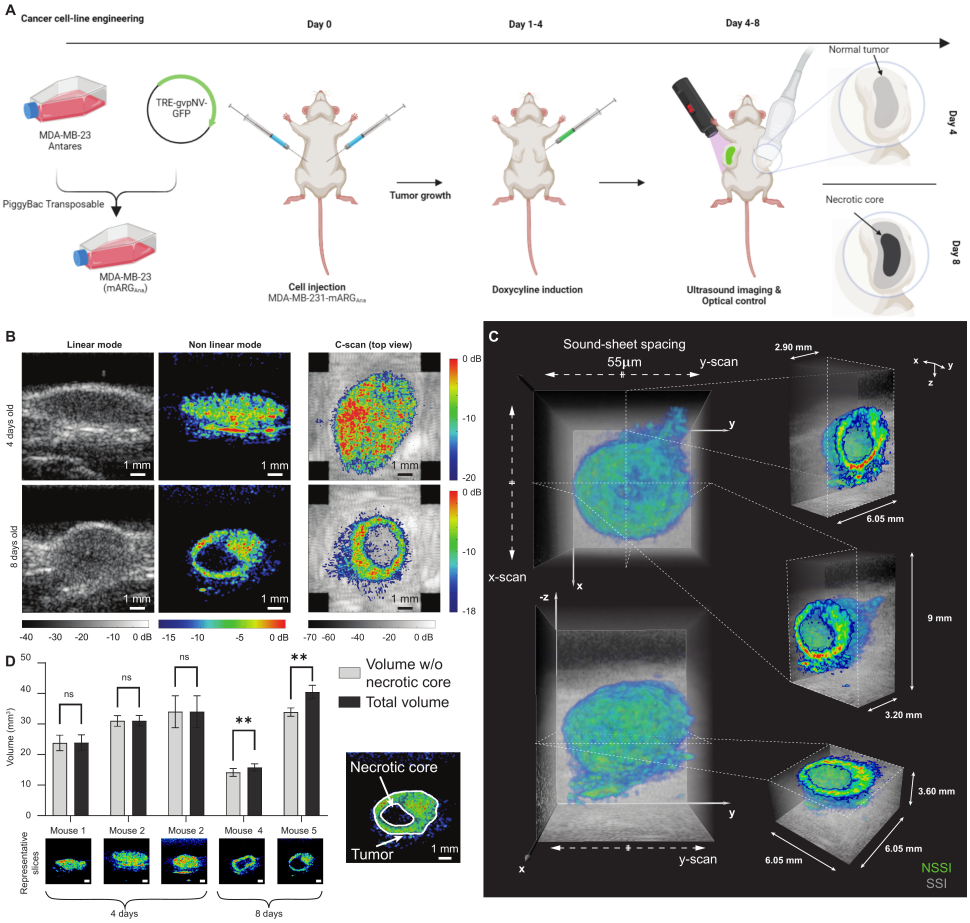

Figure 5.3 – Longitudinal NSSM of tumor gene expression (A) Protocol for ultrasound imaging of mARG expression in orthopic tumors (see Materials and Methods). **(B)** Left, SSM images of 4- and 8-days old tumors. Middle, NSSM images revealing mARG expression in tumors. Right, XY image of an orthogonal 3D NSSM scan overlaid on linear imaging data. Scalebars, 1 mm. **(C)** Representative 3D NSSM of an 8-days old tumor overlaid on the grayscale SSM volume. **(D)** Results of an automatic segmentation (tissue attenuation compensation followed by 3D Gaussian filtering, 2D binarization using Otsu's method for thresholding, and area measurement using connected components) of the tumor and necrotic core for N=5 mice. The 2D segmentation is performed in each of the scanned direction of the sound-sheets and in the transverse direction on the compounded volume (3 datapoints per animal). Light gray plots the tumor volume without the necrotic core, dark gray plots the tumor volume including the necrotic core (multiple paired t-test, $^{**}P<0.01$). Below, representative 2D NSSM of the tumors for each mouse. Scalebars, 1 mm. Right, automatic segmentation result at day 8. Scalebar, 1 mm.

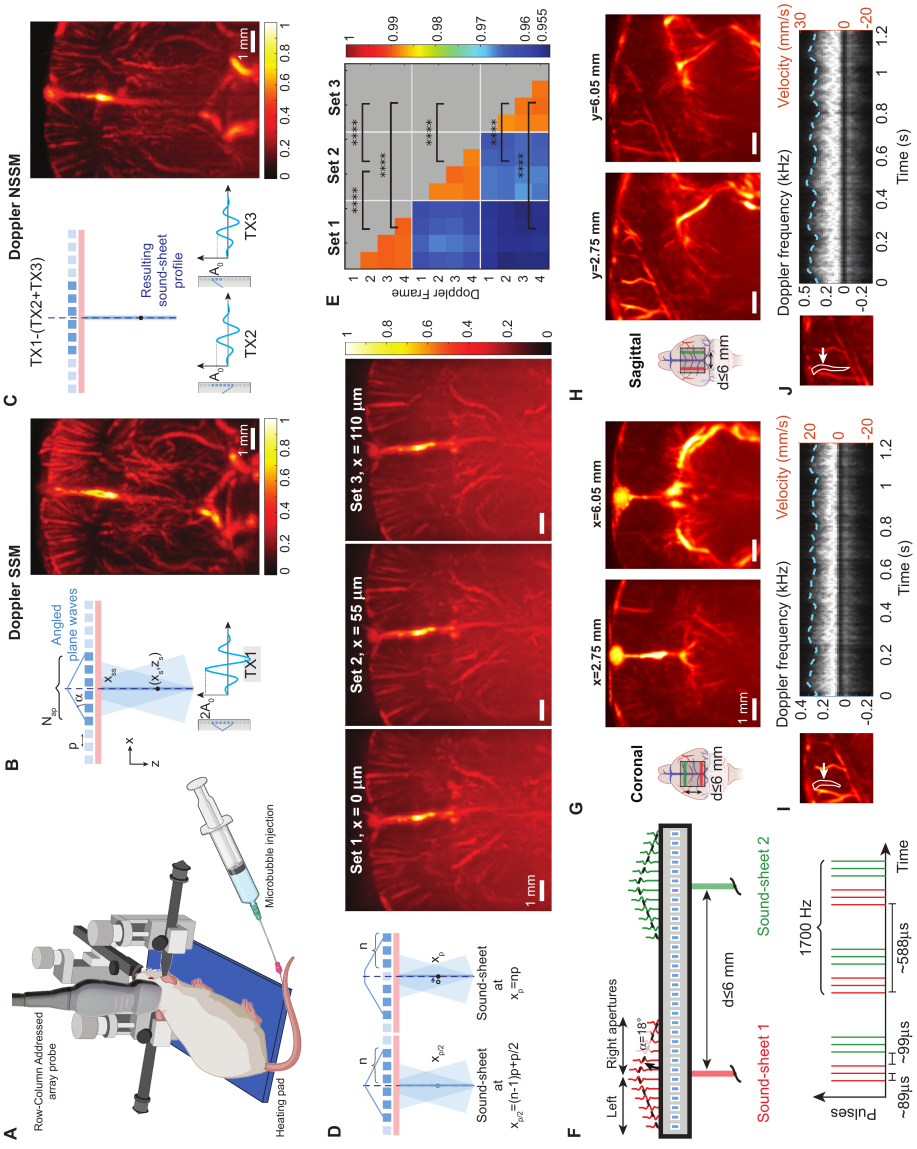

Figure 5.4 – High-speed multi-view NSSM of the rat brain vasculature – Caption continues on the next page.

Figure 5.4 – (continued) **(A)** Experimental setup. **(B)** Coronal section of the rat brain vasculature acquired with 4.4 kHz Doppler SSM after MB injection from 2100 images. **(C)** Same brain section acquired with 4.4 kHz Doppler NSSM after MB injection from 2100 images. **(D)** Doppler NSSM of three adjacent coronal brain sections with a 55μm micro-scanning step. **(E)** Structure Similarity Index Matrix calculated using 4 Doppler NSSM acquisition in each of the three adjacent planes (Asterisks show statistical significance using t-test of two independent samples (P values are all inferior to 10^{-21},$^{***}P < 0.001$, **** $P < 0.0001$). **(F)** Multi-view NSSM imaging principle using two sub-aperture of elements of the RCA-transducer. With our RCA probe, imaging planes can be spaced up to 6 mm, and imaging speed was set to 1.7 kHz per plane. **(G)** High-speed multi-view Doppler NSSM of two coronal planes. **(H)** High-speed multi-view Doppler NSSM of two symmetric sagittal planes. **(I)** Doppler spectrum revealing peak cerebral blood flow and pulsatility of a cortical arteriole of the left hemisphere. **(J)** Doppler spectrum revealing peak cerebral blood flow and pulsatility of a cortical arteriole of the right hemisphere.

scanning steps of 55 µm (Fig. 5.4D), acquiring four consecutive Doppler acquisitions per plane. We assessed vascular changes quantitatively in these adjacent planes by computing structural similarity index matrix values for each Doppler acquisition (Fig. 5.4E). Intra-sets, the structural similarity index averaged to 0.99 indicating that vascular images were nearly identical across cardiac cycles. Inter-sets, the index dropped to 0.96 confirming that we observed two separate vascular planes.

Inspired by multi-slice tomography techniques, we tested the ability of Doppler NSSM to capture multiple views of the brain simultaneously. To do so, we interleaved pulse sequence transmission using two sub-apertures of elements of the array (Fig. 5.4F and supplementary Fig. S5), because RCA arrays cannot discriminate echoes arising from two different planes in reception. In this configuration, we set our imaging rate to 1.7 kHz in both sound-sheet planes. To demonstrate the versatility of this approach, we imaged two coronal vascular planes separated by 3.3 mm using the first array of the RCA-transducer (Fig. 5.4G). Similarly, we imaged two sagittal vascular planes separated by 3.3 mm using the second array of the RCA-transducer, revealing symmetric vascular planes in each hemisphere (Fig. 5.4H). Last, we processed SSM Doppler spectrograms in each sagittal plane to show that acquisitions were continuous and co-registered in time (Fig. 5.4I-J, and Fig. S6). The Doppler-derived heartrates were equal to 298 bpm and 295 bpm in each brain hemisphere, respectively.

5.2.4 NSSLM reveals the brain capillary vasculature

In 2015, vascular ultrasound was redefined by the introduction of ultrasound localization microscopy (ULM), a super-resolution method that can map the in vivo microvasculature with a $\frac{\lambda}{8}$ resolution [184]. A drawback of current ULM processing is that SVD-based filters used to isolate MB echoes are unable to detect slowest blood flow velocities occurring in capillary beds [183, 185]. As a consequence, ULM has not been able to visualize capillaries despite capillaries representing the largest vascular territory of living organisms [186]. Because the NSSM detection of MBs relies on nonlinear MB scattering rather than MB motion, we hypothesized that the combination of NSSM and ULM could potentially reveal capillary beds in vivo.

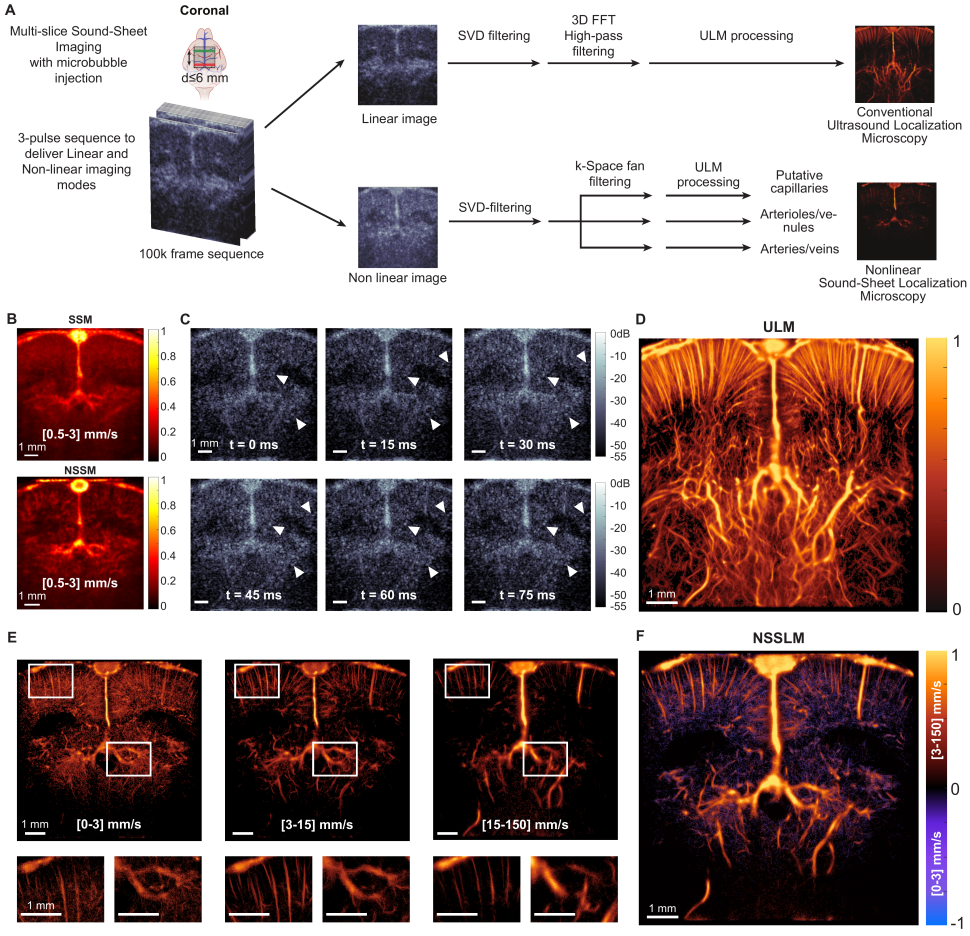

Figure 5.5 – Nonlinear sound-sheet localization microscopy of rat brain capillaries (A) ULM and NSSLM image processing pipelines. **(B)** Vascular information captured by Doppler SSM and Doppler NSSLM in the capillary blood flow velocity band (0.5-3mm/s). **(C)** NSSM frames of the NSSLM of the NSSLM sequence revealing slow MB flow in the rat brain. **(D)** ULM image generated with a state-of-the-art ULM processing pipeline (see supplementary Fig. S7). **(E)** NSSLM in the capillary flow velocity band (0.5-3 mm/s), arteriole and venule flow velocity band (3-15 mm/s) and artery and vein velocity band (15-150 mm/s). **(F)** Composite NSSLM image display all cerebral blood flow velocity bands.

We investigated nonlinear sound-sheet localization microscopy (NSSLM) of the cerebral capillary vasculature in Fig. 5.5. Craniotomized rat brains perfused with MBs were imaged at 1 kHz using NSSM in a coronal mid-brain plane over the course of 105 seconds, leading to the acquisition of 105 frames (Fig. 5.5A). Two independent post-processing pipelines were used to generate state-of-the-art ULM images and NSSLM images. For NSSLM, signal processing consisted in first filtering MB echoes with the amplitude modulation step of NSSM. Second – and to increase the signal-to-noise ratio and compensate for attenuation – the 1-lag cross-correlation of the AM signal was computed and the signal was further adjusted using an adaptive time gain compensation function. To remove residual nonlinear tissue signals, a singular value decomposition clutter filter was applied with a cutoff of 1 singular value. Finally, a 3D-FFT fan filter was implemented, and the signal was decomposed in the following velocity bands: [0-3] mm/s, [3-15] mm/s, [15-25] mm/s, [25-60] mm/s and [60-150] mm/s. The imaging dataset was transformed back to the spatiotemporal domain, and MBs were localized using the radial symmetry algorithm [187]. Individual MBs were paired with the Kuhn-Munkres [188] assignment to retrieve MB trajectories.

Fig. 5.5B displays SSM Doppler and NSSM Doppler images filtered in the capillary flow velocity band (0.5 to 3 mm/s) [189, 190], showing that NSSM retrieves vascular signals in cortical and hippocampal regions of the rat brain with a good SNR, whereas the SSM images is mostly filled with diffuse vascular noise. In particular, low velocities located at the wall of the sinus vein were visible in Doppler NSSM. Time-series of NSSM frames filtered in the capillary velocity band (Fig. 5.5C) showed the dynamic of slow flowing MBs captured with NSSM, which constitutes the basis for NSSLM post-processing. Individual microbubbles that are quasi-static are indicated with white arrows. Over the course of 75 ms, several MBs progress by less than half a wavelength (57 µm), indicating that their velocities were below 0.8 mm/s, which falls in the range of capillary flow velocities.

As a reference, we processed a state-of-the-art ULM density map using X-wave transmissions (Fig. 5.5D). In comparison, NSSLM (Fig. 5.5E-F) enabled mapping of capillary beds segmented with a 0-3 mm/s flow velocity band (Fig. 5.5E, left panel), arterioles and venules segmented with a 3-15 mm/s flow velocity band (Fig. 5.5E, middle panel) and arteries and veins segmented with a 15-150 mm/s flow velocity band (Fig. 5.5E, right panel).

A composite NSSLM image showing all vascular compartments is presented in Fig. 5.5F. Vascular structures displayed in the NSSLM image appeared clearly denser than structures detected with ULM, as expected from capillary beds [186]. The results for the second plane exhibit similar characteristics and are presented in supplementary Figs. S8 and S9.

5.3 Discussion

We report NSSM, a fast and volumetric imaging method capable of visualizing targeted biological processes at the organ scale. NSSM introduces nonlinear sound-sheet beams in the field of ultrasound imaging and is capable of detecting two major classes of ultrasound contrast agents, genetically encoded GVs and intravascular MBs. Thanks to its all-acoustic nature, NSSM circumvents certain limitations of light-sheet or multi-photon microscopy [156, 191, 192] such as phototoxicity, photobleaching of fluorescent reporters and complex single-objective microscope designs based on oblique illumination.

In 2D, NSSM achieved framerates of 4.4 kHz in thin sound-sheets of 0.1x8.8x12.9 mm^3, or 1x89x130 λ^3. We show that sound-sheet beams can be arbitrarily positioned within the 8.8x8.8 mm^2 active aperture of a 15 MHz RCA-transducer and swept electronically along each orthogonal array with a sub-wavelength precision of 55 µm ($\frac{\lambda}{2}$).

NSSM can be further tuned for speed or spatial coverage. Inspired by multi-slice imaging of the brain [193], we report fast multi-view NSSM at a framerate of 1.7 kHz, enabling Doppler imaging of the rat brain. Symmetric planes in each brain hemisphere can be observed simultaneously and enable studies of lateralized brain function. Note that single slice and multi-slice Doppler NSSM do not enable 4D ultrafast Doppler imaging because it is not illuminating the whole volume of view at once but rather sub-wavelength thin slices at kHz framerate. This multi-slice approach could be of interest to study vascular activity in a few predefined brains regions. One advantage of multi-slice Doppler NSSM compared to 4D Doppler imaging would be to significantly reduce data rate.

The 64x increase in 2D imaging speed compared to xAM imaging enabled localization microscopy of the cerebral capillary vasculature. Here, the combination of kHz imaging with specific MB detection regardless of MB velocity was fundamental to chart capillary territory and opens the way for imaging of microvascular activity deep in intact tissues. Here, we acquired 2D super-resolution vascular images in parallel coronal planes spaced by several millimeters. Future work will investigate the feasibility of 3D NSSLM of the capillary vasculature using fast electronic sweeping of sound-sheet beams along adjacent planes spaced by half a wavelength. Orthogonal NSSM microscanning enables volumetric imaging of genetically encoded bacterial and mammalian ARGs. In particular, 3D NSSM enabled longitudinal molecular ultrasound imaging of gene expression in a tumor model. The imaging method creates the possibility for in vivo tumor volume quantification in mammalian tissue. The high specificity of cross amplitude modulation was critical to reveal the necrotic core of tumors, which classical pulse sequences would underestimate owing to nonlinear wave propagation artifacts.

5.3.1 Limitations

To put our method in context, we summarize here what limits the performance of NSSM in terms of depth, speed and volume. The imaging depth of SSM and NSSM are identical and limited by the cross-propagation depth z_{cp} (see Materials and Methods). For a transmitting aperture of 64 elements, an inter-element spacing of 110 µm and a cross-propagation angle $\alpha = 15\,deg$, z_{cp} is approximately equal to 13 mm. NSSM imaging speed is limited by speed of sound in 2D, and speed of sound and the number of scanning steps in 3D. Theoretically, NSSM can reach 25 600 images/s and 233 volumes/s (see Table S1). The field of view of NSSM is limited by the size of the active surface of the transducer array. A 15 MHz RCA of 160 elements provides an accessible field of view of ~8.8x8.8x10 mm^3. A 15 MHz RCA of 256 elements would provide an accessible field of view of ~12.8x12.8x10 mm^3. For comparison purposes, the limits of 4D functional ultrasound neuroimaging reported in the literature [49] are a depth of 15 mm, a speed of 6 volumes/s and a field-of-view of 9.6x9.6x15 mm^3.

Overall, the NSSM paradigm complements the capabilities of volumetric ultrasound imaging methods such as functional ultrasound, orthogonal plane wave imaging [53],

synthetic aperture imaging [171] or xDoppler [153] that provide anatomical or vascular information at the mesoscale but do not enable molecular or cellular imaging. In addition, 2D NSSM provides an improved resolution in elevation which can be as low as 0.4 λ [172] versus $\geq 3\lambda$ [134] for linear transducer arrays.

A first limitation of NSSM is that the requirement for symmetric half-apertures to generate sound-sheet beams prevents imaging on the edge of the RCA-transducer. However, orthogonal NSSM microscanning allows the retrieval of part of this missing volume such that the surface area lost in the corners of the active surface of the RCA-transducer represents 11% (77.44 $cm^2$to 69.24 cm^2). In addition, wider RCA-transducers made of 256 elements could be operated with our current hardware and would automatically increase the field of view.

A second limitation lies in the volumetric imaging rate achievable with SSM, which lies in the hundreds of Hz and not kHz. This volume rate remains comparable to other high quality RCA volumetric imaging methods, such as functional Orthogonal Plane Wave (OPW) neuroimaging [51] or synthetic aperture B-mode imaging [55]. Compared to 2D ultrafast Doppler imaging based on tilted plane wave transmissions, Doppler NSSM requires the injection of nonlinear ultrasound contrast agents into the blood stream. Both Doppler approaches rely on the continuous transmission of ultrasound waves at kHz framerates. Doppler NSSM outperforms 2D ultrafast Doppler imaging in terms of resolution in elevation and detection of slow cerebral blood flows. Note that Doppler NSSM is not suited for 4D Doppler imaging because it is not insonifying the whole volume of view at once but rather sub-wavelength thin tissue sections. 4D ultrafast Doppler imaging has been implemented on RCA arrays using OPW transmissions [51].

A third limitation of our study is that brain imaging was performed in craniotomized animals. The transcranial potential of NSSM has not been explored. Meanwhile, NSSM will be compatible with chronic acoustic windows [194]. In light of recent advances in transcranial ULM using fully addressed or RCA probes, we foresee that transcranial NSSLM will achieve a similar sensitivity to capillary flow as sensitivity arises from the NSSLM method itself.

NSSM would also benefit from the development of monodisperse MBs tuned for high frequency ultrasound because it would improve Contrast to Noise Ratio (CNR) and allow us to reduce MB doses administered [195].

The performance of NSSM is also bound by the collapse pressure of ARGs. A tradeoff exists between imaging depth that requires high acoustic pressures, and near field detection of ARGs that would be destructed if high acoustic pressures are used. We acknowledge that validation is a long-standing challenge for super-resolution ultrasound imaging in general and NSSLM of capillary beds in particular. NSSLM provides a combination of depth and resolution inaccessible to other in vivo techniques, making cross-referencing challenging. Hierarchical phase-contrast tomography at the European Synchrotron Radiation Facility [196] could serve as a comparison in the future.

Capillary flow velocities reported in our manuscript are consistent with other studies [185], and MB entry and exit from capillaries could be observed by combining continuous

NSSLM acquisitions at kHz framerates with long ensemble SVD filters. A significant advantage of NSSLM over conventional ULM is that sound-sheet imaging confines the echoes of intravascular microbubbles to a plane with a sub-wavelength resolution in elevation. This alleviates the risk of mapping out-of-plane vessels.

5.3.2 Summary

To conclude, the combination of latest and future generation acoustic probes [197] with NSSM carries a wave of opportunities for deep tissue imaging of dynamic biological processes. NSSM offers an unprecedented high spatiotemporal resolution and coverage to explore living opaque organs across scales.

5.4 Materials and Methods

Generation of non-diffractive ultrasound beams

RCA rows or columns were used to transmit simultaneous cross-propagating plane waves from two contiguous half-apertures $\frac{N_{ap}}{2}$ at angles α and $-\alpha$ (Fig. 5.1B). The two transmitted plane waves interfere along a 2D plane, referred to as the sound-sheet plane. During cross-propagation, an X-wave with a double amplitude is generated and propagates with a supersonic velocity $\frac{c_0}{\cos(\alpha)}$ until the cross-propagation depth $z_{cp} = \frac{N_{ap}}{2}\cot(\alpha)$. Ultrasound echoes received by the array orthogonal to the transmitting array are processed to generate an image. Image reconstruction relies on a delay-and-sum beamforming algorithm with the assumption that ultrasound backscattering only arises from the sound-sheet plane. For beamforming delay laws, see the image reconstruction paragraph and reference [173].

Sub-wavelength micro-scanning and 3D ultrasound imaging

Non-diffractive beams can be generated two ways (see Fig. 5.1H). First, using two contiguous sub-apertures of RCA-transducer elements. This focuses the sound-sheet plane at a position $x_{SS} = x_{\frac{p}{2}} = (n-1)p + \frac{p}{2}$, with n the number of elements and p the pitch or inter-element spacing of the RCA-transducer. Second, using two sub-apertures of RCA-transducer elements separated by an inactive element. This focuses the cross-propagation plane at a position $x_{SS} = x_p = np$. In practice, these two transmissions generate non-diffractive beams with main-lobes separated by a distance of $\frac{p}{2}$. The thickness of the sound sheet was estimated using INCS simulations [173], the Full Width at Half Maximum (FWHM) of the main-lobe of the non-diffractive beam can be approximated with the following relation:

$$\mathrm{FWHM}_{SS} = \frac{0.32\lambda}{\sin(\alpha)}$$

In particular, the FWHM becomes smaller than the wavelength for any angle $\alpha > 18.66^{\circ}$.

By performing sound-sheet micro-scanning in X and Y, a volume is sampled. Note that sound-sheet micro-scanning can also be performed along only X or Y. Because sound-sheets are generated using two half-apertures, the field of view FoV is reduced compared to active surface of the RCA-transducer: $\mathrm{FoV} = N_{total} \times p - 2 \times \frac{N_{ap}}{2}$. The volume occupied by the main-lobe of a sound sheet beam is therefore: $z_{cp} \times \mathrm{FWHM}_{SS} \times w_{array}$, with $w_{array} = N_{total} p$

the full width of the RCA array. Therefore, the volume of sound-sheet scan along one array is equal to:

$$z_{\mathrm{cp}} \times N_{SS}\mathrm{FWHM}_{\mathrm{SS}} \times w_{\mathrm{array}}$$

with N_{SS} the number of sound sheet positions.

By using varying aperture sizes, it is possible to extend the field of view further, but then the propagation depth z_{cp} is reduced. To keep z_{cp} constant, one possibility is to decrease angle α. Considering a minimum half-aperture for sound-sheet transmission $N_{\mathrm{red}}p$, the total field of view covered by a scan in one direction is:

$$z_{\mathrm{cp}} \times (N_{\mathrm{total}} - N_{\mathrm{red}})p \times w_{\mathrm{array}} = z_{\mathrm{cp}} \times w_{\mathrm{array}}^2 - z_{\mathrm{cp}} \times w_{\mathrm{array}} \times N_{\mathrm{red}}$$

and for a 3D scan along X and Y, this becomes:

$$z_{\mathrm{cp}} \times w_{\mathrm{array}}^2 - 4(N_{\mathrm{red}}p)^2$$

5

When compared to active surface of the RCA-transducer, this leads to a field of view reduction of:

$$1 - \frac{z_{\mathrm{cp}}(N_{\mathrm{total}}^2 - 4N_{\mathrm{red}}^2)p^2}{z_{\mathrm{cp}}(N_{\mathrm{total}}p)^2} = 4\frac{N_{\mathrm{red}}^2}{N_{\mathrm{total}}^2}$$

In our study, we used a reduced aperture of as low as 12 elements, leading to a 11% loss in image volume.

Spatial confinement of nonlinear scattering via amplitude modulation:

In NSSM, the same half-apertures are used for two additional transmits, each firing independently this time (see events TX2 and TX3 in Fig. 5.1D). As no cross-propagation is taking place in this case, the acoustic pressure delivered along the sound-sheet plane has a twice lower amplitude than TX1. An amplitude-modulated signal can thus be obtained by subtracting echoes received from TX2 plus TX3 from echoes received from TX1. This operation is done on the radiofrequency data and the residual signal is beamformed and further processed. A 3D NSSM image can also be obtained by performing three xAM pulse transmissions for every sound-sheet position in X and Y.

Sound-sheet image reconstruction:

To reconstruct an image from the sound-sheet, we make the assumption that backscattered echoes originate only from the sound sheet plane. If the sound sheet plane is oriented with its normal along the $\vec{x}$ direction, then all scatterers can be assumed to have the same y coordinate. The forward delay for a scatterer at a position (x_s, y_s, z_s) can be written as:

$$t_f(x_s, y_s, z_s) = \frac{z_s}{c_{ss}} = \frac{z_s \cos(\alpha)}{c_0}$$

With c_{ss} the supersonic speed of the sound-sheet and c_0 the speed of sound in the medium.

The return delay for a scatterer at a position $(x_s, y_s,\ z_s)$ is calculated for the array orthogonal to the transmitting array to restore focusing and is written as:

$$t_r(x_s, y_s, z_s) = \frac{\sqrt{z_s^2 + y_s^2}}{c_0}$$

It is important to notice that t_f only depends on $z_s,\ x_s$ while t_r only depends on $z_s,\ \ y_s$.

Simulation of linear and nonlinear sound-sheet beams:

Linear and nonlinear sound-sheet beams reported in Fig. 5.1C and Fig. 5.1E were computed with the Iterative Nonlinear Contrast Source (INCS) method [173]. Briefly, INCS was developed to solve the four-dimensional spatiotemporal Westervelt equation describing nonlinear sound wave propagation. Simulations were conducted within a computational domain $X \times Y \times Z = 6.5 \times 13 \times 10.5\ mm^3$. The propagation medium consisted of water and was characterized by a mass density $\rho_0 = 1060 kg.m^{-3}$ and a speed of sound $c_0 = 1482\ m.s^{-1}$. The incident beam had a center frequency $f_c = 15MHz$. The simulated RCA array consisted of 64 individual elements, each with length 12.8 mm, and a pitch of 100 μm. The transmitted pulses were modelled as Gaussian-apodized sine-bursts:

$$p(t) = P_0 \exp\left[-\left(\frac{t - T_d}{T_w/2}\right)^2\right] \sin\left[2\pi f_0 (t - T_d)\right],$$

with $T_w = \frac{1.5}{f_c}$ representing the duration of the Gaussian envelope and $T_d = \frac{3}{f_c} + \Delta_n$ a total time delay. The latter consists of a fixed delay for keeping $p(t = 0) \sim 0$, plus a delay per element for the beam steering. Beams are simulated for an angle $\alpha = 20.7°$. The peak acoustic pressure of the elements surface was $P_0 = 400\ kPa$. A sampling frequency of 90 MHz was used to discretize the spatiotemporal domain.

Simulation of NSSM point spread functions:

We simulated the response of 4 resonant microbubbles in a homogeneous water medium using the k-Wave simulation toolbox. MBs were positioned at $z = 1; 2; 3\ and\ 4\ mm$ and centered in the middle of the domain. Each MB had a diameter of 1.5μm, leading to a resonance frequency of 15.625 MHz. In this simulation, the geometry of the transducer consists of 43 elements with a height of 4.3 mm, a width of 100 μm and a pitch of 100 μm, and a bandwidth of 14 to 22 MHz. 22 sound-sheet transmissions were simulated with a scanning step of 50 μm, an angle α=21°, a 4-cycles Gaussian-apodized sine-burst and an acoustic peak pressure of 400 kPa at the transducer surface. The radiofrequency data was beamformed using the delay-and-sum algorithm described above. For 3D imaging, we permuted simulation data to emulate data of the orthogonal array as our problem is symmetric.

Ultrasound imaging of a wire phantom:

A 15 MHz RCA probe with 80+80 elements (Verasonics, Kirkland, WA, USA) with a pitch or inter-element spacing of 110 µm was placed over a 3D wire phantom (model 055A from CIRS, VA, USA). The wires were oriented at an angle from the orientation of the rows and

columns elements. SSM images were obtained using a 14° angle per array (2 transmits per voxel result) and a combination of [7°, 15°, 20°] angles (6 transmits per voxel result). As reference, an orthogonal plane wave (OPW) acquisition with an angle of -18 degrees was used (2 transmits per voxel result) and 2x32 transmits ranging from -21° *to* 21° (64 transmits per voxel result). Imaging results are reported in supplementary Fig. S1. C-scans, i.e. images in the XY plane, reveal wires in diagonal. For the SSM case, micro-scanning was performed with a 55 μm step. In-plane images, i.e. XZ scans, reveal a single wire cross section. Waveforms transmitted in both case were 13.6 MHz, 0.5 cycles sine-bursts.

NSSM performance compared to xAM imaging

Imaging speed: The gold standard for non-destructive imaging of acoustic reporter genes in a tissue context is a method called cross amplitude modulation imaging (xAM). xAM image acquisition operates line by line [172]. An image is typically formed of 64 image lines, and for each line the 3 pulses of the amplitude modulation sequence are transmitted sequentially. In the end, the acquisition of one xAM image requires 3 x 64 pulse transmissions. In NSSM, cross-propagating plane waves transmitted using the long elements of a row-column array intersect along a plane. The acquisition of one 2D NSSM image requires only 3 pulse transmissions. 2D NSSM is therefore 64 times faster than 2D xAM.

Imaging volume: xAM imaging operates on linear arrays of transducer elements. The volume insonified by xAM is a function of the width of the ultrasound beam in elevation (off-plane direction). At 15 MHz, the thickness of the ultrasound beam is ~350 µm or 3.5 λ as illustrated below (see Mac'e et al. Neuron 2018, Figure S2D). A typical xAM image has a width of 64 λ (64 image lines spaced by 1 λ), a depth of 1 cm or 100 λ and an elevation of 3.5 λ. This leads to an insonified volume $V_{xAM} \cong$ 3.5x64x100 λ^3. In comparison, NSSM operates on a RCA array with an active surface of 8.8 by 8.8 mm. The imaging volume accessible is therefore $V_{NSSM} \cong$ 80x80x100 λ^3. The leads to a volume ratio $\frac{V_{NSSM}}{V_{xAM}} \cong 35$.

Ultrasound imaging of GV phantoms:

Fig. 5.2A: *Anabaena flos aquae* GVs were cultured and transferred to sterile separating funnels. Buoyant cells were separated from the growth media through natural flotation, and GVs were harvested after 48h of hypertonic lysis. A cycle of centrifugation and resuspension allows to purify the GVs further. A stock of *Anabaena flos aquae* GVs was stripped of their GvpC protein layer with a 6-M urea solution to obtain nonlinearly scattering GVs (ΔGvpC GVs). A 2% agar phantom comprising 2 mm in diameter wells was casted using custom-printed molds and imprints. For each of the 4 wells, the concentration is increased starting with a concentration measured optically at OD0.5, OD1, OD1.5 and OD2. Images were obtained with the 15 MHz RCA-transducer (Verasonics, Kirkland, WA, USA). Waveforms transmitted were 13.6 MHz, 0.5 cycles sine-bursts. The X-wave angle α was set to 19°.

Fig. 5.2D: *Escherichia coli* bacteria were grown for 20 hours at 37°C, 220 RPM flask shaking in a terrific broth medium with 0.5% arabinose, 0.2% glucose and BME vitamins. In one case, plasmid pBAD-bARGSer was transferred to the *E. coli* strain (courtesy of Shapiro Lab, derived from plasmid Addgene #192473) via electroporation. These cells produced *Serratia* GVs that are constitutively nonlinear scatterers. Both bacterial populations were then transferred to the phantom.

Ultrasound imaging of a cancer model:

All in vivo experiments were performed under protocol 1761, approved by the Institutional Animal Care and Use of Committee of the California Institute of Technology. Animals were housed in a facility maintained at 71–75 °F and 30–70% humidity, with a lighting cycle of 13 hours on and 11 hours off (light cycle 6:00–19:00). Tumor xenograft experiments were conducted in NSG mice aged 12 weeks and 6 days (Jackson Laboratory). As we relied on an orthotopic model of breast cancer, all mice were female. MDA-MB-231-mARGAna cells were grown in T225 flasks in DMEM supplemented with 10% TET-free FBS and penicillin–streptomycin until confluency as described above. Cells were harvested by trypsinization with 6 ml of trypsin/EDTA for 6 minutes and quenched with fresh media. Cells were washed once in DMEM without antibiotics or FBS before pelleting by centrifugation at 300G. Cell pellets were resuspended in a 1:1 mixture of ice-cold Matrigel (HC, GFR) (Corning, 354263) and PBS (Ca2+, Mg2+-free) at 30 million cells per milliliter. Then, 50-µl Matrigel suspensions were injected bilaterally into the 4^{th} mammary fat pads at 1.5 million cells per tumor via subcutaneous injection. Twelve hours after tumor injection and every 12 hours thereafter (except the mornings of ultrasound imaging sessions), test mice were intraperitoneally injected with 150 µl of saline containing 150 µg of doxycycline for induction of GV expression.

The 15 MHz RCA probe was operated to transmit pulses at 110 sound-sheets positions along each array, so 220 positions in total. For each sound-sheet position, waves were transmitted using 7 angles ranging from 15° to 21° with steps of 1°. For each sound-sheet position, the 3 pulses of the sequence were transmitted for the first angle, then the 3 pulses of the sequence were transmitted again for the next angle and so on until the last angle was reached. Then, the same set of transmit events was used for the next sound-sheet position. Scanning started on array 1 made of piezo-elements 1 to 80 and continued on array 2 made of piezo-elements 81 to 160. All 3D renderings were generated using the Avizo rendering software (ThermoFisher®). To segment and measure the tumor and hypoxic core, the data was first 3D-Gaussian filtered (standard deviation $\sigma = 0.6$) and interpolated twice in each direction. The data was then normalized, and log-compressed and tissue attenuation was taken into account with an average tissue attenuation factor of 0.54 dB/MHz/cm. Attenuation was further corrected to aim for a uniform noise contrast value through depth of the image. The resulting volumes were filtered using a 3D Gaussian kernel with a standard deviation of $\sigma = 50$, and an isotropic size of 21 pixels was added pre binarization to yield better results. Then, a 2D binarized image is created by calculating global image threshold using Otsu's method controlled by a threshold luminance value set for each of the directions and each of the mice. The open volume result was then closed and measured using the regionprops function in Matlab (The Mathworks Inc, Natick, MA, USA). Tumor and necrotic core volumes were estimated three times out of each 3D NSSM scan. Two estimates were calculated out of sound sheet micro-scanning in the X and Y direction respectively. After compounding volumetric data in the X and Y direction, we estimated tumor and necrotic core volumes a third time by detecting contours of gene expression digitally in the Z direction. With this approach, we calculated an average value for the volume of the tumor and hypoxic core presented in Fig. 5.3D.

Ultrasound Doppler imaging:

The RCA probe was used to image the vascular function of a rat brain (Sprague Dawley, female, 280g). All experiments were performed under CCD license number AVD8010020209725 at the Koninklijke Nederlandse Akademie van Wetenschappen with Study Dossier number 213601. Immediately after isoflurane induction, carprofen, and butorphanol were delivered subcutaneously. The animal was prepared (shaved, disinfected, placed in earbars) and surgery began no sooner than 20 minutes after injections. A catheter was placed in the tail vein. Heparin was injected to prevent blood clots forming in the catheter. 14x14 mm craniotomies were performed. Carprofen and butorphanol were delivered subcutaneously during surgery (respectively 5mg/kg and 2mg/kg). To prevent cerebral edema, dexamethasone was given subcutaneously with a dosage of 2.5mg/kg.

After craniotomy, the RCA probe was positioned over the cranial window of anesthetized animal. Sound-sheet were transmitted with an 18° angle and 38 elements were used for each half apertures. The transmitted pulses were 2-cycle sine-bursts centered at 15.6 MHz. For Fig. 5.4C, 2100 frames were acquired with a frame rate of 4400Hz. For Fig. 5.4D, 2100 frames were acquired with a frame rate of 300Hz, leading to a 7s long acquisition. For Fig. 5.4G and 4H, 2100 frames were acquired with a frame rate of 1700Hz, leading to a 1.24s long acquisition. The average heart rate throughout the experiment is 419 bpm, leading to a cardiac cycle of 143 ms which is short enough to be captured several times in our acquisition. In these experiments, 1.0×10^8 microbubbles (Micromarker® Fujifilm, Bracco) were injected in a bolus through a tail vein catheter.

The Structural Similarity Index Matrix is calculated as:

$$\mathrm{SSIM}(x,y)=\frac{(2\mu_x\mu_y+C_1)(2\sigma_{xy}+C_2)}{(\mu_x^2+\mu_y^2+C_1)(\sigma_x^2+\sigma_y^2+C_2)}$$

where μ_x, μ_y, σ_x, σ_y, and σ_{xy} are the local means, standard deviations, and cross-covariance for images x, y , obtained from the intensity images after beamforming, and C_1, C_2 are regularization constants for luminance and contrast. The Structure Similarity Index Matrix in Fig. 5.4E is calculated from the 3 adjacent frames. Asterisk show statistical significance using t-test of two independent samples (P values are all inferior to 10^{-21}) (***$P < 0.001$, **** $P < 0.0001$).

For Fig. 5.4F-J, three pulses were transmitted at sound sheet position 1 with a time between pulses set at 89 μs. These pulses were next transmitted at sound sheet position 2. This sequence was repeated to acquire data for Doppler processing in two separate planes. A total of 2100 frames was acquired per sound sheet position with a frame rate of 1700Hz, leading to a 1.24s long acquisition. The average heart rate throughout the experiment was ranging from 300-360 bpm, leading to a cardiac cycle of 166-200 ms which is short enough to be covered in between 6-8 times during our acquisition. Here as well, 1.0×10^8 microbubbles (Micromarker® Fujifilm, Bracco) were injected in a bolus through a vein catheter.

Super-resolution ultrasound imaging:

For the ULM and NSSLM experiments, similar surgical procedure and ultrasound pulse sequences were used than in the previous section. Ultrasound acquisitions were performed at a 1 kHz in two sound-sheet planes, recordings were continuous and lasted 105 seconds. Radiofrequency data for NSSLM was first filtered using the xAM operation and frames were beamformed using a delay-and-sum algorithm. Two independent post-processing pipelines were used to generate state-of-the-art ULM images and NSSLM images (see Fig. S7).

For ULM, the 1-lag cross-correlation is computed from the beamformed images, and then an adaptive TGC is computed and applied. MB echoes were retrieved using an SVD filter with a cutoff of 2 singular values. Using a 3D FFT fan filter, the resulting data is filtered in the temporal frequency domain: a hard-cutoff is implemented to get rid of low-frequency components [198–201]. The data is then processed to detect microbubbles with respect to their intensity, and then a radial symmetry localization algorithm was applied, followed by Kuhn Munkres pairing for trajectory reconstruction [188].

For NSSLM, signal processing consisted in first filtering MB echoes with the amplitude modulation step of NSSM. Second, to increase the signal-to-noise ratio and compensate for attenuation, the 1-lag cross-correlation of the AM signal was computed and the signal was further adjusted using an adaptive time gain compensation function. To remove residual nonlinear tissue signals, a singular value decomposition clutter filter was applied with a cutoff of 1 singular value. Finally, a 3D-FFT fan filter was implemented in the spatio-temporal frequency domain, and the signal was decomposed in the following velocity bands: [0-3] mm/s, [3-15] mm/s, [15-25] mm/s, [25-60] mm/s and [60-150] mm/s [198–201]. The imaging dataset was transformed back to the spatiotemporal domain, and MBs were localized using the radial symmetry algorithm [187]. Individual MBs were paired with the Kuhn-Munkres assignment to retrieve MB trajectories. For the composite rendering of NSSLM, two colorscales are applied based on different velocity domains.

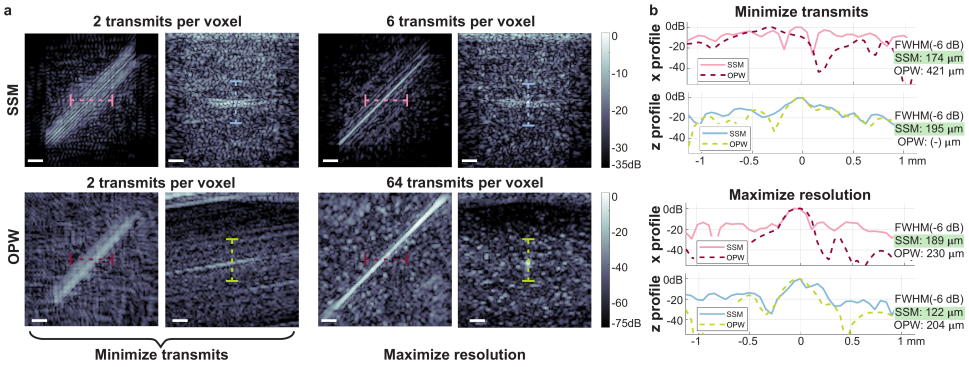

Figure S1 – Experimental SSM and Orthogonal Plane Wave (OPW) linear imaging of a wire phantom. a) Experimental SSM and Orthogonal Plane Wave (OPW) linear imaging of a wire phantom. The first 2 columns are obtained by transmitting on each of the row and column array once (one single transmit per array). The top left image displays a C-scan obtained from multiple sound sheet micro scanning of the volume in both directions while the right panel displays the result on a single sound sheet. Images in the third and fourth column are obtained with three compounded angles for SSM and 2x32 angles for OPW and show C-scan and a single compounded sound sheet. b) Intensity profiles are plotted the SSM and OPW linear images with the color code indicated on overlay in the h panel.

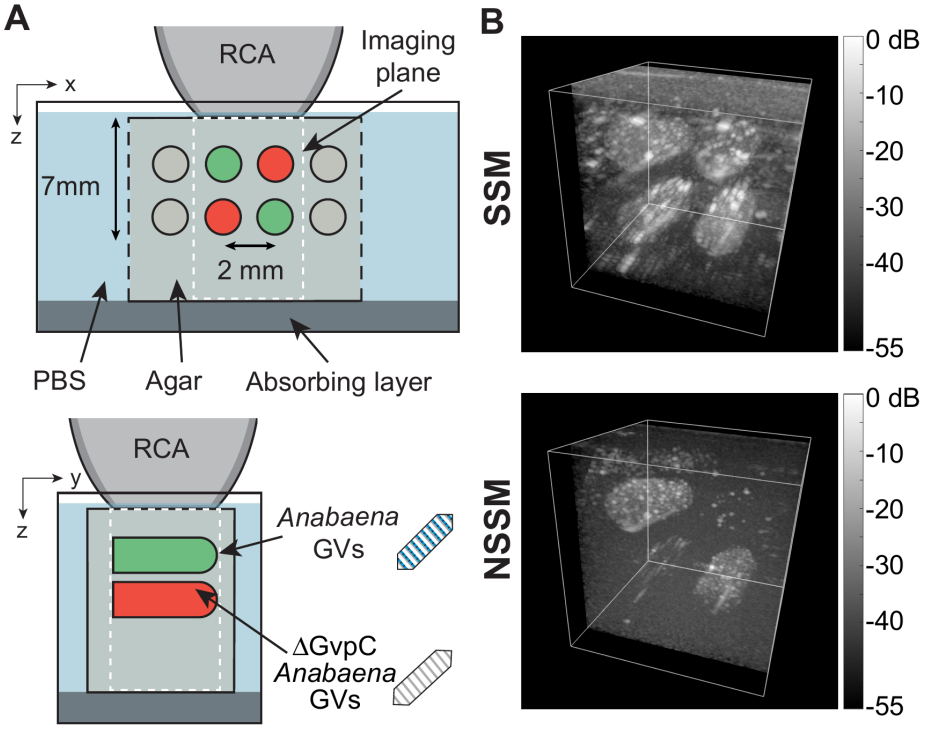

Figure S2 – Imaging of wild type Anabaena and stripped Anabaena GVs. a) Schematic of the phantom configuration. An agar phantom (gray) immerged in phosphate buffered saline (PBS) contains wells filled with agar and linearly scattering Anabaena flos aquae gas vesicles and nonlinearly scattering Anabaena flos aquae gas vesicles stripped from the accessory protein GvpC. Top, cross-sectional view of the GV wells. Bottom, long axis view of the GV wells. b) 8.8x8.8x10mm^{3}volumes obtained from SSM (top) and NSSM (bottom) single direction micro scanning sequences (108 sound sheet positions). SSM clearly picks up increased signal in the wells compared to the surrounding agar while NSSM extinguishes linear signal successfully to retain the wells containing GVs without GvpC.

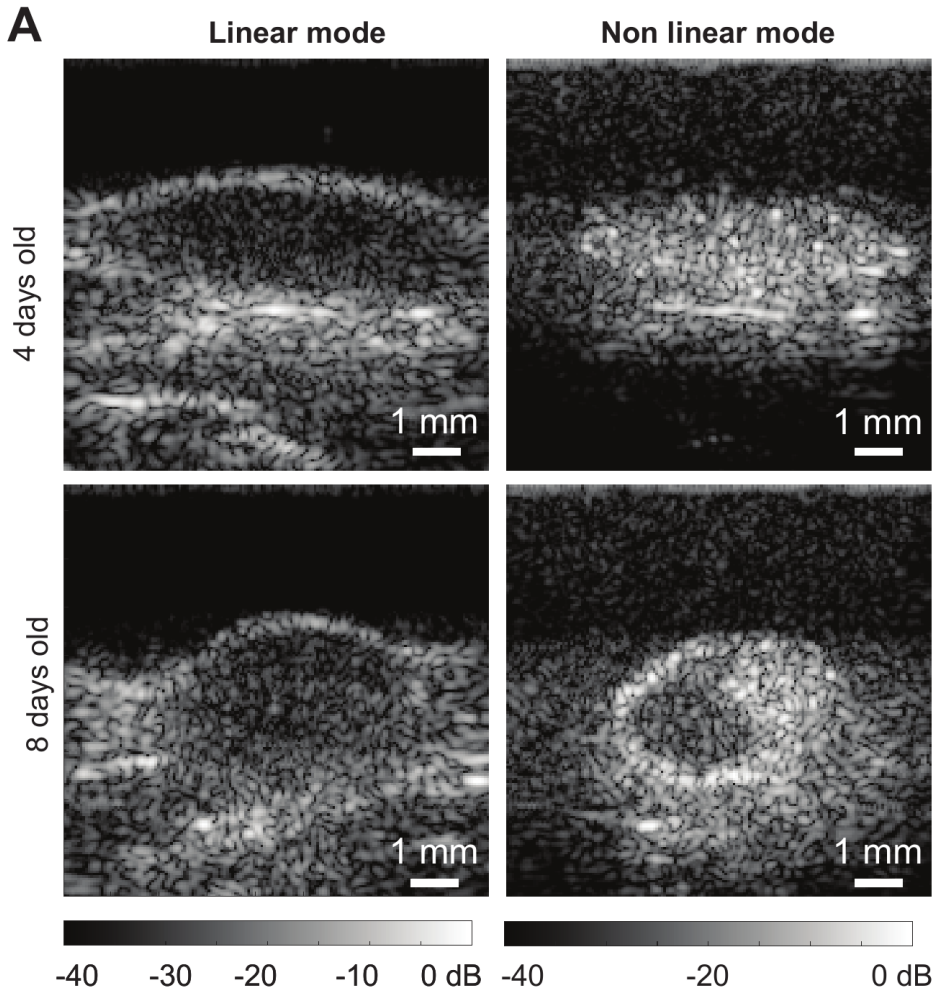

Figure S3 – Imaging of mARG-expression in tumors. a) Left, SSM images of 4- and 8-days old tumors. Right, NSSM images revealing mARG expression in tumors. All images are displayed with a 40 dB dynamic range and the same color scale.

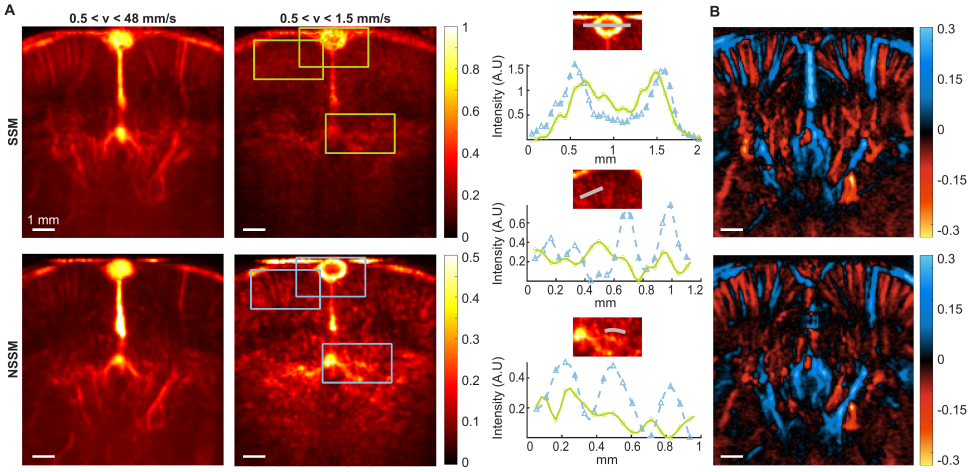

Figure S4 – Doppler NSSM of perfused craniotomized rat brains. a) Frequency filtering of sound sheet Doppler frames for linear and nonlinear imaging sequences. The linear and nonlinear imaging sequence are obtained respectively before and after injection of microbubbles with a matched incident pressure. The left column shows axial Doppler velocity obtained after 10th order Butterworth band-pass filter with cutoff frequencies corresponding to velocity range [0.5-48] mm/s while the right column is focused on the range [0.5-1.5] mm/s pertaining to capillary flow. Scalebars are 1 mm. For the capillary flow, intensity profiles are taken at specific locations indicated by gray lines in the zoomed-in inserts on the right. The profiles in green and blue show intensities (in arbitrary units) taken respectively in the linear and nonlinear sequence. b) Signed axial Doppler velocity obtained from linear (top) and nonlinear sound sheet sequence. The positive velocities (indicated in blue) are taken as upwards velocity (towards the probe). In the cortical areas, this color code shows distinction between veins (blue) and arteries (red).

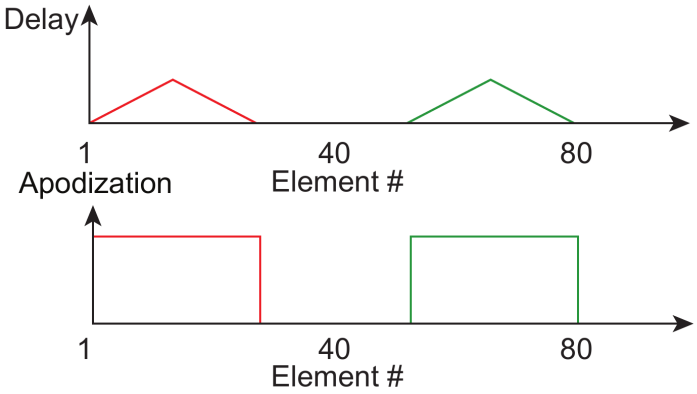

Figure S5 – Delays and apodizations used for high-speed multi-view Doppler NSSM. Ultrasound insonification scheme for multi slice NSSM in consecutive cardiac cycles. Two sound sheet positions can be arbitrarily set at positions as far as d=6 mm, with a theoretical pulse repetition frequency of 37 kHz that enables ultrafast Doppler imaging in two sound sheet planes, with a maximum framerate attainable of close to 4200 Hz. In this setup, we limit the framerate to 1700 Hz. The delays and apodization of each sound sheet are represented for an angle of 18 degrees. For the NSSI mode, the 3 pulses necessary for amplitude modulation are fired for one sound sheet, and then the 3 pulses for the next sound sheet are fired. This sequence is then looped over the number of frames.

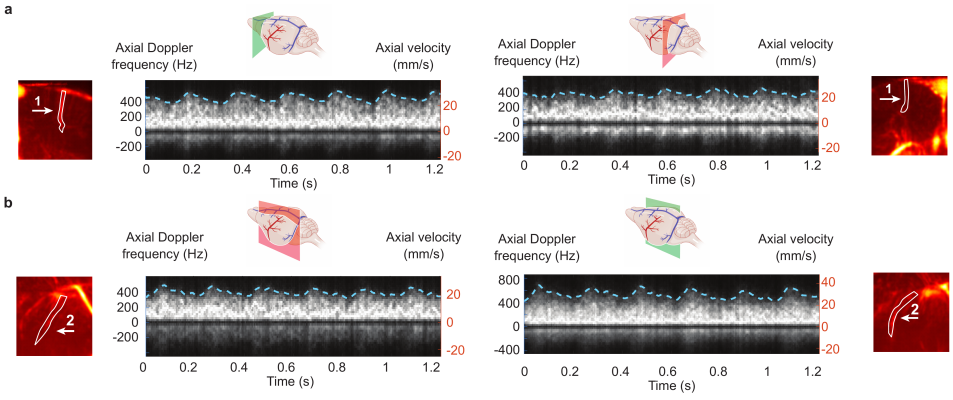

Figure S6 – High-speed multi-view NSSM spectrograms of the rat brain vasculature. a) Doppler spectrum revealing peak cerebral blood flow and pulsatility of a cortical arteriole of the right hemisphere in the first (green) and second (red) plane. b) Doppler spectrum revealing peak cerebral blood flow and pulsatility of a sub-cortical vessel of the left (red) and right (green) hemisphere.

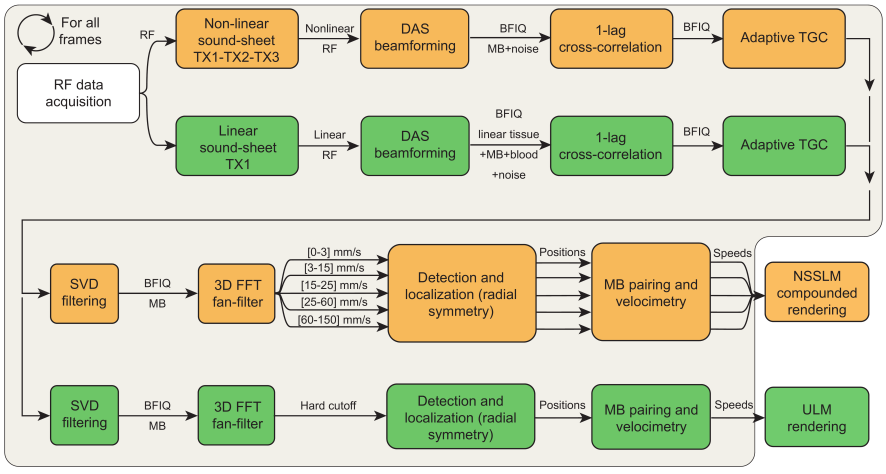

Figure S7 – Schematic of the ULM and NSSLM processing pipelines.

6

Discussion

6.1 Research overview

In this thesis the two main objectives were to (1) improve transcranial image quality to enable noninvasive brain imaging, and (2) to develop reconfigurable functional ultrasound imaging to reduce data rates in volumetric fUS.

The first challenge tackled was enabling noninvasive, transcranial brain imaging. Although transcranial fUS is currently routinely performed in young mice, fUS in older mice and species with thicker skulls relies on cranial windows to prevent image degradation due to skull induced aberrations. This limits the applicability for neuroscience research, and poses a barrier for the use of fUS in clinical setting. Developing a fully noninvasive transcranial fUS method would significantly enhance the clinical value of this neuroimaging technique. To improve image quality behind the skull, we developed an adaptive aberration correction method based on ray tracing through a four-layer tissue model. This model accounts for the following media that support wave propagation during a transcranial ultrasound imaging session: the transducer lens, gel and skin, skull, and brain. The method allows accurate estimation of wave speed in each layer, and use that in ray-tracing based aberration correction image reconstruction.

When applying this method to transcranial imaging, a first challenge appeared in defining the first lens layer: What are the wave speed and thickness of the transducer lens? These are critical inputs to the aberration correction model, since inaccurate values introduce error propagation. However, these values are rarely communicated by transducer manufacturers. To address this, we developed a method that estimates transducer lens parameters by analysis of internal reflections within the lens. Compared to existing techniques, our method is simple, non-destructive, and can be implemented across the medical ultrasound frequency range.

Originally, this characterization was intended solely as a prerequisite for aberration correction. However, it became clear that accurately knowing the transducer properties, combined with a two-layer ray tracing model (lens and tissue), enables accurate estimation

of the speed of sound in the imaging medium. Using the accurate wave speed of the medium and the characterized transducer parameters, two-layer ray tracing image reconstruction improved image resolution and contrast. This finding raises concerns for the field of quantitative speed of sound imaging and the use of speed of sound as biomarker, as our results show that speed of sound estimation is highly dependent on imaging depth when the transducer parameters are inaccurate. Our method does allow accurate speed estimation that is depth, scanner, and transducer independent.

Having developed a robust method to characterize transducer lens parameters, we proceeded with the problem of transcranial ultrasound imaging. In chapter 3, we applied the ray-tracing based aberration correction method to transcranial imaging of the rat brain. We demonstrated that we could correct skull-induced aberrations and enhance Doppler lateral resolution. The improvements were particularly significant in the cortex, since aberrations are the strongest close to the aberrating layer. These advancements lay the groundwork for noninvasive transcranial fUS.

In chapter 4, we shifted focus to address the challenge of high data rates in volumetric functional imaging, but rather, imaging of the most informative 2D plane within a 3D volume. Volumetric fUS inherently generates massive data streams, making real-time processing difficult. However, not all functional applications require imaging the full 3D brain volume. Given that brain activity is often sparse, we developed a method for selective-plane fUS, allowing to image only the regions of interest using focused transmits. This approach reduces the acquisition data rate by an order of magnitude (26x) compared to the volumetric imaging mode of the RCA, orthogonal plane wave compounding. Selective plane fUS significantly lowers memory bandwidth and computational demands, and this efficiency is expected to be especially valuable for a small footprint ultrasound based closed-loop brain-machine interfaces (BMIs), where the goal is to decode brain activity and translate it into actions in real time.

In chapter 5 we introduced Nonlinear Sound-sheet Microscopy (NSSM), a molecular ultrasound imaging technique that allows to reveal capillaries and cells in living organs. NSSM confines the detection of nonlinearly scattering ultrasound contrast agents to thin 2D planes in living tissues. Compared to the state of the art to image 3D cellular activity, light-sheet fluorescence microscopy, NSSM overcomes limitations inherent to optics such as light scattering and photobleaching. In mouse models of cancer, tumors expressing gas vesicles were imaged using NSSM, which enabled accurate assessment of tumor volume, excluding the necrotic core. NSSM also enabled to capture the first ultrasound maps of the capillary vasculature living rodent brains.

6.2 Transcranial aberration corrected brain imaging

6.2.1 Perspective for Functional Imaging

In chapter 3, we demonstrate aberration correction for Doppler vascular images. In addition to that, we also made an attempt to apply the aberration correction method to functional imaging, with visually evoked brain activity. We encountered several experimental challenges that limited the method's effectiveness.

A major challenge consisted in segmenting the skull bone in 2D ultrasound images. For clear delineation, specular reflection at the outer and inner skull surfaces is necessary, which requires the ultrasound beam to be perpendicular to the bone surfaces. Perpendicular alignment to the surfaces demands accurate positioning of the ultrasound transducer. In practice, this proved to be challenging, since a small deviation in the elevation angle of the transducer resulted in the loss of specular reflection and illumination of a different plane. After finding a transducer position that showed specular reflection, another challenge arised in comparing the power Doppler brain image with previous published coronal planes that showed functional activations. Due the angled transducer orientation, the acquired power Doppler planes were not aligned with the typically reported coronal cross-sections. Additionally, the presence of skull-induced aberrations degraded image quality, making it challenging to align the angled Doppler planes with atlas-based brain regions. As a result, accurately locating the visual brain regions proved difficult, and many acquisitions failed to capture the relevant functional regions.

Despite these challenges, we successfully acquired a few functional recordings that showed activation in the Superior Colliculus and Lateral Geniculate Nucleus, both located approximately 5 mm below the skull. After 4-layer aberration correction, we observed correlation maps that were highly comparable to thos obtained with performing a lens correction. At the depth of the SC and LGN, the method did not significantly enhance functional correlation. This can be explained by the conclusions of chapter 3, were we reported that the performance of the four-layer aberration correction method converged to that of the two-layer model with increasing depth.

Therefore, our recommendation is that the current aberration correction implementation primarily benefits functional experiments with cortical activations, where aberrations are more pronounced.

6.2.2 Remaining challenges and potential improvements

Signal attenuation

Despite the advancements made with our method, several challenges remain, particularly related to acoustic attenuation when imaging through the skull. One of the fundamental limitations is that our current approach does not address the skull attenuation problem. The skull is not uniformly thick, and in some regions, the increased thickness and the presence of trabecular bone reduces signal penetration. This makes it difficult to visualize deeper brain structures, or penetrate some skull sections in general.

A straightforward approach would be to increase the transducer's output pressure. However, the amplitude of the emitted waveform is often constrained by the electronic circuitry, the design of the probe, or safety limits such as the mechanical index. Several methods exist to improve transcranial SNR without increasing the mechanical index or sacrificing frame rate, such as multiplane wave imaging [202] and coded excitations [203]. Another option is to lower the ultrasound frequency, as lower frequencies experience less attenuation through bone. However, this comes at the cost of reduced sensitivity to red blood cells, since red blood cell scattering scales with the fourth power of frequency [166]. Furthermore, the image resolution is lower at lower frequencies, which is problematic for

accurate skull deleniation. As a result, while lowering the frequency can enhance SNR, it may compromise sensitivity in functional imaging and our capacity to segment the skull.

A hybrid aberration correction method

Our current ray-tracing-based aberration correction primarily addresses global aberrations, those arising from the overall shape and acoustic impedance mismatch between the skull and soft tissue. However, it is less effective at correcting local aberrations caused by small-scale inhomogeneities within the tissue layers. Near field phase screen aberration correction methods are better suited at correcting these local aberrations, but they often perform poorly in the presence of strong aberrations [74].

An idea is to combine ray-tracing based and near field phase screen based methods into a hybrid approach, by first applying a ray-tracing-based correction to handle global distortions, followed by a phase screen method to fine-tune local aberrations. This combination could also compensate for speed of sound and segmentation errors, potentially leading to more accurate image reconstruction.

However, phase screen-based methods come with their own limitations, particularly in the absence of bright reflectors. In brain imaging, the speckle from the brain is often weak, and determining the aberration solely by incoherent red blood cells is challenging. To overcome this, one could use contrast agents to temporarily introduce clear targets to learn the aberration law. After that, the contrast agent can wash out before performing functional imaging experiments.

3D: The ultimate solution?

To overcome the limitations associated with specular reflection and to make image acquisition operator-independent, the next step would be to extend the aberration correction method to 3D using a 2D matrix array. In 3D imaging, the requirement for precise probe positioning to acquire specular reflections is virtually eliminated. However, current 2D matrix arrays typically have lower sensitivity due to smaller element piezoelectric sizes. On the other hand, image quality is reduced compared to 1D arrays since current 2D matrix arrays have a relatively small aperture and piezoelectric elements several times the wavelength due to frabrication limitations. Luckily, the next generation of transducers offers a way forward. Capacitive Micromachined Ultrasonic Transducers (CMUT) based 2D matrix arrays are emerging as a promising alternative, offering finer element pitch, broader bandwidth, and easier integration with micro electronics on chip [204–206]. Their fabrication via standard semiconductor processes allows for higher element density and custom geometries, potentially addressing the sensitivity and resolution limitations of traditional piezoelectric matrix arrays. Furthermore, the wide bandwidth makes them excellent candidates for coded excitation sequences. Potentially, all suggestions so far, combining ray tracing and near field phase screen methods, coded exciations and CMUTs are needed to facilitate functional imaging through the adult rat skull.

Currently, the computation cost of our aberration correction method is significantly higher than conventional DAS reconstruction. Computation of the refracted time of flights takes an order of magnitude longer than in conventional DAS. Unfortunately, the algorithm

cannot be simply ported to GPU, since two point ray tracing relies on minimization of the time of flight through the medium. The number of iterations in the minimization varies per ray, and therefore the algorithm cannot be trivially parallelized on the GPU. GPUs are designed for highly parallel tasks with predictable execution patterns, while iterative minimization with varying convergence rates leads to thread divergence and inefficient use of GPU resources.

To extend the ray-tracing aberration correction method to 3D, an efficient GPU implementation is needed. Here, we can benefit from recent advances in computer graphics. The latest generation of GPUs have introduced dedicated ray tracing cores, which are designed to efficiently handle ray traversal and computation of intersection of rays with the geometry in a scene [207]. This hardware acceleration has enabled real-time ray tracing in computer graphics, allowing for realistic lighting, shadows, and reflections in games without sacrificing frame rates. On top of hardware-accelerated ray traversal, libraries like NVIDIA OptiX [208, 209] use advanced scheduling techniques to avoid inefficient use of GPU resources. This advanced scheduler is especially useful for the ray tracing aberration correction method, since the number of iterations in the minimization varies per ray. By leveraging this specialized hardware for ray tracing based aberration correction, we can significantly reduce the computational burden and potentially achieve real-time 3D aberration correction. Real-time 3D aberration correction isn't strictly necessary in preclinical studies [1]. However, it becomes essential when moving toward clinical applications

Transcranial biomolecular imaging

A limitation of our NSSM study in chapter 5 is that brain imaging was conducted in craniotomized animals. While NSSM is expected to be compatible with acoustically transparent chronic windows, its transcranial capabilities have not yet been explored. Unfortunately, combining aberration correction with NSSM and a row-column addressed (RCA) array is not straightforward. The elongated geometry of RCA elements limits the ability to synthetically refocus the beam, which is essential for aberration correction.

To enable aberration-corrected transcranial biomolecular imaging, we must transition from an RCA to a 2D matrix array. This configuration allows us to learn the aberration law from imaging data and then shape the transmit wavefront to form cross-propagating plane waves behind the skull. In receive, we can apply aberration correction as well, enabling fully aberration-corrected transmit and receive NSSM. When applying this approach to rodents, a scanner with high resolution clock is essential, as the time shifts induced by the skull are relatively small. Although this might remain challenging due to the current limitations of 2D matrix array fabrication, the method developed in chapter 3 is directly applicable to 2D xAM [172, 182].

6.2.3 Predicting the effect of aberration

Choosing the most suitable aberration correction method, and estimating its potential impact on ultrasound image quality can be quite challenging. This is especially true when working with a new animal model or imaging through a different section of the skull. While it is clear that aberration is present, deciding which correction strategy to apply is not

[1] Although helpful for the impatient researcher.

straightforward. Testing all published methods is often impractical due to the significant time investment required for implementation and validation of all methods, due to the lack of open source implementations and test data.

Furthermore, it is often challenging to simulate aberration with tools like k-Wave or Simsonic. If you want to simulate a medium with high speed of sound differences, especially at the fUS frequency range, you quickly fall prey to convergence studies to find the right grid size to avoid effects like numerical dispersion. Simulation times are typically long, further raising the bar for a quick assessment of the effect of aberration.

To make a more informed decision on whether to apply aberration correction, without the need for long simulations and convergence studies, I have developed a simulator that allows others to predict the effect of aberration on image quality. The simulator allows to define a transducer at a specific frequency, model arbitrary shaped tissue layers, and predict the aberrated wavefront for a single scatterer in the medium.

By defining the speed of sounds of the tissue layers, and using the multi layer ray tracer, one can find the aberrated return trip time of flight for a point source and scatterer location. The ray tracer computes the path length through each layer, and incident angles of at every interface. By defining an attenuation coefficient for each layer, and multiplying this with the path length, the attenuation of the signal can be estimated. Adding densities allows to compute the acoustic impedance of each layer, and with the incident and refracted angles θ_i and θ_t, the transmission factors can be computed using [210],

$$TF = \frac{2Z_2 \cos\theta_i}{Z_2 \cos\theta_i + Z_1 \cos\theta_t}. \tag{6.1}$$

Finally, taking account element directivity [122],

$$D(\theta) = \cos\theta \ \mathrm{sinc}\left(\pi \frac{W}{\lambda} \sin\theta\right), \tag{6.2}$$

with W the width of the transducer element, and λ the wavelength in the medium, you can compute the intensity of the received signal for each transducer element.

Taking all these factors into account, you can generate the aberrated RF signal for a single scatterer in the medium. This RF can be reconstructed with conventional DAS reconstruction, and the ray tracing beamformer, to compare the effect of the aberrations on the PSF. Using this, you can vary parameters as bone layer thickness, shape, speed of sound, and test across the medical ultrasound frequency range how these parameters affect the PSF. Ultimately, such a simulator can be used as a quick assessment whether it is worth to apply aberration correction, guide the choice of aberration correction method, and as a didactic tool. The simulator is available on GitHub: .

Testing with published scenarios

To check if the results of the simulator are in line with the literature, I have compared the results with a few published scenarios.

- Mozaffarzadeh *et al.* [75] used a ray tracing beamformer to correct for aberrations through the temporal bone of an *ex vivo* human skull. The temporal bone was 1.3

mm thick, and a wire phantom at a depth of 40 mm was imaged with a P4-1 at 2.5 MHz. The speed of sound in the bone was estimated as 3500 m/s using a head wave method. The authors reported a lateral resolution improvement of 37% using the aberration correction method. Implementing this scenario in the simulator, I found a resolution improvement of 30%.

- Similarly, Zhou *et al.* [82] did a phantom study with a complex shaped aberrating layer with a sound speed of 2400 m/s and a thickness of approximately 3 mm. The authors reported a lateral resolution improvement of 29% using the aberration correction method. The simulator predicts a resolution improvement of 33%.
- Comparing to the results of the transcranial rat chapter 3, we reported a resolution improvement in the cortex of 32%. Using the segmentation of the rat skull, and the estimated wave speed per layer, the simulator predicts a resolution improvement of 33% on the squared PSF (to compare power Doppler and B-mode resolutions).

Further validation is needed as this method has not been peer-reviewed and deserves further investigations.

Limitations of the simulator

In the simulator, transmission factors were determined assuming fluid-fluid interfaces. However, fluid-solid interfaces have more complex reflection and transmission factors, accounting for mode conversion from longitudinal to shear waves and vice versa [211]. Therefore, transmission factors are overestimated. Furthermore, the simulator does not model aberrations due to inhomogeneities within each layer. Therefore, attenuation due to multiple scattering is not included. Furthermore, the effect of aberrations due to local speed of sound inhomogeneities on the time of flight is not included. Potentially, this could be added by using an Eikonal solver to compute the aberrated travel times in the medium. This allows studying the magnitude of local versus global aberrations, for a wide range of applications such as transcranial or abdominal imaging.

Currently, the model assumes perfect segmentation and speed of sound estimation, which may not ne achievable in practice. However, the simulator provides a valuable opportunity to evaluate the impact of segmentation and speed of sound errors, allowing for quick sensitivity studies to identify which errors most significantly affect aberration correction performance.

6.3 Outlook

Functional ultrasound (fUS) is uniquely positioned to bridge the translational gap between preclinical cellular measurements and clinical neuroscience. It enables high-resolution studies in awake rodents and holds promise for noninvasive, transcranial imaging in humans. The following sections explore what the future of fUS may look like.

6.3.1 Bridging Cellular and Systems Neuroscience with fUS

Functional ultrasound imaging (fUS) is uniquely positioned to fill a longstanding gap in translational neuroscience: connecting cellular-level techniques performed in animal models with the whole brain hemodynamic insights from human fMRI. Until recently, there was no practical hemodynamic imaging modality for awake, behaving rodents. Conducting awake behavioral experiments in small animal using fMRI is very challenging due to problems with voluntary motion, and the MRI scanner noise induced stress in the animals. This makes fMRI unsuitable for naturalistic behavioral studies in small animals. fUS overcomes these barriers by enabling high-resolution, whole brain imaging of brain hemodynamics in awake rodents, under conditions compatible with complex behavior and physiological monitoring. This creates the possibility for labs using cellular-resolution techniques such as two-photon imaging, optogenetics, or calcium indicators to add fUS to their experiments. fUS is compatible with most cellular imaging modes, allowing a simultaneous readout of the cellular and brain hemodynamics.

This allows linking small animal findings directly to hemodynamic signatures seen in human fMRI. Conversely, human neuroscience research groups aiming to link their fMRI observations to cellular mechanisms can now adopt fUS in rodents as a scalable intermediate step. To fully leverage this translational potential, fUS platforms must support a diverse range of sensory and behavioral paradigms. This includes modular architectures that allow for customizable imaging protocols, probe upgrades (e.g., from 1D to RCA to 2D arrays), and integration with emerging non-linear biomolecular ultrasound modes. As the field moves toward cross-scale, cross-species understanding of brain function, fUS stands out as a vital tool to bridge the gap between neurons and networks, rodents and humans.

6.3.2 Towards Transcranial Human fUS

One of the most challenging goals of functional ultrasound (fUS) is to enable transcranial neuroimaging of the human brain. If fUS can reach a whole brain field of view at a spatial resolution on the order of 1-2 mm and a temporal resolution around 1 second, fUS can offer several compelling advantages compared to fMRI that could significantly accelerate neuroscientific research.

Most notably, fUS is portable, and thereby eliminates the need for subjects to remain supine and (head) motionless during fMRI scans. This makes it possible to perform experiments in more naturalistic, interactive, or mobile settings. This can expand the scope of behavioral neuroscience studies, enabling experiments that involve social interaction and sensorimotor engagement. In addition, fUS systems are quieter and less restrictive than MRI, reducing sensory and psychological confounds that can influence task performance. From a practical standpoint, fUS also offers lower operational costs, which increases accessibility

for research. Altogether, if transcranial fUS achieves robust, high-resolution transcranial imaging, it could become a transformative tool for bridging laboratory neuroscience with real-world cognitive and behavioral research.

There are several natural acoustic windows through which ultrasound can access the brain, and these are already used in clinical Transcranial Doppler (TCD) ultrasound imaging. Four acoustic windows have been described: (1) the transtemporal window, (2) the transorbital window, (3) the submandibular window, and (4) the suboccipital window [212]. These anatomical pathways provide relatively thin or accessible bone regions that allow ultrasound penetration into different parts of the brain. Clinically, these windows enable TCD to measure blood flow, and diagnose or monitor a wide range of cerebrovascular diseases.

To improve transcranial vascular image sensitivity, researchers have explored the use of multiple transducers positioned at various acoustic windows to estimate skull-induced aberrations and perform adaptive focusing [213]. Furthermore, the images from multiple windows can be fused to reconstruct a composite 3D image of the brain, revealing the geometry and flow patterns of major cerebral arteries [214, 215]. Despite these advances, TCD remains highly dependent on the quality of the acoustic windows, which is not adequate in a significant portion of the population. To access the brain in patients with poor acoustic windows, the transmit frequency often needs to be lowered to 1 MHz or below, which further compromises image resolution [216].

Current TCD approaches rely on pulse-echo imaging, which is inherently diffraction-limited. At 1 MHz, even assuming optimal aberration correction, the spatial resolution remains constrained by the diffraction limit of half the wavelength in the brain (approximately 0.75 mm). To image the brain from arbitrary positions on the scalp, allowing full brain coverage without relying on natural acoustic windows, transmit frequencies would have to be lowered even further. Moreover, lower frequencies reduce the sensitivity to small scatterers like red blood cells, making it especially challenging to capture microvascular information from arterioles, venules, and capillaries which are key targets in functional ultrasound [166, 217].

Despite these challenges, there is reason for optimism. Transducer technology has improved significantly over the last decade, especially in terms of receive sensitivity. This is clearly reflected in the dramatic improvements in power Doppler sensitivity in (uncorrected) transcranial rat imaging, as seen in the work of [113] and our work described in chapter 3. Furthermore, developments in CMUT technology allow larger bandwidth, higher sensitivity, and larger aperture ultrasound transducers [205, 206, 218]. Besides transducer technology, also innovation in reconstruction methods offer several opportunities towards transcranial human fUS.

A particularly promising technique for ultrasound neuroimaging is full waveform inversion (FWI), an advanced imaging method originally developed for geophysics. FWI has been adopted by the petroleum industry, where it is used to reconstruct detailed images of fossil fuel reservoirs deep within the Earth. Unlike traditional pulse-echo ultrasound, FWI solves the full wave equation to model how ultrasound waves propagate through heterogeneous media. This more complete physical modeling allows for the recovery of

fine grained acoustic property maps, such as variations in the speed of sound, even when using relatively low frequency transmissions [219]. In biomedical imaging, this technique has already shown strong potential in the detection and characterization of breast cancer [220–222] and brain tumors [219, 223, 224].

One promising concept for applying full waveform inversion (FWI) to brain imaging involves mounting a helmet fitted with a large number of ultrasound transducers around the head, effectively creating a wide aperture, low frequency imaging array [219]. By operating at low frequencies, the system can achieve sufficient penetration through the adult skull, mitigating one of the core limitations of transcranial ultrasound. While current applications are focused on anatomical imaging, the potential of this approach has already been demonstrated in simulation. Using a 1024 element transducer helmet, Guasch *et al.* [219] reconstructed high-resolution transcranial speed of sound maps from a two second long stimulated acquisition with source waveforms with a frequency range of 100-850 kHz. Initial simulations have shown that FWI can detect intracranial hemorrhages, highlighting its clinical potential in stroke diagnosis.

To transition FWI from anatomical to functional brain imaging, several key challenges must be addressed. The first limitation is the computational cost of the inversion process, which is several orders of magnitude higher than that of conventional pulse-echo imaging. Current reconstructions can take up to 32 hours on high performance computing clusters [219], rendering real time imaging infeasible. However, significant acceleration may be achieved through algorithmic advances and hardware improvements. For instance, ongoing developments in GPU based computing are already showing promise, and quantum computing is expected to revolutionize the field in the longer term with early demonstrations of quantum accelerated FWI emerging in geophysics [225]. However, reconstruction time is not the main bottleneck, since these could be carried out offline.

The main bottleneck is that current acquisition times remain too long for capturing dynamic brain activity. The simulation by Guasch *et al.* [219] required a two seconds acquisition time to acquire 1024 sources, limiting the frame rate to 0.5 Hz. A possible strategy would be to perform an initial long acquisition to learn a detailed model of the skull and brain anatomy, followed by faster acquisition schemes to monitor functional changes. One such approach is source encoding, in which multiple transmit events are combined into a single acquisition by encoding them with unique patterns, significantly reducing scan time [226]. Another strategy is to shape the transmitted field to focus energy on specific regions of interest in the brain, allowing for the detection of localized, time-varying changes in blood flow.

It remains an open question whether FWI will ultimately be capable of capturing hemodynamic signals for functional brain imaging, particularly given the low ultrasound frequencies typically used, which limit sensitivity to red blood cells. However, recent findings from functional Magnetic Resonance Elastography (fMRE) suggest that there exists an alternative contrast mechanism for functional imaging, not based on blood flow, but on a neuromechanical coupling [227]. Emerging evidence indicates that neuronal activity can induce measurable changes in the mechanical properties of brain tissue, such as its shear modulus.

In a pioneering study, Patz *et al.* [227] used fMRE to detect changes in brain stiffness associated with rapid neuronal activity in rodents. During repetitive electrical stimulation at frequencies up to 10 Hz, they observed local changes in the tissue's shear modulus of approximately 10% occurring on time scales as short as 100 ms. These findings provide compelling evidence of a biomechanical response to neuronal firing. More recent studies in humans have extended this line of work, reporting elasticity changes of up to 30% during cognitive task performance compared to resting baseline [228]. If this biomechanical coupling can be leveraged in functional ultrasound imaging, it could offer a significantly faster readout of neuronal activity compared to hemodynamic based methods, which are inherently limited by the delays introduced by neurovascular coupling.

If the shear modulus of brain tissue is indeed modulated by neuronal activity, this could open up a new avenue for FWI-based functional brain imaging. Under the assumption of a linear, isotropic elastic model with constant tissue density, a 10% change in shear modulus corresponds to an approximate 5% change in the speed of sound within the tissue [227]. Given that the average speed of sound in brain tissue is around 1540 m/s [229], such a modulation would result in local sound speed changes of up to 75 m/s. Notably, this magnitude is comparable to the speed of sound contrasts observed in breast tumor detection using FWI and speed of sound imaging [103, 220–222, 230].

These findings suggest that neuromechanically induced elasticity changes, if reliably detectable, could serve as a novel functional contrast in the brain. Since FWI is sensitive to small spatial variations in acoustic properties, particularly speed of sound, it potentially is well suited to capture these biomechanical changes indicating neural activity. This opens the possibility of a new class of functional neuroimaging techniques based on the biomechanics of brain tissue, providing a complementary, potentially faster, alternative to hemodynamic-based methods like fMRI and Doppler fUS.

7

Conclusion

In this thesis, the two main objectives were to (1) improve transcranial image quality to enable noninvasive brain imaging, and (2) to develop reconfigurable functional ultrasound imaging to reduce data rates in volumetric fUS. The chapters progress from fundamental ultrasound system calibration, through improved brain image quality through the skull in preclinical models, to reconfigurable ultrasound for functional and cellular imaging. Each chapter contributes to the broader goal of making ultrasound a more accurate, versatile, and scalable tool for imaging dynamic biological processes.

Ultrasound transducers have a silicone rubber lens to focus the ultrasound beam in the elevation direction. The influence of the transducer lens on image reconstruction is often overlooked. Lenses usually exhibit a lower sound speed than soft biological tissues. In academic research, the exact lens sound speed and thickness are typically unknown. In chapter 2, we described a simple, nondestructive method to estimate the transducer lens thickness, the transducer lens sound speed and the time to peak of the backscattered ultrasound pulse. We demonstrated that the combination of calibrated transducer parameters with a two-layer ray tracing reconstruction approach enables accurate sound speed estimation, and improves ultrasound image resolution and contrast up to a depth of 100 wavelengths, across the medical ultrasound frequency range.

The development of fully noninvasive, transcranial functional ultrasound (fUS) would increase the translatability and clinical potential of this neuroimaging modality. Unfortunately, transcranial fUS is hindered by skull-induced aberrations which degrade power Doppler image quality and lower sensitivity. As a result, a majority of fUS imaging studies rely on craniotomies or acoustically transparent cranial windows. In chapter 3, we developed an adaptive aberration correction method using 4-layer ray-tracing that improves image quality and spatial specificity in transcranial ultrasound Doppler imaging of the adult rat brain. The method adapts to each subject and each brain section being imaged without requiring prior information from other imaging modalities like a CT or MRI scan. The method successfully segments the transducer lens, gel & skin, skull and brain tissue layers, and estimated ultrasound wave speeds in each layer. Once a velocity model of

the imaging plane of interest is retrieved, aberration corrected ultrafast power Doppler imaging of the brain was performed. The largest improvements in Doppler imaging quality were observed in cortical brain layers adjacent to the skull, where specifically lateral resolution was improved by 32%. Our method consistently outperformed Doppler imaging based on traditional delay-and-sum (DAS) beamforming, which assumes a uniform sound speed, and holds promise for functional imaging applications that require high spatial sensitivity.

Recent advances have shown that fUS is a viable technology for brain-machine interfaces (BMIs) in both non-human primates and humans. However, 2D fUS is restricted to a plane, and potentially misses relevant information occurring out of the imaging plane. 3D fUS can potentially address this limitation but presents significant challenges in terms of data bandwidth and computational demands. In chapter 4, we introduce selective-plane fUS, a reconfigurable ultrasound neuroimaging method. By efficiently sampling targeted brain sections with focused waves, our approach significantly reduces data bandwidth and computational demands while maintaining a spatial resolution comparable to 2D fUS. Using selective-plane fUS, we successfully revealed activations in the superior colliculus in response to visual stimulation, observed similar peak correlation to 3D fUS, and measured a reduced functional signal variability. Together, our findings make real-time, multi-region decoding of the brain possible, thereby addressing a pressing need for compact and human implantable fUS-BMI paradigms.

To date, ultrasound plays a relatively minor role in the field of molecular imaging, due to the lack of tools to monitor cellular and other molecular processes. In chapter 5, we introduce Nonlinear sound-sheet microscopy (NSSM), in which we use non-diffractive ultrasonic beams in conjunction with a cross-amplitude modulation sequence and nonlinear acoustic reporters to enable fast and volumetric imaging of biological function. We demonstrated the ability of NSSM to confine nonlinear scattering of genetically encoded GVs and synthetic lipid-shelled MBs to wavelength-thin opaque tissue sections. NSSM is an imaging method that can either be tuned for speed or coverage. In two dimensions and at an ultrasound frequency of 15 MHz, NSSM can scan 1 cm deep with a theoretical frame rate of 25.6 kHz. In three dimensions, NSSM can acquire 8.8 x 8.8 x 10 mm^3 volumes of tissue with a theoretical volume rate of 233 Hz. To use NSSM to the fullest, new generations of brighter acoustic reporter genes and faster biosensors will have to be developed. Additionally, the sensitivity of NSSM should be improved further to enable single-cell detection. If we are successful, NSSM will carry a wave of opportunities for dynamic imaging studies of biological processes across scales.

Together, these chapters lay the technical foundation for next-generation functional and biomolecular ultrasound: allowing more accurate, less invasive, and high resolution brain imaging in real time. By addressing both the physical challenges of wave distortion and the computational load of volumetric data, this thesis brings fUS a step closer to clinical and translational neuroscience applications.

Bibliography

[1] J. Confais, B. E. Kilavik, A. Ponce-Alvarez, and A. Riehle, *On the Anticipatory Precue Activity in Motor Cortex,* J. Neurosci. **32**, 15359 (2012).

[2] W. Mugge, J. Schuurmans, and A. C. Schouten, *Sensory Weighting of Force and Position Feedback in Human Motor Control Tasks,* .

[3] A. C. Schouten, W. Mugge, and F. C. T. van der Helm, *NMClab, a model to assess the contributions of muscle visco-elasticity and afferent feedback to joint dynamics,* Journal of Biomechanics **41**, 1659 (2008).

[4] J. K. Brynildsen, K. Rajan, M. X. Henderson, and D. S. Bassett, *Network models to enhance the translational impact of cross-species studies,* Nat. Rev. Neurosci. **24**, 575 (2023).

[5] B. J. Edelman and E. Macé, *Functional ultrasound brain imaging: Bridging networks, neurons, and behavior,* Curr. Opin. Biomed. Eng. **18**, 100286 (2021).

[6] G. Buzsáki, *Large-scale recording of neuronal ensembles,* Nat Neurosci **7**, 446 (2004).

[7] Y. Wang, X. Yang, X. Zhang, Y. Wang, and W. Pei, *Implantable intracortical microelectrodes: Reviewing the present with a focus on the future,* Microsyst Nanoeng **9**, 1 (2023).

[8] N. A. Steinmetz, C. Aydin, A. Lebedeva, M. Okun, M. Pachitariu, M. Bauza, M. Beau, J. Bhagat, C. Böhm, M. Broux, S. Chen, J. Colonell, R. J. Gardner, B. Karsh, F. Kloosterman, D. Kostadinov, C. Mora-Lopez, J. O'Callaghan, J. Park, J. Putzeys, B. Sauerbrei, R. J. J. van Daal, A. Z. Vollan, S. Wang, M. Welkenhuysen, Z. Ye, J. T. Dudman, B. Dutta, A. W. Hantman, K. D. Harris, A. K. Lee, E. I. Moser, J. O'Keefe, A. Renart, K. Svoboda, M. Häusser, S. Haesler, M. Carandini, and T. D. Harris, *Neuropixels 2.0: A miniaturized high-density probe for stable, long-term brain recordings,* Science **372**, eabf4588 (2021).

[9] A. Boyer, S. Ramdani, H. Duffau, M. Dali, M. A. Vincent, E. Mandonnet, D. Guiraud, and F. Bonnetblanc, *Electrophysiological Mapping During Brain Tumor Surgery: Recording Cortical Potentials Evoked Locally, Subcortically and Remotely by Electrical Stimulation to Assess the Brain Connectivity On-line,* Brain Topogr **34**, 221 (2021).

[10] M. M. Shanechi, *Brain–machine interfaces from motor to mood,* Nat Neurosci **22**, 1554 (2019).

[11] J. K. Chapin, K. A. Moxon, R. S. Markowitz, and M. A. L. Nicolelis, *Real-time control of a robot arm using simultaneously recorded neurons in the motor cortex,* Nat Neurosci **2**, 664 (1999).

[12] N. K. Logothetis and J. Pfeuffer, *On the nature of the BOLD fMRI contrast mechanism,* Magnetic Resonance Imaging Proceedings of the International School on Magnetic Resonance and Brain Function, **22**, 1517 (2004).

[13] D. J. Heeger and D. Ress, *What does fMRI tell us about neuronal activity?* Nat Rev Neurosci **3**, 142 (2002).

[14] J. R. Petrella, L. M. Shah, K. M. Harris, A. H. Friedman, T. M. George, J. H. Sampson, J. S. Pekala, and J. T. Voyvodic, *Preoperative Functional MR Imaging Localization of Language and Motor Areas: Effect on Therapeutic Decision Making in Patients with Potentially Resectable Brain Tumors,* Radiology **240**, 793 (2006).

[15] T. Deffieux, C. Demené, and M. Tanter, *Functional Ultrasound Imaging: A New Imaging Modality for Neuroscience,* Neuroscience Brain Imaging, **474**, 110 (2021).

[16] D. Boido, R. L. Rungta, B.-F. Osmanski, M. Roche, T. Tsurugizawa, D. Le Bihan, L. Ciobanu, and S. Charpak, *Mesoscopic and microscopic imaging of sensory responses in the same animal,* Nat Commun **10**, 1110 (2019).

[17] S. Soloukey, A. J. P. E. Vincent, D. D. Satoer, F. Mastik, M. Smits, C. M. F. Dirven, C. Strydis, J. G. Bosch, A. F. W. van der Steen, C. I. De Zeeuw, S. K. E. Koekkoek, and P. Kruizinga, *Functional Ultrasound (fUS) During Awake Brain Surgery: The Clinical Potential of Intra-Operative Functional and Vascular Brain Mapping,* Front. Neurosci. **13** (2020), 10.3389/fnins.2019.01384.

[18] S. Soloukey, A. J. P. E. Vincent, M. Smits, C. I. De Zeeuw, S. K. E. Koekkoek, C. M. F. Dirven, and P. Kruizinga, *Functional imaging of the exposed brain,* Front. Neurosci. **17** (2023), 10.3389/fnins.2023.1087912.

[19] C. Demene, J. Baranger, M. Bernal, C. Delanoe, S. Auvin, V. Biran, M. Alison, J. Mairesse, E. Harribaud, M. Pernot, M. Tanter, and O. Baud, *Functional ultrasound imaging of brain activity in human newborns,* Sci. Transl. Med. **9**, eaah6756 (2017).

[20] J. Baranger, C. Demene, A. Frerot, F. Faure, C. Delanoë, H. Serroune, A. Houdouin, J. Mairesse, V. Biran, O. Baud, and M. Tanter, *Bedside functional monitoring of the dynamic brain connectivity in human neonates,* Nat Commun **12**, 1080 (2021).

[21] C. Rabut, S. L. Norman, W. S. Griggs, J. J. Russin, K. Jann, V. Christopoulos, C. Liu, R. A. Andersen, and M. G. Shapiro, *Functional ultrasound imaging of human brain activity through an acoustically transparent cranial window,* Sci. Transl. Med. **16**, eadj3143 (2024).

[22] S. L. Norman, D. Maresca, V. N. Christopoulos, W. S. Griggs, C. Demene, M. Tanter, M. G. Shapiro, and R. A. Andersen, *Single-trial decoding of movement intentions using functional ultrasound neuroimaging,* Neuron **109**, 1554 (2021).

[23] W. S. Griggs, S. L. Norman, T. Deffieux, F. Segura, B.-F. Osmanski, G. Chau, V. Christopoulos, C. Liu, M. Tanter, M. G. Shapiro, and R. A. Andersen, *Decoding motor plans using a closed-loop ultrasonic brain–machine interface,* Nat Neurosci **27**, 196 (2024).

[24] E. Macé, G. Montaldo, I. Cohen, M. Baulac, M. Fink, and M. Tanter, *Functional ultrasound imaging of the brain,* Nat Methods **8**, 662 (2011).

[25] G. Montaldo, M. Tanter, J. Bercoff, N. Benech, and M. Fink, *Coherent plane-wave compounding for very high frame rate ultrasonography and transient elastography,* IEEE Trans. Ultrason. Ferroelectr. Freq. Control **56**, 489 (2009).

[26] V. Perrot, M. Polichetti, F. Varray, and D. Garcia, *So you think you can DAS? A viewpoint on delay-and-sum beamforming,* Ultrasonics **111**, 106309 (2021).

[27] W. J. Dally, S. W. Keckler, and D. B. Kirk, *Evolution of the Graphics Processing Unit (GPU),* IEEE Micro **41**, 42 (2021).

[28] M. Tanter and M. Fink, *Ultrafast imaging in biomedical ultrasound,* IEEE Trans. Ultrason. Ferroelectr. Freq. Control **61**, 102 (2014).

[29] J. H. Youk, H. M. Gweon, and E. J. Son, *Shear-wave elastography in breast ultrasonography: The state of the art,* Ultrasonography **36**, 300 (2017).

[30] A. Caenen, M. Pernot, K. R. Nightingale, J.-U. Voigt, H. J. Vos, P. Segers, and J. D'hooge, *Assessing cardiac stiffness using ultrasound shear wave elastography,* Phys. Med. Biol. **67**, 02TR01 (2022).

[31] F. Piscaglia, V. Salvatore, L. Mulazzani, V. Cantisani, and C. Schiavone, *Ultrasound Shear Wave Elastography for Liver Disease. A Critical Appraisal of the Many Actors on the Stage,* Ultraschall Med. - Eur. J. Ultrasound **37**, 1 (2016).

[32] B. W. Ossenkoppele, V. Daeichin, K. E. Rodriguez Hernandez, N. de Jong, M. D. Verweij, A. C. Schouten, and W. Mugge, *System identification of ankle joint dynamics based on plane-wave ultrasound muscle imaging,* in *2019 41st Annu. Int. Conf. IEEE Eng. Med. Biol. Soc. EMBC* (2019) pp. 2111–2114.

[33] E. Lubel, B. Grandi Sgambato, D. Y. Barsakcioglu, J. Ibáñez, M.-X. Tang, and D. Farina, *Kinematics of individual muscle units in natural contractions measured in vivo using ultrafast ultrasound,* J. Neural Eng. **19**, 056005 (2022).

[34] Q. Zhang, N. Hakam, O. Akinniyi, A. Iyer, X. Bao, and N. Sharma, *AnkleImage - An ultrafast ultrasound image dataset to understand the ankle joint muscle contractility,* Sci Data **11**, 1439 (2024).

[35] J. Provost, C. Papadacci, J. E. Arango, M. Imbault, M. Fink, J.-L. Gennisson, M. Tanter, and M. Pernot, *3D ultrafast ultrasound imaging in vivo,* Phys. Med. Biol. **59**, L1 (2014).

[36] R. Waasdorp, W. Mugge, H. J. Vos, J. H. Groot, N. De Jong, M. D. Verweij, A. C. Schouten, and V. Daeichin, *Tracking electromechanical muscle dynamics using ultrafast ultrasound and high-density EMG,* in *IEEE International Ultrasonics Symposium, IUS*, Vol. 2019-Octob (2019) pp. 2137–2140.

[37] R. Waasdorp, W. Mugge, H. J. Vos, J. H. de Groot, M. D. Verweij, N. de Jong, A. C. Schouten, and V. Daeichin, *Combining Ultrafast Ultrasound and High-Density EMG to Assess Local Electromechanical Muscle Dynamics: A Feasibility Study,* IEEE Access **9**, 45277 (2021).

[38] A. Alafandi, S. S. Tbalvandany, F. Arzanforoosh, S. R. van Der Voort, F. Incekara, L. Verhoef, E. A. H. Warnert, P. Kruizinga, and M. Smits, *Probing the glioma microvasculature: A case series of the comparison between perfusion MRI and intraoperative high-frame-rate ultrafast Doppler ultrasound,* Eur Radiol Exp **8**, 13 (2024).

[39] E. Macé, G. Montaldo, B. F. Osmanski, I. Cohen, M. Fink, and M. Tanter, *Functional ultrasound imaging of the brain: Theory and basic principles,* IEEE Trans. Ultrason. Ferroelectr. Freq. Control **60**, 492 (2013).

[40] A. A. Phillips, F. H. Chan, M. M. Z. Zheng, A. V. Krassioukov, and P. N. Ainslie, *Neurovascular coupling in humans: Physiology, methodological advances and clinical implications,* J Cereb Blood Flow Metab **36**, 647 (2016).

[41] A. Y. Shih, P. Blinder, P. S. Tsai, B. Friedman, G. Stanley, P. D. Lyden, and D. Kleinfeld, *The smallest stroke: Occlusion of one penetrating vessel leads to infarction and a cognitive deficit,* Nat Neurosci **16**, 55 (2013).

[42] Y. Hirano, B. Stefanovic, and A. C. Silva, *Spatiotemporal evolution of the functional magnetic resonance imaging response to ultrashort stimuli,* J. Neurosci. **31**, 1440 (2011).

[43] A.-K. Aydin, W. D. Haselden, Y. Goulam Houssen, C. Pouzat, R. L. Rungta, C. Demené, M. Tanter, P. J. Drew, S. Charpak, and D. Boido, *Transfer functions linking neural calcium to single voxel functional ultrasound signal,* Nat Commun **11**, 2954 (2020).

[44] G. Montaldo, A. Urban, and E. Macé, *Functional Ultrasound Neuroimaging,* Annu. Rev. Neurosci. **45**, 491 (2022).

[45] C. Demené, T. Deffieux, M. Pernot, B.-F. Osmanski, V. Biran, J.-L. Gennisson, L.-A. Sieu, A. Bergel, S. Franqui, J.-M. Correas, I. Cohen, O. Baud, and M. Tanter, *Spatiotemporal Clutter Filtering of Ultrafast Ultrasound Data Highly Increases Doppler and fUltrasound Sensitivity,* IEEE Trans. Med. Imaging **34**, 2271 (2015).

[46] T. Di Ianni and R. D. Airan, *Deep-fUS: A Deep Learning Platform for Functional Ultrasound Imaging of the Brain Using Sparse Data,* IEEE Trans. Med. Imaging **41**, 1813 (2022).

[47] B. S. Generowicz, S. Dijkhuizen, C. I. De Zeeuw, S. K. E. Koekkoek, and P. Kruizinga, *Swept-3-D Ultrasound Imaging of the Mouse Brain Using a Continuously Moving 1-D-Array—Part I: Doppler Imaging,* IEEE Trans. Ultrason. Ferroelectr. Freq. Control **70**, 1714 (2023).

[48] B. S. Generowicz, S. Dijkhuizen, L. W. J. Bosman, C. I. De Zeeuw, S. K. E. Koekkoek, and P. Kruizinga, *Swept-3-D Ultrasound Imaging of the Mouse Brain Using a Continuously Moving 1-D-Array—Part II: Functional Imaging,* IEEE Trans. Ultrason. Ferroelectr. Freq. Control **70**, 1726 (2023).

[49] C. Brunner, M. Grillet, A. Sans-Dublanc, K. Farrow, T. Lambert, E. Macé, G. Montaldo, and A. Urban, *A Platform for Brain-wide Volumetric Functional Ultrasound Imaging and Analysis of Circuit Dynamics in Awake Mice,* Neuron **108**, 861 (2020).

[50] C. Rabut, M. Correia, V. Finel, S. Pezet, M. Pernot, T. Deffieux, and M. Tanter, *4D functional ultrasound imaging of whole-brain activity in rodents,* Nat Methods **16**, 994 (2019).

[51] J. Sauvage, J. Poree, C. Rabut, G. Ferin, M. Flesch, B. Rosinski, A. Nguyen-Dinh, M. Tanter, M. Pernot, and T. Deffieux, *4D Functional Imaging of the Rat Brain Using a Large Aperture Row-Column Array,* IEEE Trans. Med. Imaging **39**, 1884 (2020).

[52] B. Heiles, M. Correia, V. Hingot, M. Pernot, J. Provost, M. Tanter, and O. Couture, *Ultrafast 3D Ultrasound Localization Microscopy Using a 32 \times 32 Matrix Array,* IEEE Trans. Med. Imaging **38**, 2005 (2019).

[53] M. Flesch, M. Pernot, J. Provost, G. Ferin, A. Nguyen-Dinh, M. Tanter, and T. Deffieux, *4D in vivo ultrafast ultrasound imaging using a row-column addressed matrix and coherently-compounded orthogonal plane waves,* Phys. Med. Biol. **62**, 4571 (2017).

[54] J. Sauvage, M. Flesch, G. Férin, A. Nguyen-Dinh, J. Porée, M. Tanter, M. Pernot, and T. Deffieux, *A large aperture row column addressed probe for* in vivo *4D ultrafast doppler ultrasound imaging,* Phys. Med. Biol. **63**, 215012 (2018).

[55] J. A. Jensen, M. Schou, L. T. Jørgensen, B. G. Tomov, M. B. Stuart, M. S. Traberg, I. Taghavi, S. H. Øygaard, M. L. Ommen, K. Steenberg, E. V. Thomsen, N. S. Panduro, M. B. Nielsen, and C. M. Sørensen, *Anatomic and Functional Imaging Using Row–Column Arrays,* IEEE Trans. Ultrason. Ferroelectr. Freq. Control **69**, 2722 (2022).

[56] C. Brunner, M. Grillet, A. Urban, B. Roska, G. Montaldo, and E. Macé, *Whole-brain functional ultrasound imaging in awake head-fixed mice,* Nat Protoc **16**, 3547 (2021).

[57] C. Brunner, *Functional Ultrasound Imaging (fUSI) to Assess Brain Function in Physiological and Pathological Conditions Application to Stroke*, Ph.D. thesis, Université Paris Descartes, Sorbonne Paris Cité, Paris, France (2016).

[58] G. Pinton, J. F. Aubry, E. Bossy, M. Muller, M. Pernot, and M. Tanter, *Attenuation, scattering, and absorption of ultrasound in the skull bone,* Med. Phys. **39**, 299 (2012).

[59] G. Pinton, M. Pernot, E. Bossy, J.-F. Aubry, M. Muller, and M. Tanter, *Mechanisms of attenuation and heating dissipation of ultrasound in the skull bone: Comparison between simulation models and experiments,* in *2010 IEEE Int. Ultrason. Symp.* (2010) pp. 225–228.

[60] F. Zhu, H. Mao, A. D. C. Leonardi, C. Wagner, C. C. Chou, X. Jin, C. Bir, P. VandeVord, K. H. Yang, and A. I. King, *Development of an FE Model of the Rat Head Subjected to Air Shock Loading,* in *54th Stapp Car Crash Conference* (2010) pp. 2010–22–0011.

[61] H. Mao, C. Wagner, F. Guan, Y. N. Yeni, and K. H. Yang, *MATERIAL PROPERTIES OF ADULT RAT SKULL,* J. Mech. Med. Biol. **11**, 1199 (2011).

[62] B. F. Osmanski, C. Martin, G. Montaldo, P. Lanièce, F. Pain, M. Tanter, and H. Gurden, *Functional ultrasound imaging reveals different odor-evoked patterns of vascular activity in the main olfactory bulb and the anterior piriform cortex,* NeuroImage **95**, 176 (2014).

[63] C. Errico, B.-F. Osmanski, S. Pezet, O. Couture, Z. Lenkei, and M. Tanter, *Transcranial functional ultrasound imaging of the brain using microbubble-enhanced ultrasensitive Doppler,* NeuroImage **124**, 752 (2016).

[64] D. Maresca, T. Payen, A. Lee-Gosselin, B. Ling, D. Malounda, C. Demené, M. Tanter, and M. G. Shapiro, *Acoustic biomolecules enhance hemodynamic functional ultrasound imaging of neural activity,* NeuroImage **209**, 116467 (2020).

[65] R. Ali, T. Brevett, L. Zhuang, H. Bendjador, A. S. Podkowa, S. S. Hsieh, W. Simson, S. J. Sanabria, C. D. Herickhoff, and J. J. Dahl, *Aberration correction in diagnostic ultrasound: A review of the prior field and current directions,* Zeitschrift für Medizinische Physik (2023), 10.1016/j.zemedi.2023.01.003.

[66] R. Mallart and M. Fink, *Adaptive focusing in scattering media through sound-speed inhomogeneities: The van Cittert Zernike approach and focusing criterion,* J. Acoust. Soc. Am. **96**, 3721 (1994).

[67] S. Flax and M. O'Donnell, *Phase-aberration correction using signals from point reflectors and diffuse scatterers: Basic principles,* IEEE Trans. Ultrason. Ferroelectr. Freq. Control **35**, 758 (1988).

[68] L. Nock, G. E. Trahey, and S. W. Smith, *Phase aberration correction in medical ultrasound using speckle brightness as a quality factor,* The Journal of the Acoustical Society of America **85**, 1819 (1989).

[69] J. Robin, C. Demené, B. Heiles, V. Blanvillain, L. Puke, F. Perren, and M. Tanter, *In vivo adaptive focusing for clinical contrast-enhanced transcranial ultrasound imaging in human,* Phys. Med. Biol. **68**, 025019 (2023).

[70] N. M. Ivancevich, G. F. Pinton, H. A. Nicoletto, E. Bennett, D. T. Laskowitz, and S. W. Smith, *Real-Time 3-D Contrast-Enhanced Transcranial Ultrasound and Aberration Correction,* Ultrasound in Medicine & Biology **34**, 1387 (2008).

[71] D. E. Soulioti, D. Espíndola, P. A. Dayton, and G. F. Pinton, *Super-Resolution Imaging Through the Human Skull,* IEEE Trans. Ultrason. Ferroelectr. Freq. Control **67**, 25 (2020).

[72] N. Ivancevich, J. Dahl, G. Trahey, and S. Smith, *Phase-aberration correction with a 3-D ultrasound scanner: Feasibility study,* IEEE Trans. Ultrason. Ferroelectr. Freq. Control **53**, 1432 (2006).

[73] B.-F. Osmanski, G. Montaldo, M. Tanter, and M. Fink, *Aberration correction by time reversal of moving speckle noise,* IEEE Trans. Ultrason. Ferroelectr. Freq. Control **59**, 1575 (2012).

[74] M. Mozaffarzadeh, M. D. Verweij, N. de Jong, and G. Renaud, *Comparison of Phase-Screen and Geometry-Based Phase Aberration Correction Techniques for Real-Time Transcranial Ultrasound Imaging,* Appl. Sci. **12**, 10183 (2022).

[75] M. Mozaffarzadeh, E. Verschuur, M. D. Verweij, V. Daeichin, N. De Jong, and G. Renaud, *Refraction-Corrected Transcranial Ultrasound Imaging Through the Human Temporal Window Using a Single Probe,* IEEE Trans. Ultrason. Ferroelectr. Freq. Control **69**, 1191 (2022).

[76] G. Renaud, P. Kruizinga, D. Cassereau, and P. Laugier, *In vivo ultrasound imaging of the bone cortex,* Phys. Med. Biol. **63**, 125010 (2018).

[77] G. Renaud, P. Clouzet, D. Cassereau, and M. Talmant, *Measuring anisotropy of elastic wave velocity with ultrasound imaging and an autofocus method: Application to cortical bone,* Phys. Med. Biol. **65**, 235016 (2020).

[78] J.-F. Aubry, M. Tanter, M. Pernot, J.-L. Thomas, and M. Fink, *Experimental demonstration of noninvasive transskull adaptive focusing based on prior computed tomography scans,* The Journal of the Acoustical Society of America **113**, 84 (2003).

[79] C. Jiang, Y. Li, K. Xu, and D. Ta, *Full-Matrix Phase Shift Migration Method for Transcranial Ultrasonic Imaging,* IEEE Trans. Ultrason. Ferroelectr. Freq. Control **68**, 72 (2021).

[80] T. Wang and Y. Jing, *Transcranial ultrasound imaging with speed of sound-based phase correction: A numerical study,* Phys. Med. Biol. **58**, 6663 (2013).

[81] D. A. Waltham, *Two-point ray tracing using Fermat's principle,* Geophysical Journal International **93**, 575 (1988).

[82] J. Zhou, Y. Guo, Q. Sun, F. Lin, C. Jiang, K. Xu, and D. Ta, *Transcranial ultrafast ultrasound Doppler imaging: A phantom study,* Ultrasonics **144**, 107430 (2024).

[83] C. Jiang, B. Li, L. Xie, C. Liu, K. Xu, Y. Zhan, and D. Ta, *Ray theory-based compounded plane wave ultrasound imaging for aberration corrected transcranial imaging: Phantom experiments and simulations,* Ultrasonics **135**, 107124 (2023).

[84] M. Mozaffarzadeh, D. J. E. Verschuur, M. D. Verweij, N. de Jong, and G. Renaud, *Accelerated 2-D Real-Time Refraction-Corrected Transcranial Ultrasound Imaging,* IEEE Trans. Ultrason. Ferroelectr. Freq. Control **69**, 2599 (2022).

[85] R. Waasdorp, D. Maresca, and G. Renaud, *Assessing Transducer Parameters for Accurate Medium Sound Speed Estimation and Image Reconstruction,* IEEE Trans. Ultrason. Ferroelectr. Freq. Control **71**, 1233 (2024).

[86] K. Shung and M. Zippuro, *Ultrasonic transducers and arrays,* IEEE Eng. Med. Biol. Mag. **15**, 20 (1996).

[87] H. Favre, M. Pernot, M. Tanter, and C. Papadacci, *Transcranial 3D ultrasound localization microscopy using a large element matrix array with a multi-lens diffracting layer: An in vitro study,* Phys. Med. Biol. **68**, 075003 (2023).

[88] M. D. Gray and C. C. Coussios, *Compensation of array lens effects for improved co-registration of passive acoustic mapping and B-mode images for cavitation monitoring,* J. Acoust. Soc. Am. **146** (2019), 10.1121/1.5118238.

[89] J. A. Jensen, S. I. Nikolov, K. L. Gammelmark, and M. H. Pedersen, *Synthetic aperture ultrasound imaging,* Ultrasonics Proceedings of Ultrasonics International (UI'05) and World Congress on Ultrasonics (WCU), **44**, e5 (2006).

[90] M. E. Anderson, M. S. McKeag, and G. E. Trahey, *The impact of sound speed errors on medical ultrasound imaging,* J. Acoust. Soc. Am. **107**, 3540 (2000).

[91] J. Krucker, J. Fowlkes, and P. Carson, *Sound speed estimation using automatic ultrasound image registration,* IEEE Trans. Ultrason., Ferroelect., Freq. Contr. **51**, 1095 (2004).

[92] B. E. Treeby, T. K. Varslot, E. Z. Zhang, J. G. Laufer, and P. C. Beard, *Automatic sound speed selection in photoacoustic image reconstruction using an autofocus approach,* JBO **16**, 090501 (2011).

[93] D. Napolitano, C.-H. Chou, G. McLaughlin, T.-L. Ji, L. Mo, D. DeBusschere, and R. Steins, *Sound speed correction in ultrasound imaging,* Ultrasonics Proceedings of Ultrasonics International (UI'05) and World Congress on Ultrasonics (WCU), **44**, e43 (2006).

[94] W. Marczak, *Water as a standard in the measurements of speed of sound in liquids,* JASA **102**, 2776 (1997).

[95] B. E. Treeby and B. T. Cox, *K-Wave: MATLAB toolbox for the simulation and reconstruction of photoacoustic wave fields,* JBO **15**, 021314 (2010).

[96] P. N. T. Wells, *Biomedical Ultrasonics* (Academic Press, London, 1977).

[97] C. M. Rumack, S. Wilson, J. W. Charboneau, and D. Levine, *Diagnostic Ultrasound: 2-Volume Set,* Mo. Elsevier Mosby (2010).

[98] K. Ranganathan and W. F. Walker, *Cystic resolution: A performance metric for ultrasound imaging systems,* IEEE Trans. Ultrason. Ferroelectr. Freq. Control **54**, 782 (2007).

[99] J. Jensen, M. B. Stuart, and J. A. Jensen, *Optimized Plane Wave Imaging for Fast and High-Quality Ultrasound Imaging,* IEEE Trans. Ultrason. Ferroelectr. Freq. Control **63**, 1922 (2016).

[100] M. Jakovljevic, S. Hsieh, R. Ali, G. Chau Loo Kung, D. Hyun, and J. J. Dahl, *Local speed of sound estimation in tissue using pulse-echo ultrasound: Model-based approach,* The Journal of the Acoustical Society of America **144**, 254 (2018).

[101] H.-C. Shin, R. Prager, H. Gomersall, N. Kingsbury, G. Treece, and A. Gee, *Estimation of Average Speed of Sound Using Deconvolution of Medical Ultrasound Data,* Ultrasound in Medicine and Biology **36**, 623 (2010).

[102] M. E. Anderson and G. E. Trahey, *The direct estimation of sound speed using pulse–echo ultrasound,* J. Acoust. Soc. Am. **104**, 3099 (1998).

[103] S. J. Sanabria, E. Ozkan, M. Rominger, and O. Goksel, *Spatial domain reconstruction for imaging speed-of-sound with pulse-echo ultrasound: Simulation and in vivo study,* Phys. Med. Biol. **63**, 215015 (2018).

[104] M. Imbault, A. Faccinetto, B.-F. Osmanski, A. Tissier, T. Deffieux, J.-L. Gennisson, V. Vilgrain, and M. Tanter, *Robust sound speed estimation for ultrasound-based hepatic steatosis assessment,* Phys. Med. Biol. **62**, 3582 (2017).

[105] M. D. Burgio, M. Imbault, M. Ronot, A. Faccinetto, B. E. V. Beers, P.-E. Rautou, L. Castera, J.-L. Gennisson, M. Tanter, and V. Vilgrain, *Ultrasonic Adaptive Sound Speed Estimation for the Diagnosis and Quantification of Hepatic Steatosis: A Pilot Study,* Ultraschall Med **40**, 722 (2019).

[106] D. T. Fetzer, I. M. Rosado-Mendez, M. Wang, M. L. Robbin, A. Ozturk, K. A. Wear, J. Ormachea, T. A. Stiles, J. B. Fowlkes, T. J. Hall, and A. E. Samir, *Pulse-Echo Quantitative US Biomarkers for Liver Steatosis: Toward Technical Standardization,* Radiology **305**, 265 (2022).

[107] A. O. Nunez-Elizalde, M. Krumin, C. B. Reddy, G. Montaldo, A. Urban, K. D. Harris, and M. Carandini, *Neural correlates of blood flow measured by ultrasound,* Neuron **110**, 1631 (2022).

[108] M. Imbault, D. Chauvet, J.-L. Gennisson, L. Capelle, and M. Tanter, *Intraoperative Functional Ultrasound Imaging of Human Brain Activity,* Sci Rep **7**, 7304 (2017).

[109] A. Dizeux, M. Gesnik, H. Ahnine, K. Blaize, F. Arcizet, S. Picaud, J.-A. Sahel, T. Deffieux, P. Pouget, and M. Tanter, *Functional ultrasound imaging of the brain reveals propagation of task-related brain activity in behaving primates,* Nat Commun **10**, 1400 (2019).

[110] D. A. Hernandez, V. H. Contreras, L. Leija, A. Vera, D. Martinez-Fong, and M. I. Gutierrez, *Acoustic field simulation for focused ultrasound on skull with craniotomy for drug delivery in rat brain,* in *2017 Glob. Med. Eng. Phys. Exch. Am. Health Care Exch. GMEPEPAHCE* (2017) pp. 1–5.

[111] B. D. Lindsey and S. W. Smith, *Refraction Correction in 3D Transcranial Ultrasound Imaging,* Ultrason Imaging **36**, 35 (2014).

[112] B. Lucht, A. Hubbell, and K. Hynynen, *Contrast-Enhanced Transcranial Two-Dimensional Ultrasound Imaging Using Shear-Mode Conversion at Low Frequency,* Ultrasound in Medicine & Biology **39**, 332 (2013).

[113] E. Tiran, J. Ferrier, T. Deffieux, J.-L. Gennisson, S. Pezet, Z. Lenkei, and M. Tanter, *Transcranial Functional Ultrasound Imaging in Freely Moving Awake Mice and Anesthetized Young Rats without Contrast Agent,* Ultrasound Med. Biol. **43**, 1679 (2017).

[114] A. Bertolo, J. Ferrier, S. Cazzanelli, S. Diebolt, M. Tanter, S. Pezet, M. Pernot, B.-F. Osmanski, and T. Deffieux, *High sensitivity mapping of brain-wide functional networks in awake mice using simultaneous multi-slice fUS imaging,* Imaging Neuroscience **1**, 1 (2023).

[115] M. Li, M. J. Li, J. Huang, C. Y. Le, Y. Wang, L. Q. Zhao, C. F. Wang, C. W. Wan, and J. W. Wang, *Age-Related Changes of Material Mechanics and Bone Material Parameters of Rat Skulls,* Fa Yi Xue Za Zhi **37**, 1 (2021).

[116] A. Urban, E. Mace, C. Brunner, M. Heidmann, J. Rossier, and G. Montaldo, *Chronic assessment of cerebral hemodynamics during rat forepaw electrical stimulation using functional ultrasound imaging,* NeuroImage **101**, 138 (2014).

[117] F. Bureau, J. Robin, A. Le Ber, W. Lambert, M. Fink, and A. Aubry, *Three-dimensional ultrasound matrix imaging,* Nat Commun **14**, 6793 (2023).

[118] F. Bureau, L. Denis, A. Coudert, M. Fink, O. Couture, and A. Aubry, *Ultrasound matrix imaging for transcranial in-vivo localization microscopy,* (2024), arXiv:2410.14499 .

[119] P. Xing, J. Porée, B. Rauby, A. Malescot, E. Martineau, V. Perrot, R. L. Rungta, and J. Provost, *Phase Aberration Correction for In Vivo Ultrasound Localization Microscopy Using a Spatiotemporal Complex-Valued Neural Network,* IEEE Trans Med Imaging **43**, 662 (2024).

[120] M. Sharifzadeh, S. Goudarzi, A. Tang, H. Benali, and H. Rivaz, *Mitigating Aberration-Induced Noise: A Deep Learning-Based Aberration-to-Aberration Approach,* IEEE Trans Med Imaging , 1 (2024).

[121] J. A. Sethian, *Fast Marching Methods,* SIAM Rev. **41**, 199 (1999).

[122] A. R. Selfridge, G. S. Kino, and B. T. Khuri-Yakub, *A theory for the radiation pattern of a narrow-strip acoustic transducer,* Appl. Phys. Lett. **37**, 35 (1980).

[123] T. D. Mast, *Empirical relationships between acoustic parameters in human soft tissues,* Acoustics Research Letters Online **1**, 37 (2000).

[124] P. Harris and R. Petherick, *Ultrasonic transmission and reflection measurements of a rat skull,* in *2015 9th Int. Conf. Sens. Technol. ICST* (2015) pp. 822–827.

[125] M. A. O'Reilly, A. Muller, and K. Hynynen, *Ultrasound Insertion Loss of Rat Parietal Bone Appears to Be Proportional to Animal Mass at Submegahertz Frequencies,* Ultrasound in Medicine & Biology **37**, 1930 (2011).

[126] M. A. Aydin, M. S. Kilinc, A. S. Ergun, A. Bozkurt, and E. Deveci, *Ultrasonic transmittance of rat skull as a function of frequency,* in *2016 IEEE Int. Ultrason. Symp. IUS* (2016) pp. 1–4.

[127] M. Gerstenmayer, B. Fellah, R. Magnin, E. Selingue, and B. Larrat, *Acoustic Transmission Factor through the Rat Skull as a Function of Body Mass, Frequency and Position,* Ultrasound in Medicine & Biology **44**, 2336 (2018).

[128] R. L. Nasoni, T. Bowen, W. G. Connor, and R. R. Sholes, In Vivo *temperature dependence of ultrasound speed in tissue and its application to noninvasive temperature monitoring,* Ultrasonic Imaging **1**, 34 (1979).

[129] T. Bowen, W. G. Connor, R. L. Nasoni, A. E. Pifer, and R. R. Sholes, *Measurement of the temperature dependence of the velocity of ultrasound in soft tissues,* Ultrason. Tissue Charact. II **525**, 57 (1979).

[130] R. P. Brent, *Algorithms for Minimization without Derivatives*, Prentice-Hall Series in Automatic Computation (Prentice-Hall, Englewood Cliffs, N.J, 1973).

[131] R. Wituła and D. Słota, *Cardano's formula, square roots, Chebyshev polynomials and radicals,* Journal of Mathematical Analysis and Applications **363**, 639 (2010).

[132] J. M. Martinez de Paz and E. Macé, *Functional ultrasound imaging: A useful tool for functional connectomics?* NeuroImage **245**, 118722 (2021).

[133] K. Tripathi, T. Zhang, N. McDannold, Y.-Z. Zhang, G. Ehnholm, and Y. Okada, *Direct Activation of Cortical Neurons in the Primary Somatosensory Cortex of the Rat* in Vivo *Using Focused Ultrasound,* Ultrasound in Medicine & Biology **46**, 2349 (2020).

[134] E. Macé, G. Montaldo, S. Trenholm, C. Cowan, A. Brignall, A. Urban, and B. Roska, *Whole-Brain Functional Ultrasound Imaging Reveals Brain Modules for Visuomotor Integration,* Neuron **100**, 1241 (2018).

[135] C. Bimbard, C. Demene, C. Girard, S. Radtke-Schuller, S. Shamma, M. Tanter, and Y. Boubenec, *Multi-scale mapping along the auditory hierarchy using high-resolution functional UltraSound in the awake ferret,* eLife **7**, e35028 (2018).

[136] T. Deffieux, C. Demene, M. Pernot, and M. Tanter, *Functional ultrasound neuroimaging: A review of the preclinical and clinical state of the art,* Current Opinion in Neurobiology Neurotechnologies, **50**, 128 (2018).

[137] M. Gesnik, K. Blaize, T. Deffieux, J.-L. Gennisson, J.-A. Sahel, M. Fink, S. Picaud, and M. Tanter, *3D functional ultrasound imaging of the cerebral visual system in rodents,* NeuroImage **149**, 267 (2017).

[138] C. Brunner, M. Grillet, A. Sans-Dublanc, K. Farrow, T. Lambert, E. Mace, G. Montaldo, and A. Urban, *A Platform for Brain-Wide Functional Ultrasound Imaging and Analysis of Circuit Dynamics in Behaving Mice,* SSRN Electron. J. (2020), 10.2139/ssrn.3581369.

[139] R. Rau, P. Kruizinga, F. Mastik, M. Belau, N. de Jong, J. G. Bosch, W. Scheffer, and G. Maret, *3D functional ultrasound imaging of pigeons,* NeuroImage **183**, 469 (2018).

[140] K. Blaize, F. Arcizet, M. Gesnik, H. Ahnine, U. Ferrari, T. Deffieux, P. Pouget, F. Chavane, M. Fink, J.-A. Sahel, M. Tanter, and S. Picaud, *Functional ultrasound imaging of deep visual cortex in awake nonhuman primates,* Proc. Natl. Acad. Sci. **117**, 14453 (2020).

[141] J. L. Collinger, B. Wodlinger, J. E. Downey, W. Wang, E. C. Tyler-Kabara, D. J. Weber, A. J. McMorland, M. Velliste, M. L. Boninger, and A. B. Schwartz, *High-performance neuroprosthetic control by an individual with tetraplegia,* The Lancet **381**, 557 (2013).

[142] D. A. Moses, S. L. Metzger, J. R. Liu, G. K. Anumanchipalli, J. G. Makin, P. F. Sun, J. Chartier, M. E. Dougherty, P. M. Liu, G. M. Abrams, A. Tu-Chan, K. Ganguly, and E. F. Chang, *Neuroprosthesis for Decoding Speech in a Paralyzed Person with Anarthria,* N. Engl. J. Med. **385**, 217 (2021).

[143] J. P. Cunningham, P. Nuyujukian, V. Gilja, C. A. Chestek, S. I. Ryu, and K. V. Shenoy, *A closed-loop human simulator for investigating the role of feedback control in brain-machine interfaces,* J. Neurophysiol. **105**, 1932 (2011).

[144] H. Pan, H. Song, Q. Zhang, and W. Mi, *Review of Closed-Loop Brain–Machine Interface Systems From a Control Perspective,* IEEE Trans. Hum.-Mach. Syst. **52**, 877 (2022).

[145] B. Heiles, F. Nelissen, R. Waasdorp, D. Terwiel, B. M. Park, E. M. Ibarra, A. Matalliotakis, T. Ara, P. Barturen-Larrea, M. Duan, M. G. Shapiro, V. Gazzola, and D. Maresca, *Nonlinear sound-sheet microscopy: Imaging opaque organs at the capillary and cellular scale,* Science **388**, eads1325 (2025).

[146] J. Jensen, *Simulation of advanced ultrasound systems using Field II,* in *2004 2nd IEEE Int. Symp. Biomed. Imaging Nano Macro IEEE Cat No 04EX821* (2004) pp. 636–639 Vol. 1.

[147] J. Peirce, J. R. Gray, S. Simpson, M. MacAskill, R. Höchenberger, H. Sogo, E. Kastman, and J. K. Lindeløv, *PsychoPy2: Experiments in behavior made easy,* Behav Res **51**, 195 (2019).

[148] H. Kleven, I. E. Bjerke, F. Clascá, H. J. Groenewegen, J. G. Bjaalie, and T. B. Leergaard, *Waxholm Space atlas of the rat brain: A 3D atlas supporting data analysis and integration,* Nat Methods **20**, 1822 (2023).

[149] E. A. Papp, T. B. Leergaard, E. Calabrese, G. A. Johnson, and J. G. Bjaalie, *Waxholm Space atlas of the Sprague Dawley rat brain,* NeuroImage **97**, 374 (2014).

[150] C. Caramel, *Scan Data Visualizer V1,* https://bbbn19.gumroad.com/l/qhldu (2023).

[151] H. Zheng, L. Niu, W. Qiu, D. Liang, X. Long, G. Li, Z. Liu, and L. Meng, *The Emergence of Functional Ultrasound for Noninvasive Brain–Computer Interface,* Research **6**, 0200 (2023).

[152] J. A. Jensen, M. Schou, M. L. Ommen, K. Steenberg, E. V. Thomsen, B. G. Tomov, N. S. Panduro, C. M. Sorensen, and M. B. Stuart, *Synthetic Aperture High Quality B-mode Imaging with a Row-Column Array Compared to Linear Array Imaging,* in *2022 IEEE Int. Ultrason. Symp. IUS* (2022) pp. 1–4.

[153] A. Bertolo, J. Sauvage, M. Tanter, M. Pernot, and T. Deffieux, *XDoppler: Cross-Correlation of Orthogonal Apertures for 3D Blood Flow Imaging,* IEEE Trans. Med. Imaging **40**, 3358 (2021).

[154] *Method of the Year 2014,* Nat Methods **12**, 1 (2015).

[155] V. Voleti, K. B. Patel, W. Li, C. Perez Campos, S. Bharadwaj, H. Yu, C. Ford, M. J. Casper, R. W. Yan, W. Liang, C. Wen, K. D. Kimura, K. L. Targoff, and E. M. C. Hillman, *Real-time volumetric microscopy of in vivo dynamics and large-scale samples with SCAPE 2.0,* Nat. Methods **16**, 1054 (2019).

[156] B. Yang, M. Lange, A. Millett-Sikking, X. Zhao, J. Bragantini, S. VijayKumar, M. Kamb, R. Gómez-Sjöberg, A. C. Solak, W. Wang, H. Kobayashi, M. N. McCarroll, L. W. Whitehead, R. P. Fiolka, T. B. Kornberg, A. G. York, and L. A. Royer, *DaXi—high-resolution, large imaging volume and multi-view single-objective light-sheet microscopy,* Nat. Methods **19**, 461 (2022).

[157] K. McDole, L. Guignard, F. Amat, A. Berger, G. Malandain, L. A. Royer, S. C. Turaga, K. Branson, and P. J. Keller, *In Toto Imaging and Reconstruction of Post-Implantation Mouse Development at the Single-Cell Level,* Cell **175**, 859 (2018).

[158] J. Huisken, J. Swoger, F. Del Bene, J. Wittbrodt, and E. H. K. Stelzer, *Optical Sectioning Deep Inside Live Embryos by Selective Plane Illumination Microscopy,* Science **305**, 1007 (2004).

[159] P. J. Keller, A. D. Schmidt, J. Wittbrodt, and E. H. Stelzer, *Reconstruction of Zebrafish Early Embryonic Development by Scanned Light Sheet Microscopy,* Science **322**, 1065 (2008).

[160] E. H. K. Stelzer, F. Strobl, B.-J. Chang, F. Preusser, S. Preibisch, K. McDole, and R. Fiolka, *Light sheet fluorescence microscopy,* Nat. Rev. Methods Primer **1**, 73 (2021).

[161] P. P. Laissue, R. A. Alghamdi, P. Tomancak, E. G. Reynaud, and H. Shroff, *Assessing phototoxicity in live fluorescence imaging,* Nat. Methods **14**, 657 (2017).

[162] V. Ntziachristos, *Going deeper than microscopy: The optical imaging frontier in biology,* Nat. Methods **7**, 603 (2010).

[163] E. M. Hillman, V. Voleti, K. Patel, W. Li, H. Yu, C. Perez-Campos, S. E. Benezra, R. M. Bruno, and P. T. Galwaduge, *High-speed 3D imaging of cellular activity in the brain using axially-extended beams and light sheets,* Curr. Opin. Neurobiol. **50**, 190 (2018).

[164] M. G. Shapiro, P. W. Goodwill, A. Neogy, M. Yin, F. S. Foster, D. V. Schaffer, and S. M. Conolly, *Biogenic gas nanostructures as ultrasonic molecular reporters,* Nature Nanotech **9**, 311 (2014).

[165] D. Maresca, A. Lakshmanan, M. Abedi, A. Bar-Zion, A. Farhadi, G. J. Lu, J. O. Szablowski, D. Wu, S. Yoo, and M. G. Shapiro, *Biomolecular Ultrasound and Sonogenetics,* Annu. Rev. Chem. Biomol. Eng. **9**, 229 (2018).

[166] B. Heiles, D. Terwiel, and D. Maresca, *The Advent of Biomolecular Ultrasound Imaging,* Neuroscience , S0306452221001342 (2021).

[167] R. W. Bourdeau, A. Lee-Gosselin, A. Lakshmanan, A. Farhadi, S. R. Kumar, S. P. Nety, and M. G. Shapiro, *Acoustic reporter genes for noninvasive imaging of microorganisms in mammalian hosts,* Nature **553**, 86 (2018).

[168] A. Farhadi, G. H. Ho, D. P. Sawyer, R. W. Bourdeau, and M. G. Shapiro, *Ultrasound imaging of gene expression in mammalian cells,* Science **365**, 1469 (2019).

[169] A. Lakshmanan, G. J. Lu, A. Farhadi, S. P. Nety, M. Kunth, A. Lee-Gosselin, D. Maresca, R. W. Bourdeau, M. Yin, J. Yan, C. Witte, D. Malounda, F. S. Foster, L. Schröder, and M. G. Shapiro, *Preparation of biogenic gas vesicle nanostructures for use as contrast agents for ultrasound and MRI,* Nat. Protoc. **12**, 2050 (2017).

[170] B. Heiles, A. Chavignon, A. Bergel, V. Hingot, H. Serroune, D. Maresca, S. Pezet, M. Pernot, M. Tanter, and O. Couture, *Volumetric ultrasound localization microscopy of the whole rat brain microvasculature,* IEEE Open J. Ultrason. Ferroelectr. Freq. Control , 1 (2022).

[171] M. F. Rasmussen, T. L. Christiansen, E. V. Thomsen, and J. A. Jensen, *3-D imaging using row-column-addressed arrays with integrated apodization - part i: Apodization design and line element beamforming,* IEEE Trans. Ultrason. Ferroelectr. Freq. Control **62**, 947 (2015).

[172] D. Maresca, D. P. Sawyer, G. Renaud, A. Lee-Gosselin, and M. G. Shapiro, *Nonlinear X-Wave Ultrasound Imaging of Acoustic Biomolecules,* Phys. Rev. X **8**, 041002 (2018).

[173] A. Matalliotakis, R. Waasdorp, M. D. Verweij, and D. Maresca, *Impact of wavefront shape on nonlinear ultrasound imaging of monodisperse microbubbles,* Phys. Rev. Appl. **22**, 034062 (2024).

[174] A. Lakshmanan, Z. Jin, S. P. Nety, D. P. Sawyer, A. Lee-Gosselin, D. Malounda, M. B. Swift, D. Maresca, and M. G. Shapiro, *Acoustic biosensors for ultrasound imaging of enzyme activity,* Nat Chem Biol **16**, 988 (2020).

[175] A. Bar-Zion, A. Nourmahnad, D. R. Mittelstein, S. Shivaei, S. Yoo, M. T. Buss, R. C. Hurt, D. Malounda, M. H. Abedi, A. Lee-Gosselin, M. B. Swift, D. Maresca, and M. G. Shapiro, *Acoustically triggered mechanotherapy using genetically encoded gas vesicles,* Nat. Nanotechnol. **16**, 1403 (2021).

[176] R. C. Hurt, M. T. Buss, M. Duan, K. Wong, M. Y. You, D. P. Sawyer, M. B. Swift, P. Dutka, D. R. Mittelstein, Z. Jin, M. H. Abedi, A. Farhadi, R. Deshpande, and M. G. Shapiro, *Genomically Mined Acoustic Reporter Genes Enable* In Vivo *Monitoring of Tumors and Tumor-Homing Bacteria*, Preprint (Bioengineering, 2021).

[177] S. Nagai and K. Iizuka, *A practical ultrasound axicon for non-destructive testing,* Ultrasonics **20**, 265 (1982).

[178] T.-Y. Lai, M. Bruce, and M. A. Averkiou, *Modeling of the Acoustic Field Produced by Diagnostic Ultrasound Arrays in Plane and Diverging Wave Modes,* IEEE Trans. Ultrason., Ferroelect., Freq. Contr. **66**, 1158 (2019).

[179] D. Maresca, A. Lakshmanan, A. Lee-Gosselin, J. M. Melis, Y.-L. Ni, R. W. Bourdeau, D. M. Kochmann, and M. G. Shapiro, *Nonlinear ultrasound imaging of nanoscale acoustic biomolecules,* Applied Physics Letters **110**, 073704 (2017).

[180] A. Courbet, D. Endy, E. Renard, F. Molina, and J. Bonnet, *Detection of pathological biomarkers in human clinical samples via amplifying genetic switches and logic gates,* Sci. Transl. Med. **7** (2015), 10.1126/scitranslmed.aaa3601.

[181] M. Versluis, E. Stride, G. Lajoinie, B. Dollet, and T. Segers, *Ultrasound Contrast Agent Modeling: A Review,* Ultrasound Med. Biol. **46**, 2117 (2020).

[182] G. Renaud, J. G. Bosch, A. F. van der Steen, and N. de Jong, *Increasing specificity of contrast-enhanced ultrasound imaging using the interaction of quasi counter-propagating wavefronts: A proof of concept,* IEEE Trans. Ultrason. Ferroelectr. Freq. Control **62**, 1768 (2015).

[183] C. Tremblay-Darveau, R. Williams, L. Milot, M. Bruce, and P. N. Burns, *Combined perfusion and doppler imaging using plane-wave nonlinear detection and microbubble contrast agents,* IEEE Trans. Ultrason. Ferroelectr. Freq. Control **61**, 1988 (2014).

[184] C. Errico, J. Pierre, S. Pezet, Y. Desailly, Z. Lenkei, O. Couture, and M. Tanter, *Ultrafast ultrasound localization microscopy for deep super-resolution vascular imaging,* Nature **527**, 499 (2015).

[185] S. Lee, A. Leconte, A. Wu, J. Kinugasa, J. Poree, A. Linninger, and J. Provost, *Functional Assessment of Cerebral Capillaries using Single Capillary Reporters in Ultrasound Localization Microscopy,* .

[186] C. Kirst, S. Skriabine, A. Vieites-Prado, T. Topilko, P. Bertin, G. Gerschenfeld, F. Verny, P. Topilko, N. Michalski, M. Tessier-Lavigne, and N. Renier, *Mapping the Fine-Scale Organization and Plasticity of the Brain Vasculature,* Cell **180**, 780 (2020).

[187] B. Heiles, A. Chavignon, V. Hingot, P. Lopez, E. Teston, and O. Couture, *Performance benchmarking of microbubble-localization algorithms for ultrasound localization microscopy,* Nat. Biomed. Eng. (2022), 10.1038/s41551-021-00824-8.

[188] H. W. Kuhn, *The Hungarian method for the assignment problem,* Nav. Res. Logist. Q. **2**, 83 (1955).

[189] D. Kleinfeld, P. P. Mitra, F. Helmchen, and W. Denk, *Fluctuations and stimulus-induced changes in blood flow observed in individual capillaries in layers 2 through 4 of rat neocortex,* Proc. Natl. Acad. Sci. **95**, 15741 (1998).

[190] S. K. Piechnik, P. A. Chiarelli, and P. Jezzard, *Modelling vascular reactivity to investigate the basis of the relationship between cerebral blood volume and flow under CO2 manipulation,* NeuroImage **39**, 107 (2008).

[191] B.-C. Chen, W. R. Legant, K. Wang, L. Shao, D. E. Milkie, M. W. Davidson, C. Janetopoulos, X. S. Wu, J. A. Hammer, Z. Liu, B. P. English, Y. Mimori-Kiyosue, D. P. Romero, A. T. Ritter, J. Lippincott-Schwartz, L. Fritz-Laylin, R. D. Mullins, D. M. Mitchell, J. N. Bembenek, A.-C. Reymann, R. Böhme, S. W. Grill, J. T. Wang, G. Seydoux, U. S. Tulu, D. P. Kiehart, and E. Betzig, *Lattice light-sheet microscopy: Imaging molecules to embryos at high spatiotemporal resolution,* Science **346**, 1257998 (2014).

[192] N. G. Horton, K. Wang, D. Kobat, C. G. Clark, F. W. Wise, C. B. Schaffer, and C. Xu, *In vivo three-photon microscopy of subcortical structures within an intact mouse brain,* Nat. Photonics **7**, 205 (2013).

[193] D. A. Feinberg and K. Setsompop, *Ultra-fast MRI of the human brain with simultaneous multi-slice imaging,* J. Magn. Reson. **229**, 90 (2013).

[194] B. J. Edelman, D. Siegenthaler, P. Wanken, B. Jenkins, B. Schmid, A. Ressle, N. Gogolla, T. Frank, and E. Macé, *The COMBO window: A chronic cranial implant for multiscale circuit interrogation in mice,* PLOS Biol. .

[195] T. Segers, P. Kruizinga, M. P. Kok, G. Lajoinie, N. de Jong, and M. Versluis, *Monodisperse Versus Polydisperse Ultrasound Contrast Agents: Non-Linear Response, Sensitivity, and Deep Tissue Imaging Potential,* Ultrasound Med. Biol. **44**, 1482 (2018).

[196] Y. Jain, C. L. Walsh, E. Yagis, S. Aslani, S. Nandanwar, Y. Zhou, J. Ha, K. S. Gustilo, J. Brunet, S. Rahmani, P. Tafforeau, A. Bellier, G. M. Weber, P. D. Lee, and K. Börner, *Vasculature segmentation in 3D hierarchical phase-contrast tomography images of human kidneys,* (2024), 10.1101/2024.08.25.609595.

[197] Z. Jin, A. Lakshmanan, R. Zhang, T. A. Tran, C. Rabut, P. Dutka, M. Duan, R. C. Hurt, D. Malounda, Y. Yao, and M. G. Shapiro, *Ultrasonic reporters of calcium for deep tissue imaging of cellular signals,* (2023), 10.1101/2023.11.09.566364.

[198] C. Huang, M. R. Lowerison, J. D. Trzasko, A. Manduca, Y. Bresler, S. Tang, P. Gong, U.-W. Lok, P. Song, and S. Chen, *Short Acquisition Time Super-Resolution Ultrasound Microvessel Imaging via Microbubble Separation,* Sci. Rep. **10**, 6007 (2020).

[199] G. Koukiou and V. Anastassopoulos, *Velocity Filter Banks using 3-D FFT,* (2013).

[200] G. Koukiou and V. Anastassopoulos, *Velocity Filtering Using Quantum 3D FFT,* Photonics **10**, 483 (2023).

[201] A. Kojima, N. Sakurai, and J. Kishigami, *Motion detection using 3D-FFT spectrum,* in *IEEE Int. Conf. Acoust. Speech Signal Process.* (IEEE, Minneapolis, MN, USA, 1993) pp. 213–216 vol.5.

[202] E. Tiran, T. Deffieux, M. Correia, D. Maresca, B. F. Osmanski, L. A. Sieu, A. Bergel, I. Cohen, M. Pernot, and M. Tanter, *Multiplane wave imaging increases signal-to-noise ratio in ultrafast ultrasound imaging,* Phys. Med. Biol. **60**, 8549 (2015).

[203] E. P. Vienneau and B. C. Byram, *A Coded Excitation Framework for High SNR Transcranial Ultrasound Imaging,* IEEE Trans. Med. Imaging **42**, 2886 (2023).

[204] J. Jung, W. Lee, W. Kang, E. Shin, J. Ryu, and H. Choi, *Review of piezoelectric micromachined ultrasonic transducers and their applications,* J. Micromech. Microeng. **27**, 113001 (2017).

[205] K. Brenner, A. S. Ergun, K. Firouzi, M. F. Rasmussen, Q. Stedman, and B. P. Khuri–Yakub, *Advances in Capacitive Micromachined Ultrasonic Transducers,* Micromachines **10**, 152 (2019).

[206] J. Joseph, B. Ma, and B. T. Khuri-Yakub, *Applications of Capacitive Micromachined Ultrasonic Transducers: A Comprehensive Review,* IEEE Trans. Ultrason. Ferroelectr. Freq. Control **69**, 456 (2022).

[207] Y. Deng, Y. Ni, Z. Li, S. Mu, and W. Zhang, *Toward Real-Time Ray Tracing: A Survey on Hardware Acceleration and Microarchitecture Techniques,* ACM Comput. Surv. **50**, 1 (2018).

[208] S. G. Parker, J. Bigler, A. Dietrich, H. Friedrich, J. Hoberock, D. Luebke, D. McAllister, M. McGuire, K. Morley, A. Robison, and M. Stich, *OptiX: A general purpose ray tracing engine,* ACM Trans. Graph. **29**, 1 (2010).

[209] H. Ludvigsen, *Real-Time GPU-Based 3D Ultrasound Reconstruction and Visualization*, Master's thesis, Institutt for datateknikk og informasjonsvitenskap (2010).

[210] T. L. Szabo and P. Kaczkowski, *Essentials of Ultrasound Imaging* (Academic Press, London San Diego Cambridge Oxford, 2024).

[211] S. Salles, J. Shepherd, H. J. Vos, and G. Renaud, *Revealing Intraosseous Blood Flow in the Human Tibia With Ultrasound,* JBMR Plus **5** (2021), 10.1002/jbm4.10543.

[212] S. Purkayastha and F. Sorond, *Transcranial Doppler Ultrasound: Technique and Application*, Semin. Neurol. **32**, 411 (2013).

[213] F. Vignon, J. F. Aubry, M. Tanter, A. Margoum, and M. Fink, *Adaptive focusing for transcranial ultrasound imaging using dual arrays,* The Journal of the Acoustical Society of America **120**, 2737 (2006).

[214] B. D. Lindsey, E. D. Light, H. A. Nicoletto, E. R. Bennett, D. T. Laskowitz, and S. W. Smith, *The ultrasound brain helmet: New transducers and volume registration for in vivo simultaneous multi-transducer 3-D transcranial imaging,* IEEE Trans. Ultrason. Ferroelectr. Freq. Control **58**, 1189 (2011).

[215] B. D. Lindsey and S. W. Smith, *Pitch-catch phase aberration correction of multiple isoplanatic patches for 3-D transcranial ultrasound imaging,* IEEE Trans. Ultrason. Ferroelectr. Freq. Control **60**, 463 (2013).

[216] B. D. Lindsey, H. A. Nicoletto, E. R. Bennett, D. T. Laskowitz, and S. W. Smith, *Simultaneous Bilateral Real-Time 3-D Transcranial Ultrasound Imaging at 1 MHz Through Poor Acoustic Windows,* Ultrasound in Medicine & Biology **39**, 721 (2013).

[217] S. Zhou, X. Gao, G. Park, X. Yang, B. Qi, M. Lin, H. Huang, Y. Bian, H. Hu, X. Chen, R. S. Wu, B. Liu, W. Yue, C. Lu, R. Wang, P. Bheemreddy, S. Qin, A. Lam, K. A. Wear, M. Andre, E. B. Kistler, D. W. Newell, and S. Xu, *Transcranial volumetric imaging using a conformal ultrasound patch,* Nature **629**, 810 (2024).

[218] S. Vaithilingam, T.-J. Ma, Y. Furukawa, O. Oralkan, A. Kamaya, K. Torashima, M. Kupnik, I. O. Wygant, X. Zhuang, R. Brooke Jeffrey Jr, and B. T. Khuri-Yakub, *Investigating large 2D arrays for photoacoustic and acoustic imaging using CMUT technology,* in *2008 IEEE Ultrason. Symp.* (2008) pp. 1238–1241.

[219] L. Guasch, O. Calderón Agudo, M.-X. Tang, P. Nachev, and M. Warner, *Full-waveform inversion imaging of the human brain,* npj Digit. Med. **3**, 1 (2020).

[220] U. Taskin and K. W. A. van Dongen, *3D redatuming for breast ultrasound,* in *Med. Imaging 2020 Phys. Med. Imaging*, Vol. 11312 (SPIE, 2020) pp. 1357–1362.

[221] Y. Zhao, N. Zhang, X. Lu, Y. Yuan, and Y. Shen, *Cross-correlation Full Waveform Inversion for Sound Speed Reconstruction in Ultrasound Computed Tomography,* in *2022 44th Annu. Int. Conf. IEEE Eng. Med. Biol. Soc. EMBC* (2022) pp. 3043–3046.

[222] T. Robins, J. Camacho, O. C. Agudo, J. L. Herraiz, and L. Guasch, *Deep-Learning-Driven Full-Waveform Inversion for Ultrasound Breast Imaging,* Sensors **21**, 4570 (2021).

[223] J. Ren, J. Li, S. Chen, Y. Liu, and D. Ta, *Unveiling the potential of ultrasound in brain imaging: Innovations, challenges, and prospects,* Ultrasonics **145**, 107465 (2025).

[224] J. Ren, J. Li, C. Liu, S. Chen, L. Liang, and Y. Liu, *Deep Learning With Physics-Embedded Neural Network for Full Waveform Ultrasonic Brain Imaging,* IEEE Trans. Med. Imaging **43**, 2332 (2024).

[225] W. Jiang and Y. Lin, *QuGeo: An End-to-end Quantum Learning Framework for Geoscience — A Case Study on Full-Waveform Inversion,* in *Proc. 61st ACMIEEE Des. Autom. Conf.*, DAC '24 (Association for Computing Machinery, New York, NY, USA, 2024) pp. 1–6.

[226] J. R. Krebs, J. E. Anderson, D. Hinkley, R. Neelamani, S. Lee, A. Baumstein, and M.-D. Lacasse, *Fast full-wavefield seismic inversion using encoded sources,* GEOPHYSICS **74**, WCC177 (2009).

[227] S. Patz, D. Fovargue, K. Schregel, N. Nazari, M. Palotai, P. E. Barbone, B. Fabry, A. Hammers, S. Holm, S. Kozerke, D. Nordsletten, and R. Sinkus, *Imaging localized neuronal activity at fast time scales through biomechanics,* Sci. Adv. **5** (2019), 10.1126/sciadv.aav3816.

[228] S. Mishra, B. Deng, W. S. Hoge, Y. Tie, G. Annio, R. Sinkus, and S. Patz, *Imaging Neuronal Activity at Fast Timescales in Humans using MR Elastography,* in *ISMRM* (2022).

[229] C. Labuda, W. R. Newman, B. K. Hoffmeister, and C. K. M. Chambliss, *Two-dimensional mapping of the ultrasonic attenuation and speed of sound in brain,* Ultrasonics **124**, 106742 (2022).

[230] S. J. Sanabria, M. B. Rominger, and O. Goksel, *Speed-of-Sound Imaging Based on Reflector Delineation,* IEEE Trans. Biomed. Eng. **66**, 1949 (2019).

Curriculum Vitæ

Rick Waasdorp

September 21, 1995	Born in Heemstede, The Netherlands

Education

2007-2013	*Lyceum Sancta Maria, Gymnasium* Haarlem, The Netherlands
2013-2017	BSc. Mechanical Engineering *Delft University of Technology* Delft, The Netherlands
2017-2019	MSc. Mechanical Engineering (Cum laude) *Delft University of Technology* Delft, The Netherlands

Experience

2017	Intern R&D Department *Festool GmbH* Wendlingen, Germany
2020-2025	PhD. in Applied Physics *Delft University of Technology* Delft, The Netherlands

Awards

- Best Graduate 3mE faculty TU Delft – 2020
- Philips & KHMW Graduation Prize Technology for Healthcare Solutions – 2020
- ZonMw IMDI Talentaward – 2019-2020
- Steven Hoogendijk Thesis Award – 2019-2020
- Young Medical Delta Thesis Award – 2021
- IEEE UFFC-JS Student Poster Award – 2024

List of Publications

Journal Publications

Included in this thesis.
Won an award.

- Waasdorp, Rick, Oscar van den Heuvel, Floyd Versluis, Bram Hajee, and Murali Krishna Ghatkesar. 2018. “Accessing Individual 75-Micron Diameter Nozzles of a Desktop Inkjet Printer to Dispense Picoliter Droplets on Demand.” RSC Advances, 8(27), 14765-74.
- Waasdorp, Rick, Winfred Mugge, Hendrik J. Vos, Jurriaan H. de Groot, Nico de Jong, Martin D. Verweij, Alfred C. Schouten, and Verya Daeichin (2019). “Tracking Electromechanical Muscle Dynamics Using Ultrafast Ultrasound and High-Density EMG.” Pp. 2137-40 in Vols. 2019-Octob.

Waasdorp, Rick, Winfred Mugge, Hendrik J. Vos, Jurriaan H. de Groot, Martin D. Verweij, Nico de Jong, Alfred C. Schouten, and Verya Daeichin (2021). “Combining Ultrafast Ultrasound and High-Density EMG to Assess Local Electromechanical Muscle Dynamics: A Feasibility Study.” IEEE Access 9:45277-88.

Waasdorp, Rick, David Maresca, and Guillaume Renaud (2024). “Assessing Transducer Parameters for Accurate Medium Sound Speed Estimation and Image Reconstruction.” IEEE Transactions on Ultrasonics, Ferroelectrics, and Frequency Control 71(10):1233-43.

- Matalliotakis, Agisilaos, Rick Waasdorp, Martin D. Verweij, and David Maresca (2024). “Impact of Wavefront Shape on Nonlinear Ultrasound Imaging of Monodisperse Microbubbles.” Physical Review Applied 22(3):034062.
- Terwiel, Dion, Byung Min Park, Baptiste Heiles, Rick Waasdorp, Eleonora Muñoz-Ibarra, Tarannum Ara, Valeria Gazzola, and David Maresca (2025). “Acoustic pH Sensor for Dynamic Ultrasound Imaging of Cellular Acidification.” bioRxiv January 27, 2025.

Heiles, Baptiste, Flora Nelissen, Dion Terwiel, Byung Min Park, Eleonora Munoz Ibarra, Agisilaos Matalliotakis, Rick Waasdorp, Tarannum Ara, Pierina Barturen-Larrea, Mengtong Duan, Mikhail G. Shapiro, Valeria Gazzola, and David Maresca (2025). "Nonlinear sound-sheet microscopy: imaging opaque organs at the capillary and cellular scale." Science, 388 (6742), eads1325.

Rick Waasdorp, Eleonora Muñoz-Ibarra, Flora Nelissen, Baptiste Heiles, Valeria Gazzola, Guillaume Renaud and David Maresca (2025). "Adaptive transcranial ultrasound Doppler imaging of the brain." bioRxiv May, 2025.

Rick Waasdorp, Twan Gouwerok, Eleonora Munoz Ibarra, Flora Nelissen, Valeria Gazzola, David Maresca and Baptiste Heiles. 2025. "Selective-plane Functional Ultrasound Neuroimaging" bioRxiv June, 2025.

- Panskus R, Velea AI, Holzapfel L, Pavlou C, Li Q, Qin C, Nelissen FM, Waasdorp R, Maresca D, Gazzola V, Giagka V. Ultrasound transparent neural interfaces for multimodal interaction. bioRxiv. 2025 Jul 18:2025-07.
- Favre, Hugues, Berendsen, Merijn, Waasdorp, Rick and Maresca, David (2025). A compact 2D matrix array comprised of hexagonal transducer elements for fast volumetric ultrasound imaging. IEEE Transactions on Ultrasonics, Ferroelectrics, and Frequency Control.

Conference Contributions

- Rick Waasdorp, Winfred Mugge, Hendrik Vos, Jurriaan de Groot, Martin Verweij, Nico de Jong, Alfred Schouten, Verya Daeichin, "Tracking Electromechanical Muscle Dynamics Using Ultrafast Ultrasound and High-Density EMG", IEEE IUS 2019, Glasgow, Scotland.
- Rick Waasdorp, Baptiste Heiles, Floor Nelissen, Valeria Gazolla, Guillaume Renaud, David Maresca, "Skull-aberration correction for high contrast transcranial Doppler neuroimaging", fUSBrain 2022, Corsica, France.
- Rick Waasdorp, Baptiste Heiles, Flora Nelissen, Valeria Gazzola, Guillaume Renaud, David Maresca, "Skull-Aberration Correction for High Contrast Transcranial Doppler Neuroimaging", IEEE IUS 2022, Venice, Italy.
- Rick Waasdorp, Baptiste Heiles, Xin Tan, Floor Nelissen, Valeria Gazolla, Guillaume Renaud, David Maresca, "Skull-aberration correction for high precision transcranial sonogenetics", ISBUS 2022, Pasadena, CA, United States.
- Rick Waasdorp, David Maresca, Guillaume Renaud, "Correcting for transducer lens refraction enables high-resolution quantitative imaging", Artimino 2023, Artimino, Italy.
- Rick Waasdorp, David Maresca, Guillaume Renaud, "Estimating Transducer Lens Properties for Higher Resolution Imaging and Accurate Medium Sound Speed Retrieval", IEEE IUS 2023, Montreal, Canada.
- Rick Waasdorp, Eleonora Muñoz-Ibarra, Baptiste Heiles, Flora Nelissen, Valeria Gazzola, Guillaume Renaud, David Marescsa Lecture & Poster: "Skull-Aberration Correction for Non-Invasive Doppler Imaging of the Rat Brain", ESSPA 2024, Corsica, France.
- Rick Waasdorp, Eleonora Muñoz-Ibarra, Baptiste Heiles, Flora Nelissen, Valeria Gazzola, Guillaume Renaud, David Marescsa Lecture & Poster: "Skull-Aberration Correction for Non-Invasive Doppler Imaging of the Rat Brain", IEEE UFFC-JS 2024, Taipei, Taiwan.
- Baptiste Heiles, Floor Nelissen, Dion Terwiel, Byung Min Park, Eleonora Munez-Ibarra, Rick Waasdorp, Pierina Barturen, Mengtong Duan, Taranum Ara, Mikhail Shapiro, Valeria Gazzola, David Maresca, "Fast Volumetric Nonlinear Sound Sheet Imaging of Cellular and Microvascular Functions", IEEE UFFC-JS 2024, Taipei, Taiwan.
- Rick Waasdorp, Twan Gouwerok, Eleonora Muñoz-Ibarra, Flora Nelissen, Valeria Gazzola, Baptiste Heiles, David Maresca, "Selective Plane Functional Ultrasound Using Sound-Sheet Imaging", IEEE UFFC-JS 2024, Taipei, Taiwan.

Acknowledgments

Doing a PhD is a rollercoaster full contradictions, ups and downs, joy and frustration, confusion and clarity. But, it is a unique chance to work at the forefront of science, pushing boundaries of your knowledge, and above all, meet amazing people along the way. Especially the latter has made my PhD journey unforgettable, and in this section I would love to express my heartfelt gratitude to all the people that made this possible.

Starting with my supervisors. I would like to express my deepest gratitude to **David**. We met at a conference in Glasgow in 2019, where you told me about your previous work in ultrasound brain machine interfaces. Still new to the world of ultrasound, I was immediately fascinated by the possibilities of ultrasound that were way beyond traditional imaging. After a series of emails, I joined your young lab in Delft, where together with **Baptiste**, **Dion**, **Alina**, and **Tarannum** we built up our new research infrastructure. You were always available for discussions, and had the ability to motivate me to push forward, even when faced with setbacks. I am grateful for the freedom you gave me to explore, and look back on a fruitful collaboration. **Guillaume**, I am grateful that you joined as co-supervisor. You introduced me to the world of ultrasound ray tracing, nonlinear simulations and many more ultrasound techniques. Your expertise and guidance have been invaluable in shaping my research and become the scientist I am today. Your door was always open, and I appreciated our quick technical discussions that allowed me to have new insights and come up with new solutions. Finally, **Nico**, thank you for your guidance in the final stage of this thesis, and the fun discussions in forming the propositions accompanying this thesis. Your years of experience in seeing PhD students come and go, brought very valuable insights regarding the planning of the final stage of the thesis. Thanks for that.

To my **thesis committee**, thanks for reading my work and I look forward to our interesting discussion during the defense. Some of you I have met before, in projects or conferences. Like **Alfred**, whom I met during my master's thesis and who set me on an academic career track by awarding my work a perfect score. I'm grateful that you can now also be part of this final moment, given your excellent capabilities in judging my work. The project we worked on, I presented at the IUS conference in Glasgow, where I showed up as a total newbie. After my talk, I remember **Thomas** coming up to me and asking, "do you know this related work we did in Paris". Yes I did, though back then, I didn't yet know that you were supposed to cite papers on your slides. I'm happy that, like Alfred, you can now also be part of this defense. I'm grateful to all committee members for your time and effort in making this day so memorable.

Then, I would like to express my gratitude to all people that continuously supported me and all other colleagues in the group, making our workspace a great environment to work in. First of all, **Angela**, thank you for the support along the way, but mainly for our fun chats about life, our shared love for Italy, and organizing fun group outings that brought

all colleagues closer together. If there is ever an MI group reunion, let's go bowling, and I will try to finally beat you. To **Kelly** and **Annelies** thanks for always being there to assist with practical and administrative issues. Thanks to you both, these never formed a barrier and allowed continuous progress. To **Henry**, thanks for your endless patience. I know I have asked your many times to help me with impossible wire phantoms, and very often came with last minute requests. But you always came through with a smile on your face. Your love for cycling and your crazy trip to the Noordkaap is inspiring, and if I ever dare to take on such a trip, I would love to hear your tips and tricks. **Ronald**, thanks for being a constant source of positivity in our group, and always having an open door for questions or remarks. I always enjoyed our quick chats about compilation issues, cluster challenges, and life in general. Your laughter and loud voice echoing through the hallways always brought a smile to my face. **Karin**, thanks for your patience and perspective when I was trying to do it all at once. Your help in navigating grant applications, and making me rethink whether it was good timing to apply, was highly appreciated.

To the other PIs in Delft and Rotterdam, **Rik**, **Hans**, **Martin**, **Sebastian**, **Frans**, **Qian**, thank you for the interesting discussions, fun hallway chats and making our research environment a great place to be.

To my dear colleagues from the lab, thank you for the fun times, discussions and support along the way. From our own lab, **Alina**, **Min**, **Lumen**, **Olivia**, **Myrthe**, thanks for the fun lab meetings, coffee breaks and lunch discussions. To **Xin** and **Twan**, my first students, I hope my chaos was manageable. Thanks for giving me the chance to mentor you and teach me how to be a better supervisor, and I truly enjoyed seeing your progress. To the new generation, **Djalma**, **Ayda**, **Ilaria**, **Maša**, **Paulina**, **Chiara**, **Niccolò**, **Berat**, **Sabiju**, **Xiufeng**, and the older generation, **Verya**, **Boudewien**, **Fabian**, **Moein**, **Jack**, **Ulas**, **Martijn**, thanks for the lunch discussions, interesting MI seminars, coffee breaks and fun times at the MI retreats or impromptu beers throughout the year. **Martina**, thank you for the jolly good times at parties, and our pointless but hilarious conversations ranging from dissecting social dynamics, observing absurd internet trends, or reflecting on life decisions. **Chiara**, thanks for showing us around in Rome, what an experience to visit this majestic city with a local, showing us the hidden gems. Your stamina for walking all day long, climbing all those stairs to the top of the monuments, and still being able to party all night long is impressive. **Ayda**, thanks for giving the chance to experience the inside of an MRI scanner. Lying still for such a long time is not my forte, but maybe made me appreciate ultrasound even more. **Chih-Hsien** thanks for showing us around in Taiwan, introducing us to the amazing food at the Taipei night markets, bringing us to the most local Taiwanese restaurant, and the fun times during the dozens of king Tigers we shared.

To my office mates. **Dion**, thanks for all the fun times building the lab together, chatting about surfing, turning me into a car mechanic merely by explaining the challenges you faced with your good old cars and camper van, our boulder sessions, and for always being up for a good laugh or sharing some of the best fermented Indonesian coffee. **Gabrielle** thanks for your positive energy in our office, and our reflecting chats about life, politics, science, and being the person I could go into deep conversations about ray tracing and aberration correction. **Hugo**, your ability to simulate ultrasound wave propagation during

breaks is impressive. At least, that's how I always perceived you when you were zoning out during lunch breaks. But in between those simulations, I truly enjoyed our conversations about science, your invitation to join de Meerkoeten (a resounding success for both of us), and of course our bouldering sessions. But mostly, our adventures during the cyclone in Taiwan, walking through flooded streets, and ending up in a laundromat karaoke bar will remain unforgettable. Not sure if we ever managed to finish Inception.

Eleonora, a big, big thanks for the fun times and good conversations at and off work. I have very fond memories of our experiments together in Amsterdam. Although we were faced with many challenges, your patience and positivity, and our way of working together, listening to each other, while enjoying psychedelic salsa, was truly a special experience. Also traveling to conferences together was a blast. I will never forget the time you brought me a cup of tea during my poster presentation, when I had zero moment to catch my breath. Thank you for that and all other moments of support.

Then, **Agis**, one of my partners in many crimes. We met during my master thesis, where your first advice to me was: don't do a PhD. I ignored that advice, and although there were moments I wished I had listened to you, I am also very glad I didn't. Because then I would have missed out on all the fun times during conferences, and all other adventures outside work. I am sorry for giving you the chance to break your leg, and obstructing your path to become beast. But thank you for all the fun times we had together, meeting your family in Crete, biking through LA, and the many, many beers we had. All that made the PhD journey so much more enjoyable, and I wouldn't have wanted to miss it.

Then onto my other partner in crime, mister **Baptiste**. Where to start. You are truly an amazing person, and I am so glad that I could work together with you during these crazy years. From working in the lab, setting up experiments and infrastructure, endless coding sessions, git mistakes, mad surgeon skills, work was a pleasure with your voice of reason around. But, it was the fun times outside work where we truly bonded. Dinner with **Laura**, a trip to the School, Beach barbecue with **Agis** where sand-equalizer tractors almost liquidized us. And then we became even more crazy by combining work with fun, working late night shifts in a sinister basement lab in LA, finished by a beer next to a deserted play ground. There are too many memories to list here, but you are an amazing person that taught me so much, and I am grateful to call you my friend.

During my PhD I had the chance of meeting amazing neuroscientists at the NIN in Amsterdam. **Valeria**, your positivity and kindness made a lasting impression on me. I truly enjoyed our brief chats in the hallways prior to my experiments, your funny rope jumping tips, and of course our more serious chats about our research and paper revisions. Together with **Christian**, you made me feel very welcome at the NIN, as part of the team, making all the trips through rush hours worth it. This allowed me to be embedded in the fUSI team, where together with **Floor**, **Lorenzo**, **Camilo**, **Chaoyi**, **Ali**, **Qingying**, we had a blast in setting up the ultrasound experiments, solving TTL synchronization puzzles, and building an analysis pipeline. Your help and patience in teaching me the intricacies of fUSI, and coping with me asking again and again if you could turn on that one pc deeply buried in the animal facility, was highly appreciated. Also, the other people in the office made me feel very welcome **Fred**, **Judith**, **Cas**, **Francisca**, **Rajeev**, **Paloma**, and thanks

for the fun times in the office. But a trip to the NIN was not complete without drinks after, with forever lasting memories of the infamous cafe-rave, together with **Janne** and **Daniel**. **Francisca** thanks for hosting the lovely family dinners and your positivity and warmth. **Laura**, glad we didn't die cycling back from a party, and your persistence surrounding tablegate. Amsterdam gang, thanks for all the good vibes.

I am also grateful that I have met so many amazing people during conferences around the world. First conference after COVID in Cargèse, Corsica. Meeting the people from the papers, **Pieter**, **Thomas**. Spending nights at Au Bon Accueil, having drinks and deep conversations about life with the team from Rotterdam, **Sadaf**, **Bas**, **Luuk**,**Aybüke** (We will still do the promised boat trip ;). The fun trips to the beach, together with **Tudor**, were a nice offset from the seriousness during the day, and I have very fond memories of those moments. Then later doing it all over again in Venice, and going on a true Venice Bender after (right?) the conference program. It seems that the most fun conferences were always under the Mediterranean sun, with again unforgettable moments in Artimino with **Hein**, **Gonzalo**, **Clotilde**, **Yichuang** and **Geraldi**. But what can you expect from a conference organized at a vineyard. And last but not least **Thomas Szabo**, thank you for your interesting questions after my presentations, and of course your present of the latest version of your book on ultrasound imaging.

Switching gears to het normale leven. Begrijp me niet verkeerd, wetenschap is geweldig en kan zeker een groot deel van mijn tijd in beslag nemen, maar ontspanning en warme vriendschappen daarbuiten hebben mijn leven in balans gehouden. Ik voel me enorm gelukkig dat ik in mijn leven nu al zoveel lieve mensen om me heen heb verzameld. Dit stuk is voor jullie <3.

Een prettige woonplek is een van de belangrijkste factoren voor een gelukkig leven, aldus Maslow. Hoewel geen pyramide, hebben **Anna** en **Bart** een fijne plek waarin ik op een boerderij in de buurt van Delft, in alle rust aan mijn proefschrift kon werken. Dank jullie voor de luchtige en soms diepere gesprekken als ik thuis kwam na een lange dag werken. Dat was altijd een aangename overgang om de gedachtentrein even stil te zetten en de ontspanning op te zoeken.

Special thanks to **Menno**, die ik in mijn tijd in Delft heb leren kennen als goeie sparpartner van alle vraagstukken in het leven. Niets is je te gek. Je maakte de barbersessies bijna therapeutisch.

Thanks **Vishal** for the fun during our master projects, but mostly the fun chats about life, sharing your passion for music, art and history, and also being there for a stress relieve with some old classic video games or Call of Duty session.

Daarin zijn natuurlijk ook de **Achtervolgers** niet te vergeten. Bedankt voor de gezellige schaatsavonden, waarin we samen menigeen een hartaanval hebben bezorgd met het opzoeken van kleine ruimtes in de binnenbocht. Was er eigenlijk wel ruimte? Gelukkig is een strike ons nog bespaard gebleven. De vele (nouja veel) kilometers die we samen hebben afgelegd hebben me niet alleen fysiek sterker gemaakt, maar ook mentaal leeggetrokken. De perfecte manier om de kop leeg te maken na een lange werkdag. Als we tenminste niet te diep in de fles Schipperbitter kijken, of niet te gecompliceerde nieuwe app ideeën

produceren.

Over te diep in de fles kijken hoef je het met het **Partyplanningcomittee** niet te hebben. Tot de bodem en daarvoorbij. Dit is een club van mensen met wie je wel een feestje kunt bouwen. Random feestjes, weekenders, afters, ik heb genoten van alle momenten die we samen hebben beleefd, en de diepe conversaties die we daar hebben gevoerd, en de vlarden die we daar soms van hebben opgevangen. Jullie zijn allemaal toppers, en ik hoop dat we in de toekomst weer op een of andere rave staan te viben.

Mijn lieve huisgenootjes van **Laprowa**, bedankt voor de ontzettend fijne tijd in ons fijne studentenhuis. Ik had me geen leukere groep kunnen wensen om mee samen te wonen. Het voelt soms echt alsof we een gezin zijn, en ik geniet er altijd ontzettend van dat we ook nu allemaal heel andere dingen zijn gaan doen, nog steeds als vanouds verder kunnen als we op huisweekend of -vacance gaan. Van Karaokeith, spelletjes en bonte avonden, en de ontelbare etentjes. Sorry voor sommige huisgenoten dat het wat vaak over Matlab ging, maar ja wij nerds kunnen er niks aan doen dat Matlab ons leven beheerst.

Dan de lieve **Djensers**. Sommigen al deccenia in mijn leven, en met fantastische nieuwe aanwas door de jaren heen. Ik heb altijd ontzettend genoten van onze studeersessies in het Mraum, waar toch enigszins het fundament voor mijn wetenschappelijke carrière is gelegd, toen ik zelf nog in de ontkenningsfase zat. De chinos of dubbele essies met daarna pauze in de geheime kamer, hebben me gemotiveerd gehouden. Maar vooral bij de lijm op de bank van de BP begon de zon weer te schijnen. Van wintersport, etentjes, borrels, ik kan altijd ontzettend met jullie lachen, en op boevenpad. De Mooserwirt glazenkast is volgens mij leeg. Mede dankzij jullie heb ik de keuze gemaakt aan de PhD te beginnen, maar zeker dankzij jullie heb ik de PhD overleefd. Ben benieuwd wat er nu op de kaart staat.

Andy en **Caro**, jullie zijn echt geweldige mensen. Jullie stonden altijd klaar in moeilijkere tijden, en in de goede tijden hebben we ontzettend veel leuke dingen gedaan. De Liquido piano solo staat nog altijd in mijn geheugen gegrift. Net als de fantastische tijd in Oostenrijk, onze zeiltripjes op de plas, en natuurlijk heerlijke klussessies. Koop een boot... Bewonderenswaardig hoe jij, Andy, zo ongeveer zelf de Ferryman bent geworden. Ik hoop dat we nog veel meer avonturen samen mogen beleven waar jullie ook zijn.

Jordin en **Bingbing**, JBeast en silly p, dank jullie voor alle gezellige avonden vol schuine grappen, heerlijke etentjes, en de ontzettend bijzondere trip naar China voor jullie bruiloft. Wat een fantastische ervaring. Maar ook dichter bij huis, was het altijd een feest om jullie te zien, met gedeelde passie voor lekker eten, wijntjes en sporten.

Daphne mijn lieve overbuuf, dank voor je steun en onvoorwaardelijke vriendschap. Je bent er altijd voor me als ik dat nodig heb, en daarnaast hebben we het ontzettend gezellig. Of we nu appels gaan plukken, op avondtuur gaan naar Renesse, of een huurauto klem rijden, we hebben het altijd naar ons zin. Ik kijk nu al uit naar de volgende sportwedstrijd die we gaan kijken, en natuurlijk de zeilwedstrijd met **Veroniek** die toch al snel op het programma zal staan.

Lieve **Isabel**, je bent mijn allerwijste vriend, en ik ben zo blij dat we elkaar hebben leren kennen. Het is zo fijn om af en toe met je te kunnen sparren over belangrijke levensvragen, en het is zo ontzettend bijzonder hoe je daar direct op inspeelt met je wijze raad. Je bent

ontzettend krachtig en lief, en, ookal zul je dat nooit vragen, ik ben er altijd voor je om je te steunen of te helpen.

Dat was wel een bijzondere verassing, toen we hoorden dat we kennelijk samen zouden gaan werken aan een ultrasound project. **Floor**, al vanaf het eerste moment klikte het tussen ons, en nu na vier jaar samen werken en daarnaast heel wat avondturen verder, lijkt het alsof we elkaar al eeuwen kennen. Je bent echt een fantastische collega en vriendin geworden, en ik ben je ontzettend dankbaar voor alle reflectie momenten, belletjes als het even niet mee zat, en alle super gezellige momenten die we hebben beleefd. Van veranda struikel tot met mijn neus in de muizen uitwerpselen in het lab, alles was hilarisch met jou erbij. Ik begin niet eens over de feestjes met ook je lieve vriend **Ties** want dan wordt dit stuk te lang. Of, nou ja, te lang, wat zijn eigenlijk de regels, **Hasko**? En nu ben je mijn paranimf, wat een eer om straks samen daar vooraan te staan. Zonder jou waren deze laatste jaren niet hetzelfde geweest.

Lindert, maatje, bedankt voor je vriendschap, alle gezellige etentjes, schaatssessies, zeil avondturen, en de vele onderzoekende gesprekken die we hebben gevoerd. Je scherpe kijk op de wereld, nieuwsgierigheid en het stellen van vragen over dingen die simpel lijken maar uiteindelijk als je tot op de bodem gaat ontzettend complex blijken te zijn, hebben ontzettend veel leuke avonden opgeleverd. Zo is het nou eenmaal is nou eenmaal niet genoeg voor ons. Maar ook je belletjes aan het einde van de dag, als ik nog tot laat aan het doorwerken was, waren een heel fijne manier om de dag gezellig af te sluiten, en ervandoor te gaan. Ik ben ontzettend blij dat je nu mijn paranimf bent, en me zo hebt gesteund in de laatste fase van mijn proefschrift.

Lieve **Tessa**, mijn lieve schat, wat ben ik ontzettend blij dat ik jou in mijn leven heb. Je onvoorwaardelijke liefde, en steun helpen me zo ernorm bij alles wat ik doe. Ik zou niet weten hoe ik zonder jou de afgelopen jaren door had moeten komen. Je staat altijd voor me klaar, weet me uit dalen te trekken en hebben zoveel lol samen. Je bent zo krachtig, slim, lief, en doortastend, dat je me zelfs weet te helpen als ik dat niet toelaat. Je laat me zien wat echt belangrijk is in het leven, en ik ben zo ontzettend trots op alles wat je doet. Nu zijn we dubbel dokter, een lange weg waarin we zoveel hebben meegemaakt (Tron), en ik kijk uit naar alle momenten die we samen gaan beleven in de toekomst. Ik hou van je.

Lieve **pap** en **mam**, ik ben jullie zo dankbaar voor de onvoorwaardelijke steun en liefde die jullie me altijd hebben gegeven. Al mijn hele leven zijn jullie er voor me als ik me weer druk maak over van alles en het even niet meer zie. En daarnaast hebben we het zo gezellig als we samen zijn, hele dagen zitten we te kletsen en te geinen over van alles, en dat geeft me altijd een warm gevoel en weer nieuwe energie. Ik hou ontzettend veel van jullie en ben zo dankbaar dat ik jullie als ouders heb. Als er iets is wat ik van jullie heb geleerd, is het om altijd in mezelf te blijven geloven. jullie beiden hebbe me geleerd is om altijd in mezelf te blijven geloven, en nooit op te geven. Lieve pap, dank voor je vele relativerende en motiverende gesprekken, dat heeft me zo geholpen om door moeilijkere periodes heen te komen. Lieve mam, we hebben behoorlijk wat mee gemaakt, maar je doorzettingsvermogen, liefde en humor zijn zo bizar krachtig, dat ik met jou aan mijn zij de wereld aan kan.

Lieve pap, lieve **André**, wat mis ik je ontzettend, en het is zo ontzettend jammer dat ik dit moment niet met je kan delen. Maar ik weet dat je ontzettend trots op me zou zijn, en ik heb je voor altijd bij me.

Rick
Delft, October 2025